

**CONTROLLED THERMONUCLEAR RESEARCH
ANNUAL REPORT**

November 1, 1973

Prepared for U.S. Atomic Energy Commission under contract No. W-7405-Eng-48



**LAWRENCE
LIVERMORE
LABORATORY**

University of California/Livermore

MASTER

DISTRIBUTION OF THIS DOCUMENT IS UNLIMITED

NOTICE

"This report was prepared as an account of work sponsored by the United States Government. Neither the United States nor the United States Atomic Energy Commission, nor any of their employees, nor any of their contractors, subcontractors, or their employees, make any warranty, express or implied, or assume any legal liability or responsibility for the accuracy, completeness or usefulness of any information, apparatus, product or process disclosed, or represents that its use would not infringe privately-owned rights."

Printed in the United States of America
Available from
National Technical Information Service
U. S. Department of Commerce
5285 Port Royal Road
Springfield, Virginia 22151
Price: Printed Copy \$ *; Microfiche \$0.95

*Pages	NTIS Selling Price
1-50	\$4.00
51-150	\$5.45
151-325	\$7.60
326-500	\$10.60
501-1000	\$13.60

TID-4500, UC-20
Controlled Thermonuclear
Processes



LAWRENCE LIVERMORE LABORATORY
University of California, Livermore, California, 94550

UCRL-50002-73

CONTROLLED THERMONUCLEAR RESEARCH ANNUAL REPORT

MS. date: November 1, 1973

NOTICE

This report was prepared as an account of work sponsored by the United States Government. Neither the United States nor the United States Atomic Energy Commission, nor any of their employees, nor any of their contractors, subcontractors, or their employees, makes any warranty, express or implied, or assumes any legal liability or responsibility for the accuracy, completeness or usefulness of any information, apparatus, product or process disclosed, or represents that its use would not infringe privately owned rights.

MASTER



Contents

Abstract	1
I. Theoretical Studies	1
Introduction (L. D. Pearlstein)	1
Mirror Research	2
Computations of Plasma Equilibria in Minimum-B Mirror Devices (J. Killeen, M. E. Resnick, and C. Tull)	2
A Two-Dimension (2-D) Multi-Species Fokker-Planck Code (R. L. Berger, J. Killeen, and A. A. Mirin)	3
Separated Multi-Species Code (A. A. Mirin and J. Killeen)	3
Z-Dependent Fokker-Planck Code (A. A. Mirin and J. Killeen)	3
Guiding Center Plasma Equilibrium (L. S. Hall and B. McNamara)	4
The MHDEQU 3D Plasma Equilibrium Codes (L. S. Hall, B. McNamara, and D. Fuss)	4
Some Observations on Mirror Losses (A. H. Futch and J. R. Hiskes)	5
Numerical Studies of Advanced Mirror Devices (R. P. Freis and R. W. Moir)	5
Stability Theory	6
Effects of Electron Temperature and Finite Ion Larmor Radius on Rosenbluth-Post Convective Loss Cone Instability (D. E. Baldwin and R. C. Harding)	6
Effect of Electron Diffusion on the Drift Cone Mode (D. E. Baldwin and H. L. Berk)	6
Line Loading in High Density Mirror Machines (H. L. Berk)	6
Geometric Effects on Drift Cone Modes (D. E. Baldwin and R. P. Freis)	6
Model for Electron Diffusion Stabilization of Drift Cone Mode (D. E. Baldwin, B. McNamara, S. L. Rempel)	7
Electron Scattering by Enhanced Fluctuation in Quiescent 2XII Decay (R. E. Aamodt and D. E. Baldwin)	7
Open J-Surfaces in Baseball and its Implication for Stability (H. L. Berk)	7
Modified Negative Mass Instability During Beam-On (L. D. Pearlstein)	7
Electron Beam Heating	9
A New Electromagnetic Relativistic Plasma Simulation Code (A. B. Langdon and B. F. Lasinski)	9
Plasma Heating by Electromagnetic Waves and Electron Beams (A. B. Langdon, B. F. Lasinski and W. L. Kruer)	10
General	11
Calculations of Magnetic Surfaces and Single Motion in the Spire Stellarator (R. P. Freis and C. W. Hartman)	11
Transport in Axisymmetric Plasma (D. E. Shumaker, J. Killeen, and W. A. Newcomb)	11
Simulation of Transient Phenomena in Toroidal Devices (T. H. Johnson and J. Killeen)	11
Time Dependent Resistive Instability Calculations (J. A. Dibiase and J. Killeen)	12
Magnetic Fields near an Axis (B. McNamara and D. Fuss)	12
Additions to the MAFCO Coil Design Code (B. McNamara and C. H. Finan)	13
Efficient Use of Disc for Large Programs (B. McNamara and A. B. Langdon)	13
Reexamination of Cascade Calculations (K. H. Berkner and J. R. Hiskes)	13
Simulation of Pulse Trapping and Pulse Stacking in Astron (J. A. Byers, A. B. Langdon, J. Killeen, A. A. Mirin, M. A. Resnick, C. G. Tull)	13
Drift Shock (W. A. Newcomb)	13

II. Mirror Program	14
Introduction and Summary (R. F. Post)	14
Baseball II (C. C. Damm, J. H. Foote, A. H. Futch, R. K. Goodman, F. J. Gordon, G. W. Hamilton, A. L. Hunt, J. E. Osher, G. D. Porter, A. L. Gardner, D. O. Overskei, A. A. Mitin, E. G. Hooper)	15
Introduction	15
Injected Beam	16
Vacuum Conditions	18
Diagnostic Techniques and Instrumentation Development	20
Microwave Interferometer	20
Microwave Radiometer	22
Energy Analyzer	24
Possible Corrections to Secondary Emission Signals from He ⁺	25
Plasma Diamagnetism	25
Three-Dimensional Measurements of Plasma Density and Plasma Potential	25
Plasma Measurements	27
Instability Threshold	27
Particle-End-Flux Measurements	29
Particle-Balance Analysis	32
rf Measurements	33
Electron-Heating Experimentation	34
Low-Frequency Oscillations	34
Fokker Planck Calculations	35
Target Plasma Development	39
Experimental Facility	39
Buildup Calculations of Neutral Beam Injection into Target Plasma	40
Steady-State Beam Development	43
MATS III	43
Negative Ion Beams	46
Effect of Negative Ion Injection Upon Reactor Q	46
Baseball II Electrical Engineering (A. Waugh, A. Bogdanoff, and G. Vogtlin)	47
Operations	47
Baseball II Mechanical Engineering (T. Chargin, B. Denhoy, C. Henning, and B. Nelson)	48
Plasma Chamber Modifications	48
Cryogenic Facility Operation	49
Neutralizer Modifications	49
2XII (F. H. Coengsen, W. F. Cummins, A. W. Molvik, W. E. Nexsen, Jr., B. W. Stallard, and T. C. Simonen)	49
Introduction	49
Plasma Confinement in 2XII - Comparison with Theory	50
Confinement in Partially Gettered Operation	51
Electron Heating in 2XII	53
200 kW Neutral Beam Injection into 2XII	54
Electron Temperature Measurement	57
Neutral Analyzer	59
Fluctuation Measurements	61
Radial Longitudinal Density Profiles	62
Plasma Potential Measurement	62

	Data System	62
	2XII Electronic Engineering (G. E. Vogtlin, J. W. Robinson, and G. C. Tyler)	64
	Getter Element Monitor System	64
	Computer Control System	64
	Data Collection System	64
	High Voltage Switching	64
	2XIIB Coil System Electrical Design	64
	2XII Mechanical Engineering	66
	2XII General Support (C. J. Anderson)	66
	Diagnostics Development (J. R. Benapfl)	66
	50 Ampere Neutral Beam Modules (S. M. Hibbs)	66
	2XIIB Facility (R. H. Bulmer)	67
	Magnetic Field Calculations	67
	Force Calculations	67
	Materials Test and Selection	67
	2XIIB Winding and Impregnation (A. R. Harvey)	68
	2XIIB Magnet and Vacuum Assembly Design (M. C. Calderon)	69
	Direct Energy Conversion Program (W. L. Barr, M. O. Calderon, B. C. Howard, R. W. Moir, and R. R. Smith)	72
	Introduction	72
	Design of Direct Energy Conversion Test Facility	72
	Numerical Study of Periodic Focusing Direct Energy Converter	73
	"Venetian Blind" Direct Energy Converter Studies	75
III.	Toroidal Confinement Program — Superconducting Levitron (O. A. Anderson, D. H. Birdsall, C. W. Hartman, E. B. Hooper, and R. H. Munger)	75
	Introduction	75
	Hot Electron Plasma Studies	75
	Experimental Results	75
	Dense Plasma Experiments	76
	Heating Experiments	76
	Measurements of Dense Plasma Confinement	78
	Stability Theory of a Hot-Electron Plasma (H. L. Berk, C. W. Hartman, and E. B. Hooper, Jr.)	80
	Theory of Plasma Production and Heating by Energetic Electrons (R. C. Harding, C. W. Hartman, and E. B. Hooper, Jr.)	81
IV.	Astron Program	87
	Introduction (R. J. Briggs)	87
	Experimental Highlights (R. J. Briggs, R. E. Hester, G. D. Porter, J. Taska, C. W. Walker, and P. B. Weiss)	88
	Astron Beam Delay Line (N. C. Christofilos, R. E. Hester, C. A. Hurley, W. A. Sherwood, B. H. Smith, and R. L. Spoerlein)	88
	Introduction	88
	Engineering and Construction	89
	General Description	89
	Bending Magnets	90
	Vacuum System and Supports	90
	Kicker Magnet Development for the Astron 150-nsec Delay Line	91
	Operation of Delay Line	91
V.	Neutral Beam Research and Development — Berkeley (W. R. Baker, K. H. Berkner, W. S. Cooper, K. W. Ehlers, W. B. Kunkel, R. V. Pyle, and J. W. Stearns)	92

Introduction	92
Ion Sources	92
20 kV, 10A (Equivalent) D^0 Sources for the 2XII Experiment	92
Low-Voltage, 10 sec BBII Source	92
50 A D^0 Module	93
General Development	93
New Ion Extractor Optimization Program	93
Diagnostics	93
Mechanical Tolerances and Beam Focusing	93
Staging to Higher Beam Energy	94
Gas Efficiency	94
Electrical Equipment	94
VI. High-Current Neutral Beam Development at LLL (J. W. Beal)	95
VII. Plasma and Atomic Research — Berkeley	95
High-Frequency Stark Effect in Hydrogen and Helium (W. W. Hicks)	95
Theory	95
Experiment	95
Multiple-Beam Spectroscopy (? S. Rostler and B. D. Billard)	96
Beam-Plasma Interaction (R. A. Hess)	97
Berkeley Laser Plasma Experiment (T. R. Jarboe and A. F. Lietzke)	97
Introduction	97
Apparatus	97
Diagnostics	98
Results	98
Further Investigations	98
Theoretical Studies — General	98
Parallel Cascade for Beat Heating (B. I. Cohen and A. N. Kaufman)	98
Space Time Analysis of Nonlinear Interaction of Opposed Electromagnetic Waves (B. I. Cohen)	98
VIII. CTR Technology	99
Reactor Studies (R. W. Werner, G. A. Carlson, J. D. Lee, P. B. Mohr, M. A. Peterson, J. Hovingh and R. W. Moir)	99
200-MWe Reactor System Design Study	99
Reactor Component Studies	99
Liquid Metal Loop Experiment	99
Small Angle Scattering and Selective Leakage	99
Blanket Designs for Mirror Machines	99
Electrical Losses in Collectors	100
Vacuum Pumping the Collector Region	100
Recovery of Residual Ion Energy in Collectors	100
Injector System Study	100
Fusion-Fission Hybrid Reactors	100
Materials (P. B. Mohr and C. Logan)	101
Radiation Damage in 304 Stainless Steel using 5-MeV N_2^{++} Ions	101
Proton Simulation of 14-MeV Neutron Effects	101

	CTR Tritium Technology (R. Hickman)	101
	Examination of Tritium Problems	101
	Insulator/Lithium Compatibility Problem	102
	Hydrogen Diffusivity in Lithium	103
	Magnet Technology	103
	Magnets for Open-Ended Fusion Reactors (R. W. Moir and C. E. Taylor)	103
	Superconducting Magnet Development (C. D. Henning, R. L. Nelson, and C. O. Ward)	103
IX.	Talks and Publications	108
	Talks	108
	Publications	112
	Theses	114
X.	References	115

CONTROLLED THERMONUCLEAR RESEARCH ANNUAL REPORT

Abstract

The Controlled Thermonuclear Research (CTR) program at Lawrence Livermore Laboratory (LLL) during FY 1973 has resulted in several significant encouraging developments which have re-focused the mirror program. These include demonstrations in 2XII, a pulsed, compression-heating experiment of quiescent hot, dense plasma which decays at a rate which is nearly classical and which can be theoretically explained. High-current (10 A, 20 keV) neutral beam injection was initiated with encouraging results. These observations and the rapid progress of our high-current beam development program have resulted in plans to re-build 2XII for very high-current beam heating experiments. In BBII, a d.c. experiment with a superconducting magnet, extremely good vacuum conditions have allowed charge-exchange effects to be greatly reduced, and classical decay rates are observed. Investigation of target plasma possibilities for enhancing buildup has begun.

The Astron program was terminated in February 1973 in order to direct more efforts to other experiments. E-layers with about half the strength required for field reversal were achieved.

The Superconducting Levitron was also discontinued at the end of FY 1973 for similar reasons. During the year, dense high- β hot electron plasma confinement

was achieved and progress was made toward heating of ions by this electron plasma.

Neutral beam development at Lawrence Berkeley Laboratory (LBL) has progressed rapidly. The 10-A 20-keV pulsed source was successfully used on 2XII and work was started to extend this source capability to 50 A. A near-dc (10-sec pulse length) source is being developed to provide 1 A at 3 keV for injection into BBII. At LLL, a 200-A pulsed source development was started to provide for future 2XII-B requirements as well as long-range needs.

A new direct energy conversion facility has been nearly completed which is capable of guiding protons of 1.5 keV from a 30-kG region through an expander coil to 100 G at the collector end. This facility will allow testing of most of the critical physics features of direct converters.

A more practical Nb₃Sn tape superconductor has been developed using an aluminum stabilizer and nickel reinforcing.

Other technology efforts have included completion of a design study of a 200-MWe mirror reactor, along with detailed studies of reactor components such as blanket design, direct converter, superconducting coils and injectors. Preliminary parameter studies were started for a Fusion Engineering Test Facility (FERF).

I. Theoretical Studies

INTRODUCTION

L. D. Pearlstein

With the closing down of the Astron and SCL facilities, the theory effort has been concentrated in the mirror confinement area. This effort can be broadly subdivided into two groups, one being work

in direct support of the major experimental facilities at LLL (2XII, Baseball, and Direct Converter), and the other being general research in the mirror confinement area to establish scaling laws to aid in the design of larger devices. Also, during the past year ongoing research in the Astron and SCL area was completed.

To a large extent the research in the area of mirror confinement is primarily computational, and

consequently the lion's share of this work has been code development. Representative work is described.

Studies of stability of relevance to Baseball and 2X are described in the next section. Some of this work is an extension of work described in the previous progress report, and some contains new ideas such as diffusion stabilization and line loading in the presence of fanning.

Section 6 describes a two-dimensional (2-D) computer code which simulates electron-beam plasma interaction in connection with plasma heating. Finally, the last section rounds out the theoretical studies and includes the work in areas no longer emphasized.

MIRROR RESEARCH

Computations of Plasma Equilibria in Minimum-B Mirror Devices

J. Killeen, M. E. Rensink and C. Tull

The three-dimensional code developed by Anderson and Killeen¹ is being modified to include collisional pressure distributions and the ambipolar potential. High- β plasmas in several different minimum-B configurations are being studied with this code.

The original version of the code assumes a plasma pressure tensor which is a function of mod-B only. The particular model used in the computations is based on the ion distribution function given by Taylor² which, when integrated, yields the pressure

$$p_{||}(B) = CB(B_0 - B)^m \theta(B_0 - B)$$

with

$$p_{\perp}(B) = p_{||}(B) + B p'_{||}(B)$$

The unit step function is denoted by $\theta(B_0 - B)$ and the value of mod-B at the plasma boundary is specified by B_0 .

More realistic pressure profiles may be obtained by using Holdren's analytic approximation to the collisional equilibrium distribution function.³ This yields the result

$$\begin{aligned} p_{||}(B) &= C \{ (2R - 3) (\tanh^{-1} x - x - x^3/3) + 1/5 \\ &\quad \times (B_0/B)x^5 \} \theta(B_0 - B) \\ x &\equiv (1 - B/B_0)^{1/2} \\ R &\equiv B_0/B_{\min} \end{aligned}$$

where B_{\min} is the minimum value of mod-B within the plasma value. Analysis by Hall⁴ indicated that for this case the maximum stable plasma pressure should be less than that for the Taylor distributions. A comparison of the code results for these two pressure profiles is in progress.

To include the ambipolar potential in these equilibrium calculations, we assume a simple model in which the distribution functions for both ions and electrons have simple analytical forms:

$$f_a = F_a [\epsilon, \mu] \quad a = \text{ions, electrons}$$

where ϵ and μ are constants of the motion. In this case, the energy ϵ contains a term $q_a \phi$ which represents the effect of the ambipolar potential, ϕ . From these distribution functions, we calculate the charge and current densities to be used in Maxwell's equation. Then for our model, it can be shown that the problem reduces to two coupled nonlinear partial differential equations for the magnetic and electric potentials. Writing B in the form

$$\bar{B} \equiv \gamma^{-1} \nabla \chi$$

where

$$\gamma \equiv B^{-2} (p_{||} - p_{\perp}) - 1,$$

the equations to be solved are:

$$\nabla \cdot (\gamma^{-1} \nabla \chi) = 0$$

and

$$-\nabla^2 \phi = \tau$$

where τ and γ are now functionals of both ϕ and B . These equations could be solved directly, but a simpler procedure is to impose the charge neutrality condition,

$$\tau[\phi, B] = 0.$$

This gives a simple analytical relation between ϕ and B which reduces the problem to a single equation for the magnetic potential, χ . The original form of the code written by Anderson and Killeen¹ can then be used to obtain the solution. A report containing details of this scheme is being written at the present time.

A Two-Dimensional (2-D) Multi-Species Fokker-Planck Code

R. L. Berger, J. Killeen and A. A. Mirin

The need for more realistic Q calculations requires a 2-D, multispecies Fokker-Planck code. In response to this need, we are developing such a code. Unlike the current Fokker-Planck codes, the 2-D multispecies code does not assume isotropic Rosenbluth potentials or separated solutions, and treats electrons on an equal footing with ions in a two-dimensional velocity space.

A desirable feature of a 2-D multispecies code is a fast way to compute the Rosenbluth potentials. To accomplish this, our present research is directed toward using Poisson's equation to solve for the Rosenbluth potentials.

Separated Multi-Species Code

A. A. Mirin and J. Killeen

The one-dimensional isotropic multispecies code has been extended to consider several normal modes. We write

$$F_a(v, \mu, t) = \sum_{L=0}^{L_x} F_a^{(L)}(v, t) M_a^{(L)}(\mu)$$

and solve Eq. (18)* with $\lambda_a^{(L)}$ and $F_a^{(L)}$ replacing λ_a and F_a , respectively. Then h_a and g_a are defined by Eqs. (19) and (20), respectively, with $\sum_{L=0}^{L_x} F_b^{(L)}(V')$ replacing $f_b(V')$ and $\lambda_a^{(L)}$ replacing λ_a . $\lambda_a^{(L)}$ represents the $(L+1)$ smallest solution to Eq. (17), with the correction $\theta_{Lc} = \sin^{-1}(1/\sqrt{R_m})$.

*Equation references refer to a published paper.⁵

The solutions of Eq. (17) satisfy

$$\int_{-\mu_{Lc}}^{\mu_{Lc}} M_a^{(L)}(\mu) M_a^{(L')}(\mu) d\mu = 0 \text{ if } L \neq L',$$

and are normalized so that

$$\int_{-\mu_{Lc}}^{+\mu_{Lc}} (M_a^{(L)}(\mu))^2 d\mu = 1,$$

and

$$M_a^{(L)}(0) < 0, \quad (\mu_{Lc} = \cos \theta_{Lc}).$$

At present there are two options for initializing the source and distribution functions. The first option calls for specifying the first normal mode (as in the regular multispecies code), and setting the others equal to zero. The second option calls for specifying $F_a(v, \mu)$ and $S_a(v, \mu)$ as gaussians, and then defining

$$F_a^{(L)}(v) = \int_{-\mu_{Lc}}^{\mu_{Lc}} F_a(v, \mu) M_a^{(L)}(\mu) d\mu,$$

and $S_a^{(L)}(v)$ similarly.

The loss term C_a considers the effective mirror ratio (R_{eff}) at each velocity point rather than the given mirror ratio R_m , so that $\lambda_a^{(L)}$ (replacing λ_a in C_a) must be appropriately modified. An independent code has shown that $\lambda_a^{(0)} \approx 1/\log_{10} R_m$, and that $\lambda_a^{(L)}/\lambda_a^{(0)}$ may be approximated by piecewise linear functions of $\log_{10} R_m$.

Z-Dependent Fokker-Planck Code

A. A. Mirin and J. Killeen

Program IONS, the two-dimensional v - θ Fokker-Planck code for one ion species and Maxwellian electrons, has been modified to include spatial dependence. The spatial domain is divided into several zones, and the v - θ Fokker-Planck collision operator is applied separately in each zone. The total change per cycle in the ion distribution function is then computed by integrating over guiding-center orbits in v - θ - z space. A more complete description is given in Ref. 6.

Guiding Center Plasma Equilibrium

L. S. Hall and B. McNamara

Theory

Practical methods have been developed for solving the G-C fluid equilibrium equations for pressure profiles corresponding to collisional Fokker-Planck equilibria in mirror machines. The equations solved are

$$\vec{J} \times \vec{B} = \nabla \cdot \underline{\underline{P}}, \quad \nabla \times \vec{B} = \vec{I}, \quad \nabla \cdot \vec{B} = 0. \quad (1-1)$$

Using Holdren's approximation to the equilibrium distribution function, we choose the components of the pressure tensor as

$$p_{\parallel} = \psi(\alpha, \beta) [(2R_w - 3) (\tanh^{-1} |x| - x - x^3/3) + x^5/5B] \equiv \psi \hat{p}_{\parallel} \quad (1-2)$$

$$p_{\perp} = \psi(\alpha, \beta) [2R_w - 3) (\tanh^{-1} |x| - x + x^3/6) + (4+B)x^3/10B]$$

$$x = \sqrt{(1 - B/B_{\max}(\alpha, \beta))}, \quad R_w = R_w(\alpha, \beta) \text{ mirror ratio,}$$

where α, β = field line coordinates. The magnetic field \vec{B} is determined in terms of a scalar potential ϕ and a magnetization vector \vec{D} by

$$\left(1 + 4\pi \frac{p_{\perp} - p_{\parallel}}{B^2}\right) \vec{B} = \nabla \phi + \vec{D} \quad (1-3)$$

where

$$\vec{D} = D_{\alpha} \nabla_{\alpha} + D_{\beta} \nabla_{\beta} \quad (1-4)$$

and

$$D_{\alpha}(L) = \int_0^L \frac{dL}{B} 4\pi \frac{\partial p_{\parallel}}{\partial \alpha} \quad D_{\beta}(L) = \int_0^L \frac{dL}{B} \times 4\pi \frac{\partial p_{\parallel}}{\partial \beta} \quad (1-5)$$

The radial pressure profile ψ is found by solving the equation $\vec{B} \cdot \nabla \times \vec{B} = 0$ outside the plasma. This can

be written in terms of $\vec{D}_{\perp} = \vec{D}(L)$, the total magnetization as

$$\frac{\partial D_{\alpha L}}{\partial \beta} - \frac{\partial D_{\beta L}}{\partial \alpha} = 0. \quad (1-6)$$

The coordinates (α, β) and the magnetizations D_{α}, D_{β} can be found most readily by solving the "magnetic equations" of the form $\nabla \cdot \underline{\underline{D}}_{\alpha\beta} = 4\pi \partial p_{\parallel} / \partial \alpha$,

$\nabla \cdot \underline{\underline{D}}_{\beta\alpha} = 0$. This is more straightforward than solving for field line trajectories and doing field line integrals.

Having thus found \vec{D} one finally solves a Poisson-type equation for ϕ , using $\nabla \cdot \vec{B} = 0$. The system of equations must be iterated to find self-consistent equilibria at finite β . A trivial change of boundary conditions allows us to treat toroidal equilibria similarly. If we assume that the plasma potential is small, $e\phi/kT_i \ll 1$, we can include the ambipolar potential in the equilibrium.

The theory outlined here is a development of previous work⁷ and is free of singularities, describes the radial pressure balance, applies to the most general pressure tensors $\underline{\underline{P}} = \underline{\underline{P}}(\alpha, \beta, s)$, and involves only the solution of a simple set of equations of the forms $\nabla \cdot \underline{\underline{q}}\vec{B} = p$, $\nabla^2 \phi = \rho$.

The MHDEQU 3-D Plasma Equilibrium Codes

L. S. Hall, B. McNamara and D. Fuss

The theory sketched above is being implemented in a series of codes (by D. Fuss) directed at Baseball 2XII, and future mirror experiments. The first code, MHEQU1, gives a complete description of the low- β equilibria in mirrors by solving the magnetic equations

$$\nabla \cdot \underline{\underline{q}}\vec{B} = p \quad (1-7)$$

for q given $\vec{B}(x, y, z)$, $p(x, y, z)$ and $q(x, y, z = 0)$ on a boundary. The simplest such equilibrium is given by solving, with $R_w = \text{const}$,

$$\nabla \cdot \underline{\underline{D}}\vec{B} = \hat{p}_{\parallel} \quad D(z=L) = 0. \quad (1-8)$$

Integrating this equation from the mirror throats to the midplane gives the required line integrals.

$D_L = \oint d\mathbf{r}/B \hat{p}_B$. The radial pressure balance equation in the midplane simplifies to

$$\frac{\partial D_L}{\partial \alpha} \frac{\partial \psi}{\partial \beta} - \frac{\partial D_L}{\partial \beta} \frac{\partial \psi}{\partial \alpha} = 0 \quad (1-9)$$

and so $\psi = \psi(D_L)$ is the solution. The 3-D pressure profile is completed by integrating

$$\nabla \cdot \psi \mathbf{B} = 0 \quad (1-10)$$

from the midplane to the mirror throat. Thus, two "magnetic equations" specify the equilibrium in a given field.

Injected equilibria can also be found by finding the particle drift surfaces $J(\alpha, \beta, \nu) = \oint dL \sqrt{1 - \nu B}$ from a set of "magnetic equations"

$$\begin{aligned} \nabla \cdot j \mathbf{B} &= B \sqrt{1 - \nu B} & j(z=0) &= 0 \\ \nabla \cdot j \mathbf{B} &= 0 & j(z=L) &= j(z=L). \end{aligned} \quad (1-11)$$

MHDEQUI gets $\vec{B}(x, y, z)$ from the modified MAFCO code. The MHDEQUI code is written in Startran, making extensive use of vectorized operations. Startran offers a set of hand-coded vector routines which run at stack-loop speeds on the 7600. The code has an immediate upward compatibility with the CDC-STAR when the vector operations compile to single machine instructions. The difference scheme for integrating (1) is either the standard A-D-I method or a fully centered A-D-I scheme if a good guess or previous iteration on q is known. The alternating directions of the scheme are achieved by a physical transposition of q, B, p so that the vector operations can go full speed. Our current tests show that the Startran is about twice as fast as optimized Fortran.

The next code in the series, MHDEQUI2, will include a 3-D Poisson solver to enable self-consistent determination of $\{B, p\}$ at finite β .

Som. Observations on Mirror Losses

A. H. Futch and J. R. Hiskes

In an attempt to estimate the neutral beam requirements for sustaining the 2XII plasma or buildups of

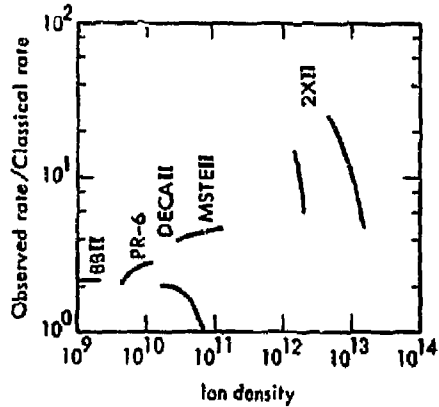


Fig. 1. Comparison of observed loss rates with calculated loss rates

the plasma in BBII, we have compared the observed loss rates of several mirror machines with the Fokker-Planck loss rates (see Fig. 1). The BBII, PR-6, DECAII, MSTII and 2XII experiments provide a sequence of keV collisional plasmas of increasing density whose decay rates are believed to be determined by other than charge-exchange losses. By comparing the ratio of the observed decay rates with calculated rates, we have tentatively concluded that this ratio is a monotonically increasing function from a density of 10^9 to 10^{13} ions cm^{-3} , the ratio ranging in magnitude from about three at the low densities to about ten or twenty at the high densities. At the highest densities, as shown by 2XII data, the ratio falls sharply toward unity. The high-density turnover occurs at that density where the electron $\epsilon = \omega_{pe}^2 / \omega_{ce}^2$ is of order unity. This high-density behavior has been discussed by Baldwin.

Numerical Studies of Advanced Mirror Devices

R. P. Freis and R. W. Moir

A numerical study is being conducted of single particle orbits and magnetic field shapes of advanced mirror devices. A report is in preparation on a particular configuration which presents details of drift surfaces, adiabatic invariants, angular drift velocities, and stability to low-frequency flute modes.

STABILITY THEORY

Effects of Electron Temperature and Finite Ion Larmor Radius on Rosenbluth-Post Convective Loss Cone Instability

D. E. Baldwin and R. C. Harding

A computer program has been written to evaluate the amplification of the Rosenbluth-Post convective loss cone instability, including magnetic field and density variables, magnetic line fanning, and finite electron temperature. It has been found that the strong stabilizing effect of increasing electron temperature found by Horton⁸ is reduced with the inclusion of an ambipolar cutoff in ion energy which is proportional to electron temperature. The net result is an energy dependence of the ion scattering rate calculated by Baldwin and Callen⁹ which is at variance with that observed in 2XII.

Recently it has been realized that the narrow ion distributions present in the low-energy 2XII runs invalidate the neglect of magnetic field on the ion orbits. These finite ion Larmor radius effects are under investigation, and will be reported at a later time.

Effect of Electron Diffusion on the Drift Cone Mode

D. E. Baldwin and H. L. Berk

An existing computer program solving the line-averaged, drift-cone dispersion relation has been modified to include the effect of self-diffusion on the electron orbits through the approximation of replacing ω by $\omega + ik^2 D_e$ where appropriate in the perturbed electron density. A similar replacement was made in the ion charge density, although D_i was taken about $0.1 D_e$. Stabilization of the drift cone mode was achieved with $D_e \sim 0.01 \omega_{ci} a^2$, where ω_{ci} and a are the ion cyclotron frequency and Larmor radius. Work is now in progress to examine whether this simple diffusion is a good approximation to the nonlinear wave interaction with the electrons, and to calculate the ion diffusion to be expected from the implied turbulence level.

Line Loading in High-Density Mirror Machines

H. L. Berk

When the scale length of a mirror machine is small enough, the wave properties of the system is governed by a dispersion relation of the form,

$$\int_0^{L_c} \frac{ds}{B(s)} D(S, \omega) = 0 \quad (1-12)$$

where L_c is a cutoff distance along a field line, and this distance can extend outside the plasma trap. The internal contribution to Eq. (1-12) tends to be destabilizing as we are averaging over a loss cone distribution; while the external contribution, which consists of untrapped particles, tends to be stabilizing if it is a Maxwellian distribution (or some other monotonic distribution). In particular, the external contribution is most effective as a stabilizing influence if the temperature ratio,

$$\frac{T_{in}}{T_{ex}} < A \quad (1-13)$$

where T_{in} is the temperature of the internal plasma, T_{ex} is the temperature of the external plasma density and A is the fanning factor of the field lines. For 2XII parameters, $A \approx 10$, and it is found from order-of-magnitude estimates that an external plasma density of more than 5% the internal density can stabilize the flute drift loss cone instability. More details of this work are given elsewhere.¹⁰

Geometric Effects on Drift Cone Modes

D. E. Baldwin and R. P. Freis

We have begun a numerical study to determine the effects of geometric field line fanning upon flute drift cone modes in a non-axisymmetric mirror machine. In the initial phase, electron modes will be examined while the proper terms for the ions are being developed for later inclusion. By the use of the α, β, χ magnetic coordinate system and a subsequent averaging over χ , the problem is reduced to a two-dimensional partial differential equation which is further reduced by

separation of variables and finite difference techniques to an algebraic eigenvalue problem of the form $(\underline{A} - \lambda \underline{B}) \underline{X} = 0$. This is solved by the QZ algorithm of Moler and Stewart.¹¹

Model for Electron Diffusion Stabilization of Drift Cone Mode

D. E. Baldwin, B. McNamara and S. L. Rompel

As a test for the notion of stabilization of the drift cone mode by electron diffusion, a fluid computer simulation is being written in which the nonuniform electron density flows at the local $\underline{E} \times \underline{B}$ drift velocity, and each \underline{k} component of the ion density satisfies the driven harmonic oscillator equation,

$$\left[\frac{\partial^2}{\partial t^2} + \omega_{ci}^2 \right] \rho_i(\underline{k}, t) = C(\underline{k}) \phi(\underline{k}, t)$$

For proper choice of $C(\underline{k})$, when this density is combined with the linearized electron equation in Poisson's equation, linear instability is predicted. Since in the simulation the only nonlinear process at work is in the electron motion, we expect to determine the amount of electron diffusion and the electric field fluctuation level necessary to stabilize a given linear growth rate. This model generalizes the diffusion studies of Taylor and McNamara¹² to include waves with real frequencies and positive growth rates.

Electron Scattering by Enhanced Fluctuation in Quiescent 2XII Decay

R. E. Aamodt and D. E. Baldwin

It is shown¹³ that, under condition of quiescent 2XII decay, electron-electron collisions dominate the electron scattering due to the Rosenbluth-Post convective loss cone instability as long as the ion-ion collision rate does not exceed its classical value by a factor of more than $\sqrt{m_i/m_e}$. A Maxwellian electron distribution function is then maintained, justifying the assumption by Baldwin and Callen⁹ of Maxwellian electrons in their calculation of the effect of electron Landau damping.

Open J-Surfaces in Baseball and Its Implication for Stability

H. L. Berk

A possible explanation for the Baseball results lies in the open J-surfaces near the mirror throats. If the J-surfaces are open enough (what is enough needs to be determined) the particle density will go to zero on a given field line some distance away from the mirror throats. On these lines total wave reflection occurs, and hence convectively unstable waves will grow absolutely. The most open J-surfaces occur near the radial edges of the machine, and thus these are most likely to be unstable. Hence one can have a situation where the outer field lines are unstable and the inner field lines stable. As the density builds up by neutral injection, one can then reach a situation where instability occurs at the edge and limits density buildup, while the buildup continues at the center. During this buildup stage, noisy oscillations will arise at the plasma edge. When the beam is turned off, the noise quickly damps as the unstable region, which was hovering near threshold during buildup, dips below the density threshold relatively quickly in the decay, and the bulk of the plasma is stable. The above scenario is tailored to explain qualitatively the observed data, and further experimental and theoretical investigation is needed to confirm this point.

Modified Negative Mass Instability During Beam-On

L. D. Pearlstein

The Baseball II experiment has long been plagued with instability in the ion cyclotron frequency range which was accompanied by enhanced sporadic end losses inhibiting plasma buildup. It has now been ascertained that the instability only persists while the neutral beam is on. That is, after the beam is turned off there is no evidence of rf activity or sporadic end losses. In this note it is proposed that it is the anomalously sharp pitch angle distribution of the injected particles that is responsible for the fluctuations. Since the neutral beam has little angular divergence (the spread is on the order of 2°) at any given time during beam-on, there is a population of particles

with this anomalously sharp distribution (compared with collisional distribution) the actual magnitude being a detailed function of trapping efficiencies, collisional spreading and particle losses.

The particles with the strongly peaked pitch angle distribution are a modified negative mass drive. Specifically, we have¹⁴

$$4\pi n_B' = \phi(s) \omega_B^2 \int \left[\frac{\partial f}{\partial \epsilon} \mu + \frac{n \omega_c}{B} \frac{\partial f}{\partial \mu} \right] \times \frac{d\epsilon d\mu B}{\sqrt{\epsilon - \mu B}} \frac{J_n^2 \left(\frac{k \sqrt{2\mu B}}{\omega_c} \right)}{\omega - n \omega_c} \quad (I-14)$$

where f is normalized to unity and the bounce-averaged cyclotron frequency is

$$\bar{\omega}_c = \omega_c \frac{1+\lambda}{2\lambda} + \frac{k_\perp^2 v^2}{\omega_c^2 R_m} (2-\lambda)$$

where

$$\lambda = \frac{\mu B_0}{\epsilon} \quad (I-15)$$

and ϵ is the particle energy, μ is magnetic moment, k_\perp is the perpendicular wavenumber, ω_B the beam particle plasma frequency and ϕ the perturbed potential. In arriving at Eq. (I-14) we have assumed that $\oint (\omega - \omega_c) dt \ll 1$ and $(\omega_c - n \bar{\omega}_c) \tau_B \ll 1$ the standard requirements which are satisfied by sharp pitch angle distributions with particles localized at the midplane. In addition, we anticipate a flute-type mode so that $\phi(s)$ can be extracted from the orbit integrals. The conditions for validity can be written with a parabolic magnetic field (we neglect the ∇B drift since it is small)

$$\left(\omega - n \omega_{ci} \frac{1+\lambda}{2\lambda} \right) \frac{L_m}{\sqrt{2\epsilon\lambda}} \ll 1$$

$$\omega_{ci} \frac{1-\lambda}{2\lambda} \frac{L_m}{\sqrt{2\epsilon\lambda}} \ll 1 \quad (I-16)$$

which is obviously satisfied for a particular harmonic with $1 - \lambda$ small enough.

To evaluate the integral in Eq. (I-14) we assume a distribution

$$f \sim \epsilon^{1/2} e^{-\epsilon/\epsilon_0} \delta(\lambda - \lambda_0) \quad (I-17)$$

and find (we neglect the drift) with ϕ constant

$$\frac{\int \frac{ds}{B} n_B}{\int \frac{ds}{B}} = \frac{1}{2} \frac{\omega_B^2}{\omega_{ci}^2} k_\perp^2 \left(\frac{1-\lambda_0}{\lambda_0} \right)^{1/2} \frac{n \omega_c}{\omega - n \omega_c} \times \left[\frac{d}{db} \left\{ n e^{-b} - \frac{1}{b} n e^{-b} \right\} \frac{n \omega_c}{\omega - n \omega_c} \right] \times \frac{1-\lambda_0}{4\lambda_0} \Big|_b = \frac{k_\perp^2 \epsilon_0 \lambda_0}{\omega_c^2} \quad (I-18)$$

Now the Poisson equation is¹⁵

$$\frac{d}{ds} \frac{\omega_{pe}^2}{\omega^2} \frac{d\phi}{ds} = -k_\perp^2 \left[1 - \frac{\omega_{pi}^2}{\omega^2 - \omega_{ci}^2} \right] \phi + 4\pi n_B' \quad (I-19)$$

To obtain any effects from the small fraction of beam particles, we must have

$$\omega \approx \omega_c \frac{1+\lambda_0}{2\lambda_0}$$

so that

$$L^2 k_\parallel^2(s) \approx -k_\perp^2 L^2 \frac{\omega_{ci}^2}{\omega_{pi}^2} \frac{m}{M} L^2 \frac{\omega_{pi}^2}{\omega_{ci}^2} \frac{\lambda_0}{1-\lambda_0}$$

thus the condition for a flute mode is

$$k_\perp^2 L^2 \frac{m}{M} \frac{\lambda_0}{1-\lambda_0} \ll 1 \quad (I-20)$$

Now following Ref. 15, we find that the localization condition perpendicular to the field is (R_M is the radial scale length of the magnetic field)

$$k_{\perp}^2 a_i R_M \approx 1 \quad (I-21)$$

so that we must have

$$\frac{L^2}{a_i R_M} \frac{m}{M} \frac{\lambda}{1-\lambda} \ll 1$$

which, in general, is satisfied. Thus, our dispersion relation is the line average of the left-hand side of Eq. (I-19) set equal to zero, or

$$1 + \pi i \frac{\omega_{pi}^2}{\omega_{ci}^2} \frac{1}{\sqrt{\omega_{ci}^2 - 1}} - \frac{\omega_{pi}^2}{2\omega_{ci}^2} \Delta \left(\frac{1-\lambda_0}{\lambda_0} \right)^{1/2} \quad (I-22)$$

$$\times \left[\frac{1}{\Omega} - \frac{1-\lambda_0}{4\lambda_0} \frac{1}{\Omega^2} \right]$$

with

$$\Delta = \frac{N_B}{n} \quad (I-23)$$

$$\Omega = \frac{\omega}{\omega_{ci}} - \frac{1+\lambda_0}{2\lambda_0}$$

Now with $\Omega \approx 0$,

$$\Omega = \frac{1-\lambda_0}{\lambda_0} \frac{\Delta}{4\pi i + \xi} \left[1 \pm i \sqrt{2 \frac{\xi + \pi i - 1}{\Delta}} \right]$$

$$\Omega = i \frac{1-\lambda_0}{\lambda_0} \left(\frac{\Delta}{8} \right)^{1/2} \frac{1}{\sqrt{\xi + \pi i}}$$

with

$$\xi = \frac{\omega_{ci}^2}{\omega_p^2} \sqrt{\frac{1-\lambda_0}{\lambda_0}}$$

Finally, if spread in pitch angle is included, we obtain as a stability criteria

$$\frac{\gamma}{\omega_{ci}} = i \frac{1-\lambda_0}{4\lambda_0} \sqrt{\Delta \frac{\xi + \sqrt{\pi^2 + \xi^2}}{\pi^2 + \xi^2}} < \frac{\delta\lambda}{2\lambda_0}$$

For example, with $\lambda_0 \approx 0.9$ and $\Delta = 0.1$,

$$\frac{\omega_{pi}^2}{\omega_{ci}^2} \approx 0.2, \frac{\gamma}{\omega_{ci}} = 0.005 \text{ and } \delta\lambda > 0.01$$

Thus, with

$$\frac{B(s)}{B(0)} - 1 = \delta\lambda, \delta_{\max} = 0.1 \text{ L}$$

Thus a beam width of 5-10 cm is needed to stabilize the mode. At present, the radial equation is being solved assuming a flute average along the line.

ELECTRON BEAM HEATING

A New Electromagnetic Relativistic Plasma Simulation Code

A. B. Langdon and B. F. Lasinski

A new code has been constructed for studying electromagnetic or relativistic plasma instabilities, such as occur when intense electron beams or electromagnetic radiation passes through a plasma. This is a two-dimensional, many-particle plasma simulation code, with a wide variety of diagnostics. Immediate applications are to electron beam and laser or microwave heating of plasmas.

A side effect of this work is that coding procedures are being developed which will efficiently use the hardware organization of LLL's CDC 7600 computers and the LLL operating system. Attention is being given to the problems of efficient simulation of large systems (50,000 cells), and the boundary conditions to be used for the fields and particles. The code is interfaced to a microfiche plotting system so that the enormous volume of graphical output produced is in a compact yet accessible form. Such techniques will also be applicable to other large simulation codes in the CTR program.

This new code, ZOHAR, brings together the best algorithms from several sources. The underlying principle is still that of the PIC codes, in which the plasma has a Lagrangian representation using large numbers of "particles," and the electromagnetic fields are in Eulerian partial differential equation form. Several such codes have been in use for some time, and it is now profitable to reconsider their algorithms and design.

For the integration of the particle equations of motion in the nonrelativistic limit, the scheme of Hockney and Buneman is nearly universally used.¹⁶ Its error is second order in Δt , and it is time reversible (with change of sign of B). Reversibility avoids the worst kinds of long-term error build-up, which can be troublesome in low-order schemes. There is some difficulty maintaining reversibility with relativistic equations of motion. A relativistic LASL code¹⁷ uses a two-step nonreversible algorithm requiring three time-consuming square roots per particle. We use a reversible relativistic algorithm with two square roots¹⁸ which becomes especially simple in problems for which B has only one nonzero component.¹⁹

A lot of time can be spent interpolating the fields and collecting density contributions from each particle. This is cumbersome in other codes because there are four sets of grid locations at which various fields are defined,^{19, 20} and weights must be assigned to all of these. We have arranged to redefine the fields to one common grid during the particle integration. For large systems, the fields must be stored in large-core memory (LCM), which works poorly for single-word references. Therefore, we store all fields or densities for a given grid point contiguously.

A version of this part of the code has been rewritten in CPU76 assembly language by R. Judd, carefully exploiting the parallel operation capabilities of the 7600. This approximately doubles the overall running speed of the code as compared to optimized LRLTRAN.

The use of the potentials A and ϕ in the Coulomb gauge has been advocated.¹⁸ ZOHAR works directly with E and B , integrating the Maxwell equations forward in time. Fewer large field arrays need be stored and less arithmetic and fewer LCM references are needed. Rather than using flux-conserving current density [Refs. 20 and 17 (Method A)] we use area-

weighting in collecting J_z and then do a flux correction¹⁹ on E . This requires one solution of Poisson's equation (versus two Poisson solutions for the Coulomb gauge). This correction at the end of the field time step appears to, but actually does not, destroy reversibility.

Morse and Nielson had trouble with field noise radiation in their E, B code and believed that the improvement in "Method B" was due to the use of potentials.¹⁷ However, we have shown²¹ that the above method can generate exactly the same E and B fields as the potentials do for given ρ and J_z .

Since the Poisson solution is used to compute a very localized (the source term is quadrupolar)²¹ correction field instead of large long-range fields like ϕ and J_z , we hope that the boundary conditions used in the Poisson solution on open sides will no longer affect the results.

The code is now being used for plasma heating studies, as discussed elsewhere.

Plasma Heating by Electromagnetic Waves and Electron Beams

A. B. Langdon, B. F. Lasinski and W. L. Kruer

We have begun a study, by means of computer simulation, of plasma heating by electromagnetic waves and by electron beams. The mechanisms we are interested in for microwave or laser heating apply to an underdense plasma (wave frequency $\omega_0 <$ plasma frequency ω_{pe}), in contrast to the more usually discussed mechanisms for which $\omega_0 \approx \omega_{pe}$. Electron beam heating is by the relativistic two-stream instability and by the ion-acoustic instability driven by the plasma current in a current-neutralized beam. A report²² has been written discussing mechanisms in which a wave heats the electrons at the surface where the density is one-quarter "critical," i.e., where the wave frequency is twice the local electron plasma frequency.

Two theoretical paths that are important to investigate are:

1. The detailed structure of the J-surface anisotropy. This requires detailed computer investigation.
2. The determination of electron Landau damping which always causes some wave absorption, and

one needs to determine if this is enough for stabilization. A perturbation scheme has been developed.¹⁰ and numerical work is now necessary to determine the precise results.

GENERAL

Calculations of Magnetic Surfaces and Single Particle Motion in the Spire Stellarator

R. P. Freis and C. W. Hartman

A study described in the last annual report (Ref. 23, p. 38) has been completed, and a report is in progress on calculations of magnetic fields and electron orbits in an $\ell = 3$, $m = 1$ toroidal stellarator (major radius = 50 cm, minor radius = 15 cm). To briefly summarize, we find (on the basis of single-particle calculations) electrons circulating around the major axis on so-called passing orbits with energies up to a few hundred keV, for central B fields of 3 to 4 kG. For energies greater than this, the particles drift out. We also find there is a separation of drift surfaces which depends on the direction of v_{\parallel} and results in a current density in the central region. Finally, we have transferred particles from mirror-trapped orbits to central-passing orbits by introducing an electric field E_{θ} .

Transport in Axisymmetric Plasma

D. E. Shumaker, J. Killeen and W. A. Newcomb

A program is in progress to calculate the transport coefficients in an axisymmetric plasma. The calculation assumes a two-component plasma (ion and electrons) near local kinetic equilibrium. It is assumed that the gyration radius is much less than any characteristic length of macroscopic spatial variation. The poloidal magnetic field is characterized by a magnetic stream function ψ . In this case, the density and temperature are a function only of ψ . In previous analyses, an expansion in aspect ratio was made. This is not necessary in the present calculation. Also, the calculation can be performed for any concentric flux surfaces, i.e., surface of constant ψ (e.g., elliptical). The transport coefficients are calculated using the variational principle developed by Bernstein.²⁴ In the present calculation, the inductive electric

field will be calculated self-consistently. The potential part of the electric field is calculated from the quasi-neutrality condition.

After the transport coefficients have been calculated and compared with existing theories, the theory will be implemented to describe the motion of the flux surfaces due to transport of matter and energy. Our existing one-dimensional transport code is being modified to make the independent variable ψ rather than r . The poloidal flux surfaces, $\psi = \text{constant}$, will be computed using our existing two-dimensional equilibrium code.

Simulation of Transient Phenomena in Toroidal Devices

T. H. Johnson and J. Killeen

We have written a particle simulation code (GUIDON) to study transient phenomena in axisymmetric toroidal accelerators and containment devices. The existing version of the code treats an arbitrary number of electrons (assumed macroscopically neutralized) surrounded by a perfectly conducting liner in a 2½-dimensional cylindrical geometry as shown; R and Z are the explicitly-treated independent space variables. The θ -coordinate is assumed to be ignorable with regard to magnetic fields, but is calculated for particle motion so that an accelerating electric potential may be applied to the electrons (considering them as a transformer secondary). Vacuum B-fields are calculated for an arbitrary distribution of coils by integrating the Biot-Savart Law. It is then assumed that only the θ -component of the particles' velocity contributes significantly to altering the confining field, and at each time step a self-consistent B-field is calculated for the electrons to move in. At present no electric field (except the accelerating potential) are in the code, but a new version will include the Coulomb potentials of the electrons.

Motion of the electrons is calculated using the fully-relativistic guiding center equations (assuming conservation of magnetic moment).

This version of the code is useful for simulating the operation of the proposed Spire and Tokolator experiments (toroidal plasma betatrons) and analyses of their predicted performance are underway. In the future

we plan to include ion motion (and consequent charge-separation effects) in GUIDON so that it will also be a useful tool for calculating rapid transient phenomena in Tokamak-type devices.

GUIDON produces physical and velocity phase space plots of all particles, B-field and flux surface plots and velocity and energy distribution functions; it also plots and prints the detailed motion of a representative particle.

Time-Dependent Resistive Instability Calculations

J. A. Dibiase and J. Killeen

A hydromagnetic model has been developed to study resistive instabilities²⁵ in cylindrical geometry, and the model is applied to study specific diffuse pinch configurations. The magneto-hydrodynamic equations include the effects of compressibility, finite resistivity, viscosity and thermal conductivity. Isotropic resistivity is assumed, and the dissipative terms are taken to be constant in space and time. The plasma equilibrium configuration is assumed known, and is specified by $B_{\theta 0}(r)$, $B_{z0}(r)$, $\eta_0(r)$, $\rho_0(r)$, $T_0(r)$; these functions can be chosen to describe a particular experiment. Perturbations of the form $f_1(r, t)e^{i(m\theta + kz)}$ are used for all plasma and field variables,²⁵ and the resulting linear partial differential equations are solved numerically as an initial value problem using an implicit difference scheme. For the incompressible case with no dissipation, a set of four equations for B_{r1} , $B_{\theta 1}$, v_{r1} , $v_{\theta 1}$ is obtained, and the computer code that solves this set is called RIPPLE 4A. For the compressible case with dissipation,²⁶ a set of six equations for B_{r1} , $B_{\theta 1}$, T_1 , v_{r1} , $v_{\theta 1}$, v_{z1} is obtained, and the computer code that solves this set is called RESTAB. To start the calculation an initial perturbation v_{r1} is given, and the boundary conditions and equilibrium values must be specified. To specify a particular problem, the wave numbers m and k must also be given as well as the parameter $S = \tau_R/\tau_H$, the ratio of resistive diffusion time to hydromagnetic transit time. For certain cases an exponential growth occurs, and the

growth rate $p(m, k, S)$ is calculated. The model can be used to test equilibrium field configurations against both the tearing and rippling modes. Results for the tearing mode using a force-free Bessel function model agree with analytic theory.²⁷ Extensive parameter studies have been performed on a reversed field²⁸ pinch model and three Tokamak²⁹ models. The effect of finite resistance on the reversed field pinch is such as to require closer proximity of the conducting wall to the plasma for stability and in the Tokamak models the stability windows³⁰ at higher values of q are considerably reduced.

Magnetic Fields Near an Axis

B. McNamara and D. Fuss

The theory of (toroidal) magnetic fields near an arbitrary axis as formulated by Solov'ev and Shafranov³¹ has been incorporated in a single code to evaluate the well depth $V''(0)$, rotational transform i , magnetic surfaces $\psi(\rho, \theta, s)$, and find absolute minima of $|B|$ for any configurations having an axis. The theory is in terms of seven fundamental functions of distance s along the axis: B_0 , the field on the axis; κ, k , the curvature and torsion of the axis; ϵ, δ , the ellipticity and twist of the lowest-order magnetic surfaces; and P, Q , the third-order coefficients in the expansion of the magnetic scalar potential ϕ . Field configurations have been found³² which link absolute min $|B|$ regions into a torus having a net $-V''$. Work is proceeding on optimization of the choice of parameters, design of suitable coils, and investigation of particle orbits. The theory has some simple and useful consequences:

It is readily shown from the Russian work that $\epsilon > \sqrt{3/2}$ is required for a good contribution to V'' on a straight section of the axis. Choosing $B_0^3(1 - \epsilon^2) = \text{constant}$ and $\delta = 0$ ensures that all contributions to V'' are favorable, making a $-V''$ system easy to design. Conditions for absolute min $|B|$ are incompatible with this, and so one must design coils for min- B and $-V''$ separately on different sections of the axis.

Additions to the MAFCO Coil Design Code

B. McNamara and C. H. Finan

The MAFCO code has been updated to run under CHAT and ORDER. The code has been modified to do the following:

1. The code will still accept data in standard form.
2. Additional routines can be supplied to set up arbitrary coil configuration directly instead of having to generate data cards for the standard MAFCO operation.
3. The code will follow arrays of field lines from a given X-Y plane, calculating the integrals $U(X,Y) = \oint dJ/B$ $J(X,Y,\nu) = \oint d[\sqrt{1-\nu B}]$. The J-surfaces determine the guiding center drift surfaces for charged particles and quickly show the regions of stable plasma confinement. The code puts out contour maps of $U, J(\nu)$.
4. The code will generate \vec{B} on a regular mesh, spanning a cube or segment of a cylinder in any coil configuration. The field \vec{B} will be used by the new MHD equilibrium codes now under construction.

Efficient Use of Disc for Large Programs

B. McNamara and A. B. Langdon

Particle simulations and MHD codes often use large amounts of data which have to be stored on disc. A subroutine package³³ has been written to provide efficient, simple and powerful handling of disc files for such codes. The buffering system is described in terms of linked lists of command words. Several common sets of command cycles are offered, including file initialization, closedown and restart procedures. The package is as portable as possible (Fortran IV plus one set of low-level disc I/O routines), and is run simply by a CALL RUNTRI to (fetch) each new buffer in a cycle.

Reexamination of Cascade Calculations

K. H. Berkner and J. R. Hiskes

The observation of collisional excitation and Lorentz ionization processes in BBII has prompted a

reexamination of the cascading processes. The extent to which the problem of collisional excitations is easily discussed analytically has been summarized.³⁴

To account properly for these processes in a quantitative way, however, necessitates a numerical integration of the appropriate simultaneous equation involving collisional excitation and ionization. During the last ten years, a large number of theoretical and experimental papers have appeared which deal with these collision processes. Unfortunately, there is as yet insufficient experimental data upon which to base a calculation of the net ionization of an atomic beam; recourse must be made to theoretical models for extrapolation of the data to relevant excited levels. But while there exists a dearth of experimental data, the number of theoretical models concur on the values of the cross sections near their maxima. The literature has been summarized.³⁵ Numerical calculations are now underway to determine ionization rates as a function of energy and density in neutral injection systems.

Simulation of Pulse Trapping and Pulse Stacking in Astron

J. A. Byers, A. B. Langdon, J. Killeen, A. A. Mirin, M. A. Rensink, C. G. Tuli

In the past year the continuing code work on pulse-stacking in Astron concentrated on the following: (1) the elucidation of the radial expansion discovered earlier (see Ref. 23, p. 23), (2) vacuum pulse-stacking, and (3) high current pulses. Radial expansion during pulse-stacking occurs in all cases, and now appears to be substantiated as physical (not numerical) in origin. This is a reflection of the breakdown of the radial adiabatic invariant during stacking. The code does conserve the appropriate invariants under other, slowly changing conditions, such as occur during slow charge neutralization.

The radial expansion is more severe for vacuum layers. This occurs because of a basic radial defocussing property of the self-fields which is due to the cylindrical geometry. It can be shown that the radial force can be cast in the form of a negative gradient of a potential where the contribution of the self-fields to the potential in vacuum always has

the shape of potential hill (defocussing); also in general the radial defocussing force in vacuum is larger than the familiar $1/\gamma^2$, resulting in slab geometry. The resistors can enhance the radial forces, but they are not essential to the radial expansion. Even if considerable radial room is allowed in vacuum, there always occurs radial loss to the resistors at some layer strength still short of reversal.

Pulse-stacking to field reversal in a perfect vacuum is prevented by the radial defocussing. Under the idealized code conditions, starting with 1000-A, 100-nsec pulses, presumably obtainable in the Astron experiment, we have obtained a two-pulse vacuum layer with a $\xi = 0.9$, which is quite high but still well short of field reversal. This layer is on the point of incipient radial loss, and further pulse stacking results in no further increase in layer strength. Field reversal is obtained, however, by adiabatic charge neutralization of this layer which results in further axial compression and a final $\xi = 1.7$, just barely enough for field reversal. The axial compression due to the neutralization is $L_0/L = 40 \text{ cm}/16 \text{ cm} = 2.5$, and this agrees well with a short layer form of the adiabatic compression law $L_0/L = (1/\eta_0)^{1/2} = 2.8$, where η_0 is measured in vacuum just prior to neutralization and is defined by $(\eta_0 = 1 - \int_0^{L/2} E_z dz / \int_0^{L/2} v_\theta B_r dz)$. This should be compared to the long-layer compression law $L_0/L = 1/\eta_0$.

Vacuum pulse-stacking with subsequent adiabatic neutralization was a major thrust of the experimental plan. The computational work supports the basic ideas involved in this process, and indeed indicates that field reversal is obtainable with current levels (1000 A) presumably obtainable in the experiment.

However, the vacuum layer required prior to neutralization is just on the verge of incipient radial loss, even with a considerable amount of radial room allowed. This fact, plus other idealizations not expected to be realized in the experiment, indicates that this result is marginal and likely not to be achievable under realistic conditions. Indeed, we were unable to obtain a vacuum layer with ξ in excess of approximately 0.15 during the experiment. Much of the high ξ vacuum layer code work may represent an impossible experimental realm if violent negative mass instabilities (requiring θ asymmetry) cannot be avoided as other independent numerical work suggests (see Ref. 23 p. 28).

High-current (in the range 2500 A) neutralized pulses produce field reversal with one pulse in the code. Unlike the vacuum result, this process does not appear sensitive to idealizations in the code. Other physical processes not present in the code such as plasma currents are likely to affect this result, but the basic approach appears viable. The computational work of the entire past two years is being prepared for publication in *The Physics of Fluids*.

Drift Shock

W. A. Newcomb

A study has been made of drift waves of finite amplitude in a two-dimensional, guiding-center plasma. It was shown, in particular, that a new type of shock arises from the drift wave as a result of nonlinear effects.³⁶

II. Mirror Program

INTRODUCTION AND SUMMARY

R. F. Post

During FY 1973, there were several significant scientific developments in the Mirror Program. These have resulted in a substantial reshaping in our program emphasis, having opened up new opportunities.

The main developments of note are:

- Demonstration of plasma conditions in 2XII which lead to quiescent plasmas that decay, within experimental error, at the classical rate.
- Injection of a 200-kW (10-A, 20-keV) pulsed neutral beam into the 2XII plasma, and the demonstration that this beam does not drive instabilities nor enhance the fluctuation level within the limits of detection.

- Virtual elimination of charge exchange as a significant loss mechanism in Baseball II, and documentation of a stable decaying plasma, escaping at the classical rate within experimental error.

The change in program emphasis, the implementation of which we are now undertaking, has been stimulated by two factors: First, clear evidence from 2XII that high-density plasmas are more stable, in terms of lower fluctuation levels and closer approach to classical rates of decay, than intermediate-density plasmas. These results, which appear to correlate with a theory proposed by Baldwin-Callen suggest that the high-density regime (electron plasma frequency large compared to electron cyclotron frequency) should be a very favorable one for a mirror reactor.

The second factor is the emergence of the technical capability of injecting very high currents of energetic neutral atoms into mirror plasmas. Injected currents are now at the 10-A level, but plans are being made to inject up to 600-A of 20-keV beams (12 MW) into 2XII B after modifications to the coil. This possibility arises from developments, now underway, of 50-A (LBL) and 200-A (LLL) neutral beam source modules, building on the success of the LBL 10-A sources. At the 600-A level it should be possible to build up and maintain plasmas in 2XII with densities and temperatures far above those possible with the present plasma sources. We are also preparing to incorporate high-current beams (up to 50-A) in the Baseball II experiment, where they will be used in conjunction with an initiating target plasma to achieve rapid buildup to high plasma density. In this way, both the 2XII and Baseball II program will be converging on the key issue for a mirror reactor – can high-density, high-temperature plasmas be created and maintained by neutral beam injection?

Finally, first tests have now been made of the performance of the new direct conversion test facility, using a "venetian blind" type of collector system. This new facility is aimed at a testing, on a small scale, all aspects of the LLL electrostatic direct conversion technique – magnetic expansion, separation of ions and electrons, and electrostatic deceleration and collection of ions. These tests are being guided by extensive computer-simulation calculations. These calculations predict the eventual

possibility of achieving 80% to 90% conversion efficiencies. Direct conversion is a key element in our concepts of a mirror reactor.

BASEBALL II

C. C. Damm, J. H. Foote, A. H. Futch, R. K. Goodman, F. J. Gordon, G. W. Hamilton, A. L. Hunt, J. E. Osher, and G. D. Porter. A. L. Gardner,* D. O. Overskei,** A. A. Mirin and E. B. Hooper

Electrical Engineering – A. F. Waugh, A. Bogdanoff and G. Vogtlin

Mechanical Engineering – B. Denhoy, T. Chargin, C. Henning and R. Nelson

Introduction

Operation of the Baseball II experiment during this year became much more reliable when we eliminated all helium leaks from the magnet system into the plasma region and made some refinements of our liquid helium cryogenic system. Other improvements to the vacuum, detailed below, have resulted in a reduction of the plasma charge-exchange losses so that we can now examine the stability of plasmas, formed by neutral injection with beams in the energy range from 0.5 to 2 keV, whose ion distributions are strongly broadened by ion-ion collisions. The primary observations are that: (1) even with a well-broadened ion distribution, a density threshold for ion-cyclotron instability exists and anomalous particle losses occur above this threshold; and (2) this instability ceases within milliseconds after beam turnoff. At present, we do not have a proven correlation with instability theory to explain our observations. Consequently, we have expanded our diagnostic system to provide more clues as to the origin of this instability which is hindering the buildup of density with increased beam intensity and energy. If we can understand this instability, the possibility of circumventing it would be enhanced. We have, for instance, observed a substantial change in instability threshold by microwave heating of electrons with a few milliwatts of power at the electron-cyclotron frequency.

*Consultant, Brigham Young University.

**Summer employee (student at MIT).

An expanded array of end-loss detectors has enabled us to begin a detailed particle inventory, making at least approximate separation of losses into charge-exchange, classical scattering, and anomalous scattering categories. Using these detectors, we can also do a spatial resolution of the end losses. More detailed studies are underway of the rf spectrum during instability in the range of the ion-cyclotron frequency and harmonics. We have also recorded plasma oscillations in a much lower frequency range (5-25 kHz) which are correlated with both the high-frequency rf and the particle losses. Some preliminary feedback stabilization experiments at the low frequency have yielded at least partial suppression of high-frequency rf and particle losses.

Although we had several operating periods during the year, most of the data pertinent to the particle inventory and instability studies were obtained in a run which extended into FY 1974. Much of these data are therefore still to be analyzed, and some of the reports below are preliminary.

In view of the difficulties encountered in the vacuum buildup, we have initiated a reorientation of our program, which leads to another approach to plasma buildup in Baseball II. The high-intensity pulsed neutral beams developed by LBL for the 2XII experiment ease the requirements for a target-type buildup. We have therefore begun a target development program with the objective of generating a cold-ion plasma in a suitable vacuum environment to match these high-intensity beams. Achievement of a high-density, hot-ion plasma in this way could avoid the instability problem presently limiting the density buildup, and, since the Baseball field is steady-state, could lead to a sustained hot plasma at high ($\sim 10^{13} \text{ cm}^{-3}$) density. Changes to the injector line to accept the high-intensity pulsed beams have been planned, and designs for some of the components are in progress.

Injected Beam

Work was continued for reliable performance of the MATS I and II sources for low-energy steady-state, or quasi-steady-state neutral beam operation for Baseball II experiments. The major operation problems for this period were those of

electronic auxiliary power supplies and overall neutral beam performance. The auxiliary solid-state power supplies for the source and shaping magnets were subject to frequent breakdown, apparently from the arc rf and high-voltage switching transients. The ion source performance as measured by drain and reliability was in general quite good; however, overall beam performance continued to be lower than expected. The known problems include various amounts of beam misalignment, inadequate space charge neutralization near the source, the effect of $\sim 1\text{-G}$ magnetic field penetrating the shielding, and a source operation limitation on the charge-exchange cell background pressure for N_2 or H_2O near the extraction electrodes. The compromise for maximum $I^0 f^* r$ (product of total beam, excited fraction and containment time) includes the tight collimation restrictions to only $\pm 1.1^\circ$ in the final configuration, use of a thin N_2 cell to limit N_2 streaming (only $\sim 50\%$ conversion to H^0) and use of a thick Ne screen (with a beam loss of 25-50% through beam reionization and scattering). Beam losses due to residual space charge and magnetic fields were most severe (by an overall factor of 2 to 5) at low energy.

Operation in FY 1973 included a new beam line shown in Fig. 2 with prompt charge exchange as close to the source as possible. This minimizes the previous problems of beam deflection due to stray magnetic fields and allows magnetic sweeping of the residual charged beam into a dump in the source pumping tank before it enters the cryogenic section, which is now used only as a Ne screen. The operation of the new beam line did achieve a distinct reduction in observed N_2 streaming and lower operating pressures, but with the same relatively low beam yields as in previous operation.

Use of H_2 in place of N_2 as the neutralizing gas was unsatisfactory because of inadequate H_2 pumping and consequent charge-exchange loss of trapped plasma. A condensable neutralizing gas such as H_2O is expected to be usable at higher density with consequent better conversion efficiency.

A ball joint with a hole through its center was installed between the MATS source and the cryogenic neutralizer to facilitate the beam alignment. With this arrangement, the beam can be steered for an

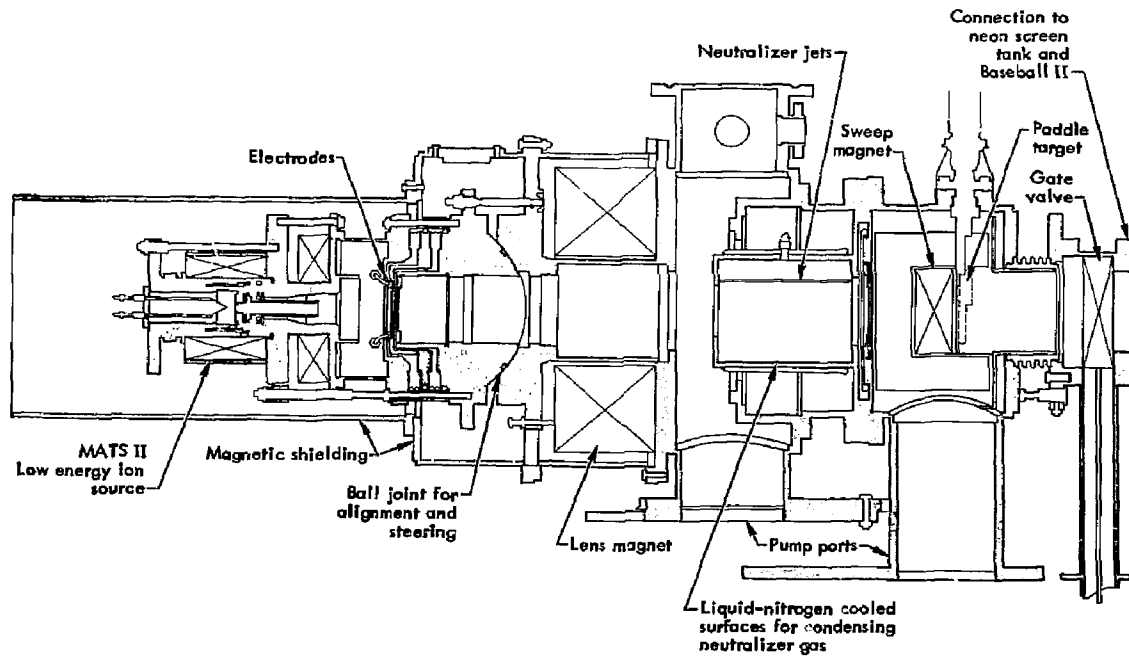


Fig. 2. New steady-state beam design.

optimum alignment on a gridded beam profilometer when the superconducting magnet and other components inside the plasma chamber are at cryogenic temperature and the machine is in operation.

Vacuum Conditions

A significant improvement in the operating vacuum has been achieved this year. Figure 3 compares typical mass spectra, obtained by the low-energy ion spectrometer (LEIS), from a recent run and a similar run last year. Each of these shots had a comparable beam of 2.0 keV H^0 and also similar ion densities and plasma decay times. Note the absence of helium ($m/e = 4$), and the reduction of hydrogen ($m/e = 2$)

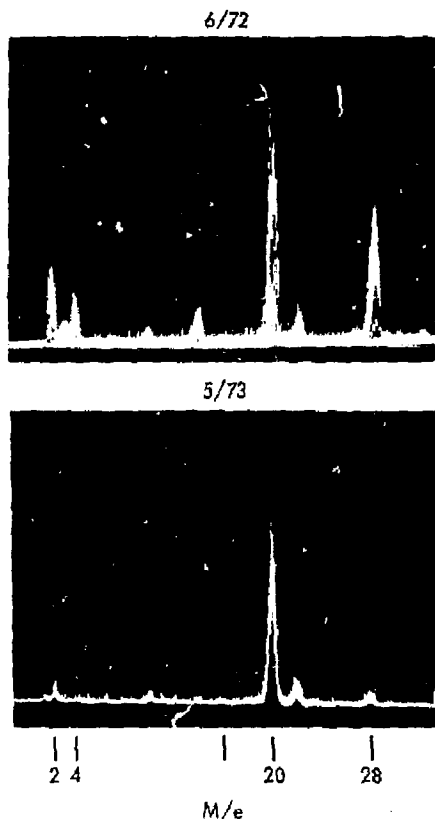


Fig. 3. Comparison spectra showing the improvement, over the past year, of the neutral gas densities in the plasma region. (Hydrogen, $m/e = 2$; helium, $m/e = 4$; neon, $m/e = 20$; nitrogen, $m/e = 28$.)

and nitrogen ($m/e = 28$) in the recent run. (The sharp noise spikes, particularly evident in the recent photograph, are thought to be due to energetic protons. These are not mass-analyzed, and should be disregarded). These spectra, obtained during beam injection, correspond to total neutral gas densities in the range of 10^8 molecules/cm³. The base background density in the plasma region is considerably lower than this. It is now typically 3×10^5 molecules/cm³ as measured by a bent-beam gauge when the magnetic field is off. If the gas is approximately 80°K, this density corresponds to a base pressure of 2.5×10^{-12} Torr.

The high nitrogen contamination in the plasma, seen in the earlier run, evidently originated in the use of nitrogen gas as the charge-exchange medium for the generation of the neutral hydrogen beam. The nitrogen was injected through an arrangement of capillaries³⁷ in a directed way to form a neutralization cavity in which the nitrogen was pumped by condensation on a liquid helium dewar. A variety of tests, including the independence of the nitrogen level on the density of the neon gas screen, indicated that the nitrogen was conducted to the plasma region by some route other than coaxial transport with the neutral beam.

The first attempt to remedy this problem was installation of a sheet metal gas block between the 80°K radiation shield around the liquid-helium-cooled dewar and the room-temperature vacuum wall of the neutralizer tank. This remedy proved to be only slightly effective. It was therefore postulated that since it was unlikely that the nitrogen could flow between two surfaces where one surface was at liquid helium temperature and the other surface was at 80°K, the transport of the nitrogen occurred on the 80°K shield surface in the form of a highly mobile multilayer³⁸⁻⁴⁰ film. This unusual phenomenon is perhaps unique to a cryopump on which very large pumping rates are imposed and in which the gas pumped can be adsorbed on the radiation shields and yet still remain highly mobile.

The neutralizer nitrogen gas, in our case, was pumped at a rate of 10^3 std cm³/min. Nitrogen condensed on the 80°K shield at the high-pressure side of the cryopump and then rapidly spread as an almost liquid multilayer to the low-pressure side of the

cyropump dewar, and there desorbed from the 80°K surface as it attempted to establish a high gas phase pressure in equilibrium with the incident nitrogen. Thus, the nitrogen could be transported past the 2°K cryopump surface.

This situation was corrected by placing a sheet metal barrier in contact with the helium dewar and between the dewar and the 80°K radiation shield so that the mobile nitrogen film was forced to pass over a surface of sufficiently low temperature so that it was no longer mobile. (This solution also blocked any vapor phase transport between the helium dewar and the shield, and as such its success does not constitute proof of the postulated mobile multi-layer.) The additional power load on the dewar and the resulting added liquid helium consumption was minimal.

In retrospect, it is evident that this problem is very similar to that encountered in the early stages of the development of ultra-high vacua when it was realized that it was necessary to include anti-migration barriers in the diffusion pump cold traps to prevent surface migration of pump fluid into the ultra-high vacuum space. It might have been possible in our case to reduce the mobile multilayer transport in the cryogenic neutralizer by using a lower temperature shield or to force all the nitrogen into the gas phase and into contact with the helium dewar by increasing the temperature of the radiation shield.

The helium background was eliminated when two bellows on the liquid-helium storage dewar above the magnet were replaced. One of these bellows had a small cold leak that was below the sensitivity of our leak-checking techniques (see Ref. 23 p. 50). In addition, the pumping speed for helium and hydrogen has been greatly increased by the application of a bonded zeolite coating to another large liquid-helium dewar inside the vacuum system. With the zeolite coating it is no longer necessary to sub-cool this pumping dewar to 2°K, as was previously done (see Ref. 23, p. 51) to achieve a large pumping speed for helium and hydrogen. This dewar can also be heated to dump the adsorbed gases whenever this becomes necessary. With our present vacuum conditions, we can operate the experiment for at least a month before the pumping dewar becomes saturated and a gas pump is required.

Before the elimination of the helium leak, a large helium pumping speed was observed when gas desorbed from the liquid-nitrogen-cooled liner due to a liquid-nitrogen system failure which allowed the liner temperature to rise. This gas was then re-adsorbed on the liquid-helium-cooled surfaces and in the process gettered the gas phase helium. As a result the helium peak temporarily disappeared from the mass spectrum. This indicates that gas gettering can be an effective helium pump in a cryogenic system. To utilize this gas gettering in the event that additional helium pumping is required, we have included provisions for gas deposition on a large 4°K surface.

The improved hydrogen background is a result of the greatly increased hydrogen pumping speed. This pumping speed is obtained from the zeolite-coated dewar discussed above, and also from the heavy titanium coating which is laid down by the 14 large titanium sublimators recently installed in the plasma trapping chamber. Since these sublimators will not operate in the magnetic field, all of the heavy sublimation is done each day before the magnet is energized. To absorb most of the power from these sublimators, a liquid-nitrogen-cooled copper liner was installed on the magnet walls that face the plasma. This higher temperature wall also increases the speed of any desorbed gas molecules, which in turn lowers their density in the plasma region. The sublimators are located so that all of the surfaces seen by the plasma can be heavily coated with titanium.

Analysis of the low-energy ion spectrometer (LEIS) data (see Ref. 23, pp. 52, 53) indicates that the nitrogen density in the plasma region is now 2×10^6 molecules/cm³ for a plasma formed by injecting a 10-mA, 2.0-keV H⁰ beam. This is almost a factor of 10 lower than a year ago, and is very close to the value predicted when the neutralizer was designed. Figure 4 gives the LEIS results for a series of shots in which the neon flow in the neutralizer screen section (Ref. 41, p. 2-7) was varied. (This run was after the effective nitrogen block in the neutralizer, described above, had been installed.) It can be seen that the neon screen is effective and can reduce the nitrogen density in the plasma region by a factor of 100.

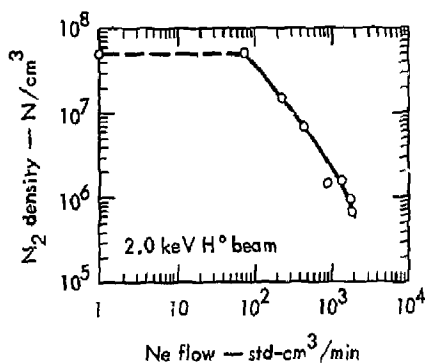


Fig. 4. Nitrogen density in the plasma region versus neon flow in neutralizer sweep section.

Other LEIS data show that the hydrogen gas density, seen by the plasma, is now 2×10^7 molecules/cm³ for a 10 mA, 2.0 keV H⁰ beam. These data also indicate that the hydrogen density is slightly beam-dependent. It is believed that some of this dependency is due to the lack of hydrogen pumping speed in the neutralizer tank. Some revisions of the neutralizer to correct this are now under design.

Although there has been a large improvement in the background neutral gas density of the plasma region, there has been very little improvement in the plasma ion density and decay time. Analysis, near stability threshold, of retarding potential measurements on the ion currents emerging through the mirrors shows that the part of the low-energy ion current due to charge exchange is of the same order as the high-energy ion current which is due to scattering. This is true even with 2.0 keV H⁰ injection. Any instability losses would further lower the fraction of the total losses that are due to charge exchange. These results indicate that, under our good vacuum conditions, the plasma loss processes are no longer dominated by charge exchange. This conclusion is also supported by the ability of feedback stabilization to substantially increase the plasma ion density even with a rather high injected beam current. Thus, a reduction in the instability loss rate significantly raises the plasma density, while a large improvement in the vacuum condition does not.

Diagnostic Techniques and Instrumentation Development

Microwave Interferometer

We have developed a double-pass microwave interferometer employing synchronous detection and having several unique advantages for measuring the small phase shifts produced by a tenuous plasma. These advantages include: (1) a significant reduction in the effect of stray reflections, (2) an absolute calibration technique, (3) increased sensitivity, and (4) an improved signal-to-noise ratio.

The new microwave interferometer is mounted on the coil with an aluminum reflector with a 12-in. diameter and 30-in. spherical radius of curvature. The horn is rectangular in cross section, 4 × 5.2 in. at the open end and 12 in. long. The reflector has 0.0096-in. phase shift calibrating motion. The reflector and the horn can be aligned from outside to correct any misalignment accumulated during cooldown.

Stray reflections along the "plasma path" of an interferometer can falsify phase shift measurements of electron density by permitting some of the microwave energy to by-pass the plasma. This effect is reduced by the use of a double-pass system in which a reflector sends the microwave beam which has traversed the plasma back through the plasma to the launching horn.

A measured longitudinal displacement of the reflector gives an absolute calibration of the sensitivity of the overall system to the change-of-phase length through the plasma. Stray wall reflections which send energy directly back to the horn without traversing the plasma are properly accounted for by this calibration procedure. Furthermore, possible multiple reflections which would allow the beam to (1) traverse the plasma, miss the reflector and re-enter the horn, or (2) by-pass the plasma, encounter the reflector and re-enter the horn are negligible to higher order. The double transit also has the advantage of doubling the effective thickness of the plasma, thereby increasing the interferometer sensitivity.

A schematic diagram of the interferometer system is shown in Fig. 5. The signal from the microwave generator is divided into two paths by a directional coupler. The signal in the plasma arm passes through a circulator before traversing the plasma. After

traversing the plasma the signal is reflected, enters the horn, and is directed by the circulator to a magic tee where the signal is divided. One half of the microwave signal produces an electrical signal at the crystal detector, the other half is absorbed at the load. Similarly, the signal in the reference arm passes through a circulator, is reflected and directed to the crystal detector. For minimum frequency sensitivity, the path lengths in both arms should be approximately the same. The reflected signals from each arm recombine at the detector, depending upon their phase. A

circuit similar to this has been described previously by Gardner.⁴²

A varactor diode, which is dc biased to operate in its linear region, is employed to phase-modulate the signal in the reference arm. The interferometer output as a function of phase is illustrated by the solid curve of Fig. 6. If the interferometer is not in its null position, a modulating voltage applied to the varator produces an ac signal of the same frequency and the same or opposite phase as the crystal detector. A "lock-in" amplifier detects this signal

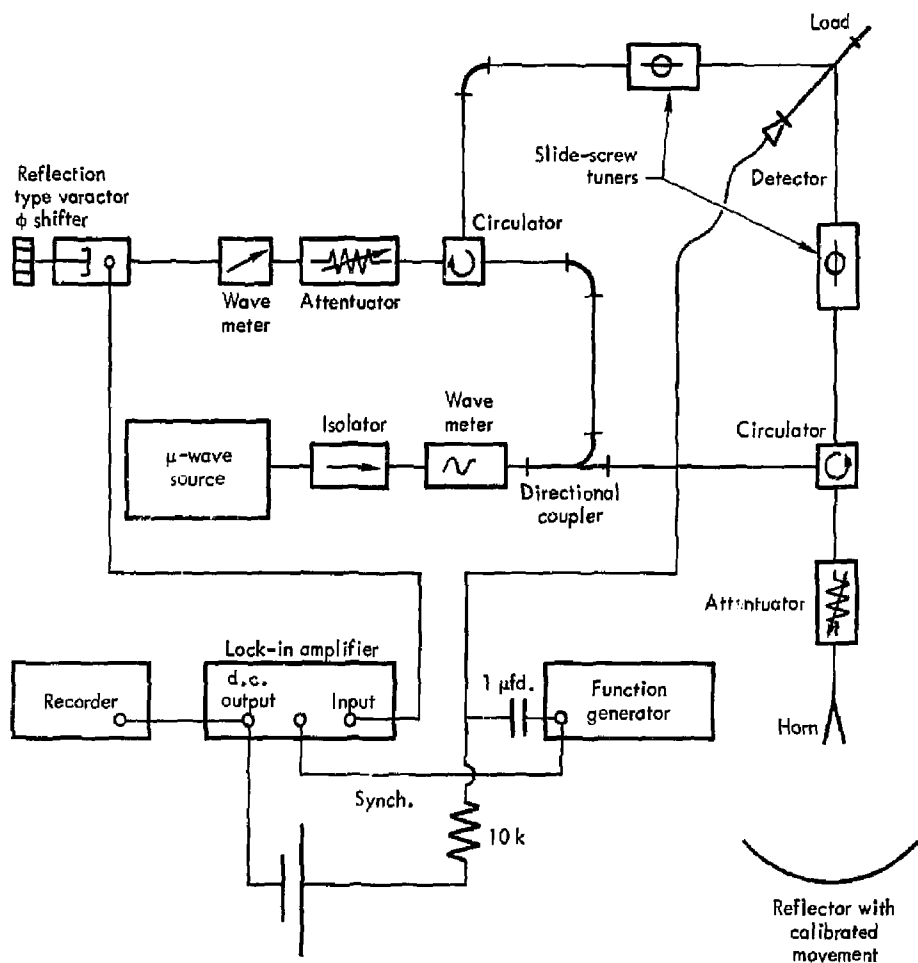


Fig. 5. Schematic diagram of interferometer circuit.

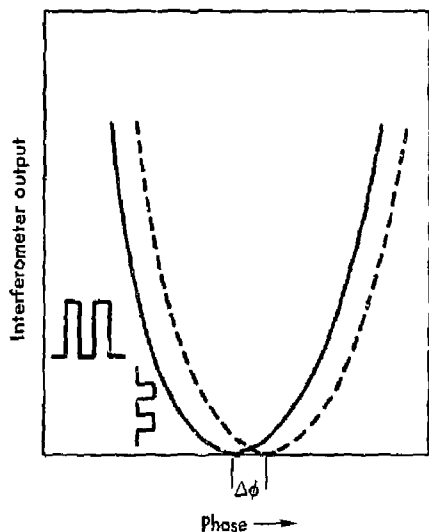


Fig. 6. Interferometer output versus phase.

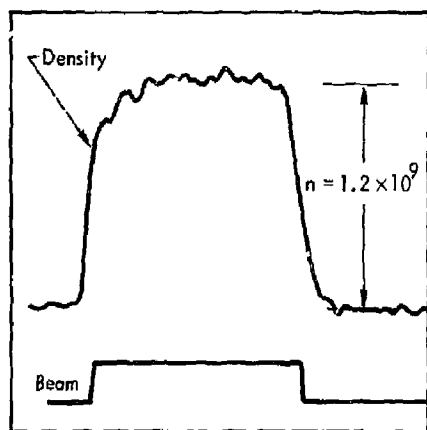


Fig. 7. Density measurement using microwave circuit of Fig. 5.

and provides a dc output which is fed back into the varactor.

In practice, a manually adjustable phase shifter is used to initially null the interferometer. In the presence of a plasma, the output of the interferometer will be shifted by $\Delta\phi$, as indicated by the dashed curve of Fig. 6. When connected as part of the feedback circuit, the dc output of the "lock-in"

amplifier is just enough to re-null the interferometer. This output, which also goes to a recorder, is linearly proportional to the phase shift $\Delta\phi$, and is easily calibrated before each measurement. A typical example of a plasma density measurement made with the circuit of Fig. 5 is shown in Fig. 7. The measured plasma density in this example was 1.2×10^9 electrons/cm³.

Densities of approximately 10^7 electrons/cm³ may be easily measured by feeding the dc output from the "lock-in" amplifier of Fig. 5 into a second lock-in amplifier and modulating the plasma density by turning the neutral beam on and off at a frequency which is low enough that plasma decay occurs during a one-half cycle. The second lock-in amplifier is synchronized to the modulation frequency of the neutral beam. An example of data taken using this procedure is illustrated in Fig. 8. In this case, the plasma density was 10^8 electrons/cm³. The neutral-beam modulating frequency was 0.5 cycles/sec.

Microwave Radiometer

The electron-cyclotron radiation emitted from the Baseball II plasma has been measured using a microwave radiometer in the 26.5-40 GHz band (8 mm). The radiation was monitored by a circular horn 15 cm

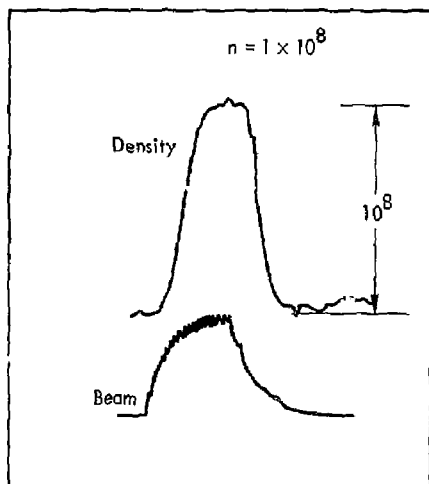


Fig. 8. Density measurement using modified circuit of Fig. 5 employing two "lock-in" amplifiers.

in diameter located in a plane perpendicular to the Z-axis and passing through the plasma center. The Z-axis is defined by the only straight field line that passes through the plasma. Both sidebands were used to sample radiation from between two nested closed shells within the plasma. For a tenuous

plasma, this radiation is proportional to the product of the electron density and the electron temperature.

From independent measurements with gridded probe detectors, the plasma potential can be determined by the bias voltage necessary to prevent slow plasma ions from being detected. Since the measured plasma

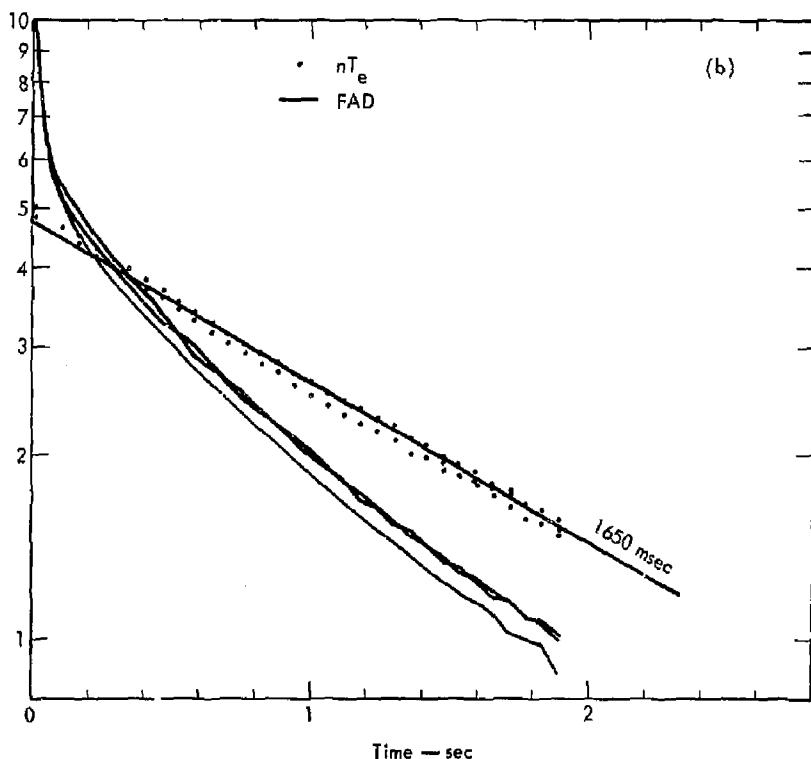
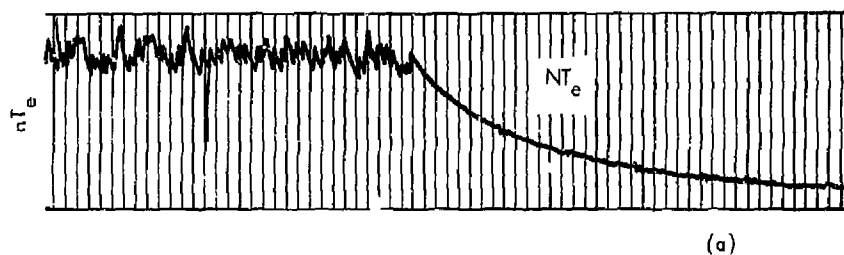


Fig. 9. Electron cyclotron radiation versus time.

potential is proportional to the electron temperature T_e , the relative plasma density can be determined by dividing the electron radiation signal by the measured plasma potential ϕ . Conversely, a relative measurement of the electron temperature can be obtained by dividing the electron radiation signal by the plasma density obtained from another detector such as the interferometer. Thus, both relative measurements of T_e and n^+ can be obtained from the microwave radiometer.

Figure 9(a) shows the radiometer signal nT_e as a function of time for a 2-keV H^+ plasma. Figure 9(b) shows the decay of nT_e and the fast atom detector (FAD) signal as a function of time following beam turn-off for four different decays. The decay of nT_e is exponential and provides the only good measurement of the plasma lifetime which is available. Previous estimates of the plasma decay times depended on the decay of the secondary electron detector, FAD. The FAD signal was shown to decay faster than the plasma density because of the steep energy dependence of the charge-exchange cross section and the energy sensitivity of the detectors.

Another important observation was a calibration of the magnetic field versus the coil current. As the local oscillator frequency of the radiometer is reduced, the radiometer signal approaches zero as the frequency decreases to the magnetic field minimum. The observed magnetic field minimum was 13% higher than calculated values for the Baseball II magnet, giving a calibration factor of 8.45 G/A. Subsequent measurement of the magnetic field using a three-dimensional Hall-effect probe gave a calibration factor of 8.59 G/A, in good agreement with the radiometer measurement. This observation is important since it places the region of maximum instability activity near the center of the plasma. The "cut-off" of radiation at the highest frequency is a crude measure of the plasma radius which is in qualitative agreement with the predicted radius based on plasma trapping. The experimental data showing nT_e versus frequency is shown in Fig. 10.

Energy Analyzer

The energy analyzer system described by R. G. Mallon in the previous progress reports has been re-built. The chief modification has been

reduction of the residual magnetic field within the analyzer to less than 0.1 G. It was hoped that this improvement in the magnetic field shielding would result in more reliable operation of the analyzer. Unfortunately, problems in voltage breakdown between the grids still occur, and additional modifications will probably be needed.

A significant improvement in the storage and data handling ability of the system has been accomplished. In the present system, the integral spectrum is electronically differentiated at each bias setting and stored in a pulse height analyzer operating in the multi-channel scaling mode. This system should make it possible to obtain a complete spectrum during one "beam-on" pulse subject to normal statistical errors based on the count rate.

The design of the system is based on the following requirements:

1. Count all particles above an energy threshold,
2. determine the distribution of H^+ ions from the stripping cell by the H.V. applied to a grid, and
3. use existing pulse height analyzer (PHA).

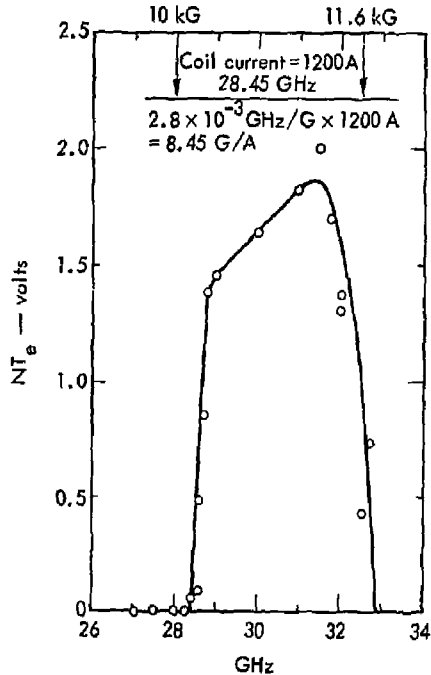


Fig. 10. Electron cyclotron radiation versus frequency.

A modulating voltage in the form of a square wave is superimposed on a dc voltage and applied to a grid. The particles detected are counted in an Up-Down mode which is synchronized to the modulating square wave. This, then, accumulates a window of energetic particles which is then stored in the first channel of the PHA (the PHA is used in the multi-channel sealer (MCS) mode instead of pulse height mode). The cycle is repeated again; however, the H.V. is stepped up to a higher value to form a new base for the next window of energy. After many windows of energetic particles have been stored in successive channels of the PHA, the results can be displayed on the PHA's oscilloscope, thus showing the energy distribution of the escaping particles.

The system consists of six chassis:

1. Tennenlic 541 timers (3 each)
2. H. P. counter
3. CMC 1-MHz oscillator
4. Northern Scientific PHA
5. Programmable isolated H.V. power supply
6. Control chassis

A detailed description of how the system works is being written up in a separate report.

Possible Corrections to Secondary Emission Signals from He* — The analysis and calculations for possible signal contributions to secondary emission-type detectors such as FAD were expanded from the brief discussion of the previous progress report (see Ref. 23) and the details are published elsewhere.⁴³ The conclusions remain essentially as previously stated except that use of a revised and lower cross section for $\text{He}(2^3s) \rightarrow \text{He}(2^1p)$ leads to somewhat higher density before onset of plasma shielding reduces the He* flux.

Plasma Diamagnetism

We investigated the feasibility of measuring plasma density and mean plasma energy under Baseball conditions by the diamagnetism of trapped particles by installing a 48,000-turn pickup coil on the z-axis of the Baseball field 80 cm from the center of the trapped plasma. This measurement was initiated by R. G. Mallon. It was not possible to install such a coil in the preferred position around the plasma at the midplane. The problem in this measurement was not sensitivity itself, but the separation of the signal due

to plasma diamagnetism (about 10^{-5} G) from the magnetic noise caused by fluctuations in the Baseball magnetic field (10^4 G) and in the ambient magnetic field (1 G). Our main result was a measurement of the residual noise level (10^{-3} G) which could not be further reduced or separated under operating conditions of Baseball II. This noise level is equivalent to the diamagnetic signal from a trapped plasma with a total energy $N_T (kT_1 + kT_2)$ of about 1 J. This is two orders of magnitude larger than the energy of the present low-energy Baseball plasma, but is comparable to or smaller than the energy of the high-energy plasma expected later in the Baseball buildup program. We therefore intend to return to this technique when conditions are suitable.

The principal noise source is mechanical vibration of the Baseball coil assembly suspended within the large vacuum tank. Rigid external bracing to prevent vibration of the cryogenic coil assembly is not possible because of heat leaks. We reduced this effect by mounting the 48,000-turn coil rigidly on the Baseball coil structure; however, we were still affected by induced currents in the vacuum tank and in the aluminum and copper tank liners which were due to the coil vibration. The effect is largest at 20 Hz, most of which could be filtered out by a low-pass ($RC \approx 0.2$ sec) filter or by synchronous detection of a magnetic signal pulsed repeatedly at 1 Hz. These techniques were used to reduce the residual noise level to 10^{-3} G; they were suitable only for plasmas sustained longer than 0.2 sec.

Other noise sources are due to fluctuations in the magnet power supply, thermal e.m.f.'s, and building and electronic noises. The effects of power supply fluctuations and thermal e.m.f.'s were compensated for by bucking circuits that were effective on a slow time scale (seconds) but which were not effective on a fast time scale because of flux jumps.

Three-Dimensional Measurements of Plasma Density and Plasma Potential

Arrays of end-loss detectors with biased grids have been installed in Baseball for measurement of several phenomena: fast ion losses by Coulomb scattering and by instabilities, slow ion production in the background gas by ionization and by charge exchange, and slow ion acceleration by the positive

plasma potential. These data have been used to infer the potential at the center of the trapped plasma and the transverse distribution $n(x)$ of the plasma density (see following sections). We now propose to extend these techniques to a three-dimensional measurement of time-resolved spatial distributions of the plasma density $n(x,y,z,t)$ and plasma potential $\phi(x,y,z,t)$, computed from the slow-ion current measurements $i(V)$ as a function of the retarding voltage V applied to the detector grids.

Conversion of the measured data $i(V)$ into longitudinal distributions of density and potential, $n(s)$ and $\phi(s)$, begins by differentiating by the chain rule, considering that the grid bias V is equal to the potential $\phi(s)$. The coordinate s is measured along the tube of flux defined by the detector.

$$\frac{di}{dV} = \frac{di}{ds} \frac{ds}{dn} \frac{dn}{d\phi} \quad (II-1)$$

The rate of production of slow ions within the volume element ($A ds$) by ionization and charge exchange of the background gas is

$$di \approx n_{\text{gas}} n (\sigma_{\text{ion}} + \sigma_{\text{cx}}) q A ds \quad (II-2)$$

Since the area $A(s)$ of the flux tube is inversely proportional to the magnetic field $B(s)$,

$$\frac{di}{ds} = \frac{Cn}{B} \quad (II-3)$$

where C is a constant calibration factor, proportional to the effective area of the detector.

We can now obtain the density profile $n(s)$ from differential Eq. (II-1) if we know $dn/d\phi$, the relationship between the local plasma density and the local plasma potential. This relationship is determined by the energy distribution of the electrons because they are confined and spatially distributed by the electrostatic potential. If the electron distribution is Maxwellian, $n(\phi) = n_0 \exp((\phi - \phi_0)/T_e)$, where n_0 and ϕ_0 are the maximum values of density and potential; and $dn/d\phi = n/T_e$.

The Maxwellian solution is inaccurate except when $\phi \gg T_e$, but it is useful because differential Eq. (II-1) can be solved analytically with a Maxwellian electron

distribution. The analytic solution can be compared with numerical solutions of the same equation using a Fokker-Planck electron distribution function. Debugging and checking of Fokker-Planck solutions is therefore simple and assured.

Electron energy distributions computed from Fokker-Planck equations are available either from a Multi-Species numerical computation⁵ or from Berk's simplified analytical solution.⁴⁴ These two distributions have been found to agree within 8% when identical values of ϕ_0/T_e were specified.

We have therefore written subroutines to solve numerically differential Eq. (II-1) and thereby obtain values of n and s corresponding to each specified value of ϕ . This computation uses Berk's Fokker-Planck electron distribution function, measured values of di/dV and V , the area of each detector, and the known magnetic field profile $B(s)$ along the flux tube defined by each detector. The effective area and the effective bias voltage of each detector is corrected for the angle between the magnetic field and the plane of the detector. The calibration factor C is computed from the known length of the plasma. The ratio ϕ_0/T_e is pre-computed by the Multi-Species Code. The coordinate s is converted to x - y - z coordinates for each data point; the results of $n(y,z,t)$ and $\phi(x,y,z,t)$ are presented in tabular form and also as contour maps of the Baseball x - z plane and y - z plane, using data from several detector arrays.

A substantial quantity of digitized data is required to compute density and potential profiles measured by an array of six or more detectors several times during a single plasma buildup and decay. The end detector data $i(V)$ and V were measured as usual by applying a saw-toothed retarding voltage V to the grids and recording V and $i(V)$ on a 14-channel analog tape recorder. The derivative di/dV was computed by an analog differentiator and transcribed onto a multi-channel oscillograph. Coordinates of points on the oscillograph record were mechanically measured and digitized in preparation for reading into the computer. These steps are now in progress.

The only serious limitation yet encountered in this technique is the requirement for plasma stability during the 0.1 sec required to measure $i(V)$ as V is swept from 0 to 150 V.

Plasma Measurements

Instability Threshold

Figure 11 shows experimental values of instability threshold in Baseball II obtained during recent operation. We have plotted values of $\epsilon \approx (\omega_{pi}/\omega_{ci})^2 \propto n^+/B^2$ at threshold versus $e\phi/W_i$, where ϕ is the plasma potential and W_i the ion energy. Threshold for a given set of conditions is defined as the value

of ϵ , as the plasma density is increased, at which definite sharp bursts of fast ions out the mirrors begin to appear.

The Baseball II instability-threshold measurements are a continuation of a similar series made in Baseball I. Those earlier results and their interpretation in terms of an ion-cyclotron instability with Landau damping were discussed in a previous publication.⁴⁵ The upper end of the average-threshold 45° line obtained in the

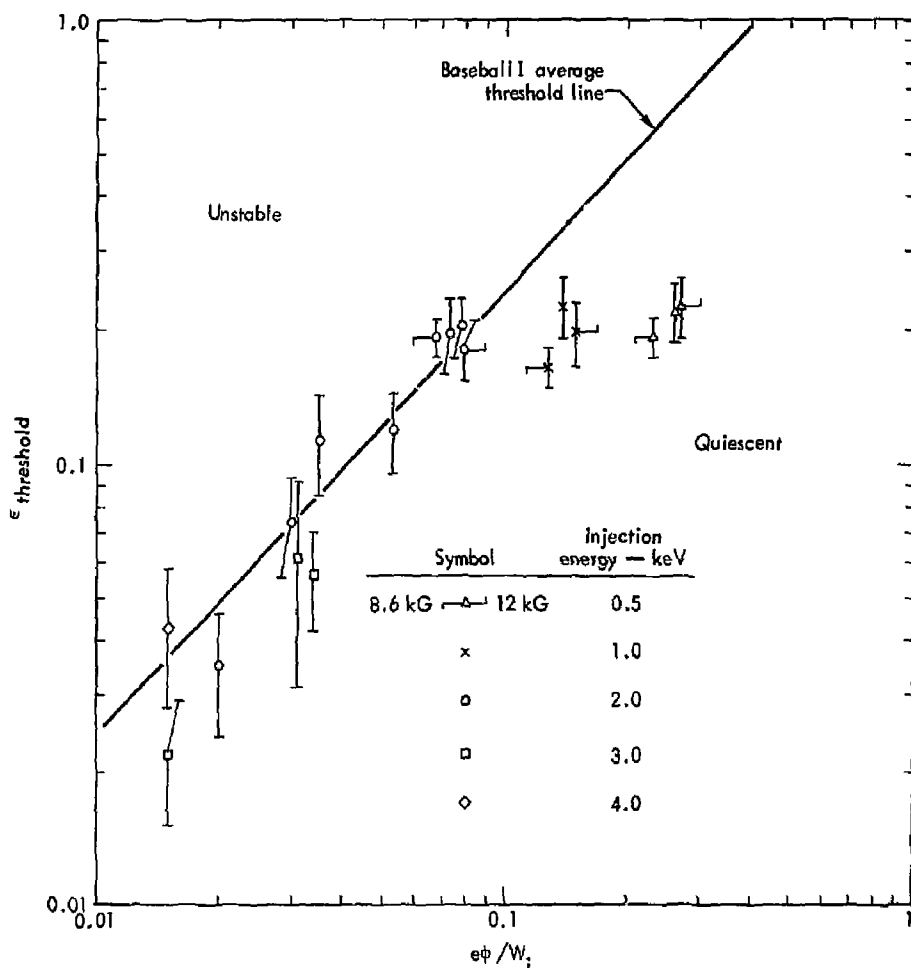


Fig. 11. Experimental values of ϵ at threshold for instability in Baseball II as a function of $e\phi/W_i$. The magnetic field at the center is about 10.3 kG, unless otherwise noted by the symbol.

Baseball I analysis is reproduced in Fig. 11 and extended further upward to provide a comparison with our earlier work.

The ion density (n^+) and the plasma potential used in the instability analysis are experimental measurements, B is calculated from the coil current, and W_i is taken as the full energy of the injected neutral hydrogen beam. A double-pass microwave interferometer measurement gives the values of n^+ , the average density over the microwave path through the plasma. The diameter of the plasma is assumed to be 20 cm for this calculation. For the lower- ϵ threshold points in Fig. 11 microwave-interferometer density measurements were not always possible. There, relative values of $(nT_e)/\phi$ are used, normalized to the microwave readings at higher densities. The quantity (nT_e) is determined from a signal emitted by the plasma at the electron-cyclotron frequency, the amplitude of which is assumed proportional to the product of electron density times electron temperature. We assume that $kT_e \propto e\phi$ over a limited range of ϕ , so that we can eliminate T_e by dividing by ϕ . Values of ϕ used here and in $e\phi/W_i$ are obtained from a retarding-grid analyzer positioned on or near the magnetic axis considerably outside the mirror. The plasma potential, ϕ , is defined as the maximum energy of the slow-ion component leaving the plasma.

Although the error bars in Fig. 11 are at times large, the trend is clear. The threshold data points at the lower left seem generally to follow the variation of the Baseball I line. They steadily increase with $e\phi/W_i$ until the region near $e\phi \approx 0.1 W_i$ is reached. At that point, a limit on further upward progress abruptly sets in. A plateau is apparently reached.

It was expected in Baseball II that a scattered ion distribution would raise the instability-threshold level, i.e., the experimental points would eventually rise above the 45° line. Considerable scattering is evidently occurring at the plasma conditions of the threshold points out on the ϵ plateau because the escaping end flux of particles with energy greater than the plasma potential (assumed to be scattered fast plasma ions) is comparable to the slow ion end signal (from charge exchange and ionization). Yet, just the opposite to the expected threshold behavior apparently occurs. Possibly a different instability becomes dominant near $e\phi \approx 0.1 W_i$. Electric fields

in or around the plasma could become influential in this region. Or, possibly the existing theory, valid for Baseball I and for the lower $e\phi/W_i$ region of Baseball II, does not apply to the higher regime of Baseball II.

The horizontal spread in the threshold points creating the plateau arises from the variation in W_i in the horizontal parameter, $e\phi/W_i$. The variables ϵ and ϕ change very little over these points. As W_i , assumed the full beam energy, is lowered from 2.0 to 1.0 to 0.5 keV, the plotted threshold points move out to the right, creating the plateau. Because of plasma energy-loss processes, the mean energy of these good-vacuum threshold points in the scattering regime is probably considerably lower than the injection energy. (We presently have no direct measurement of the mean plasma energy.) If we use estimated values of the mean energy to calculate $e\phi/W_i$, the plateau data points will be moved even further to the right, creating a wider plateau. The threshold measurements down the 45° line would not be expected to shift horizontally significantly because the degraded vacuum conditions there would probably prevent much decrease of mean energy from the injected energy. (The significant fraction of half-energy particles sometimes present in the injected neutral beam confuses the situation somewhat.)

It is uncertain at this time whether the plateau behavior persists when we vary ϕ in $e\phi/W_i$ instead of W_i . That is, if we sit out on the plateau and lower $e\phi/W_i$ by lowering ϕ rather than by raising W_i , do we move to the left approximately following the plateau, or do we move down a 45° line passing through the starting point? If the original ion-cyclotron-instability theory is no longer valid for the upper ϵ points, $e\phi/W_i$ may no longer be the pertinent parameter and our continued plotting against it may be misleading. To experimentally decrease ϕ while holding the injection energy constant, the background-gas density is increased. A higher beam current is then usually needed to make the plasma go unstable. Our experimental evidence on the variation of the threshold ϵ value with ϕ is presently inconclusive because at the lower energies there is scarcely enough spare beam available to vary ϕ significantly and

still go unstable. We also need the measurement of W_j .

In spite of the unexpected behavior of the upper threshold points in Fig. 11, the quantity ϵ (rather than n^+ , for example) still seems to be the pertinent parameter to plot. The threshold measurements along the plateau were obtained at three different magnetic fields, as indicated. Considerably less vertical spread in the data is obtained by plotting $\epsilon \propto n^+/B^2$ rather than just n^+ . It appears that it is ϵ at threshold that is remaining constant and not n^+ . Also, when using a deuterium instead of a hydrogen beam and comparing the threshold of a D^+ plasma with that of a H^+ plasma, where the mass difference gives a change of a factor of two in the ϵ equation, it is again ϵ rather than n^+ that is more nearly constant.

Further instability-threshold study needs to be done, both experimentally and theoretically. We hope eventually to have a measurement of \bar{W}_p , a presently uncertain but important parameter. We need to vary ϕ in the plateau region and observe any change in threshold ϵ . If a limitation by a different instability is causing the break from the 45° line, we might be able to detect differences in the instability characteristics. On the theoretical side, we need an explanation for the threshold plateau. An understanding of this limitation possibly could then point to a method of overcoming it, and lead to higher plasma densities in Baseball II.

Particle-End-Flux Measurements

Collector plates, preceded by grids that can be biased, detect charged particles leaving the Baseball II plasma through the mirrors along magnetic-field lines. Seventeen plates are installed, where space and lack of obstructions permit, on the 1.2-m-radius cylindrical liner outside and surrounding the coil. Each of the four tungsten-mesh grids before the plates has about 94% open area. The magnetic-field lines are approximately perpendicular to the planes of the grids and plates. For an ion that just escapes through the maximum-field region, with almost all of its energy perpendicular to the field lines there, about 87% of its energy is transformed parallel to the field lines by the time it reaches an end-loss detector.

Figure 12 shows the areas of the collector plates projected along magnetic-field lines to the midplane

(the plane perpendicular to the magnetic axis and including the center of the well). The behavior of the curving field lines causes the distorted shape of the projections. The table in the figure gives actual plate dimensions, actual and projected areas, and range of radii of the projected areas. Although the areas shown in the figure are those projected on to the $z = 0$ plane, the numbers given in the table have been corrected to represent these areas projected perpendicular to the field lines there. The projected areas of H-FELD 2, V-FELD 5, and GD have been additionally decreased because of obstacles blocking some of the field lines to these plates.

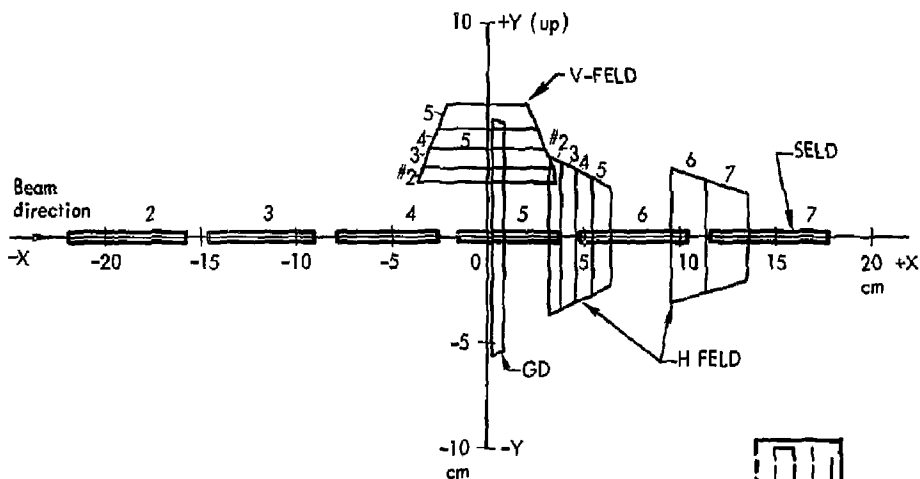
To decipher the detector nomenclature: H-FELD and V-FELD are End-Loss Detectors in the horizontal and vertical fans, GD is our original gridded detector in Baseball II, and SELD is an end-loss detector at the south end of the machine, near the magnetic axis. The V-FELD detector plates as well as the SELD plates are at the south end of the machine, while H-FELD and GD are at the north end.

The asymmetric positioning of the SELD plates in Fig. 12 with respect to the magnetic (plasma) axis at $x = y = 0$ is caused by ~ 0.4 -cm misalignment of the geometric center of SELD during installation. This correction was determined by measuring the steady-ion-current profile for a stable plasma, and assuming that its center of symmetry represents the magnetic axis.

Figure 13 shows samples of results obtained with our end-detector array at 2-kV source voltage. Considering the restraints on the detector placement and the distortions caused when projecting the plate areas along field lines, the resulting profiles are quite informative. The plotted data points show the total steady ion current (per cm^2 of area projected to the midplane) from a stable plasma right after beam turn off to the various detector plates. This current is constituted mainly of "slow" ions, which arise from charge exchange of the fast trapped ions on the background gas, or from ionization of the background gas, particularly by the trapped electrons. The resulting slow ions are then pushed out along the field lines by the positive plasma potential, thus emerging with energy corresponding to that potential. About 25%, on the average, of each plate current plotted in Fig. 13 corresponds to

scattered fast trapped ions, i.e., particles leaving the plasma with energy greater than the plasma potential. The slow-ion-signal distribution in particular should reflect the plasma-density distribution, and the minor fraction of fast ions should not modify the result greatly. The radial width shown for each plotted point is the radial extent of that detector-plate projected area given in the table of Fig. 12. Curve

A in Fig. 13 is an approximate fit to the data. Of the three plates not plotted, one was not used in these measurements and the currents to the other two fell excessively low on the plot. The justification used for excluding the latter two is that each plate has part of its view of the plasma obstructed, so that our estimate of the useful areas may be incorrect.



Detector	No.	Plate dimensions (cm) X × Y	Plate area (cm ²)	Projected area at Z = 0 (cm ²)	Range of radii (cm)
H-FELD	2	8.3 × 1.9	15.8	4.00	3.3 - 5.3
	3	↓	↓	4.81	3.9 - 5.8
	4	↓	↓	4.84	4.7 - 6.3
	5	↓	↓	4.42	5.5 - 6.9
	6	8.3 × 3.8	31.5	7.90	9.6 - 11.8
	7	↓	↓	7.44	11.4 - 13.7
V-FELD	2	1.9 × 11.4	21.7	4.73	2.6 - 4.7
	3	↓	↓	5.32	3.3 - 5.2
	4	↓	↓	5.37	4.1 - 5.8
	5	↓	↓	3.79	5.1 - 6.6
GD	-	12.4 × 1.9	23.6	6.05	0.3 - 5.6
SELD	2	1.0 × 10.0	10.0	1.55	15.7 - 21.9
	3	↓	↓	2.09	9.0 - 14.6
	4	↓	↓	2.50	2.6 - 7.9
	5	↓	↓	2.64	0 - 3.7
	6	↓	↓	2.37	4.8 - 10.4
	7	↓	↓	1.87	11.5 - 17.7

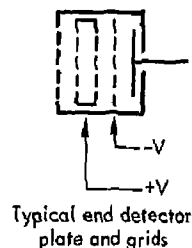


Fig. 12. Mapping of end-detector plates along magnetic field lines to the midplane, and dimension and area information about the plates.

Curve B in Fig. 13 is also obtained from experimental data, and is our estimate of the radial profile of the fast trapped ions lost in bursts from the plasma because of the instability (at 2-kV source voltage). To obtain these results, the ion-retarding-grid bias was set at +300 V, somewhat above twice the plasma

potential. The bias on the electron-retarding grid was set at -300 V.

In obtaining Curve B, we have tried to reduce the possibility that accelerated slow ions contribute significantly and thus obscure the interpretation of the data as fast-ion loss. For example, at the time of

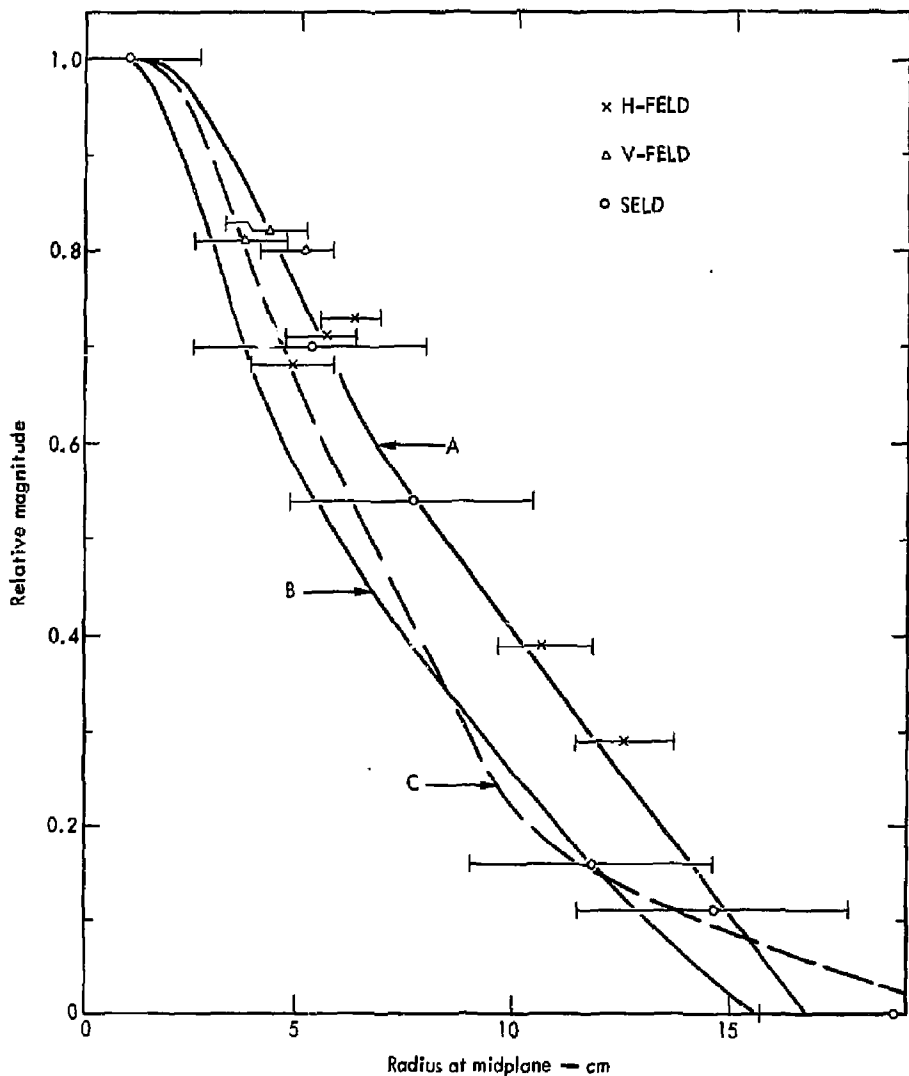


Fig. 13. Plasma radial profiles. The data points show the total steady ion current (per cm^2 of projected area) from a stable plasma to the various end-detector plates. Curve A is a fit to these data. Curve B represents the radial profile of the fast-trapped-ion instability end loss. Curve C is a computed radial density distribution.

instability the plasma potential may momentarily shoot up because of additional electron loss. If the potential should rise above +300 V, then slow ions leaving the plasma could gain enough energy to be detected. Also, if the electrons in the plasma gain energy, more slow ions would be produced because of increased ionization rate, thus contributing further to the slow-ion end signals. These possible bursts of slow ions would likely come at the same time as bursts of fast trapped ions lost by the instability. The escaping fast ions could arise from trapped fast ions with velocity vectors near the loss cone, which are then pushed into the loss cone by the momentary increase in plasma potential.

To attempt to separate the accelerated slow ions from the escaping fast ions, we use the apparent and accidental asymmetry in maximum magnetic-field strength at the north and south magnetic-field-line fans, presumably arising from asymmetries in the superconducting-coil fabrication. The slow ions, born with thermal energy and then pushed out along the field lines by the plasma potential, should not be influenced by the field asymmetry and therefore should come out equally at the north and south ends. But the escaping fast ions might be expected to come out mainly through the weaker south-end mirror region. This assumes that the momentary instability plasma-potential increase is slow compared with the ion axial-reflection period, so that a trapped ion has time to sample the magnetic field at both ends as its reflection regions are pushed outward. It would then tend to go out the weaker south mirror. We therefore obtain what we call the fast-trapped-ion loss rate and radial profile from the difference between the average ion current flow (per cm^2 of projected area) under the end-loss instability spikes out the south and north mirror regions. (The normalized north-end signals typically are 10-20% of those at the south end.)

In this analysis, we assume that the instability does not give the slow ions enough perpendicular energy to cause them to be temporarily trapped and thus possibly contribute to the south-north asymmetry. But even if we were not able to completely eliminate the slow ions from our data, the resulting profiles of the instability fast end losses should still be a measure of the region of instability activity in the plasma. The

uncertainty would arise when integrating under the radial profile to obtain the total fast-ion loss rate.

The dashed curve (C) in Fig. 13 is a computed radial density distribution. A series of single-particle orbits was calculated using the computer code TIBRO, and then summed as described elsewhere.⁴⁶ The orbit starting points are distributed over the beam region on the entrance side of the magnetic axis, with the beam direction perpendicular to the magnetic axis as in Baseball II. Actually, the density-distribution calculations were done earlier for Baseball I. The results were then scaled up by 50% in each dimension to approximately correspond to Baseball II, in which the beam and magnetic-field dimensions are about 50% larger than in Baseball I. For Curve C, the trapped-ion charge-exchange loss rate on the streaming gas in the beam region is assumed ten times the loss rate on the background gas in the same region. The orbit radius at the center used in the calculations, scaled up by 50%, is 3.7 cm, as compared with ≤ 0.6 cm for the actual Baseball II plasma. This large orbit size, unrealistic for Baseball II, would tend to extend radially the tail of the calculated distribution further than in the actual plasma. While the computed curve represents the plasma-density radial distribution, the experimental results are line-integral current measurements. That is, any variation of path length through the plasma has not been removed in the experimental results.

The three curves in Fig. 13 all have the same general behavior. The fast-ion instability-loss profile was obtained at full beam intensity, where the plasma is highly unstable. Its width is less than but approaches that of the slow-ion profile for a stable plasma, which represents the density distribution. Thus, the instability-activity profile resembles the density profile. (The radial profile for ion instability loss just above the instability threshold is more sharply peaked about the magnetic axis.) The approximately calculated density radial profile is similar to the measured profile. So it appears that we have consistent and useful information on the plasma radial distribution.

Particle-Balance Analysis

An important aspect of the experiment is the manner in which the trapped plasma ions are lost.

We have made a preliminary attempt to quantitatively account for all the ions. Table 1 gives a trapping-rate and loss-rate comparison for 2-kV source voltage, injected beam of 18 mA, and central field of 10.3 kG. These numbers are presently only approximate and tentative, but give an indication of how the losses are distributed for a plasma well above the instability threshold.

Table 1. Typical trapping and loss rates in Baseball II.

Total trapping rate (estimated)	4.0 μ A
Trapped-ion loss rates	
Charge exchange	1.4 μ A
Scattering (classical)	0.1
End	2.3
Radial	0.5
Total loss	4.3 μ A

By examining the numbers in the table, one may obtain a better understanding of the present situation in Baseball II. The uncertainties involved allow a larger discrepancy between the trapping and total loss rates than the numbers show. The total trapping rate is estimated by scaling from the trapping rate at the instability threshold. To obtain the end-loss rate, we integrate under the instability bursts of fast ions out the mirrors, discussed in the section on particle-end-flux measurements. Similarly, the radial loss is the area under the positive bursts to the radial limiter during the instability periods. The radial limiter is a movable flat metal plate whose inner edge is set close to the plasma boundary for these measurements, and which is biased at -30 V. The numbers in the table suggest that the main trapped-ion losses no longer arise from charge exchange, but are caused by the plasma instability.

rf Measurements

Spectral and time-resolved measurements of the plasma rf have been made using a pickup loop oriented to receive emission from a current in the azimuthal direction of the plasma, J_θ . Another loop, oriented for emission from a longitudinal current J_z was also installed, but due to cable problems inside the vacuum system this loop was not usable. A

rough calibration of the J_θ loop with a test rf source and a rf field strength meter indicated that the detectable field strength limit of the system for rf emission was of the order of 30 μ V/m at the frequencies of interest.

The observed rf spectrum shows emission at multiples of ω_{ci} , where ω_{ci} corresponds to the ion-cyclotron frequency near the center of the magnetic well. Harmonics as high as 6 ω_{ci} are sometimes present. For a plasma produced by an injected beam of 2.0-keV H^0 , typical rf emission at ω_{ci} has a field strength of the order of 2 mV/m. These rf signals are generally correlated with the plasma losses that are seen on the gridded end-loss detectors (see earlier section). As the plasma approaches the stability threshold, the rf signals drop below the detectable limit while some instability signals are still observed on the gridded detectors. Thus, these gridded detector signals appear to be a more sensitive indication of plasma instability than the rf signals.

In addition to the emission at harmonics of ω_{ci} , weaker emission at 0.5 ω_{ci} is also observed from a plasma formed by injecting a beam of primarily H^0 . This is tentatively identified as an impurity mode for which there may be two possible sources. The first arises from the fact that the injected beam contains a percentage of H_2^0 , some of which may be trapped as H_2^+ . Under instability conditions these ions could produce rf emission at 0.5 ω_{ci} where ω_{ci} is evaluated for H^+ . The other possibility is due to the H_2 background gas in the plasma region. Some of this thermal gas is ionized by the plasma to H_2^+ as shown by LEIS ($m/e = 2$). If the density of these ions is high enough they could produce a two-component mode with 0.5 ω_{ci} emission, even though they are not trapped.

Time-resolved measurements of the rf signals show that, for a central magnetic field of 10 kG, the emission at ω_{ci} may persist as long as 35 msec after beam turn-off. For a central magnetic field of 5 kG, strong emission at ω_{ci} has been observed up to 90 msec after beam turn-off. Thus, the instability associated with the rf emission at ω_{ci} does not abruptly cease when the beam injection is terminated. This indicates a relaxation process, possibly in the ion distribution. (Compare the calculated ion distributions before and after beam turn-off in the section on Fokker-Planck calculations).

Electron-Heating Experimentation

In an attempt to influence the plasma-instability characteristics, power in the electron-cyclotron frequency range was introduced into the plasma region. For a preliminary try, we used the 8-mm radiometer system, normally employed to detect plasma radiation and to provide a signal proportional to nT_e . Later, a more optimum arrangement was provided by inserting a microwave horn through a vacuum lock along a line in the horizontal plane aimed toward the origin at a 29° angle with the normal to the magnetic axis. The horn was kept well outside the plasma. The microwave-power amplifier was then placed close to the lock, for more efficient coupling.

We were able to observe a positive effect on the instability threshold with both systems. Up to 80% increase in plasma density at threshold was observed in the electron-heating experiments, for density measured either by the microwave-interferometer line-integral method (80% increase) or by relative values of $(nT_e)/\phi$ (69% increase) as described in the instability-threshold section.

A detailed investigation has not yet been carried out to understand or optimize this effect. A short survey was made in which we tried a fixed heating frequency or swept over a frequency range during the beam-injection time, tried different fixed frequencies or ranges on different shots, and tried different sweeping rates (periods of 20 msec to 20 sec). In this cursory survey, we found no combination of parameters that gave a bigger positive effect than when we set the frequency at a value a few percent above the electron-cyclotron frequency at the center of the magnetic well, and either left it fixed or rapidly varied it over a small range. For the second, more optimum, power-introduction arrangement, only a few milliwatts of power out of the amplifier seemed needed. Increasing the power further eventually decreased the positive effect.

A yet unexplained phenomenon is the effect on the instability threshold, during electron heating, of varying the amount of nitrogen gas in the neutralizing section right after the ion source. On our final day of electron-heating experiments, the N_2 pressure in the neutralizer was raised to three times the standard

operating level; the threshold increase with electron heating applied then went from about no observable effect to the approximate 80% increase earlier mentioned. The heating power was then turned off while the N_2 pressure was still tripled, and the positive threshold increase disappeared.

Some enhancement in the plasma potential ϕ is observed with the threshold increase arising from electron heating. In one early run, ϕ increased by 22% when the threshold density increased by $\sim 56\%$. During the more recent run when the threshold increased by $\sim 80\%$, the apparent enhancement in ϕ was only $\sim 6\%$. So the electron heating may be doing more than just shifting the threshold up the $45^\circ e (\alpha n^+/B^2)$ vs $e\phi/W_i$ line, although that in itself could be an interesting effect.

Figure 14 shows the beneficial influence on the plasma of electron heating at low injected-beam level. The power was turned on almost halfway through the shot. While the beam intensity remained constant, the nT_e and FAD signals increased and became steady. Both the fast and slow components (ions with energy greater than and less than ϕ) of the V-FELD end signal increased, and the instability activity in this signal decreased. The RF activity (not shown) also decreased.

Low-Frequency Oscillations

A review of the neutral beam trapping calculations for Baseball II predicts a well defined central region for magnetically trapping the injected fast ions, surrounded by the much larger volume where electrons can be electrostatically trapped. The plasma potential in the hot-ion — hot-electron region could be expected to have a sharp sheath-like gradient at the boundary with the outer cold electron region. If the resultant $\vec{E} \times \vec{B}$ in this boundary region exceeds the ion ∇B drift, an argument can be made for a flute-like instability around 15 kHz.

Measurements on the BBII plasma show a low frequency 5 to 25-kHz oscillation. The observed spectrum is nearly independent of W_i or B , rather than following W_i/B as would be expected for ion ∇B drifts. The disc (capacitive) electrodes located 90° apart in the midplane of BBII show rotation in both the ion ∇B and $\vec{E} \times \vec{B}$ drift senses. The oscillation appears present much of the time at

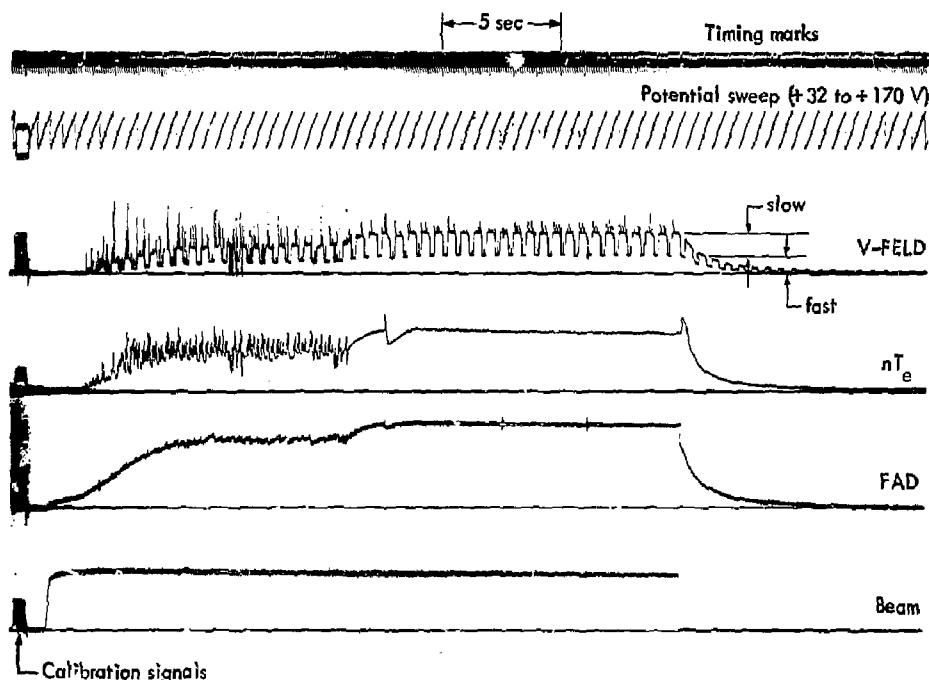


Fig. 14. Effect of turning on electron-heating power during shot. The V-FELD signal is the combined ion currents to all four plates.

higher densities with abrupt increases in amplitude in correlation with the energetic ion loss bursts (or rf spikes at ω_{ci}). The low-frequency oscillation tends to disappear at beam turn-off, returning as lower frequency bursts after 15-30 sec of quiet (depending upon density and plasma conditions).

Near the end of this reporting period, feedback stabilization experiments were started on these low-frequency oscillations using available internal electrodes. The signal from one of the disc detectors was amplified, phase-shifted, and then applied across a pair of deflection plates in the south vertical fan. The choice of gain and phase shift was found critical for a beneficial effect. Only partial stabilization was achieved during the preliminary tests, clearly limited in part by a phase shifter being frequency-dependent (hence we could only optimize the phase shift for a narrow band of frequencies, and higher or lower frequencies were then incorrect).

Figure 15 shows some of the best results obtained by feedback stabilization during this reporting period.

The plasma density as measured by a fast atom detector and the microwave emission of the plasma is shown, together with a signal from an end loss detector and the rf at ω_{ci} (ω_g rf only). The feedback was turned off for the last several seconds. Clearly, there is a dramatic decrease in both the rf and particle loss bursts when the feedback is applied. The density also increases by about 30% with the application of feedback. Work on interpreting the character of this oscillation is continuing, as are preparation for more refined feedback stabilization experiments.

Fokker-Planck Calculations

The Baseball II plasma is unstable during beam injection, but is stable following beam "turn-off". This behavior suggests that the instability is being driven by the beam. The hot ions injected by the beam are highly peaked in angle and essentially mono-energetic.

Before beam "turn-off," an equilibrium ion distribution is reached in the presence of this peaked

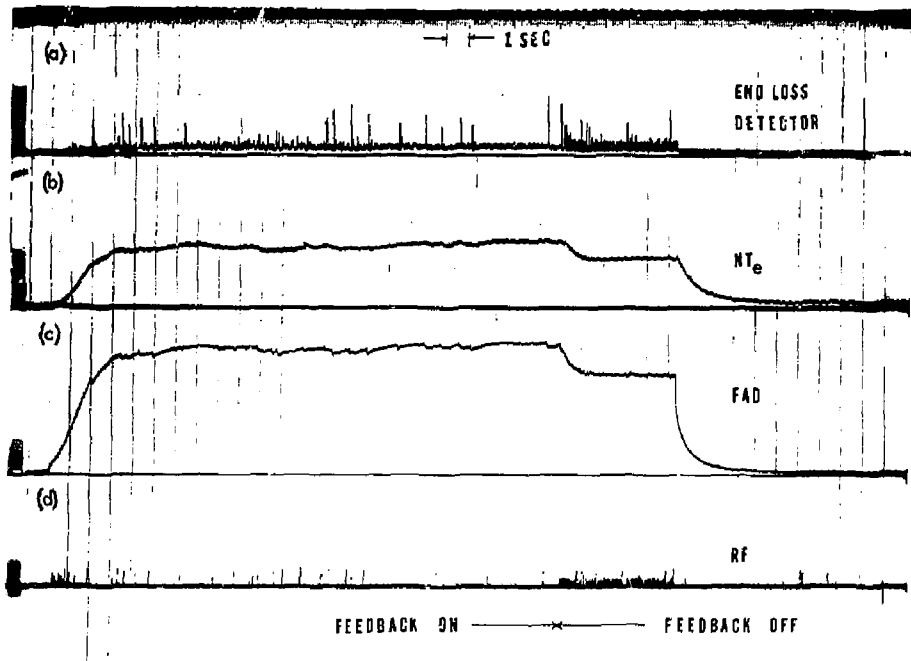


Fig. 15. Effect of feedback stabilization on the BBII plasma. The signals are: (a) end-loss detector, (b) microwave radiation from plasma (proportional to nT_e), (c) fast atom detector, and (d) j_0 radio frequency at the ion-cyclotron frequency.

source which maintains both the plasma density and its energy. Therefore, beam trapping may be regarded as a process which tends to maintain a peaked distribution. The characteristic time associated with beam trapping τ_t is equal to the plasma density n^+ , divided by the plasma trapping rate per unit volume J , i.e.,

$$\tau_t = n^+/J.$$

For negligible distortion of the distribution due to the beam, this characteristic trapping time must be much longer than the corresponding times for diffusion in either velocity or angle, i.e.,

$$\tau_t/\tau_c \gg 1$$

$$\tau_t/\tau_s \gg 1$$

respectively, where τ_c is the characteristic time for ion cooling by energy transfer to the electrons and τ_s is the Coulomb scattering time. However, the nature of the equilibrium process requires the foregoing ratios to be of order unity in the absence of charge exchange losses. Therefore, some distortion of the ion distribution function during beam injection can be expected. However, this distribution is independent of the source or beam magnitude, as pointed out, by Fowler and Rankin.⁴⁷ The presence of charge exchange losses would not significantly affect the foregoing arguments as long as the charge-exchange time is equal to or greater than both τ_c and τ_s .

Charge exchange of a plasma ion with a neutral beam atom replaces an ion from the plasma distribution which has been spread in both angle and energy with a beam particle which is highly peaked

in angle and essentially mono-energetic. The conditions for negligible distortion of the distribution function due to charge exchange with the beam in either velocity or angle are

$$\tau_{cx}^b / \tau_c >> 1$$

and

$$\tau_{cx}^b / \tau_s >> 1$$

respectively, where the characteristic time τ_{cx}^b for charge exchange with the beam is

$$\tau_{cx}^b = \frac{1}{n_b \sigma_{cx}^a v} \left(\frac{V_p}{V_b} \right)$$

In this formula, n_b is the density of beam particles, $\sigma_{cx}^a v$ is the rate parameter for charge exchange with the beam and (V_p/V_b) is the ratio of the plasma volume to the beam volume.

The first column of Table 2 shows values of these various ratios calculated from the multi-species Fokker-Planck code for a plasma density of 4.2×10^9 ions/cm³. The input trapping rate was 9.7×10^9 hydrogen ions/cm³ at an energy of 1 keV. A background gas pressure was chosen which produced a charge-exchange time of 1 sec. Charge exchange with the beam was also an input parameter, and had a calculated value of 13.3 sec. These beam and vacuum conditions are typical for a beam energy of 1 keV.

Table 2. Values of various ratios calculated using various codes.

	MS Code	Spitzer's formula	Time (sec)
τ_t / τ_c	0.64	0.79	$\tau_t = 0.432$ $\tau_c(\text{MS}) = 0.67$
τ_t / τ_s	0.588	0.09	$\tau_c(\text{Spitzer}) = 0.544$ $\tau_s(\text{MS}) = 0.735$
τ_{cx}^b / τ_c	19.8	24.4	$\tau_s(\text{Spitzer}) = 4.78$ $\tau_{cx}^b = 13.3$
τ_{cx}^b / τ_s	18.1	2.78	

The second column of Table 2 shows these ratios calculated using values for τ_c and τ_s calculated from Spitzer's formulas. Values for the ratios τ_t / τ_c and τ_{cx}^b / τ_c are in good agreement with the corresponding values from the Multi-Species Code. As expected, the ratios τ_t / τ_s and τ_{cx}^b / τ_s are not in good agreement since scattering times calculated from Spitzer's formula do not include the effects of electron cooling and plasma potential on the scattering time.

From the calculated ratios given in Table 2, the following two conclusions can be made: (1) Charge exchange with the beam has a negligible effect on the ion distribution function, and (2) the presence of the source should produce an observable change in the ion distribution function. These conclusions are consistent both with our previous calculations using the Multi-Species Codes and with recent calculations using the unseparated two-dimensional (2-D) code of Marx.⁴⁸

Figure 16(a) shows an equilibrium ion distribution as calculated by the Multi-Species Code. Charge exchange with the beam was included in these calculations. Although a peak in the distribution does not occur at the source energy, a distortion of the distribution by the source is evident. Figure 16(b) shows that the distribution has relaxed into a normal loss-cone distribution within 100 msec after beam turn-off. Although not shown here, no observable difference was evident if charge exchange with the beam was not included in the calculation. Figures 16(c) and 16(d) are the corresponding distributions as calculated using the two-dimensional code for an injected source distribution having a broad angular distribution similar to the normal mode distribution of the Multi-Species Code. The distribution was sharply peaked in velocity space. The velocity dependence of curves (c) and (d) (2D code) are very similar to curves (a) and (b) (MS code).

Two-dimensional calculations using a source which is sharply peaked in both angle and velocity space are shown in Fig. 17. Curves (a) and (b) contain charge exchange with the beam and should be compared with curves (c) and (d), respectively, which do not contain charge exchange with the beam. No significant difference is observed due to charge exchange. However, a sharp peak in the equilibrium ion distribution now occurs at the injection energy and angle, in contrast to the case where the source

has a broad angular distribution. This sharp peak disappeared within 55 msec after beam turn-off. This disappearing peak could possibly be associated with the stable plasma observed after the beam is turned off.

Many additional Fokker-Planck runs have been made during the past year to provide calculated values of plasma parameters for a variety of energies and beam current. Figures 18 and 19 illustrate a typical set of curves for an injection energy of 1 keV. In obtaining these curves, the background gas

composition and pressure was varied as a function of beam current to agree with the experimental data. Measurements made by Goodman (see Ref. 23) show only two gases were present in quantities having a significant effect on plasma parameters - H_2 and Ne. The densities of these gases were found to vary with beam current as follows:

$$n_{H_2} = 5 \times 10^{16} (ma)$$

$$n_{Ne} = 1.5 \times 10^8 \{I(ma)\}^{0.52}$$

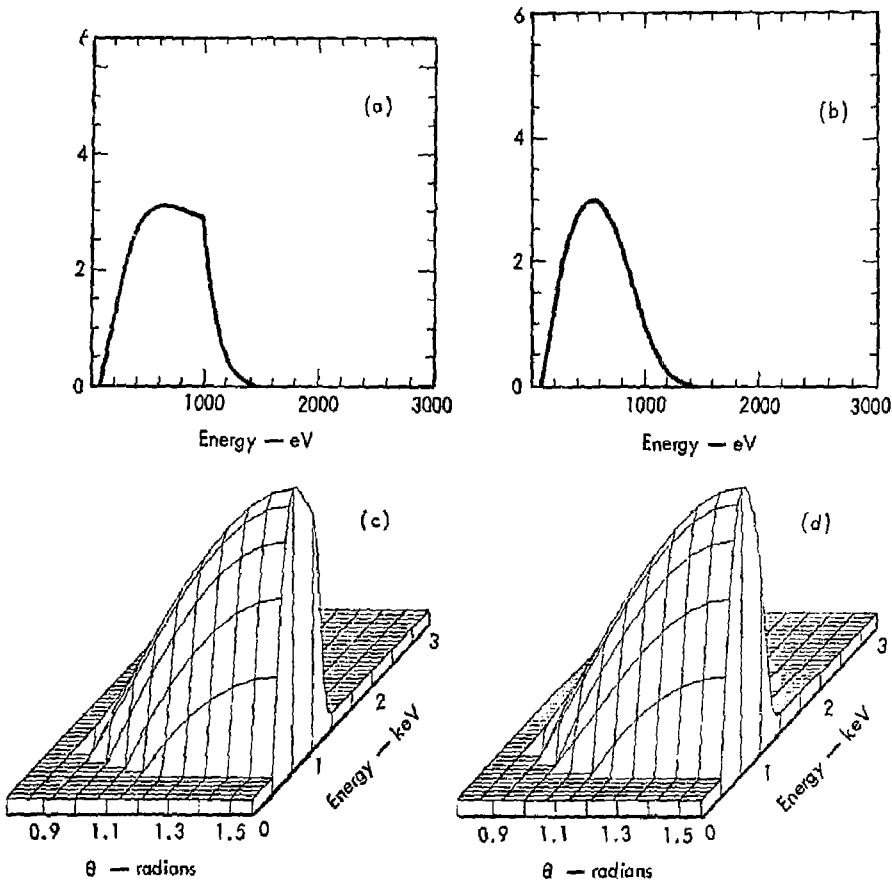


Fig. 16. Calculated ion distribution functions: (a) equilibrium distribution as calculated by the multi-species (MS) code, (b) distribution as calculated by the MS code 100 msec after beam turn-off, (c) equilibrium distribution as calculated by the two-dimensional (2D) code for an injected source having a broad angular distribution, and (d) distribution 55 msec after beam turn-off as calculated by the 2-D code.

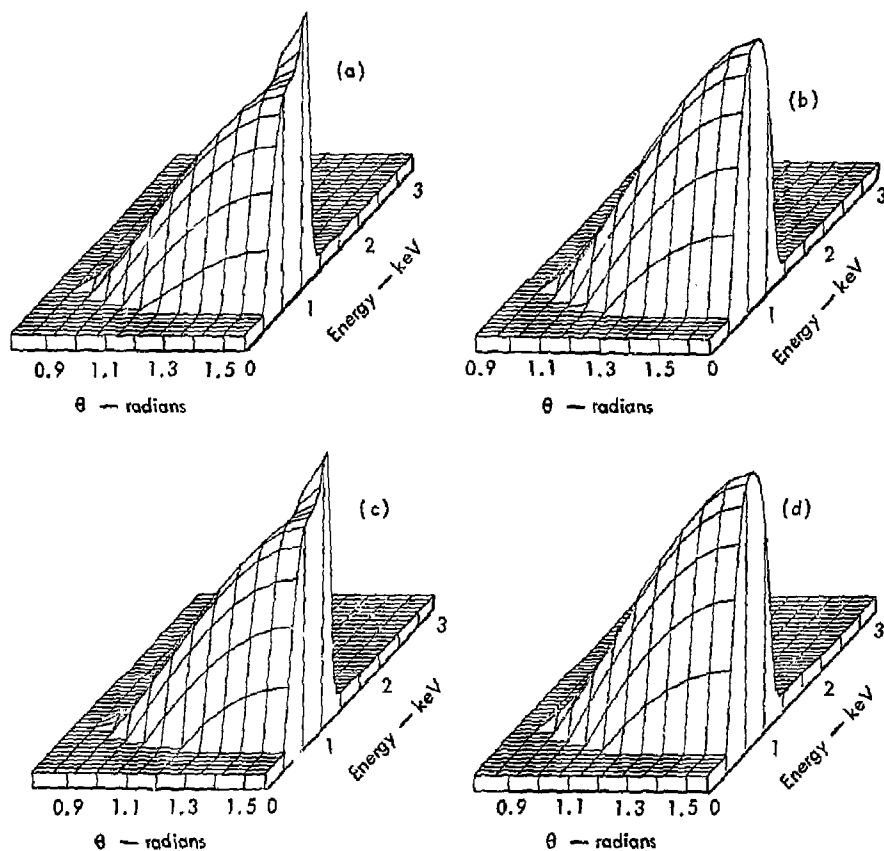


Fig. 17. Calculated ion distribution functions using the 2-D code: (a) equilibrium distribution in the presence of the source and including change exchange with the beam, (b) distribution 55 msec after beam turn-off, (c) equilibrium distribution in the presence of the source but not including change exchange with the beam, and (d) distribution 55 msec after beam turn-off.

Fokker-Planck input parameters were also changed following beam turn-off corresponding to an observed decrease in the hydrogen gas pressure by a factor of 3. In Fig. 19 the plasma lifetime τ was calculated by

$$\tau = \frac{\tau_{cx} \tau_s}{\tau_s + \tau_{cx}}$$

where τ_{cx} and τ_s are the charge-exchange lifetime and scattering lifetime, respectively.

Target Plasma Development

Experimental Facility

Preparation for target plasma development for neutral injection in the BBII experiment was started in June 1973. The BBI magnet will be operated in a pulsed, water-cooled mode, yielding fields of 5 kG for about 1 sec. The BBI vacuum chamber is being modified to give better access to one magnetic field fan; a new vacuum tank is being designed for future installation to provide access to both fans (see Fig. 20).

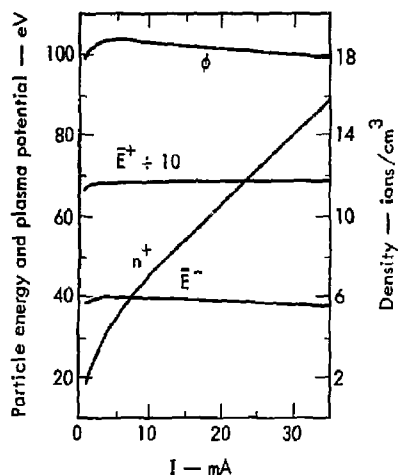


Fig. 18. Calculated plasma parameters versus equivalent neutral beam current for an injection energy of 1 keV.

This flexible facility will permit testing of a variety of target plasmas. Initial experiments on arc discharges will begin early in FY 1974.

The use of a target buildup mode on BBII requires high-intensity pulsed beams, and we plan to inject up to ~50 A of neutrals. Redesign of the beam-line components to accept such large beams, while maintaining the stringent vacuum requirements, is underway. A revised source pumping tank, neon-jet screen tank and beam disposal tanks are all required, as well as enlargement of the access holes in the main vacuum chamber of BBII. Fabrication of the screen tank and source tank has begun. It is also necessary to redesign part of the BBII magnet structure to provide access through the mirrors for an externally-generated target plasma. Redesign of the structure is underway.

Buildup Calculations of Neutral Beam Injection Into Target Plasma

The hot-ion density buildup may be modeled by a simple approximation balancing the input with losses due to classical scattering on the target plasma.

Results of this model were compared with detailed Fokker-Planck calculations using the multi-species code.⁵ Three species were included in these calcu-

lations: cold H^+ ions, hot electrons, and energetic H^+ ions trapped by neutral beam injection. Parameters were chosen to produce an equilibrium target plasma at a density of 10^{14} ions cm^{-3} . The hot electron distribution was Maxwellian. The results were found to be essentially independent of the target ion distribution with both loss-cone and Maxwellian distributions assumed in the calculations. Time-dependent buildup calculations were obtained for the hot ions as a function of the target plasma electron temperature. Nonclassical losses were not considered in these calculations.

The model is established as follows: The dominant mechanism for beam trapping is charge exchange on the target ions. Thus,

$$\left(\frac{dn_h}{dt}\right)_{\text{trap}} \equiv n_t \approx \frac{I}{V} (1 - e^{-\alpha L}), \quad (11-4)$$

with n_h the hot-ion density, I the equivalent neutral beam current, V the plasma volume, and L is length

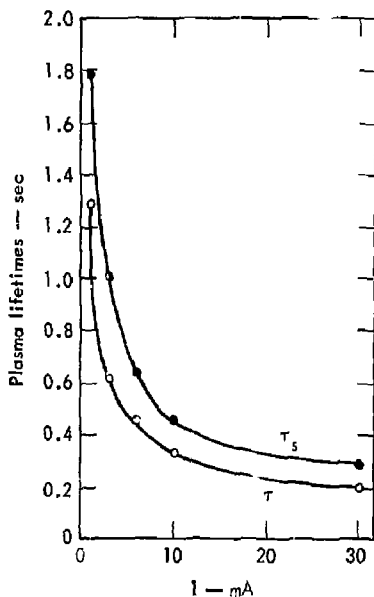


Fig. 19. Calculated plasma lifetimes versus equivalent neutral beam current for an injection energy of 1 keV.

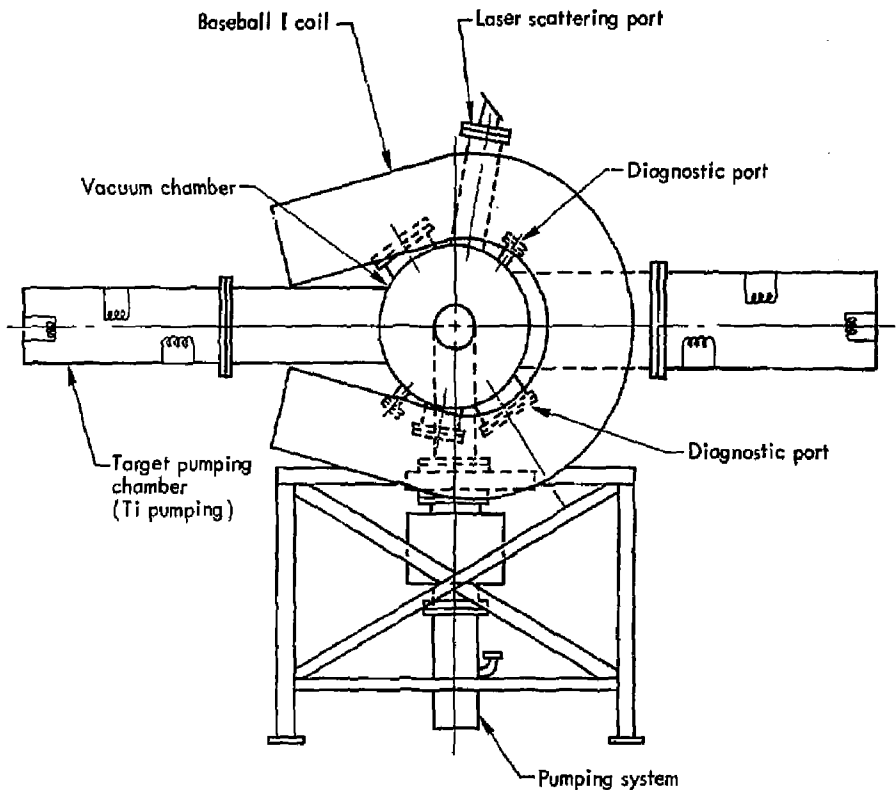


Fig. 20. Target test facility.

along the beam. Also, $\alpha = \sigma_{cx} n_t$, the product of charge-exchange cross section and n_t the target density.

The loss processes are more complicated, as the injected beam will lose energy to electrons and ions, but scatter out the loss cone primarily by scattering on ions.⁴⁹ At low electron temperatures, energy loss on electrons will cool the injected ions until they scatter, so we approximate the loss rate by the "slowing down" time,⁵⁰

$$\tau_{se} \approx 6.3 \times 10^8 T_e^{3/2} / n_t \ln \Lambda,$$

with T_e in eV and the electron density approximately equal to n_t .

For $16 T_e$ greater than the hot-ion energy (the factor of 16 holds for protons), collision with cold ions are more important than with electrons. Characteristic times for scattering into the loss cone (for a

mirror ratio of 2) approximately equal the energy-exchange time. As the latter degrades the hot-ion energy leading to an increased loss through the mirror, we pick the characteristic time as half the energy loss time,

$$\tau_{Ei} = 5.5 \times 10^6 E^{3/2} / n_t \ln \Lambda,$$

with E the injected energy in eV. Thus the loss rate for hot ions is

$$\frac{dn_h}{dt}_{\text{Loss}} \equiv \frac{n_h}{\tau_L} = -n_h \left(\frac{1}{\tau_{se}} + \frac{2}{\tau_{Ei}} \right). \quad (\text{II-5})$$

Combining Eqs. (II-4) and (II-5),

$$\frac{dn}{dt} = \dot{n}_t - \frac{n_h}{\tau_L}, \quad (\text{II-6})$$

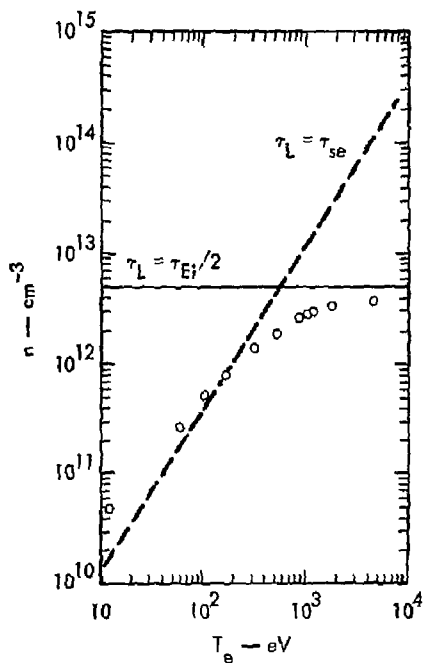


Fig. 21. Calculated hot-ion density as a function of T_e . Points are the result of the Fokker-Planck calculation. Trapped current is $10^{15}/\text{cm}^2\text{-sec}$ of protons at 20 keV. Target density is 10^{14} cm^{-3} .

and, in equilibrium,

$$n_h = \hat{n}_i \tau_L. \quad (11-7)$$

This result is compared with Fokker-Planck results in Fig. 21. The two lines correspond to balancing trapping against electron and ion times only. Build-up times (not shown) are to good approximation given by τ_L ; at $T_e = 10^3\text{ eV}$ and $n_i = 10^{14}$, for example, 1.5 msec is required.

The average trapped ion energy is shown in Fig. 22. As suggested above, the average ion energy increases with the electron temperature.

A typical hot-ion distribution function is shown in Fig. 23. The dropoff at low ion velocities will be filled in by two effects not included; the cold-ion distribution function and decreased loss rates when the ion mean-free-path becomes less than the machine

length. These effects and their influence on stability are being investigated. Figure 24 shows the time-dependence of the hot-ion density and average energy for the same electron temperature used in Fig. 23.

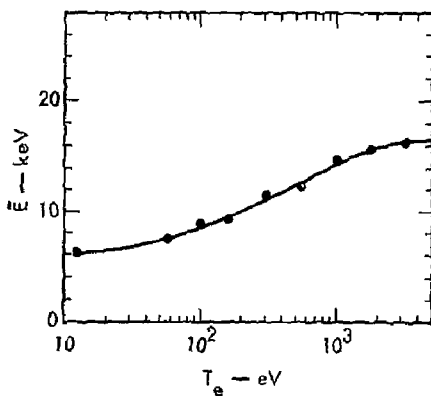


Fig. 22. Average hot-ion energy calculated for the same set of conditions as in Fig. 21.

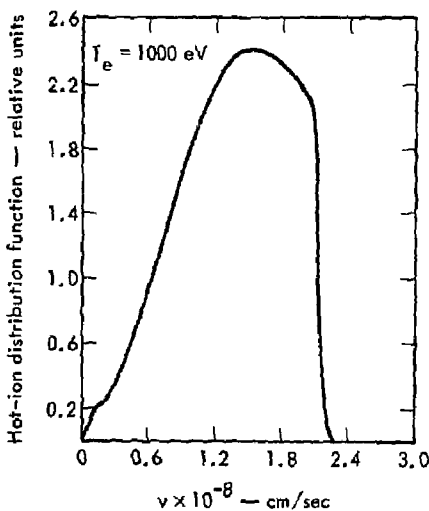


Fig. 23. Example of hot-ion distribution function; $T_e = 1000\text{ eV}$.

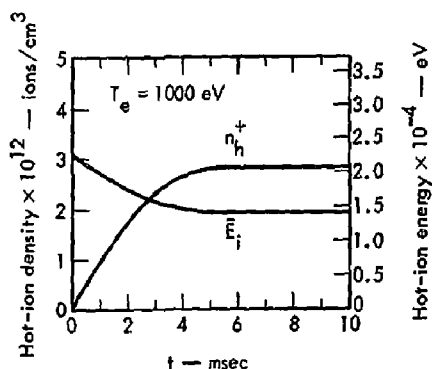


Fig. 24. Buildup of hot-ion density and variation of average hot-ion energy.

STEADY-STATE BEAM DEVELOPMENT

Mats III — Initial development of the higher-energy (5 to 20 keV) MATS III was described in the previous annual report (Ref. 23) which included assembly drawings of MATS III and its water-cooled electrodes, and a layout of the vertical beam line with MATS III installed. During the present reporting period, this source was put into test-stand operation with a 20-kV, 2-A extraction power supply. The first accel-decel grid assembly to be tested consisted of an array of 63 circular apertures, 4 mm in diameter, shaped and spaced as optimized by the Berkeley group for pulsed operation.⁵¹ However, in order to provide sufficient electrode thickness for water cooling as required for continuous operation, the Berkeley aperture sizes and spacings were each scaled up with the thickness by a factor of 2. As shown in Table 3, the transparency of the design was only 25%. The increase in dimensions was expected to result in a loss of beam density and beam brightness by a factor of 4, but was nevertheless expected to fulfill the beam requirements of the Baseball Coulomb-scattered vacuum buildup program. These expectations were fulfilled by the first series of MATS III tests; we then began a series of tests to further improve the yield by increasing the grid transparency and by reducing the extraction electrode gap.

Figure 25 shows the MATS III total beam calorimetrically measured by a target simulating the

Baseball $\pm 1.3^\circ$ acceptance angle. Our total (charged plus neutral) target beam was 0.82 A at 20 keV, and obeyed the $V^{3/2}$ law throughout the range of measurements (5 to 20 keV). This first approach was straightforward and predictable, but not necessarily optimum. For comparison, Fig. 25 also shows the corresponding beams produced by the calutron source operating at 4 to 20 keV and by the low-energy sources MATS I and MATS II operating in the range 1 to 5 keV. The MATS III beam data are shown for two different accel gaps:

1. The 4.7-mm accel gap (the scaled Berkeley gap) was first used for comparison with the Berkeley results. At energies above 12 keV, agreement was established within $\pm 25\%$ which we consider to be satisfactory in view of the fluctuations inherent to MATS III reflex arc. The only significant difference between our results and those of LBL was noted when we reduced the accel to 5 kV while increasing the decel voltage to maintain a nearly constant extraction voltage rather than by the usual method of simply reducing the accel voltage with a decel voltage $< 10\%$ accel. We observed that although the total extracted beam was then independent of the accel voltage, the effective beam divergence was adversely affected by the higher decel voltage, contrary to LBL's observation.⁵² Therefore, this technique resulted in only a small gain in target current, in comparison with the more usual technique of maintaining a constant ratio of accel-decel voltages. The difference between our results and those of LBL may be attributable to the lower hydrogen background pressure in the MATS III decel region.

2. Since the large accel gap was chosen for optical reasons but was not required to hold voltage, we reduced the gap to 3.7 mm and found an improved target current, especially in the intermediate range of 5 to 10 keV. Under this condition the large decel voltage was advantageous; this was because the reduced gap resulted in a larger total beam and a larger beam divergence. Therefore, the effect of the decel voltage upon the beam divergence was less critical because the reduced-gap divergence was already $\pm 2^\circ$ to $\pm 3^\circ$. One of the conclusions from this test was that we had not yet found the optimum extraction geometry in this energy range using electrodes thick enough (1.4 mm) for water-cooling and continuous operation.

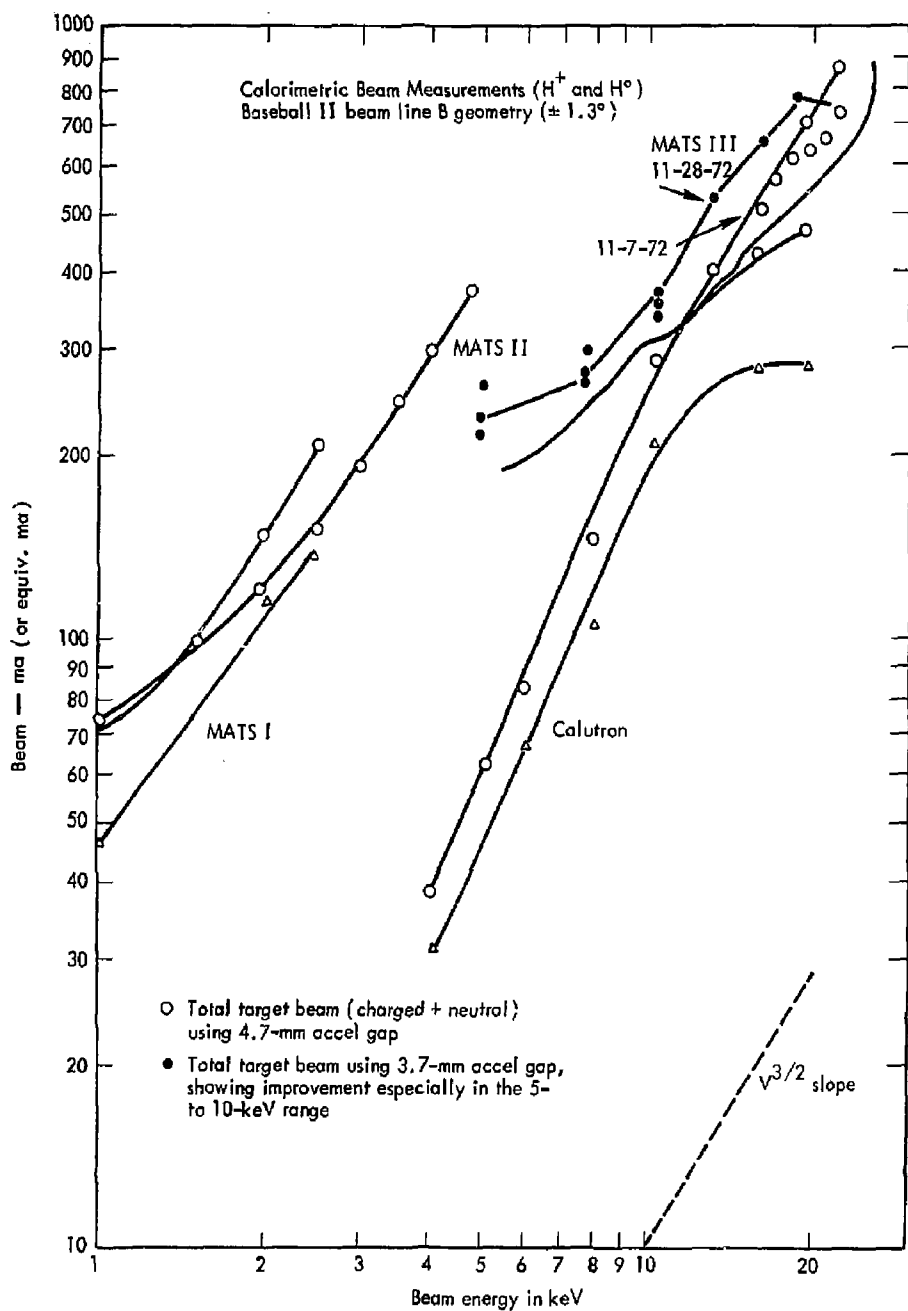


Fig. 25. MATS III beam output compared with beams from MATS I, MATS II and Calutron, measured in the same geometry ($\pm 1.3^\circ$).

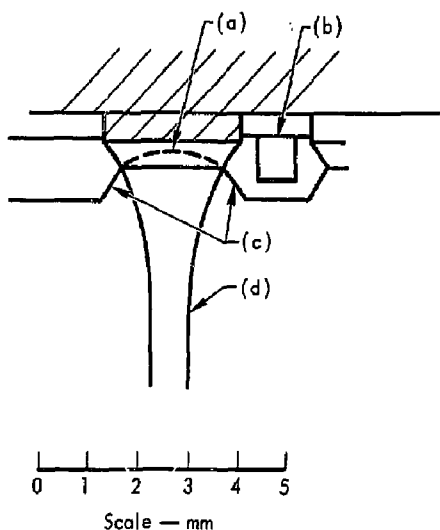


Fig. 26. Detail of water-cooled slotted electrode, shaped in accordance with LBL design. (a) Intended position of plasma surface, (b) water channel between slots formed by brazed sandwich, (c) beveled surface as in LBL design, and (d) extracted beam.

Although the performance shown by Fig. 25 exceeds the minimum beam requirements for Baseball buildup, we fabricated two alternative electrode sets (also listed in Table 3) to improve the transparency and to further reduce the accel gap. The new designs were based upon the following considerations:

1. Tests and computations at Culham Laboratory have resulted in the recommendation⁵³ that the electrode recess required by the Berkeley design be eliminated to improve the transparency and to eliminate the possible cooling problem caused by the sharp edge of the recess. It has been claimed that the gain in transparency will more than compensate for the effect of the recess upon beam divergence. An electrode set (similar to that used for MATS I and II) has been fabricated to check out this recommendation under MATS III conditions, with the transparency increased to 40%.

2. It may be possible to use the Berkeley design without doubling the dimensions if the plasma can be made to penetrate through the thick electrode to form the plasma surface at the desired location.

Such a slot design, shown in Fig. 26, would provide the best combination of optics, transparency (46%) and water-cooling. Table 3 shows that such a design would yield 11 A of total beam at 20 kV if limited only by space charge. However, the 2-A capacity of our existing power supply and plasma source would limit the full-current usefulness of this grid to voltages below 7 kV.

A series regulator is being fabricated to provide for MATS III high-voltage requirements beyond the existing 2-A capability. The regulator assembly will pass up to 10 A at 25-kV regulated output voltage with provision for voltage-programming and current-limitation. The regulator may be fed by one of the existing non-regulated supplies, which are capable of either 5 A at 10 kV or 3.5 A at 25 kV.

Tests are also planned to augment the present reflex arc with a new second annular arc to improve the plasma source radial uniformity and increase the ion density available for steady-state extraction.

We made several studies of possible new beam injectors for Baseball II. The goal was to inject as intense a beam as possible using two criteria as the limit for the maximum dimensions: (1) the beam must pass through the Baseball II coil without hitting it, and (2) the extreme ray beam spray must clear all surfaces until it reaches the target in the burial chamber. The maximum beam size for typical source divergences and locations was 194 cm^2 as measured at the centerline of the Baseball II. At that point the beam would be approximately rectangular in cross section, $18.5 \times 10.5 \text{ cm}$ in size. The beam line will be versatile so that it can be operated with any of the existing MATS sources as well as 1-A d.c., 10- and 50-A pulsed sources presently under development at LBL. The construction will be accomplished in several steps. Initially, we plan to convert the cryogenic neutralizer to a screen tank, that is a tank in which we will try to minimize streaming with a gas curtain and maximize hydrogen pumping with large LHe surfaces as well as LN_2 -cooled titanium covered surfaces. The total pumping area surrounding the beam in the new screen tank is $50,000 \text{ cm}^2$ of LHe surface and $25,000 \text{ cm}^2$ of titanium surface.

A re-orientation of the physics requirements of Baseball plasma buildup has resulted in the deferment

Table 3. Plasma areas, transparencies, and expected beams from three water-cooled electrode assemblies designed for MATS III.

	Case 1—63 holes (LBL recessed design, double size)	Case 2—63 holes (Culham recommendation— no recesses)	Case 3—14 slots (LBL recessed design, full size)
Source diameter	6.4 cm	6.4 cm	6.4 cm
Overall area	32 cm ²	32 cm ²	32 cm ²
Aperture size	4.0 mm diam	5.1 mm diam	2.0 mm slots
Transparency	25%	40%	46%
Accel gap	4.7 mm max	4.7 mm max	2.3 mm
Expected total beam if space-charge limited at 20 kV	1.5 A	2.4 A	11.0 A

of the dc vacuum buildup high-energy injection system. Therefore, completion of MATS III development will proceed on a low-priority basis. One planned use is for negative ion production using charge exchange of 7 keV D⁺ in a Na cell.

Negative Ion Beams — Preliminary experiments to obtain intense negative ion beams were described in the previous Annual Report (see Ref. 23, p. 85). More complete details of experiments to obtain a 50-mA D⁻ beam through electron capture from a 200-mA D⁺ beam at 1.5 keV passing through a cesium charge-exchange cell were reported at the Second International Conference on Ion Sources⁵⁴ as was a summary of available low-energy ion beams⁵⁵ for this or other usage. Attempts to obtain even higher yields with MATS I or MATS II⁵⁶ by coupling the cesium cell closer to the ion sources were stunted by problems from cesium entering the extraction electrode region. Work is being continued to obtain higher total negative ion currents and current densities by use of a 7-keV D⁺ beam from MATS III in a sodium charge-exchange cell. As an outgrowth of the development of high-current negative ion sources, we also conducted a design study for a 14,000-A injection system for a fusion reactor⁵⁷ and cooperated with LASL in assembly of a MATS II source for negative ion use with high-energy accelerators there.

Effect of Negative Ion Injection Upon Reactor Q

In Ref. 57 a technique was proposed of injecting negative ions (D⁻, T⁻, and/or He⁻) into a mirror or

toroidal fusion reactor along a magnetic guide field. It was concluded that by this technique injection and trapping of beams of the order of 14,000 A can be shown to be within the reach of existing technology, and that an improvement in reactor Q would result under proper conditions because of the acceleration of the negative ions by the positive ambipolar potential of the reactor plasma. The effect upon Q of the final acceleration was not computed in Ref. 57 but was estimated as not more than 20% to 30%.

Using multi-species Fokker-Planck computations,⁵ we have computed this effect, including the fact that two or more electrons are injected into the reactor plasma with each negative ion, while only one electron is injected with each D⁰ or T⁰ in the case of neutral injection.⁴ Consequently, the positive potential is reduced and the rate of ion-electron energy transfer is increased. These effects can be computed by the multi-species code merely by specifying the injection of two or more electrons with each trapped D⁺ or T⁺.

We must also consider the fact that if the trapping fraction is less than 100%, some additional electrons will be produced from the injected beam that is ionized in the reactor plasma but not trapped. The effect of these extra electrons will apply to both neutral injection and negative ion injection:

$$\text{i.e., } J_e/J_i = \frac{\text{electrons injected current}}{\text{ion injected current}}$$

$$= 1/\text{trapping fraction for D}^0 \text{ or T}^0 \text{ injection}$$

or $= 2/\text{trapping fraction for } D^-, T^-, \text{ or } He^0 \text{ injection}$

or $= 3/\text{trapping fraction for } He^- \text{ injection.}$

The reactor Q computed by the Multi-Species Code is defined as the ratio of fusion power produced per unit volume to the injected power per unit volume required to sustain the plasma, where the injected power density $E_i J_i$ is defined as the power injected after the final acceleration. Neglecting the energy of the injected electrons, we may write

$$\text{Injected power density (M-S Code)} = E_i J_i = (V + k\phi) J_i,$$

where V is the voltage applied by the external accelerator, and where the negative ions are further accelerated some fraction k of the plasma potential ϕ .

For negative ion injection, we wish to compute the Q defined by the power $V_i J_i$ of the external injection system. Since the injected power is in the denominator, the correction to Q is the following, if other conditions are equal:

$$\frac{Q(\text{negative ions})}{Q(\text{neutrals, M-S Code})} = \frac{E_i J_i}{V_i J_i} = \frac{E_i}{E_i - k\phi}.$$

The most optimistic (and perhaps correct) assumption is that the ambipolar potential gradient is applied at a thin sheath at the boundary of the reactor plasma. Therefore the negative ion will receive the full acceleration as it enters the plasma, and we can justifiably assume $k = 1$. The correction factor $E_i/(E_i - k\phi)$ may be as large as 1.5 under favorable conditions.

Using ratios J_e/J_i determined by several specified trapping fractions, we have computed ϕ and Q by the Multi-Species Code for the case $E_i = 200$ keV, with injection of equal currents of D and T. The results after applying the correction factor are shown in Fig. 27. We find that Q is enhanced by negative-ion injection by a maximum of 21% if we assume 100% trapping, but that negative-ion injection will result in lower Q than for neutral injection if the trapping fraction is less than 65%. We note that in Ref. 57 the computed trapping fraction varied from 30% to 84% for conditions of interest, depending upon mirror ratio, field curvature, and plasma thickness.

Baseball II Electrical Engineering

A. Waugh, A. Bogdanoff, G. Vogtlin

Operations

Operation of the superconducting Baseball magnet to current levels of 1400 A (Min-B field of approx. 12 kG) has become quite reliable and routine.

A system for automatically inserting 100 mΩ of energy-absorbing discharge resistor in series with the magnet if it goes normal has been in service during this past year of operations. The two conditions which must exist simultaneously to trigger this

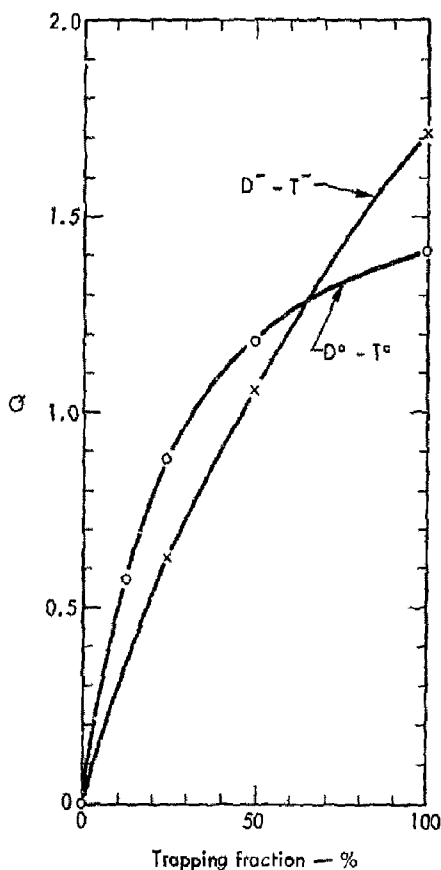


Fig. 27. Effect upon reactor Q of extra electrons due to untrapped ions. For $D^0 - T^0$ injection, $J(\text{electrons})/J(\text{ions}) = (\text{trapping fraction})^{-1}$. For $D^- - T^-$ injection, $J(\text{electrons})/J(\text{ions}) = 2 \times (\text{trapping fraction})^{-1}$.

action are: (1) low liquid helium level in the 500-liter dewar directly above the magnet, and (2) excessive helium gas pressure in this same dewar.

Actions to be taken in the event of the occurrence of other abnormal magnet operating conditions are still dependent on trained, alert, continuous operator supervision. Audible and visual alarms are activated by the following conditions: excessive charging or discharging voltage, over current above set level, excessive voltage drop across helium-gas-cooled magnet-feedthrough current leads, and low cooling water flow to critical magnet-power-supply components.

Reliable operation of the machine vacuum system continues from the "vacuum map" status light, push-button control panels. This control system has been updated to follow changes in the machine configuration.

More reliable operation of the MATS ion-source remote-controlled power-supply system has been achieved. This improvement is the result of better interconnection of the equipment in the high-voltage "hot rack," installation of an rf filter at the end of the high-voltage duct as close to the source as possible, and the purchase of more reliable power supplies for installation in the hot rack.

Successful gang programming of the source accel voltage, decel voltage, lens-magnet current, and hydrogen gas flow was accomplished using several rotating drum-type curve-follower programmers operating together. Square-wave modulation of the accel high voltage over peak-to-peak levels of several kilovolts at basic frequencies of 20 to 40 Hz with variable on/off duty cycles was done.

Design and fabrication of a power supply system for the operation of the LBL 1-A, 10-sec ion source as a neutral beam injector on the Baseball II machine is in progress. The major components of the system are: a 10-V, 1500-A filament supply and a 150-W, 600-A arc supply floating at accel high-voltage potential, an accel voltage regulator with an output of 2 to 25 kV at 10 A, and a decel voltage regulator with an output of 1 to 10 kV at 2 A.

Baseball II Mechanical Engineering

T. Chargin, B. Denhoy, C. Henning and R. Nelson

Plasma Chamber Modifications — To improve wall conditions surrounding the plasma, we installed a copper liner around LHe surfaces that are in the direct line-of-sight of the plasma. The liner is constructed of 1/16-in.-thick sheets that closely conform to the inner coil form and associated tubing, but are separated from these surfaces by 1-in.-long, No. 4 size stainless steel screws. The thermal coupling between the liner and the coil through radiation and conduction through screws is approximately 5 W if the liner is operated at LN₂ temperature. The liner can be temperature-controlled, depending upon the fluid temperature that is supplied through the liner tubing. To keep the liner walls clean, we mounted 26 sublimator filaments in 13 locations around the liner. The filaments are rated at 2 kW each, but only two can be operated at one time and that is only when the magnetic field is not turned on. To cover the liner surfaces with titanium when the magnetic field is on, we designed and built a new retractable sublimator that is pneumatically actuated and can reach to the center of the magnet.

We eliminated the 2°K surface surrounding the final beam collimator mounted on the coil and instead we installed 16 300-W titanium sublimators that can be operated in the strong magnetic field. In an attempt to measure the effectiveness of pumping by cryogenic trapping, we constructed a small network of tubing that would spray nitrogen gas onto LHe surfaces and thereby pump helium in the nitrogen ice.

A zeolite-coated LHe dewar was installed inside the plasma chamber to improve the hydrogen and helium gas pumping capabilities. The base vacuum in the plasma chamber was improved by eliminating the cold leaks with these changes:

- Two 10-in. bellows between the 500 LHe dewar inside the chamber and the cover plate had bolted joints; these were welded.

- Tie bar and LHe liner fill methods were changed from internal fill to external. This will allow isolating either or both of these circuits in case of an internal vacuum leak.
- Eight 1-in. flanges inside the plasma chamber were replaced by welded connections.

In connection with a possible future target plasma experiment with the Baseball II magnet, we redesigned the tie bar support system. We are studying these changes in more detail to insure the structural integrity of the magnet.

Cryogenic Facility Operation – During the past 12-month period, the helium liquifier ran a total of 3400 hours, 2400 of these between January 1 and July of this year. Major modifications were made to both the compressor and turbo expander last December to improve reliability. Since then, maintenance has been limited to routine piston ring and seal inspection or replacement every 2000 hours. The turbo expander now in service was installed on December 14th and has 2600 hours running time. A second compressor is scheduled for installation the end of August. It will be connected in parallel with the existing unit, and will provide increased liquefaction capacity as well as redundancy.

A surplus helium purifier, manufactured by Cryenco, was installed last September. Operation to date has been very satisfactory. Before this equipment was installed it was necessary to regenerate the old purifier about twice each day. The Cryenco unit requires regeneration about once a month, and purity is better than our high-purity sample gas.

Neutralizer Modifications – The previous modifications to the cryogenic neutralizer showed that improved electrostatic shielding between the beam and the ice on cold surfaces, as well as improved magnetic shielding, contributed significantly to the neutralizer performance. Therefore, we changed the beam collimation scheme at the entrance of the neutralizer to maximize the effectiveness of heated electrostatic shielding screens. We were also able to improve the efficiency of the iron magnetic shielding at the entrance because the end effects were reduced with the new collimator geometry. To further study

the effects of the magnetic field that penetrated the superconducting shielding, we installed two coils in the neon section that could produce a 50-G longitudinal field in the opposite direction to the field that penetrated the region. To improve pumping of hydrogen in the neutralizer tank, we welded zeolite-covered plates in the dump section following the sweep magnet.

To reduce beam losses due to charged beams passing through the magnetic field that was not shielded out in the cryogenic neutralizer, we built a new neutralizer for the Baseball II beam line. We inserted this neutralizer close to the source extractor to reduce the total distance travelled by the charged beam. The cryogenic neutralizer was then used only as a screen for the streaming gas.

2XII

F. H. Coengsen, Wm. F. Cummins,
A. W. Melvik, W. E. Nexsen, Jr.,
B. W. Stallard and T. C. Simonen

Introduction

During the period covered by this report, 2XII has been operated for the most part with injection conditions adjusted to produce "quiescent" (see Ref. 23) plasma conditions, where "quiescent" indicates near absence of scattering of 4-mm microwaves and a lack of ion energy spreading to higher energies. The mean ion energy for these conditions is in the range from 1 to 5 keV, and T_e is in the range 30 to 100 eV.

The cross section of the experiment shown in Fig. 28 is included to show the location of plasma measurements, pulsed magnet and vacuum chamber elements. This past year, 2XII operated with a magnetic compression time of 400 μ sec. Addition of the LBL 10-A neutral beam⁵⁸ and introduction of electron heating constitute the major changes in the experiment during this report period.

As discussed in the 2XII Program Plan,⁵⁹ to increase n_r in 2XII, T_i and T_e/T_i should both be increased and the density should be sustained so $\omega_{pe} > \omega_{ce}$. Our goal as outlined in the Program Plan is to demonstrate near-classical confinement of a 10-keV plasma sustained through injection of neutral beams. Plasmas with mean ion energy in this range are now available

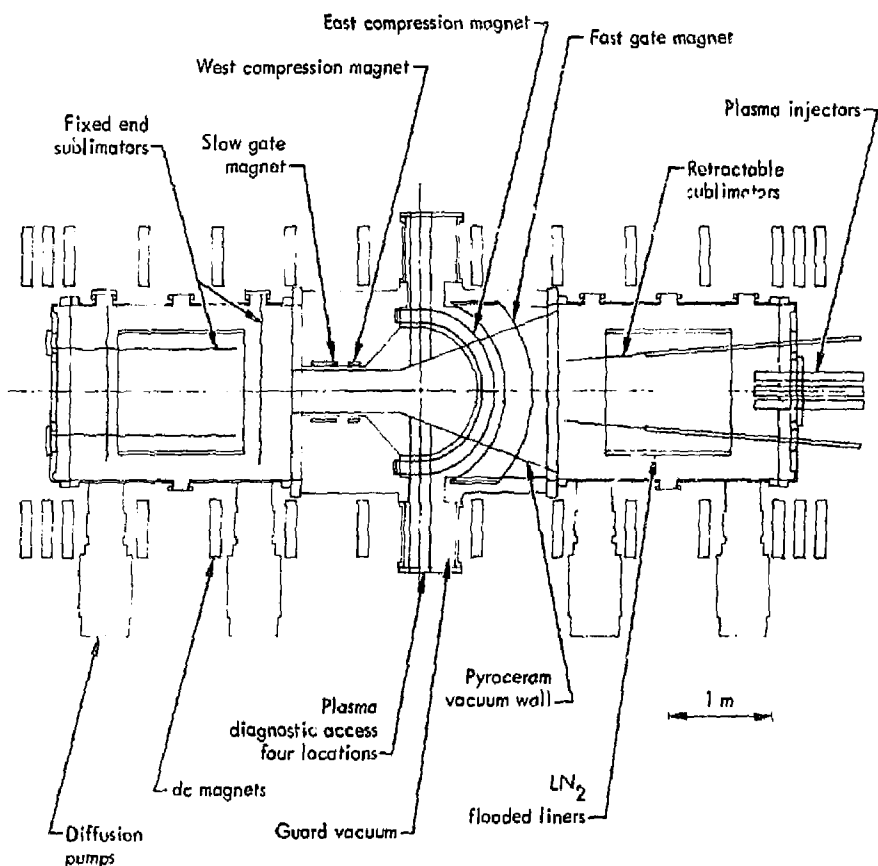


Fig. 28. Schematic cross section of 2XII.

in 2XII. Several methods to independently heat the electrons have been considered, two of which are being implemented and are discussed below. Two groups are preparing high-current neutral beam modules to sustain the 2XII plasma. The LBL CTR group is making a one-dimensional scaleup of their 10-A source to achieve a 50-A module, and a more ambitious scaleup to produce a 200-A module is underway at LLL. Obviously, the beam intensity required to sustain the 2XII plasma depends on the lifetime of the plasma ions. Several combinations of

2XII plasmas and neutral beam requirements are discussed in the Program Plan.

Plasma Confinement in 2XII - Comparison with Theory

We have previously reported^{59, 60} limited evidence that for selected 2XII plasma decays the density dependence on $n\tau$ at high densities [i.e., $(\omega_{pe}/\omega_{ce})^2 > 1$] appears to agree with that calculated by Baldwin and Callen⁶¹ for plasma losses arising from quasi-classical scattering.

From Baldwin and Callen,

$$\frac{1}{n^2} \frac{dn}{dt} = \frac{1}{nr} = \frac{1}{(nr)_c} + \frac{A \exp \left\{ \frac{1}{a_i} \int ds \operatorname{Im}[yF(y)] \frac{(n/B^2)^{1/2}}{(1+n/B^2)^{1/2}} \right\}}{T_e^{3/2} \left(\frac{n}{B^2} \right)^{1/2} \left(1 + \frac{n}{B^2} \right)^{3/2}} \quad (11-8)$$

where

$$\epsilon_c = \left(\frac{\omega_{pe}}{\omega_{ce}} \right)^2 \approx \frac{n}{B^2}$$

if n is in units of 10^{13} cm^{-3} and B in units of 10^4 gauss. The exponential is independent of density if $\epsilon_c \gg 1$. Hence, in the higher density range if T_i , T_e and the form of the ion velocity function all remain constant as the plasma density decreases, the last term of the above expression is just a product of a constant and a function of n/B^2 . For these conditions, the graph of $1/nr$ versus $(n/B^2)^{-1/2} (1 + n/B^2)^{-3/2}$ should be a straight line with an intercept equal to $1/(nr)_c$ where $(nr)_c$ is the value calculated for Coulomb scattering. The slope of the line is proportional to the amplification of the unstable wave. Data from two relatively low-energy runs which did not show evidence of plasma turbulence are shown in Fig. 29. It is seen that a straight line can be drawn through the high-density data for each run. The values of $(nr)_c$ derived from the intercepts of these two lines agree within the accuracy of the experiment with those calculated numerically using a two-dimensional Fokker-Planck⁶² code. Also, within the accuracy of the data $(nr)_c$ values derived from the intercepts increase as $T_i^{3/2}$, in agreement with Coulomb scattering. The comparison of these data with theory is limited by uncertainties in the values of T_i which are derived from the energy spectrum of the fast atom flux arising from charge-exchange of the plasma ions with neutrals. For the 2XII densities and electron temperatures, the mean-free-path for ionization of thermal neutrals is

much less than the plasma radius. Thus, the low-energy end of the measured ion energy distribution is dominated by contributions from the low-density plasma boundary, and is possibly not representative of the bulk of the plasma. To some degree, the uncertainty is reduced by using the energy distribution later in time when the plasma density has decreased and neutrals penetrate deeper into the plasma. The validity of the late date is corroborated in a limited number of runs described below where a modulated neutral H^0 beam was used to probe the plasma interior.

The fact that the slope of the B-C curve for the 2.7-keV run is about six times greater than that of the 1.3-keV run (Fig. 29) is in disagreement with the behavior expected from the $1/a_i$ factor in the exponent of Eq. (11-8). However, the value of the integral is a function of T_e/T_i and under certain conditions could decrease with T_e/T_i . The slopes of the B-C curves for several runs are plotted as functions of T_e , T_i , and T_e/T_i in Figs. 30(a), (b) and (c). The open data points are from quiescent runs, and the solid data points are from slightly turbulent runs. Electron temperatures at 400 μsec are determined from 90° Thomson scattering of ruby laser light. The large change in slope that occurs with modest changes in T_e and T_i may be because the exponential integral depends on the shape of the ion energy distribution which may vary from run to run. Some of the random scatter of the data points in 30(a) and (b) occurs because T_e does not increase as much as T_i in the higher energy runs. The trend of the data in 30(c) tends to confirm the earlier hypothesis that the anomalous plasma loss rate can be reduced by increasing the ratio T_e/T_i .

Confinement in Partially Gettered Operation

Two interesting aspects of plasma confinement in 2XII are the late plasma dumps and the apparent improvement of plasma confinement in a partially gotten system. In partially gotten operation getting of the central ceramic vacuum vessel is discontinued, but titanium is deposited before each run in the end tanks, neutral beam chamber, beam burial chamber and all side arms. In such operations, the mean ion energy is lowered and the energy distribution is changed.

With good vacuum conditions, including freshly gotten interior walls, a late plasma dump is always

observed at densities below 10^{12} cm^{-3} . This dump appears at earlier times and at higher densities as the wall conditions (and hence vacuum conditions) improve. Consequently, the dump does not exhibit either a simple density or an $\epsilon = (\omega_{pi}/\omega_{ci})^2$ threshold.

In partially gettered operation, the late dump is eliminated. Also, with partial gettering we find that

the plasma containment time increased by a factor ~ 2 and that the density also increased. The combined effect is an increase of a factor of two to three in the apparent $n\tau$ values, as illustrated in Fig. 31 where $n\tau$ values at peak of maximum compression ($t = 400 \mu\text{sec}$) are compared with those observed for quiescent and slightly turbulent runs in fully gettered

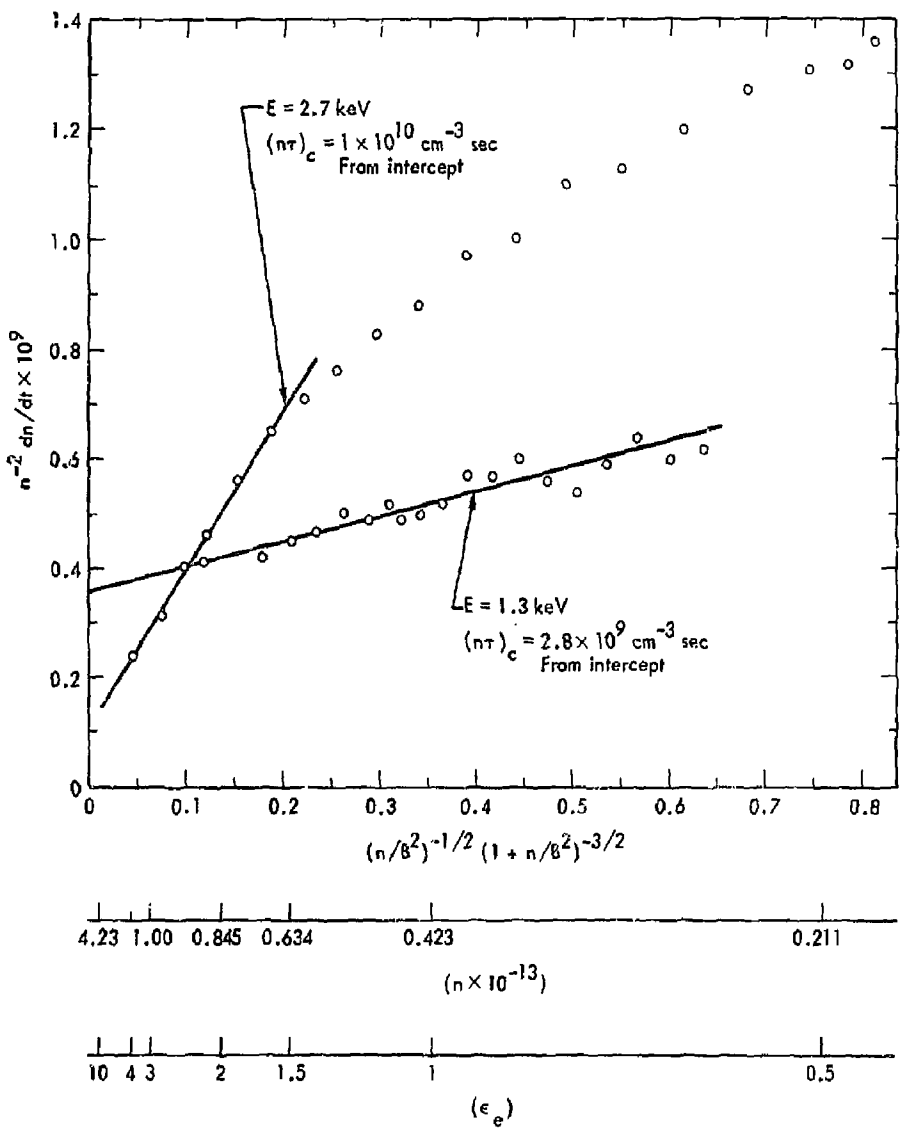


Fig. 29. Comparison of 2XII data with the Baldwin-Callen scaling law.

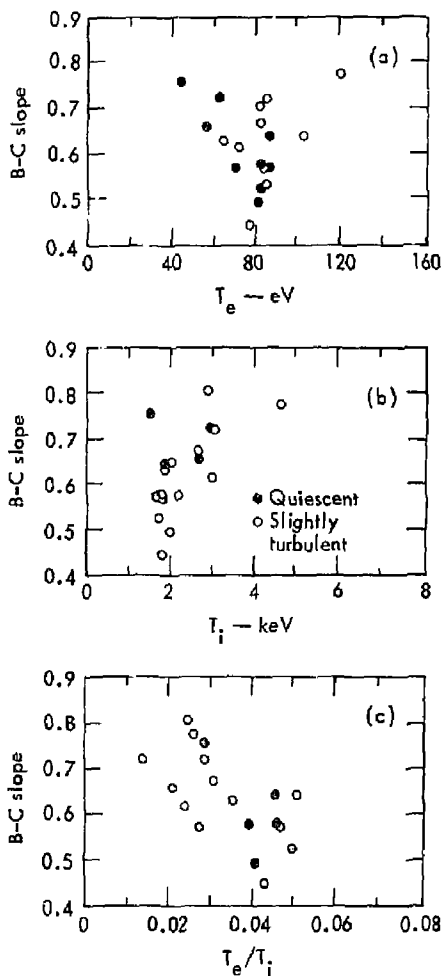


Fig. 30. Slope of B-C curve as a function of: (a) T_e , (b) T_i , and (c) T_e/T_i .

operation. Densities have been cross-checked, using the intensity of Thompson scattered laser light. The increase in density in partially gettered operation probably results from reionization of plasma which strikes the central vacuum chamber walls during injection. In such operation, the mean ion energy is lowered and the energy distribution is changed. Plasma radii, as estimated from the central density which is derived from the scattered laser light, and $\int n_e dl$, derived from the μ wave interferometer, appear

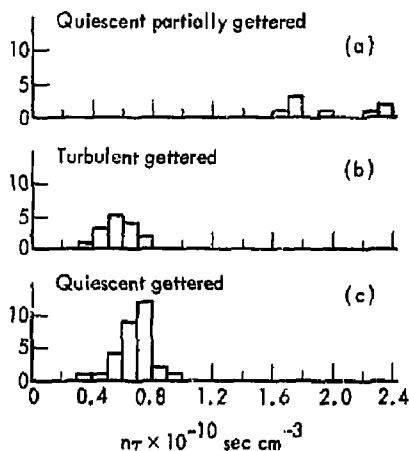


Fig. 31. Effect of partial gettering on $n\tau$. (a) for quiescent plasmas in partially gettered operation. (b) for turbulent plasmas in fully gettered operation. (c) for quiescent plasmas in fully gettered operation.

the same for partial and completely gettered operation.

For partially gettered operation, the external density is about a factor of five higher than fully gettered operations. The improved plasma containment and suppression of the late instability appear to be associated with this increase of external plasma density. As the plasma potential ejects lower energy ions, we are reluctant to ascribe the effects to partial filling of the mirror loss cone distribution, but the improved confinement may be due to suppression of ion cyclotron modes due to line tying or line weighting. Broadening of the ion energy distribution might also have a significant effect through reduced amplification of the convective waves (i.e. reduction of the value of integral in the exponent of Eq. (II-8)).

Electron Heating in 2XII

As stated above, we wish to independently increase the electron temperature to increase $n\tau$ in accordance with the Baldwin-Callen scaling law.

Turbulent heating by a short intense current along the magnetic field has met with success in experiments⁶³ with $T_e > T_i$. However, turbulent heating of the 2XII plasma is predicted to be more difficult since $T_i > T_e$. This precludes heating by ion acoustic

instability at modest electron drift velocities. Electron heating by the electron two-stream instability requires electron drift velocities of the order of the thermal velocity at the end of heating. If we consider that a demonstration of the heating method requires a final temperature of 200 eV, then for a density of 10^{13} cm^{-3} the critical current density is 1.3 kA/cm^2 . By aperturing to reduce the plasma column diameter and by lowering the plasma density, we expect to test the heating method; however, to this time we have not been successful. The last run with a 15-kJ energy storage system consisting of parallel rolls of RG19 cable, capable of being charged to a maximum of 200 kV, terminated after only a few shots because the high-voltage insulator vacuum leadthrough failed. A new leadthrough is being fabricated, and another attempt will be made this summer.

The second approach we plan to use for electron heating is the injection of an energetic electron beam through a mirror. An electron gun consisting of a hot tungsten filament cathode and gridded anode has been designed and is being fabricated. The rectangular cross section of the gun is threaded by the magnetic field lines which pass through the plasma interior. The gun design voltage is 50 kV at 2000 A, and provision has been made for increasing or decreasing the gun voltage by a factor of 2. The RG19 cable system will be connected in series for the desired pulse length. For a 10- μsec pulse, the nominal value of delivered beam energy is 1000 J.

Initial experiments will be carried out by injecting electrons along field lines with little perpendicular energy. The dominant interaction is expected to be the two-stream instability between the plasma and beam electrons. It is expected that of the order of 1% of the beam energy should be deposited in the plasma.⁶⁴ Thus the plasma electrons should have their energy increased of the order of 10 J which should double 2XII electron temperature.

Additional heating experiments can be carried out by injecting electrons with appreciable perpendicular energy. By orienting the gun at an angle with respect to the field lines, an E \times B drift in the gun imparts a perpendicular energy to the beam. Experiments by Seidl and Sunka⁶⁵ have shown that under certain conditions such beams can couple to cyclotron waves and heat electrons.

200-kW Neutral Beam Injection Into 2XII

Up to 9.3 A of hydrogen or deuterium neutral atoms at 20 keV have been injected into 2XII. These beams have been used to:

- Search for problems such as instabilities which may be associated with neutral injection.
- Study effects of neutral injection on T_e .
- Study ion slowing-down rates in a hot plasma and compare with Spitzer rates⁶⁶ and with measurements made in cooler plasmas.⁶⁷
- Extend density measurements above the microwave interferometer cutoff at $6 \times 10^{13} \text{ cm}^{-3}$.
- Measure radial plasma density profiles during and after compression.
- Determine the ion energy spectrum at the burned-out center of the 2XII plasma by providing a charge-exchange target.

The first operation of the neutral beam with 2XII in October 1972 was with energies of 10-14 keV and equivalent currents of about 3 A. Modifications by the Berkeley group to the source and power supplies allowed operation at higher energies and currents. During operation in February 1973, the beam operated at up to 20 keV and 9.3 A (including ions) with deuterium. Subsequently, a hydrogen beam has been operated at 15 keV with optimized beam current and up to 19 keV at reduced current levels. The reduction was due to power supply limitations.

The source is located 340 cm from the plasma in a 3000-liter chamber. Both vessels are extensively gettered with fresh titanium before each run. No increase in charge exchange flux, line radiation, or change in other plasma parameters is detected when the source gas supply is pulsed on, indicating that the source gas does not contribute any problems. The beam is monitored by input and output calorimeters, secondary emitters, and also anode current and voltage monitors.

Some of the neutral beam which is ionized by the plasma is not contained because its orbit intercepts a vacuum wall. The fraction of the ionized beam contained has been calculated as a function of time from the beginning of compression until peak field 400 μsec later. The results are shown in Fig. 32 for various values of d.c. guide field and for the maximum energy deuterium beam. For lower energies or for hydrogen, the contained fraction is higher. With the larger

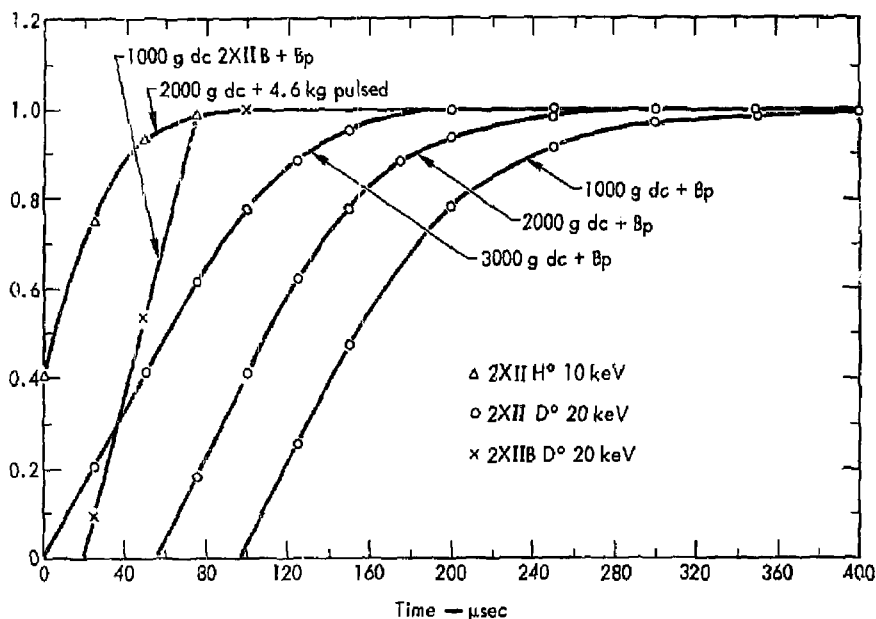


Fig. 32. Fraction of injected neutral beam contained in 2XII plasma chamber.

Table 4. Twelve shots D⁰ into D⁺ plasma.

	$n \times 10^{-13}$ (cm ⁻³)	τ (μsec)	$n\tau \times 10^{-10}$ (sec/cm ⁻³)	E_i (keV)	T_e (eV)
Beam out	1.8 - 2.7	260 - 330	0.53 - 0.88	1.7 - 2.5	42 - 103
Average		300 ± 8	0.70 ± 0.03		69 ± 5
Beam in	2.0 - 3.5	240 - 340	0.58 - 0.97	4.8 - 6.7	45 - 140
Average		285 ± 9	0.67 ± 0.04	See text	73 ± 8

vacuum chamber of 2XII B a much smaller fraction of the ionized beam will be intercepted by the walls.

Approximately 10 J of energy is delivered to the plasma through beam trapping. In comparison, the energy content of a 2-keV 2XII plasma at $2 \times 10^{13} \text{ cm}^{-3}$ is 32 J. In estimating the energy delivered by the injected particles, heating by the rising magnetic field of those particles trapped during magnetic compression is included. Density measurements with and without neutral beam injection show only small differences. About 2×10^{15} particles are trapped. If the angular velocity distribution does not change, the resulting density contribution from the

beam in the center plane is $\sim 1 \times 10^{12} \text{ cm}^{-3}$. However, the trapped ions decelerate rapidly and become part of the plasma ion distribution, and consequently are lost at the same rate. Tables 4 and 5 indicate that the beam does not significantly change $n\tau$.

Coulomb scattering of plasma ions by 20-keV beam particles occurs much slower than particle deceleration by electron dynamical friction. The plasma ion energy could change faster if the beam stimulated high-level instabilities. Table 5 indicates no measurable change occurs with approximately 5-10 J of 15-keV hydrogen atoms deposited in the plasma. Hydrogen injection permits charge-exchange measurements of the

Table 5. Seven shots H^0 into D^+ plasma

	$n \times 10^{-13}$ (cm^{-3})	τ (μsec)	$n\tau \times 10^{-10}$ (sec/cm^3)	\bar{E}_i (keV)	T_e (eV)
Beam out	2.4 - 2.7	290 - 355	0.74 - 0.86	1.2 - 2.2	63 - 115
Average		320 ± 10	0.79 ± 0.02	1.7 ± 0.1	83 ± 5
Beam in	2.1 - 2.6	315 - 370	0.71 - 0.87	1.1 - 1.8	70 - 117
Average		345 ± 8	0.81 ± 0.02	1.4 ± 0.1	86 ± 10

deuterium 2X11 plasma. The apparent deuterium energy increase in Table 4 is not ion heating but rather due to the orientation of the charge-exchange detector acceptance angle coinciding with the peaked 90° angular distribution of trapped neutral beam particles.

The effect of beam injection on electron temperature for the data of Table 4 is estimated to be 10%. Such a change is within the uncertainty in the Thomson scattering measurement.

Forward-angle 4-mm microwave scattering and electrostatic probe measurements show no significant increase in noise in the frequency range $0.2 < \omega/\omega_{ci} < 3$ with neutral beam injection.

To measure the deceleration of the injected beam particles, the beam is switched on after the peak of the magnetic field. The delay time is measured between beam turn-on and the appearance of signal in a channel tuned to a lower energy. ΔE then is the difference between the energy of the injected beam particles and the highest energy detectable by the analyzer channel. This measurement of ΔE involves measuring the small difference of two large numbers. An alternative is to measure the risetime of the neutral signal since this is a measure of the time it takes the trapped ion distribution to spread downward a ΔE equal to the range of energies accepted by the analyzer channel. We also must measure the average electron density and electron temperature over the ion orbit to compare with theory. The microwave interferometer furnishes line density from which we determined the average density over the ion orbit. The central electron temperature is obtained by Thomson scattering. Our preliminary results indicate deceleration exceeding the Coulomb rate.

An example of neutral beam transmission through the center of the plasma is shown in Fig. 33(a). These data have been normalized to the input beam current measured with a secondary emitter to eliminate the effects of small changes in source output current. Using charge-exchange and impact ionization cross sections,⁶⁸ the plasma line density was determined and compared with the line density from a microwave interferometer. Figures 33(b) and (c) compare densities determined by both methods. The neutral beam attenuation measurement is especially useful at high densities where the microwave transmission is cut off.

Neutral beam attenuation is monitored at 1.5-cm intervals by an array of 15 secondary emitters located in the burial tank. An Abel inversion of these line density data (Fig. 34) then yields the plasma density versus radius. These preliminary measurements indicate that the plasma adiabatically compresses to about the radius expected from probe measurements of the injected radial profile.^{69, 70} However, the plasma fans sufficiently from a cylindrical shape over the 10-cm length that opposite ends of a channel measure plasma on flux surfaces separated by more than the channel separation and the applicability of Abel inversions is in doubt. Thus, while the data in Fig. 35 are consistent with the assumption of adiabatic compression with no cold plasma skirts, they do not prove it.

Modifications are underway to reduce noise pick-up which makes attenuation measurements difficult beyond 7-cm radius, and to reduce the length along field lines of the plasma sampled so that fanning effects are less than the 1.5-cm channel separation.

By turning a H^0 beam on and off at a 5 kHz rate, the energy analyzer signals are modulated, as shown

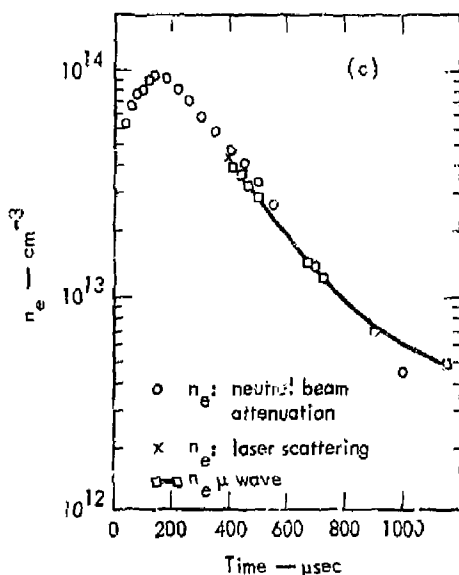
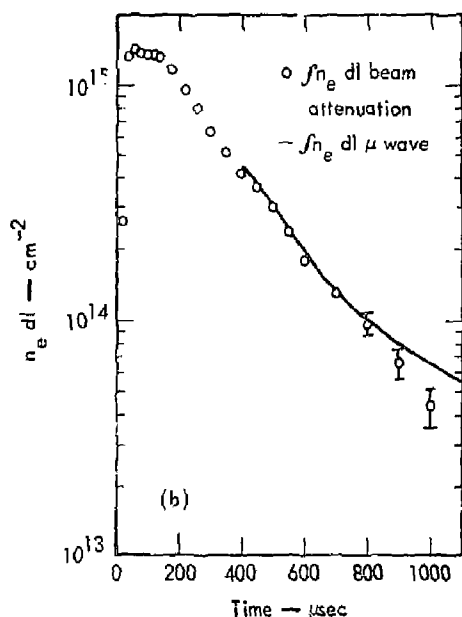
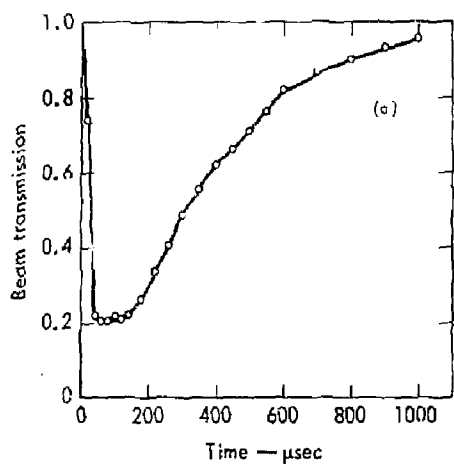


Fig. 33. (a) Time dependence of transmitted neutral beams in 2XII. (b) Comparison of $\int n_e dl$ versus time as derived from neutral beam attenuation and the 70-GHz microwave interferometer. (c) Comparison of 2XII central densities derived from neutral beam attenuation, microwave interferometer and scattered laser light.

by the examples in Fig. 35. The differences between the peaks and valleys are the contribution from the plasma interior due to charge exchange on the neutral beam. The data confirm our previous postulate that the low-energy ions are primarily concentrated in the plasma boundary.

Electron Temperature Measurement

It is recognized that electron temperature plays an important role in determining ion lifetime due to the following:

- Ion cooling by electrons affects the ion scattering rate as well as the breadth of the ion energy distribution.
- Electron temperature dependent mechanisms which limit instability amplitudes.
- Electron temperature dependence of the plasma potential.

For the above reasons, electron temperature measurements have been made in the past year using Thomson scattering of light from a 6-J ruby laser with a 40-nsec pulselength. The laser layout is shown

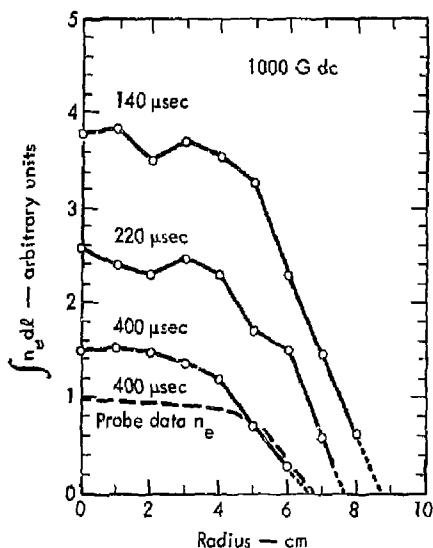


Fig. 34. 2XII radial density profiles derived from neutral beam attenuation.

in Fig. 36. The laser was assembled from the following components: a 1/2- X 6-in. ruby oscillator, a KD*P Pockells cell Q-switch, and a 3/4- X 8-in. ruby amplifier. The detector consists of a polychromator with eight 70-Å-wide channels. Two channels are located above and five below the ruby wavelength, 6943 Å. Quantum enhancement of selected RCA 8552 photomultiplier tubes (Q.E. > 6%) is used. These PM tubes are electronically gated on for 1.5 μsec during the laser pulse. The system is absolutely calibrated with a standard lamp and by Rayleigh scattering off dry N₂ gas. Stray light at the ruby wavelength is completely eliminated with dye glass baffles. Except for the two channels furthest below the ruby wavelength, Thomson scattering signals are well above plasma radiation. Electron temperature can be measured to approximately $1 \times 10^{13} \text{ cm}^{-3}$; however, for accuracies exceeding 20%, densities above $2 \times 10^{13} \text{ cm}^{-3}$ are required.

The laser system is presently being interfaced to the on-line data acquisition system and a second ruby amplifier which is being built to double the output energy. The laser has been double-pulsed with 3-J pulses spaced 200 μsec apart.

Electron temperatures ranging between 30 and 200 eV have been measured. For plasmas with average ion energies W_i in the range of 1.2 to 3 keV, electron temperatures between 50 and 100 eV are typical. Figure 37(a) shows a frequency count of the ratio U_e/W_i ($U_e = 1.5kT_e$) for low-ion-energy plasmas. Most of the data lie in the range $U_e/W_i = 0.05$. This is the range calculated on the basis of Coulomb heating by ions in the presence of losses several times classical⁵⁹

$$U_e/W_i = \left[\frac{0.014 n_e^{13} \tau_{\text{msec}}}{W_i^{3/2} \text{keV} (\phi/U_e - 1)} \right]^{2/5}$$

For higher ion energy plasmas, where turbulence is detected, the ratio U_e/W_i is lower as shown in

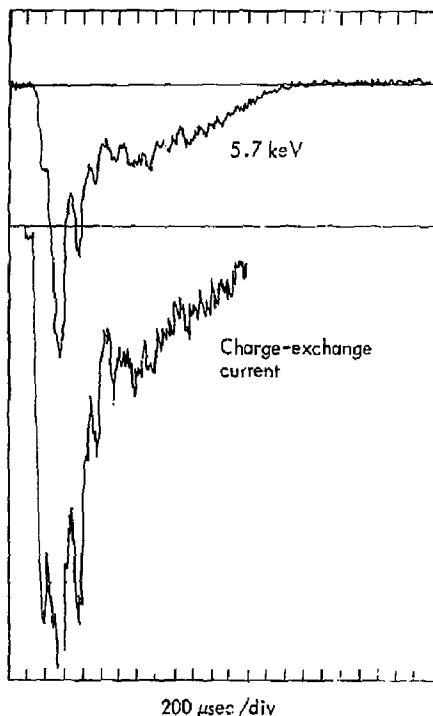


Fig. 35. Modulations of neutral analyzer signals resulting from injections of a 5-kHz modulated H⁰ beam.

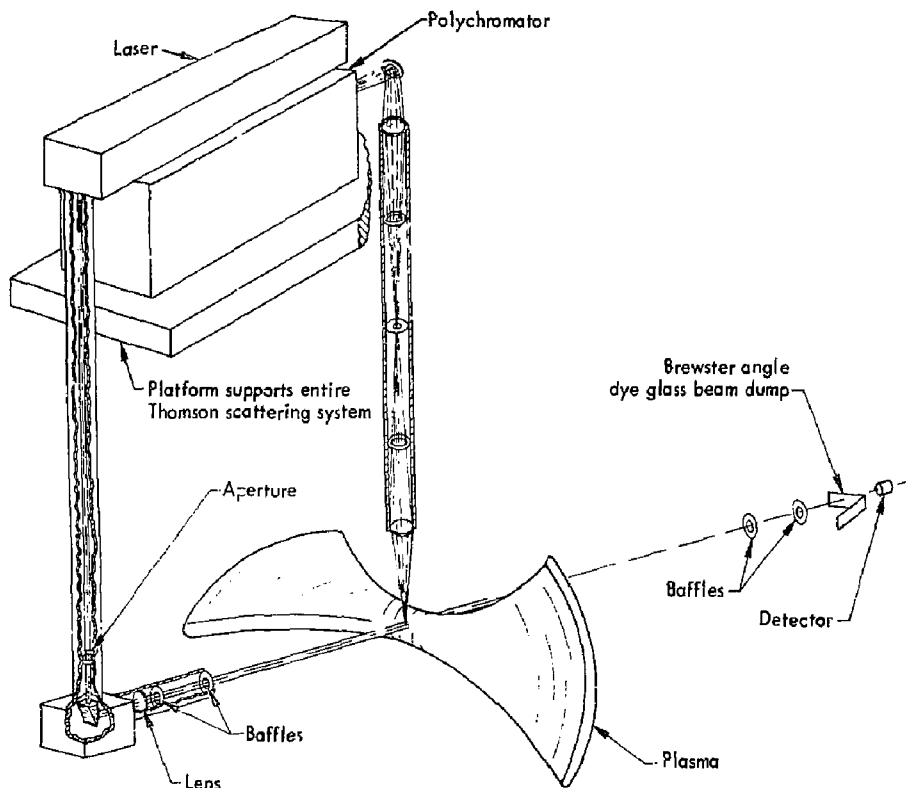


Fig. 36. Schematic diagram of electron temperature measurement using ruby laser.

Fig. 37(b). Measurements of T_e as a function of time compiled over a number of shots shows that for such high-energy plasmas $W_i > 3$ keV in which W_i increases with time, T_e rises with time; but that the ratio U_e/W_i increases more slowly. In contrast, for lower energy quiescent plasmas in which W_i remains approximately constant with time, the electron temperature remains relatively constant or may even decrease slightly.

Neutral Analyzer

Continued work with the calibration of the neutral analyzer and the reduction of its data have led to a better understanding of its accuracy and limitations. This was reported at the Monterey⁷¹ meeting, and is summarized here.

If one asks how well does the energy spectrum represent the actual energy distribution of the bulk

of the plasma, the question divides itself naturally into two parts: (1) what is the accuracy of the measurement of the spectrum of energetic neutrals detected by the analyzer? (2) What assumptions are made to obtain a plasma energy distribution from this spectrum?

Details of the calibration methods and procedure have been reported.⁷² We conclude that our present values for sensitivity and energy resolution are probably accurate to within $\pm 10\%$; the relative values of the angular acceptance are also known to this same accuracy, although the accuracy of the absolute values is not quite as good.

It is presently impossible to place the calibration source at the same distance or position as the plasma. The sensitivity calibration consists of comparing the stripped current at the analyzer entrance with the signal from the detector. Since the transmission of

the channels is in general less than one, the detector intercepts only a part of the beam entering the analyzer. If the transmission should change when the source is moved from the calibration position to the plasma, then the sensitivity will change. Such a change in the transmission can be due both to a change in the divergence of the beam, in the plane containing the analyzer magnetic field, and a change in the position of the image produced by the analyzer magnet in the plane perpendicular to the magnetic field. Scattering of the beam in the stripping cell reduces this effect, and in the case of the lowest energy channels eliminates it. Over most of the channels the correction is on the order of 25% or less increase in sensitivity.

To obtain a plasma energy distribution from the fast atom spectrum, one must make a number of assumptions.

First, we need to know the composition of the background gas. In a well-gettered system, the background gas is almost completely methane. During the trapping and heating of the plasma, the gas density exterior to the plasma increases by several orders of magnitude. It is assumed that this is due either to desorption of gas from the walls or neutralization and scattering from the walls of some of the injected plasma. Thus there is an ambiguity in the identity of the background gas. However, it seems certain that the signal detected by the analyzer is due to charge-exchange on atomic hydrogen. This is because the depth of penetration of thermal methane in the plasma would be only a fraction of a millimeter. The charge-exchange neutrals from this reaction would come off tangentially and not be detected by the analyzer which has a field of view small compared with the plasma diameter. Thus we have assumed that the charge-exchange gas is atomic hydrogen of a few eV energy which could be present both from Franck-Condon breakup of the methane molecule and neutralization of the initially injected plasma.

The plasma ion angular distribution is also needed for reduction of data. We have assumed a separable, normal mode, angular distribution, using an analytic expression of Holdren.⁷³ During compression of our plasma, there is a great deal of plasma noise and turbulence and a loss of a large fraction of the injected plasma and apparently a relaxation of the angular

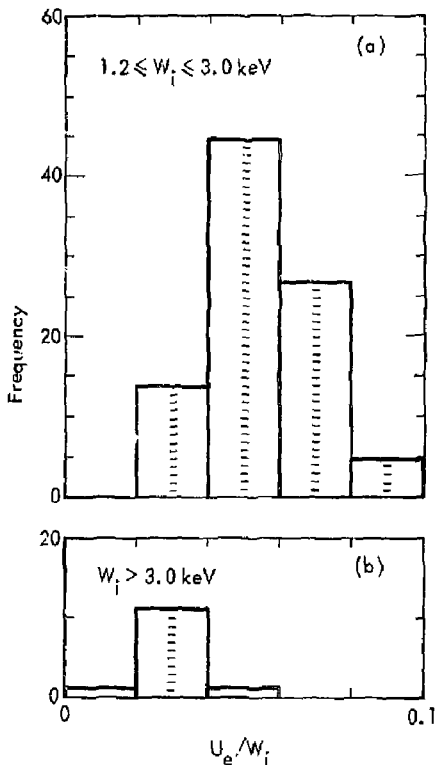


Fig. 37. Ratio of electron energy to ion energy for plasmas of mean ion energies (a) between 1.2 and 3.0 keV, and (b) greater than 3 keV.

distribution. Microwave measurements of the z -dependence of our plasma density indicate that the ion angular distribution closely resembles a collisional normal mode following compression.

There are two effects which are not included in the present reduction of the data due to lack of necessary data. One of these arises from the fact mentioned above that the charge-exchange event must take place at least an ion Larmor radius into the plasma for the charge-exchange neutral to be emitted within the small acceptance angle of the neutral analyzer. Figure 38 illustrates the problem with a particular example. We assume a central plasma density of 10^{13} and a representative plasma radial distribution as shown in curve 1.

Curve 2 shows how the density of hydrogen atoms of mean energy of 1 eV would vary with distance

from the plasma surface. (About 1-eV average energy hydrogen atoms would be created by Franck-Condon break-up of methane). The numbered point on curve 2 refers to the eleven analyzer channels and indicates the fraction of the original neutrals which penetrate the plasma to a depth equal to the Larmor radius (in a field of 6 kG) of a proton of the energy that will be detected by that particular channel. The reciprocal of this fraction is therefore the weighting factor that should be applied to each signal to correct for this effect. These weighting factors are of course a function of ion type, plasma radial distribution, and density (and therefore time).

Also, the plasma potential will cause the effective mirror ratio to be a function of energy and thus the angular distribution is a function of ion energy. Lower energy particles have larger loss cones, and the solid angle of acceptance of the analyzer will be a larger fraction of the total solid angle of containment than for the higher energy particles. The effect of this correction would be to decrease the lower energy end of the spectrum.

Figure 39 shows the effects of these two corrections on a sample plot. Curves 2 and 3 are obtained from the uncorrected data (curve 1) if we assume a plasma

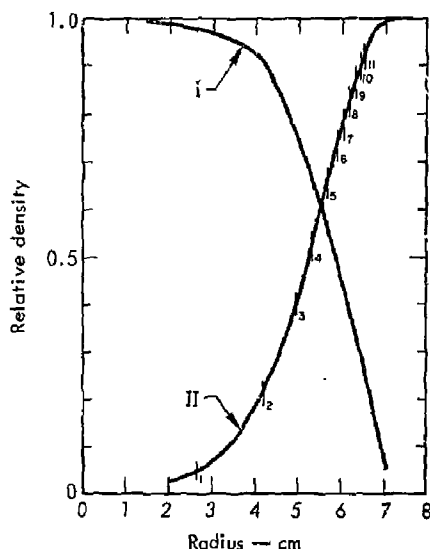


Fig. 38. Relative density of 1-eV neutrals as a function of plasma radius.

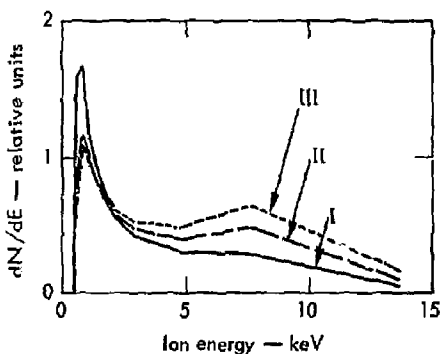


Fig. 39. Magnitude of correction to ion energy distribution from the plasma potential.

- I): Uncorrected energy distribution.
- II): Energy distribution corrected for angular distribution assuming plasma potential of 400 V and central density of $7 \times 10^{12} \text{ cm}^{-3}$.
- III): Energy distribution corrected for angular distribution assuming a plasma potential of 400 V and a central density of 10^{13} cm^{-3} .

potential of 400 V and central densities of 7×10^{12} and 10^{13} cm^{-3} . Curve 2 corresponds to the actual density at the time of measurement, while curve 3 indicates the sensitivity to density of the finite orbit effects. The reduction of the height of the low-energy peak reflects the influence of plasma potential on the angular distribution.

Fluctuation Measurements

We have reported⁷⁰ measurements of 4-mm, forward-angle microwave scattering in the frequency range $0.2 < \omega/\omega_{ci} < 3.0$. During the past year we increased the receiver sensitivity and transmitter power to extend the microwave scattering measurements to lower fluctuation levels, and thus extend the detection of scattering over a wider range of plasma parameters. The sensitivity is in the range of 100 V/cm for wavelengths $\lambda_1 > 4 \text{ cm}$.

Improvements presently underway include further increasing the receiver sensitivity by use of a balanced Schottky barrier mixer and increasing transmitter power from 0.4 to 50 W with an extended interaction oscillator.

Microwave scattering distinguishes between turbulent and quiescent plasmas as discussed earlier

(Ref. 23) and measures the scattered frequency spectrum, but without an extensive receiving antenna array does not measure wavelength. Consequently, electric field fluctuation levels can only be estimated by assuming a characteristic wavelength $\lambda_1 \sim 2 a_1$. To measure fluctuation wavelengths as well as amplitudes, we have made probe measurements in the end regions beyond the mirrors. Except for the high-frequency Post-Rosenbluth modes, the dominant modes predicted for 2XII are "flute-like modes" which extend well beyond the mirrors. Consequently, fluctuations in the interior can be monitored in the end regions without perturbing the confined plasma. Two types of probes have been used. First, a double high-impedance probe whose tips can be moved across field lines to measure wavelength. The frequency response of this probe is limited to $f \sim 3f_{ci} \approx 15$ MHz. Second, a coaxial probe with much higher frequency response located only a few centimeters beyond the mirrors capable of detecting high-frequency fluctuations.

The preliminary conclusions of the probe measurements are:

1. Frequency: $0.2 < \omega/\omega_{ci} < 1.2$ Early in time ($t \sim 0.4$ msec) $\omega \sim \omega_{ci}$
Late in time ($t > 1$ msec) $\omega \sim 0.2 \omega_{ci}$.
2. Wavelength: $\lambda_1 \sim 2 a_1$.
3. Wave phase velocity: In diamagnetic current direction.
4. Fluctuation levels: ~ 100 V rms ($T_e \sim 100$ eV).
5. High-level fluctuations correlate with rapid plasma loss.
6. Fluctuations generally correlate with microwave scattering.
7. Fluctuations are located radially on field lines that connect to interior plasma.
8. Fluctuations above $3\omega_{ci}$ have not been detected.

Although the origin of these fluctuations has not been positively identified, the probe measurements are consistent with some theoretical models⁷⁴ for drift cone fluctuations limited in amplitude to the electron temperature. The probe measurements are presently being extended and the data analyzed in detail to pin down the driving mechanism for these fluctuations and to evaluate their consequence on plasma confinement.

Radial Longitudinal Density Profiles

We completed microwave interferometer measurements of radial and longitudinal electron density profiles. The mean plasma radius determined from a radially offset interferometer agrees with electrostatic probe and laser measurements. The longitudinal profile measured with a scanning interferometer confirms that the ion angular distribution is collisional. After compression, the plasma shape remains approximately constant. The results of this study are described elsewhere.⁶⁹

Plasma Potential Measurement

A knowledge of the plasma potential $\phi(t)$ is necessary to determine the amplification factor in the Baldwin-Callen theory. Most mirror experiments determine $\phi(t)$ from the low-energy cutoff of the end-loss ion energy distribution. End-loss analyzers have not operated successfully on 2XII, primarily because of the large initial burst of plasma during injection and because the relatively high ion energies in the several-keV range resulted in large ion orbits within the analyzer. A new end-loss analyzer has been constructed with Schottky diodes to protect the current amplifier from overloading during injection, and with enough diameter to accommodate gyro-orbits of deuterons ($E \leq 8.6$ keV) which are lost through the mirror due to small-angle scattering. This analyzer has been installed, and is being tested.

Data System

The digital data acquisition system on 2XII has been expanded in the past year with the addition of a new computer main-frame, a digital disc system and a plotter. Along with the hardware expansion there is a continuous effort to enlarge and modify the software system.

Within a year's operation of the original data system⁷⁵ using a computer with 8 K words of memory, it became apparent that more core was needed to increase the flexibility and scope of the operating system. Rather than increasing storage in the original main-frame to 32 K, it was more economical to acquire a newer, faster computer with 32 K of core installed. This releases the 8-K main-frame to be used as a monitor-control computer for the experiment's operation. Also, it remains as

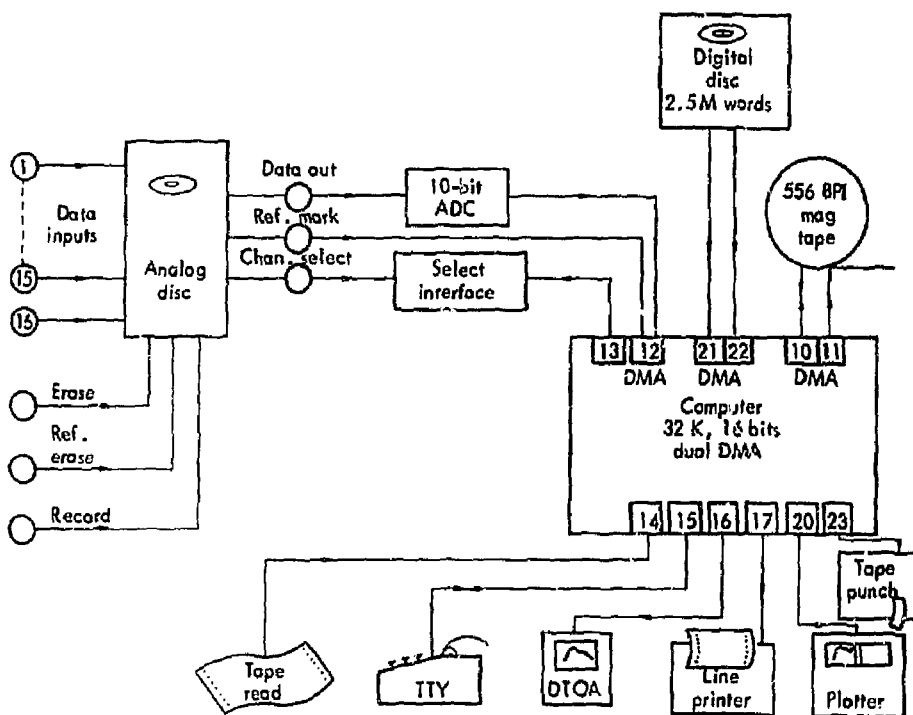


Fig. 40. 2X11 data system.

an emergency backup for the data system. At the same time, the need arose for a rapid access mass storage device to handle the increasing number of programs being written for off-line data retrieval and analysis. We also felt it would be useful to have the ability to store several data shots for rapid comparison without having to do a lot of mag tape operations.

These considerations led to the construction of the data system shown in Fig. 40. The digital disc drive has a total capacity of 2.5 M words, divided equally between one fixed disc and one removable cartridge disc. This unit in conjunction with the new 32-K main-frame allows us to rapidly write and modify programs in Fortran IV which, although inefficient in core usage, cuts the programming man-hours required for a given job by a factor of 2 or 3, in comparison with assembler language.

The software effort has and continues to be concentrated on implementing the digital disc operating

system to the experimental effort, modifying existing programs for greater flexibility, and the reduction of the sinusoidal microwave interferometer output to a plasma density-versus-time plot. Disc system programs had to be written to operate the line printer and the mag tape. In the former case the printer is not part of the vendor's equipment line, while in the latter the mag tape software supplied by the vendor was faulty.

With the larger computer more options have and are being added to the production routine used during data acquisition, and to the mag tape retrieval and reduction code. These changes include the calculation of the velocity distribution function dn/dv versus v for both hydrogen and deuterium, and the absolute neutral flux at mid-plane. Additionally, programs have been written to allow large amounts of data reduction and graphical output to be processed on one of the Lab's CDC 6600's at night.

The phase output of our 70-GHz interferometer⁷⁶ is a time-deformed sinusoid. A series of algorithms has been developed which take these data, correct for imbalances or dc voltage offsets, determine which angular quadrant ($n\pi/2$, $n = 1, 2, 3$, etc.) a data point is in, and calculate plasma line density, peak density (given the radial distributions and compression ratio), $1/\text{line density}$, and $1/\text{peak density}$ as a function of time. This information is available both as printer and plotter output. An example of the interferometer output and the resulting plot is shown in Fig. 41. The sensitivity of the interferometer in conjunction with the digital processing has now given us the ability to follow the density decay down another order of magnitude from the low 10^{11}cm^{-3} range obtained with photographic reduction down to the system noise level in the low 10^{10}cm^{-3} range.

2XII Electronic Engineering

G. E. Voglin, J. W. Robinson and G. C. Tyler

Getter Element Monitor System

A 60-channel getter element monitor was installed. These units sense current in getter elements and give visual indication of getter failure if no current flows with the getter power supplies on. Getter power supplies are 80 VAC at 120 A with output adjustable.

Computer Control System

The major components for the computer control system have been specified and approved for purchase. This system will have 128 differential analog inputs, 60 digital inputs, 108 relay output closures and 12 bits of TTL level output. This equipment, along with LLL fabricated designs, should allow us to put 54 getters under control. The remaining 74 channels of analog input will be used to monitor the ignition tube current distribution in our crowbar switch. A 100-channel reed scanner will be used to monitor bank voltages, vacuum settings, water values, temperature, and interlock systems. Much work remains to adapt 2XII to computer control, as many of the above parameters are located in serial chains or tree-like interlinked patterns not easily available for monitoring or control.

The present control room timing system employs analog RC timing chassis in the traditional parallel-serial manner which produces a mesh of large delays trimmed by smaller delays. A more accurate system has been specified using digital timing delay chassis in a parallel mode which will allow timing of events to less than 100 nsec with millisecond overall delays.

Data Collection System

A second line printer and magnetic tape unit and a high-speed paper tape punch have been specified and purchased. The printer will increase the system reliability. The magnetic tape unit will increase our data-collecting capacity to maintain our present data reduction power with analog disc expansion from 16 to 32 analog channels. The high-speed punch reduces the time required to produce new software programs.

Two optical amplifiers were used to interface the microwave interferometer to the analog disc, and the increase in data accuracy was clearly visible. The optical isolation removes ground loops and high-frequency interference.

The Thomson scattering laser experiment is being interfaced to the analog disc system as soon as channel expansion is complete. Five analog channels will be required. The discriminators, integrators, and timing and gating chassis have been checked out.

High-Voltage Switching

A system of discharging 20 RG-19 cables charged to 150 kV was developed and fired through the 2XII machine at up to 140 kV. The switch uses a surface gap which is graded to hold the potentials. The result is a low-impedance, high-voltage switch that discharges 20,000 ft of RG-19 in multiples of 1.5 μsec , depending on the load impedance. The system also has the capability of double ending for shorter pulses of lower impedance and 200-kV peak voltage. Two failures of the ceramic feedthrough have delayed high-voltage operation.

2XII-B Coil System Electrical Design

A 1/8-scale model of the 2XII-B pulsed magnet system was built and tested. The purpose of the tests was to verify the calculated magnetic field characteristics, and to obtain values for other electrical properties of the magnet windings. Close agreement between

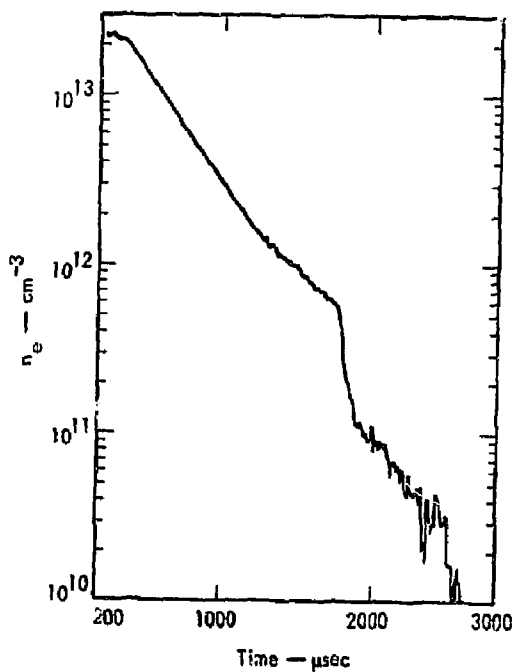
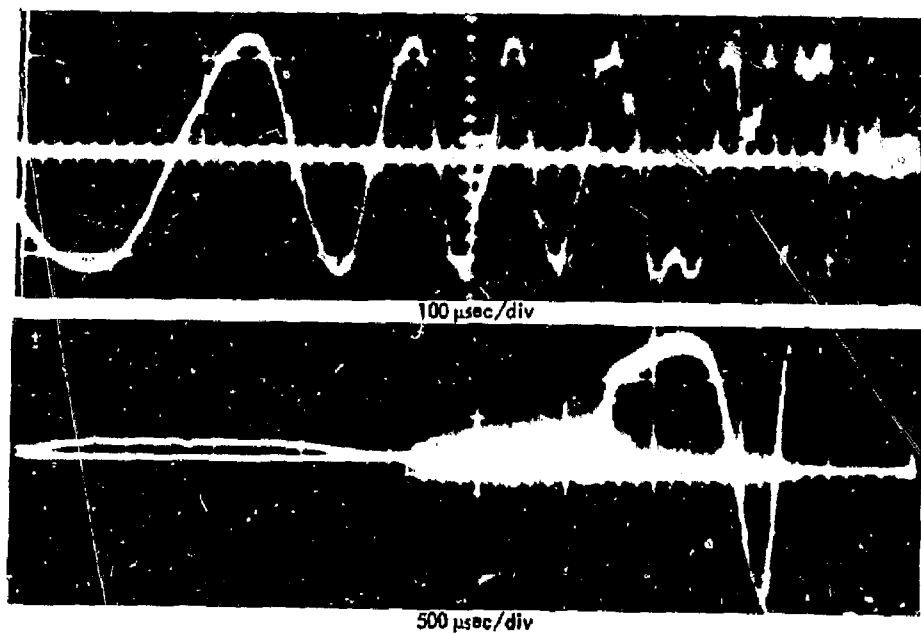


Fig. 41. An example of 2XII interferometer output and density plot.

calculated and measured values was demonstrated for both field shape and magnitude. Among the other properties of the new magnet system evaluated through use of the model were: inductance, resistance, mutual coupling between coils, and induced voltages. The coupling affects the coil design since the induced voltage from the fast gate can significantly increase the electrical stress on the compression coil insulation under certain fault conditions.

Various insulation techniques for the new 2XII coil have been tested using military specifications 27C and 202D method 201, and ASTM standard D-1868. A test for corona has indicated that many of the test specimens have air voids, and greater precautions will be taken to avoid this problem.

2XII Mechanical Engineering

2XII General Support

C. J. Anderson

The beam-line source tank and burial chamber for use with the Berkeley 10-A - 20-keV pulsed neutral beam were completed and installed on the 2XII experiment. Operation of the source into the 2XII plasma indicated that vacuum and pumping problems had been successfully solved.

We have redesigned the vacuum test and plasma source facility for 2XII and added six d.c. magnets. This facility now more nearly approximates the end tanks of the experiment. The work is about 60% completed, and is progressing with low priority.

Surface and vacuum studies are a continuing effort in the 2XII experiment. We have evaluated the titanium surface used and examined the transient pumping obtained in greater detail than previously. We have also studied extrapolation to larger systems and/or high-current neutral beam injection. Summaries have been published.⁷⁷

A number of design studies have been done on pulsed d.c. magnet systems. These studies have accounted for heat transfer and heat capacity and have supplied impedance matches to several possible power supplies. We have also examined problems associated with scaling up the size of the experiment. This work was done to examine the feasibility of

expanding the available energy for a larger compression experiment.

We have conducted a feasibility study of the use of pulsed superconductors for plasma compression magnets. It appears that the technology now in use by synchrotron designers is not capable of extension to millisecond pulses because of the extremely high heat transfer rates required (see Ref. 78 for details). We have estimated detailed cost, time, and manpower for the 2XIIIB modification as well as for 4X design study.⁶⁶

Diagnostics Development

J. R. Benapfl

Installation of the LBL neutral beam required relocating the vacuum ultraviolet grazing incidence spectrometer and redesigning the laser input lens assembly to inject the ruby laser beam without obstructing the neutral beam. We have also designed and built a differential screw adjustment mechanism for the laser viewing system.

We have designed and constructed a 15-channel beam detector unit to measure attenuation of the LBL beam by the plasma. Pairs of slits in front of each secondary electron detector accept only those particles that have traversed a given 1.8-cm-wide chord of plasma. Adjacent detectors are separated by 1.5 cm. This unit also includes a 9-channel calorimeter.

Other devices designed included two small gridded ion energy analyzers, a swinging charge exchange analyzer, several rf probes, and a ceramic insulator for a 50-keV electron gun.

A double door aperture was designed to reduce wall bombardment during plasma injection. The doors open to allow passage of long retractable getters during the gettering phase of the machine cycle, then swing shut to form a circular aperture. Design of new getters for horizontal side arms and new retractable getters for the trapezoidal sections was completed.

50-Ampere Neutral Beam Modules

S. M. Hibbs

To coordinate and accelerate the delivery of 50-A neutral beam modules, one mechanical engineer has

been working since mid-March in collaboration with the LBL source group. The LBL effort has been to extend the technology of their 10-A source to a 50-A module by scaling up the existing source and changing from a round to a rectangular shape to fit space limitations. The development and fabrication of a suitable extractor-grid assembly for the large area source is a difficult task because of thermal expansion and gradient problems. The extractor must also provide beam steering, something not required of the 10-A source. Mechanical engineering and the Livermore Precision Shop have contributed in this effort.

2XII B Facility

R. Bulmer

Mechanical design for the 2XII B coil set started in November 1972. The new coil system is similar in layout to the present 2XII system, but modifications are planned to improve the plasma-trapping conditions and to accommodate neutral beams of up to 1000 A. The coil set consists of a Yin-Yang geometry compression pair, fast gate, slow gate, and several solenoids distributed along the length of the machine.

Magnetic Field Calculations — Magnetic field calculations were made using MAFCO to determine the effect of increasing the minor radius of the compression set for larger area neutral beams. These calculations also included variations in the coil winding cross section to simulate several sizes of conductors. In all, fields were computed for over 50 different configurations from which the longitudinal and transverse mirror ratios were determined. The compression pair selected is wound in a 4-filar, 2-1/2 turn pattern having the following parameters:

Major radius	70 cm
Minor radius	42 cm
Aperture	45 cm to coil
Plasma aperture	33 cm to wall
Winding cross section	2.07 cm X 23.5 cm

With an effective bank potential of 60 kV, a current of 10^6 ampere-turns will be produced in the coil.

With a risetime of 250 μ sec, this yields a 9-kG central field when the quasi-static base field is 3 kG. The longitudinal mirror ratio is 2:1, and the transverse mirror ratio at the vacuum wall is 1.27:1. Good field line curvature is maintained out to the mirror points. The multifilar winding increases the intrinsic L/R of the coil to about 50 msec. Magnetic field calculations have also been made for the fast and slow gate coils to evaluate various designs. In addition to the pulse magnets, two 9-ft id solenoids have been designed to supplement the existing d.c. coils for operation at 3kG.

Force Calculations — The FORCE code has been utilized to calculate magnetic forces on the high-current pulse magnets. Forces in the compression coil pair appear as compressive stresses of 5700 psi on the insulation between turns. Magnetic pressures on the winding surface vary from 500 to 800 psi and integrating this pressure, a force of about 550,000 lb is found to act on the magnet lobes. As on the present 2XII coil, fiber reinforced epoxy will be used to build up a beam structure between the windings of the compression coil pair, as well as for reinforcing beams in the gate coils. The three-coil subunits are then located with respect to each other and more epoxy composite is layed up until a cylindrical assembly is achieved. Final structural members of a hoop wrap around the magnets and axial tie rods are then applied.

Materials Test and Selection — An extensive testing and evaluation program has been developed to select materials for both the coil insulation and structural material. Preliminary test results prompted a re-evaluation of our vacuum impregnation methods and epoxy formulations used for magnet insulation. The magnet insulation must not only hold voltages of at least 60 V/mil for normal operation, but up to 300 V/mil to insure against failure under certain fault conditions. Various film and fibrous materials are under consideration as candidate materials for use with epoxy. These include dacron sleeving, fiberglass sleeving and tape, polyimide coating, mylar tape and polyester composite film (DMD). Several epoxy formulations are also being evaluated. Personnel from the organic materials section of the Chemistry Department have acted as consultants and

conducted numerous tests. For comparison, materials used on the present 2XII coil were also tested with the new materials.

Mechanical tests of epoxy resins with and without fiber reinforcement have been performed to determine strength, modulus and elongation. Dynamic properties of the materials have been determined for high rate impact loading using the Hopkinson split-bar facility located in the Chemistry and Materials Science Department. Dielectric strength tests have been made by casting two insulated conductors in epoxy. These samples are then loaded in compression using a hydraulic press for several thousand cycles at and above the working loads in the coil. The sample is electrically stressed to a high potential every few hundred cycles to determine at what point mechanical failure causes electrical breakdown. The final candidate materials are then used to fabricate a small-scale pulse coil which can be cycled on a capacitor bank to test the materials under conditions they will experience on the full-size coil.

Materials selection for the structural materials has been in progress since January. The structural reinforcement of the pulse magnets is a large job requiring a hand layup of about 9 tons of epoxy fiberglass. The requirements of the fiber-epoxy system used are:

- Low toxicity and exotherm
- Sufficiently long pot life so that care can be taken during the layup.
- Use at or near room temperature.
- High strength and modulus.
- A capability to absorb high rate impact loading without propagating cracks.

Tests were begun on several epoxy resins recommended by the Chemistry Department. Copy-bar data indicated that a standard pure epoxy resin with an amine curing agent modified with a liquid rubber (CTBN) for toughness offered good dynamic properties while satisfying all of the processing and handling requirements. Tests were then made using this epoxy system with glass fiber reinforcement and with PRD-49, a high-strength, high-modulus organic fiber recently in commercial production. The tests included tensile and compressive strength, modulus and elongation under static loading, and also compressive data for impact loading. Several fiber orientations were tested. Based on the results of

these tests, PRD-49 was eliminated because its exceptional properties were only realized when the composite was loaded in tension, its compressive properties being below those of glass reinforcement.

An important way to get a good composite is to insure uniform, thorough impregnation of the fiber bundles. Poor fiber wetting is especially evident in delamination failure, so flexural specimens are being fabricated and tested. Complete impregnation is difficult on a large-scale hand layup, so the use of wet-preimpregnated cloth is being considered. The glass cloth is saturated with the mixed epoxy system, rolled out to eliminate excess resin, then refrigerated until ready for use. This material was used to mock-up a portion of the coil beam structure. Handling of this material was very easy, and allowed for a clean job of buildup. However, the epoxy did not cure properly because of poor reaction with the CTBN modifier. Tests are underway to eliminate this problem.

2XII-B - Winding and Impregnation

A. Harvey

Each half of the compression magnet set consists of 2-½ turns of 0.814-in. square X 0.501-in. i.d., hollow copper-conductor-wound 4-filar with terminations at the quarter points. Each conductor is insulated with three woven dacron sleeves, and turns are separated by a dacron-mylar-dacron (DMD) strip.

The magnet geometry makes the winding mandrel captive. The mandrel, therefore, is collapsible for removal. The wound magnet is transferred to an impregnation fixture which maintains the magnet shape during mandrel removal and subsequent vacuum impregnation.

To maintain a dead soft temper, the conductor is processed as follows: The conductor supply (in flat-wound pancakes) is drawn through straightening rolls by a variable-speed roller drive. The conductor then passes through a sand blaster to remove surface oxides and enhance bonding, followed in turn by a three-section electric annealing furnace and a water quench. The conductor is stored in a 90-ft-long trough. Both the conductor bore and the furnace are purged with argon gas to prevent oxidation during the

annealing process. Several passes were made to select an optimum speed and oven temperature. The following values, based on conductor hardness and inspection of grain size in etched specimens, were selected:

Conductor speed		7.2 in./min
Furnace temperature	Entrance	1610°F
	Center	1675°F
	Exit	1675°F

Tests were performed to determine both spring back and keystoning of the annealed conductor on an inside bend radius of 15 in. Spring back of 7/16 in. and keystoning of 0.020 in. were observed with 300 lb applied tension. A minimum bend radius of 3 in. was selected for leads, and resulting keystone was removed with 15 tons applied force. All forming was done on a fully insulated conductor with no visible damage to the insulation. The winding of one-half of a set was performed with minimum applied tension to enable the conductor to take a dead set during forming. A degree of overbending was also applied in all areas of directional change in curvature. This method provided a stable, satisfactory winding.

The vacuum mold for the conductor is to consist of aluminum skin plates and edge sealing bars. Grooved polyethylene sheets will be sandwiched between the coil faces and skin plates to provide an evacuation and resin distribution network during impregnation. The assembly will be sealed with an RTV silicone rubber. Bakeout and evacuation of the mold for a minimum of 48 hr will precede impregnation. Feed and cure temperatures will be maintained by circulation of heated water through the conductor bore. Resin mixing, outgassing and transfer will all be under vacuum. The impregnation is expected to take approximately 2 hr, and sight glasses in the mold will be provided for observing the resin flow so that uniform feed rates may be maintained. After impregnation, both the feed and vacuum reservoirs will be under atmospheric pressure. This procedure has been used for many test samples and has given thoroughly impregnated, void-free castings.

2XIIB Magnet and Vacuum Assembly Design

M. Calderon

The 2XIIB facility will be composed of a new magnet system having the same overall length as the present system to make it compatible with existing pumping, service facilities, end tanks, and coils. Only a few modifications to the end sections are necessary. Major changes predicated by the new compression coil design include a 6.5-ft o.d. and an inside cavity which now flares to follow the coil-angled lobe surfaces. Larger mid-plane ports with nominal openings of 24 X 21 in. are included. Figures 42 and 43 show the general arrangement of the new system.

Primary elements of the center magnet system are the compression coils together with the fast and slow gates, assembled as one integral unit. The fast gate power ring has an o.d. of 98 in. and is composed of two parallel circular rings 4 in. wide, 1/2 in. thick and spaced 1/2 in. apart. Four leads from the fast gate coil tie to this copper ring, as do the power supply cables.

This ring will be assembled in sections. The slow gate coil has a single pair of leads which terminate on a terminal "TEE". This ring segment has the same general dimensions as its opposite end ring. Its location on the top of the coil relieves below-coil crowding, and allows for rough vacuum pumping of the magnet internal cavity through two 6-in.-diam ports located on the horizontal centerline and at 180° apart. Optimum use of space has been made to accommodate the added members and to leave insofar as practical, open space for the access ports.

Support for the magnet weight of approximately 22,000 lb is provided by two structures located inside the gate coil rings and resting on the existing laminate beams. These members are of non-conducting material, and contact the magnet for about 20% of its circumference.

Two new d.c. coils of a nominal 12-ft o.d., 9-ft i.d. and 6-in. width are located adjacent to the supports. These coils represent a 30% size increase from the existing d.c. group. The supporting structure for a

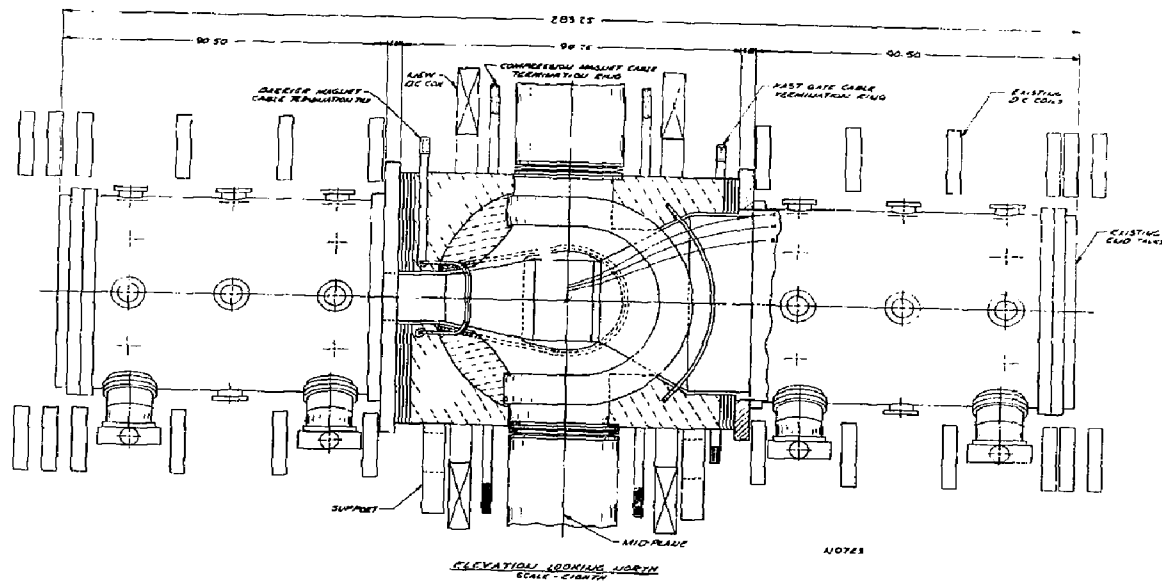


Fig. 42. 2XIIIB elevation.

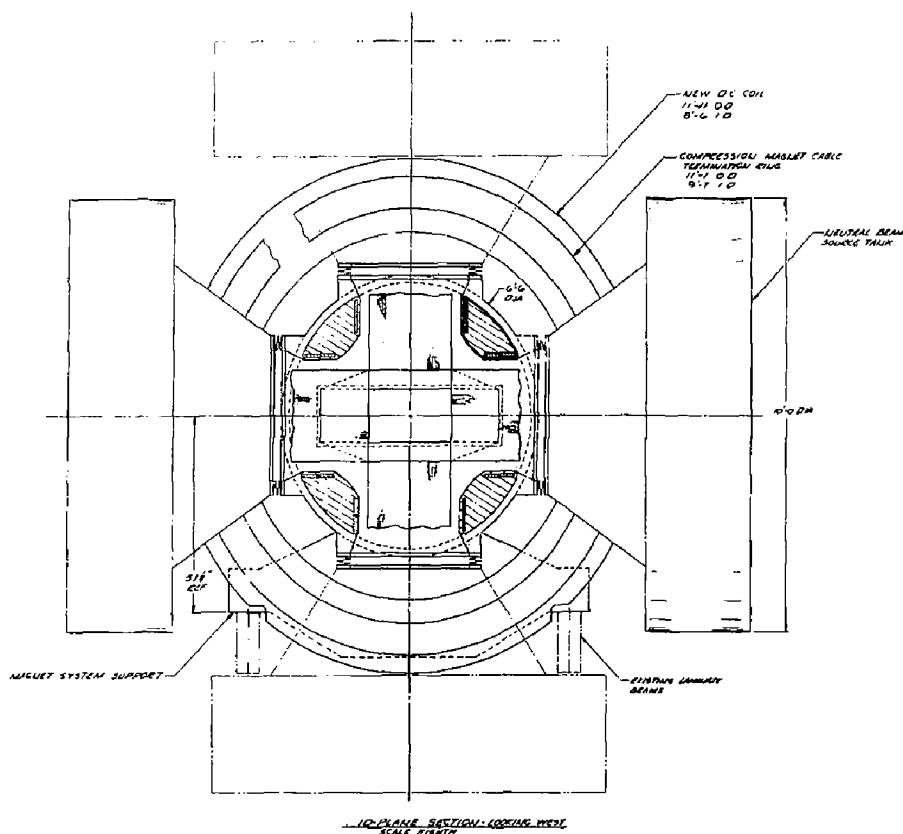


Fig. 43. 2XIIB midplane cross section.

weight of 7000 lb has been confined to the 6-in. width owing to the crowding in this area. Internal construction of these coils is three potted pancakes using 0.814-in. hollow conductor and shielded with an external aluminum shell. The entire group of d.c. coils are tied together to resist both magnetic and structural loads.

Power to the main compression coils is delivered through a pair of 11-ft-diam rings. Each set is fabricated of two 8-in.-wide copper plate rings 1/2-in. thick and spaced 1/2-in. apart. As with the other units, these rings will be made in sections to aid in assembly.

The new compression coil design has resulted in important changes to the geometry of the high-vacuum chamber. The principal advantages include

a larger internal volume, together with greater accessibility to that space. The new arrangement, although requiring a more complex design and greater assembly difficulty, does not offer any new problems. Again, the basic chamber construction will consist of a supportive epoxy-glass laminate overstructure which incorporates water cooling. The chamber pyroceram panels attach to this overstructure with RTV silastic bonds which form structural support, provide isolation from shock, and allow for pumping of the space between these two surfaces.

The inside surfaces of the vacuum chamber are totally shielded by a system of loose pyroceram panels so arranged to support each other, and are spaced from the chamber walls to allow for pumping.

In addition, all panels are removable to permit cleaning of the titanium deposits.

When assembled, high-vacuum chamber seals are made at the joints between the end tanks and the center section and at each of the four projecting ports. The chamber hangs as a unit from a structure over the magnet center section and is thus isolated from shock during pulsing of the machine. Pumping of the inner space is through the ends of the four beam ports.

DIRECT ENERGY CONVERSION PROGRAM

W. L. Barr, M. O. Calderon, B. C. Howard,
R. W. Moir and R. R. Smith

Introduction

Construction is nearly complete on the direct energy conversion facility which was described in last year's Annual report²³ (see Fig. 44). The magnetic expander was carefully optimized⁷⁹ so

as to guide protons of energy 1.5 keV or less from the 30-kG peak field end down the expander to the 100-G end, keeping the particle's magnetic moment conserved. Initial experiments with an electron beam indicate the magnetic field is accurate enough. Direct collection experiments will be done in FY 1974 initially using ions from a source which has been developed to produce on the order 1 μ A of H^+ ions at 300 eV. Further acceleration will give an energy spread from 300 to 1200 eV.

Design of Direct Energy Conversion Test Facility

Preliminary testing of major components is now in progress for the Direct Energy Conversion Experiment. The machine experiment is composed of three main sections, as shown in Fig. 44. These are the ion source, the expander and the collector. The collector tank, its support and the support rack for the module are being assembled. Fabrication of the collector modules was completed in August. This completes the initial building phase of the machine.

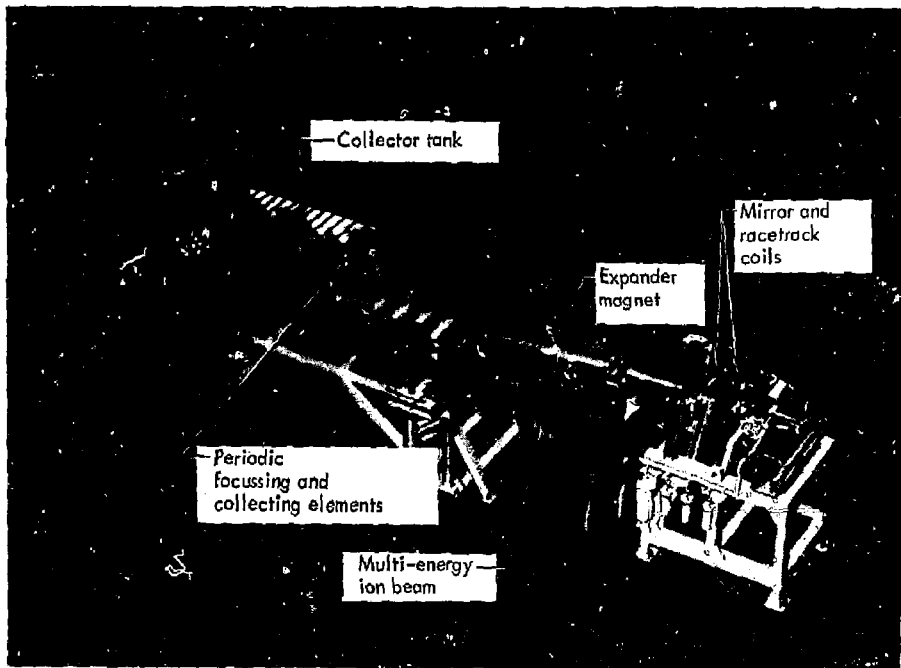


Fig. 44. Direct conversion test facility.

The ion source section of the machine is composed of a source magnet, a coil-set magnet, and a vacuum system pumped with a 500-liter/sec vac-ion pump. The system is initially pumped by cryosorption pumps which are in turn backed up by carbon vane mechanical pumps. The coil-set magnet is a combination of a solenoid and oblong-shaped coil electrically in series and designed to be powered to a maximum of 2000 A and 222 V by two temescal power supplies in series. Both of these coils are constructed of 0.340-in. square hollow conductors and wound bifilar with separate water-cooled leads from each pancake to provide for the necessary heat dissipation. A common mandrel, which is also a part of the vacuum system, supports both coils which together produce a maximum field of 31.5 kG. The coil-set magnet, together with the source magnet, combined to form a single mirror region in front of the source.

The three basic parts of the expander section are the vacuum vessel, the expander magnet windings, and the two end coils which help shape the field and separate the electrons after the expansion. The vacuum vessel is a trapezoidal-shaped chamber which was fabricated from two channel halves whose shape expands in two directions. The corners of these 1/2-in.-plate channel halves were formed with a 2-in. radius to avoid a sharp bend of the conductor. These channel halves were then seam-welded to form the trapezoid vessel section. A plenum section at the source end of the expander provides a tie to the flange of the coil set, and has a provision for pumping at the lower end and a port at the top for diagnostics. The downstream end is a 4-ft-diam ring which matches the collector tank and houses the two end coils. Pumping and diagnostic ports are also located in this area. Additionally, the trapezoidal section has a pair of 2-in.-wide, full-height diagnostic ports on each side. A total of 163 expander magnet conductors wind counterclockwise around the vacuum vessel and produce a field which ranges from a high of 30 kG at the source to an average field of 100 G at the end of the expansion. Great care has been taken in the placement of these conductors to assure the vertical alignment of the top and bottom conductors. The first 58 turns of the 0.255-in.-square hollow conductor were placed on the insulated surface of the vessel using a series of graduated

spacers to accomplish the proper separation. The remaining 105 conductor turns have been located by grooved laminate plates that have been machined by a tape-controlled mill. In this manner, the location of the upper and lower same-turn conductor faces have been placed within 0.015 in. of each other. Three hydraulic circuits have been formed in these windings to satisfy cooling requirements. The expander end coils are two independent rectangular-shaped coils which locate crosswise to the axis of the machine inside the vacuum chamber and have their downstream faces in vertical alignment. Both of these coils are canned, and their leads exit through separate flange ports in the expander ring face. The innermost end coil is a 24-turn, 3 X 8 conductor cross section magnet. A 25-turn bucking coil with a 5 X 5 conductor cross section locates around the end coil. Both of these coils are formed from 0.255-in.-square hollow conductor and are independent hydraulically. All three expander windings are electrically in-series, and are powered by a 200-A 60-V power supply.

The collector section of the machine contains a 4-ft-diam tank 10 ft long which houses a system of 22 modules to decelerate, focus and collect the positive ions at different energy levels. These modules mount in a rack which ties to the end flange of the tank, and has rollers at one end to permit disassembly of these two units for access to the modules. All leads from the modules pass through an adjacent vacuum seal into a 3-in.-diam tube which runs parallel and alongside the modules. Provision has been made for pumping of this tube in the event of a leak. Pumping for the vessel consists of one 500-liter/sec vac-ion pump and two sublimator pumps of 6000 and 5700 liters/sec respectively. Roughing is performed with a series of four cryosorption pumps to insure a clean system. Again, backup is provided by carbon vane mechanical pumps.

Numerical Study of Periodic Focusing Direct Energy Converter

The DART trajectory code was used to optimize the design of the collector structure. The code follows trajectories down the magnetic expander, through the fringing magnetic field at the end of

the expander, along the electrostatic focusing region, and on to collection on an electrode. The code records the fraction of the particles that strike each type of surface so that the collection process can be followed in detail as the voltages and geometry are varied.

Scaling for the experiment was determined by running H^+ with energies from 333 to 1000 eV started with 90% of their energy perpendicular to the field and forming a 6.35-mm-diam beam at the strongest magnetic field. Optimum scale length turned out to be 22.5 cm for one full spatial period which is the length of two collector stages. The efficiency of energy recovery is $88 \pm 1\%$ if all retrograde ions are assumed lost, or $90 \pm 1\%$ if those retrogrades are included which are magnetically reflected and caught.

Scaling for a reactor was determined by running D^+ with energies from 400 to 1200 keV, started with 90% of their energy perpendicular to the field with guiding centers inside a 32-cm-diam flux tube at the 150-kG mirror. Optimum scale length L is

2.0 m. The efficiency of energy recovery at low-power density is again $88 \pm 1\%$ and $90 \pm 1\%$, depending on the magnetically reflected retrogrades. Other processes will reduce the efficiency by an estimated 16%. These processes include losses due to space charge, secondary electron emission, charge exchange and ionization, column interception, and coupling to the reactor.

The DART code has now been modified to include space-charge effects, and is being used to determine the power-handling ability of this system. Preliminary results showing the efficiency versus power (i.e. space-charge) are shown in Fig. 45 along with previous results calculated by Moir et al.⁸⁰ and the theoretical results calculated by Marcus and Watson⁸¹ after normalization to our value at zero density.

Two accessory codes were developed. COP82 is a code to determine the optimum potentials for a given number of collectors. Another code⁸³ will, by the techniques of relaxation and rezoning, calculate the potential in a system containing small grid wires.

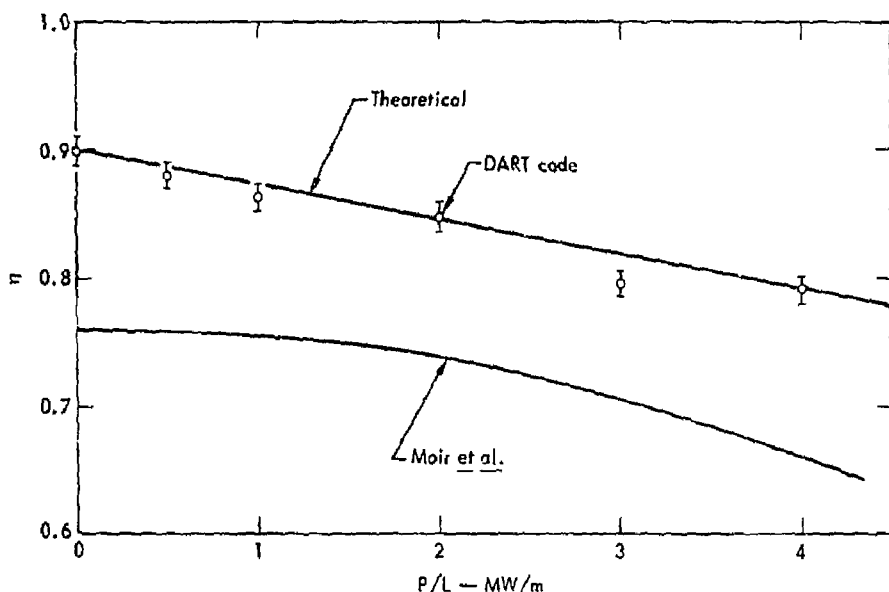


Fig. 45. Efficiency versus power per circumferential length of the direct converter. The error bars represent statistical variations due to simulation with only 360 particles. Our efficiencies are higher than those calculated by Moir et al., due in part to our detailed treatment of the collector cup region. The theoretical curve of Marcus and Watson⁹⁶ was normalized to our value at zero density.

"Venetian Blind" Direct-Energy Converter Studies

The concept of the "venetian blind" direct-energy converter,⁸⁴ which uses the angular-dependent transmission of ribbon grids which resemble venetian blinds to recover the energy of particles leaking out of a fusion reactor has been developed further.

Our study^{85, 86} adapts this converter concept to a mirror fusion reactor. When the engineering and economic constraint are considered, we find that the energy which can be handled can be as low as 170

keV (equivalent to 150-keV injection into a D-T mirror-confined plasma), and the efficiency is predicted to be about 65%. The "venetian blind" converter can handle more space charge (lower energies), but is less efficient by comparison to the periodic focusing direct converter. We find that a severe limitation to adapting the venetian blind concept and perhaps others to toroidal reactors will be the increasing loss due to charge-exchange or background gas of ions passing through the expander to the collector.

III. Toroidal Confinement Program – Superconducting Levitron (O.A. Anderson, D.H. Birdsall, C.W. Hartman, E.B. Hooper, and R.H. Munger)

INTRODUCTION

In the superconducting Levitron during the past year the following objectives were pursued: (1) producing a high- β hot-electron plasma by microwave heating, and (2) heating a dense plasma by thermalization with the hot-electron plasma. Experiments were conducted under successively improved vacuum conditions and as the control of wall degassing became better, improved plasma parameters were achieved. However, before the SCL experiment was terminated at the end of FY 1973, we had not reached burn-out conditions important to strong dense plasma heating.

Discussed subsequently are: (1) studies of hot-electron plasmas where we believe we have cast light on new mechanisms responsible for stable confinement; (2) an experimental demonstration that current induced in a hot-electron plasma flows stably for a number of seconds as required for the SPIRIT concept; and (3) studies of dense plasma heating and confinement where we found that plasma-cooling by gas outside the plasma limited strong heating.

HOT-ELECTRON PLASMA STUDIES

Experimental Results

During the past year, studies of hot-electron plasma were conducted under continually improved

vacuum conditions, and with better diagnostics. A year ago, the hot-electron plasma was found to be persistently anisotropic (mirror-trapped) in the Min-B configuration. A slightly modified Min-B configuration which maximized the poloidal flux has been used, and essentially isotropic plasma has been achieved. The isotropy and confinement is discussed in Ref. 100. We have found that Bohm-like diffusion has no relevancy, and that confinement is essentially classical.

As discussed elsewhere,^{87, 88} cold plasma plays an important role in the confinement of hot-electron plasma. It was found that values of $n_{ecold}/n_{ehot} \approx 10-100$ were required to achieve stable decays at low toroidal field ($I_z \lesssim 60$ kAT). At high toroidal field, and hence Min-B trapping, results were ambiguous. The characteristic instability bursts (at $\sim 10-100$ MHz) and pump-out of hot electrons seen at $I_z \lesssim 60$ kAT were not observed, but on the other hand confinement of cold plasma improved with I_z so that n_{ecold}/n_{ehot} increased with I_z .

On the last experimental run we achieved the cleanest plasma environment yet, and correspondingly n_{ecold}/n_{ehot} decreased. It was found that the characteristic instability bursts were present for all $I_z \lesssim 240$ kAT, i.e., even when a Min-B mirror-trapping region was present. The results are shown in Fig. 46. Our tentative interpretation of this result (as discussed later) is that the interchange instability or a trapped

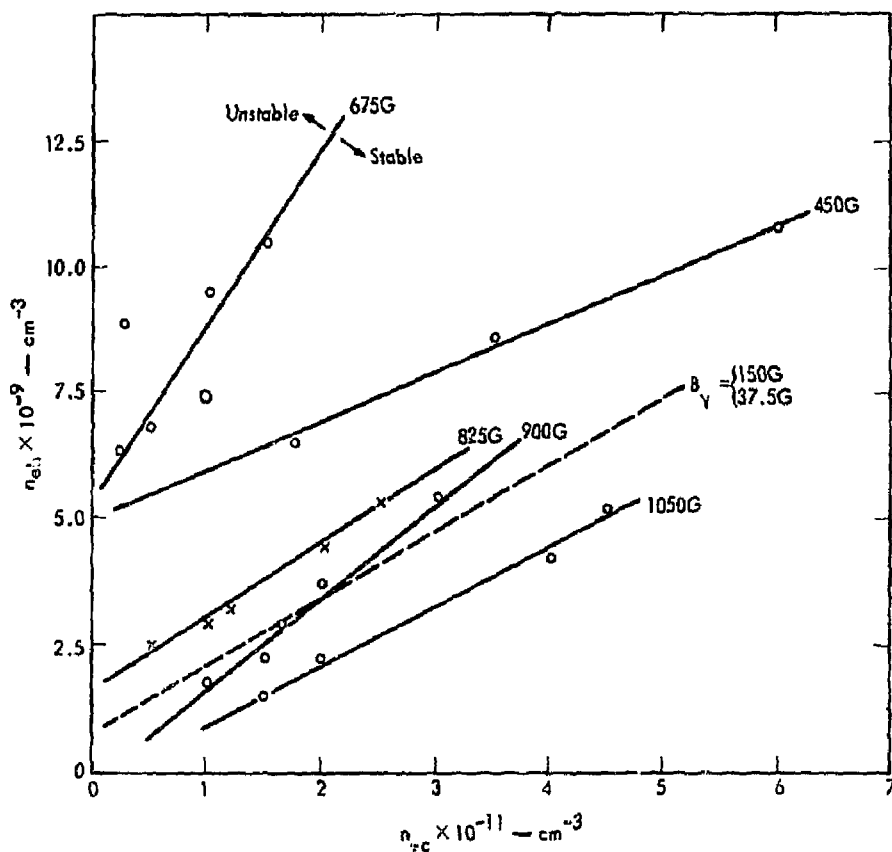


Fig. 46. Marginal stability curves, Min-B configuration, $I_R = 225$ kAT. The single point shown as O is a corresponding marginal stability point for the Min- $\partial B/\partial S$ configuration $I_R = 150$ kAT, $B_y = 75$ G.

particle variant are not involved at all; instead a drift-wave-type interaction takes place between the hot electrons and background plasma. Such an interaction is predicted to be insensitive to field curvature.

We have also examined experimentally the possibility of inducing current in a hot-electron plasma pursuant to the general possibility of fusion by magnetic confinement formed with beams. The results are discussed in Ref. 89. Briefly, current induced by changing the toroidal field is found to behave consistently with a classical acceleration and confinement model. Currents of up to 7 kA were induced which decayed in typically 3-5 sec as expected from classical scattering. This result

suggests that the inductive limit of the Spire concept is a viable means of forming a stabilized pinch using the high-conductivity aspect of a hot-electron plasma.

DENSE PLASMA EXPERIMENTS

Heating Experiments

Dense warm plasma was formed in the superconducting Levitron by injecting cold helium or hydrogen into the hot-electron plasma obtained by microwave heating. An 8-mm interferometer and a massive Langmuir probe were used to measure n_{ec} and T_{ec} . The ambient neutral gas density n_0 was monitored with a fast ion gage.

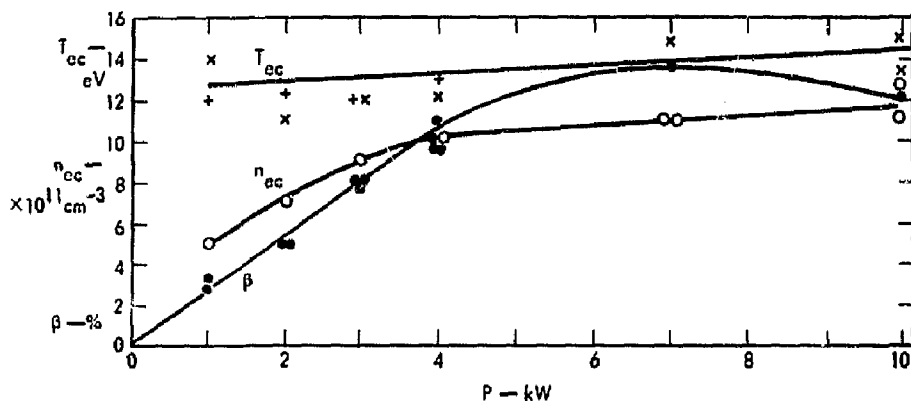


Fig. 47. Heating of injected hydrogen gas by hot electrons, at various microwave power levels. The hot-electron β (peak local value) at time of injection is shown, along with measured cold plasma density and temperature.

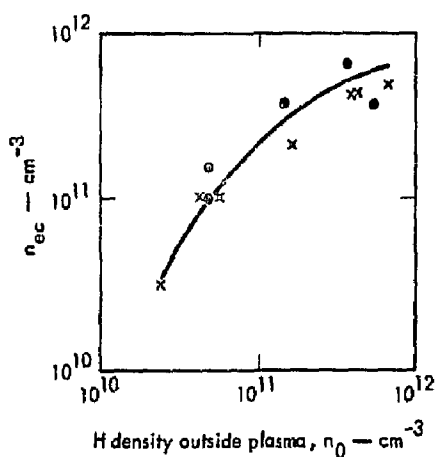


Fig. 48. Cold plasma density for various quantities of injected hydrogen.

During the rf heating time, the fast ion gage showed gas evolving from the walls and the floating ring. At low rf power this gas was predominantly helium, but at higher power levels a monochromator study showed the presence of heavy impurities. In attempting to find the best combination of stored energy and purity for the hot-electron plasma, a number of parameters were varied.

1. Filling pressure: This influenced the formation and stability of the hot-electron plasma. When

the machine was in normally clean condition, around $3 \times 10^{10} \text{ cm}^{-3}$ of He gave good results.

2. Gas puff delay time: A delay of around 0.3 sec allowed enough time after rf turnoff for impurities to condense without too much loss of hot-electron β .

3. rf duration: This was normally long enough (up to 2 sec) to allow full buildup of hot-electron β . At high power levels, however, the buildup of β was cut back somewhat to hold the impurity level down.

4. rf power: The hot-electron β for a given power depended on the impurity history of the machine; e.g., at 1 kW, the peak β was about 6% on best days and 2% or less on others. The results on an average day are shown in Fig. 47. The β is 3% at 1 kW and almost linear up to 4 kW, leveling off at higher powers. Figure 48 also shows that, for a small puff of H_2 ($n_0 = 1.8 \times 10^{11}$), the power variation has relatively little effect on the density and even less on the temperature of the cold plasma.

Additional parameters were varied in trying to optimize the cold plasma density and temperature.

5. Type of gas puffed in, hydrogen or helium: Hydrogen condensed rapidly on the nearby cryogenic surfaces, helping to promote a burnout condition, but unfortunately the plasma densities achieved were rather small.

6. **Sampling time:** Optimum density and temperature occurred in a few milliseconds. With hydrogen, n_0 (and sometimes n_{ec}) decreased in a few tenths of microseconds.

7. **Puff pressure:** Figures 48 and 49 show the variation of n_{ec} and T_{ec} with n_0 for hydrogen. Evidently, $n_{ec} \approx n_0$ over a wide range, while T_{ec} is fairly insensitive to n_0 .

8. **Ionization pulse:** The trapping of cold plasma may be assisted by applying a short burst of microwave power around the time of the gas puff. The power, pulse length and pulse timing were varied.

Figures 50 and 51 show n_{ec} and T_{ec} for helium injected simultaneously with a 4-msec, 20-kW rf burst, 0.35 sec after the end of the main heating pulse. The machine wall conditions were favorable, and 1 kW of power for 2 sec produced $n_{ch} \approx 2.5 \times 10^{10}$, $T_{ch} = 250$ keV. In these figures, the parameter n_0 was varied by adjusting the quantity of helium injected. Shown for comparison are the computed equilibrium values of n_{ec} and T_{ec} (see previous section). The density fit is quite good, considering the uncertainties involved. The temperature, however, is two to three times lower than expected on the basis of measured diffusion coefficients (see next section). One mechanism not included in the computation which may be holding the

temperature down is cooling by impurities, but the impurity level is not known quantitatively.

Measurements of Dense Plasma Confinement

A circular double limiter extending around the periphery of the confinement zone measured the outward flux of plasma. A direct check was made of the efficiency of flux collection: the Langmuir

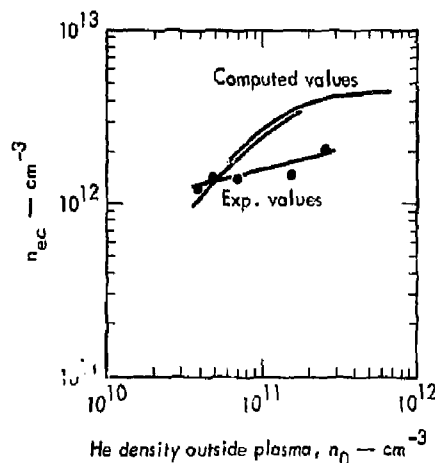


Fig. 50. Cold plasma density for various quantities of injected helium, compared with computed values.

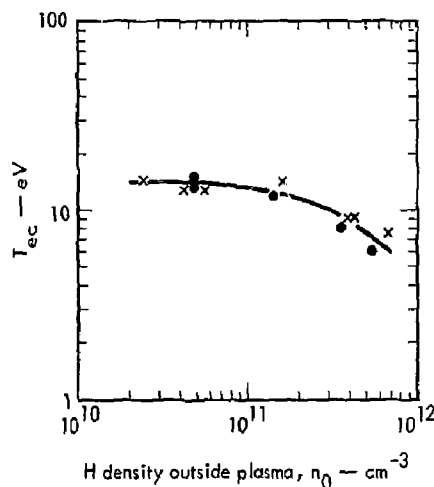


Fig. 49. Cold plasma temperature for various quantities of injected hydrogen.

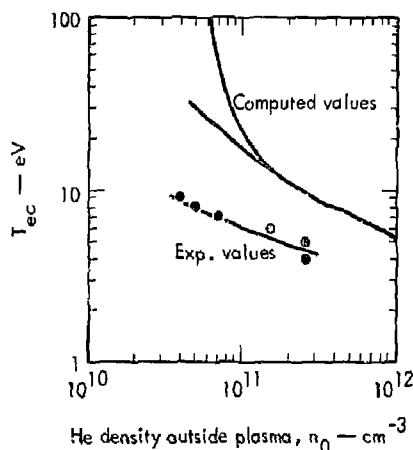


Fig. 51. Cold plasma temperature for conditions of Fig. 50.

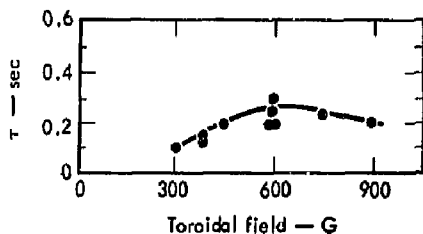


Fig. 52. Dense plasma confinement time, calculated from measured plasma flux and density as a function of stabilizing toroidal field strength. Ring current, 150 kA-turns; helium gas.

probe used for temperature measurements (previous section) was placed in its normal position on an outer magnetic surface. When the circular limiter was moved downward a few millimeters past this same magnetic surface, the current collected by the Langmuir probe disappeared completely, showing that the circular limiter collected all the flux.

Figure 52 shows confinement times calculated from the relationship $n_{ec}eV/I_{CL}$ where I_{CL} is the circular limiter saturation current, n_{ec} is measured with the interferometer, and V is the plasma volume (taken as $5 \times 10^4 \text{ cm}^3$). The measurements were made a few tenths of a second after injecting a puff of helium into the hot-electron plasma. The confinement time is seen to optimize for a toroidal field of about 600 G. (This same field was previously found to give optimum hot-electron β .) For $T_{ec} = 5 \text{ keV}$, the Bohm time is about 0.75 msec, so that the measured τ corresponds to about 350 Bohm times.

In many cases, low-frequency oscillations were observed on the outside of the plasma during the decay. In taking the data for Fig. 52, the frequency of these oscillations was observed to vary from 120 to 300 Hz, depending on the toroidal field strength and the quantity of gas injected. The percentage modulation of I_{CL} was 50% or more; an average was used for Fig. 52.

The oscillations were observed with probes placed on the same magnetic surface at points along and across the field. No phase shift was found, indicating an $m = 0$ mode (radial oscillations).

In Fig. 53, gas was bled in during the rf heating rather than puffed in afterward. The density n_{ec} in the afterglow was low ($\sim 10^{11} \text{ cm}^{-3}$). Under

these conditions, x-ray bursts were observed which originated on the circular limiter. These are seen to occur at the same rate as the cold plasma oscillations. Evidently, the hot electrons participate in the radial excursions.

In some cases, the oscillations were strong enough to appear on the interferometer signal. Figure 54 shows a particular case in which a small puff of helium was introduced at $t = 2.2 \text{ sec}$, after a 2-sec heating pulse. The cold plasma density is seen to build up on an unusually long time scale ($\sim 30 \text{ msec}$), according to the probe current signal and the interferometer signal. Both signals also show a strong modulation at 140 Hz.

Working with helium, the radial oscillations were relatively reproducible, their frequency increasing (but less than linearly) with n_0 . With hydrogen, these pulsations were generally lower in frequency (as low as 33 Hz). After a few shots with hydrogen, the pulsations tended to become small or disappear. Although no systematic study was made for this case,

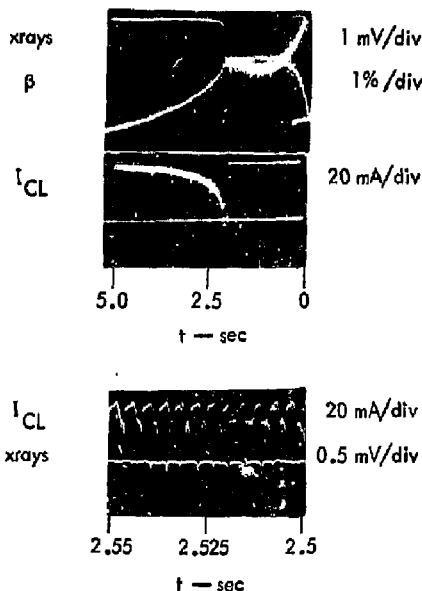


Fig. 53. Plasma flux signal I_{CL} and x-ray signals at two different sweep speeds. The flux signal is disconnected during hot-electron heating (up to $t = 2 \text{ sec}$) to avoid overdriving the oscilloscope amplifier.

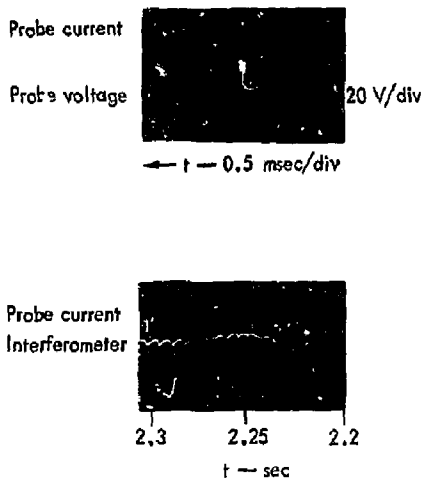


Fig. 54. Signals from heavy Langmuir probe and interferometer, showing modulation at 140 Hz.

it was felt that a changing evolution of wall-adsorbed gas could be responsible for such variations.

On another occasion when the radial oscillations were not strong, they were suppressed by increasing the toroidal field to 1.2 kG. This seemed to lead to some improvement in n_{ec} decay time, but since a flux measurement was not available on that occasion, the actual confinement time was unknown. However, it is safe to say that in all observed cases, the slow oscillations had at most a small effect on cold plasma confinement.

STABILITY THEORY OF A HOT-ELECTRON PLASMA

H. L. Berk, C. W. Hartman and E. B. Hooper, Jr.

The stability of a hot electron plasma alters considerably from MHD theory when the electron temperature is large enough that the drift frequencies exceed the ion-cyclotron frequency. In this case, MHD theory fails as it is based on the assumption that all frequencies of interest are less than the ion-cyclotron frequency. For the levitron, the curvature drift is given by

$$\omega_D = \frac{M}{m} k_y \frac{a_H^2}{R_c} \omega_{ci} > \frac{M}{m} \frac{a_H^2}{R_p R_c} \omega_{ci}$$

where R_c is the curvature radius, R_p the minor radius, $k_y = \ell/R_p$ where ℓ is an integer and a_H is the hot electron Larmor radius. For $R_p = 10$ cm and $R_c = 20$ cm, $B = 3 \times 10^3$ G, then $\omega_D > \omega_{ci}$ for all ℓ for a helium plasma when the electron temperature exceeds 20 keV. The hot electron plasma in the levitron exceeds this value, and therefore the usual MHD stability theory does not apply in this case.

A mechanism for instability is still present as long as $\omega < \omega^*$, the hot electron diamagnetic drift frequency,

$$\omega^* = \frac{k_y a_H^2}{R_p} \omega_{ce} \lesssim \frac{a_e^2}{R_p^2} \omega_{ce}$$

This mechanism is a variation of the usual inverse Landau damping that arises in drift-wave instabilities. For a 200-keV plasma, one can expect instability frequencies to range up to 2×10^7 Hz.

As a first approach to stability analysis, an infinite medium dispersion relation has been derived which has the form,

$$(1 - \alpha) \frac{k_{\perp}^2 \omega_{pe}^2}{k_{\perp}^2 \omega^2} + \frac{\omega_{pi}^2}{\omega^2 - \omega_{ci}^2} \left(1 - \frac{\delta \omega_{ci}}{\omega} \right) - \left(1 + \frac{\omega_{pe}^2}{\omega_{ce}^2} \right) - \frac{(1 - \alpha) \delta \omega_{pi}^2}{\omega \omega_{ci}} + \frac{\alpha \omega_{pi}^2}{k_{\perp}^2 v_{th}^2} \int \frac{d^3 v F_e(k_{\parallel} v_{\parallel} - \omega^* - \omega_{DH})}{\omega - \omega_{DH} - k_{\parallel} v_{\parallel}} = 0 \quad (III-1)$$

where α is the fraction of hot electrons, $\omega_{pe} = \omega_{ce}^2 \times k_{\perp}^2 c^2 / (k_{\perp}^2 c^2 + (1 - \alpha) \omega_{pe}^2)$, $\delta = k_y / k_{\perp}^2 R_p$, k_{\perp} is the total wave number perpendicular to the magnetic field, $F_e = 1 / (2\pi v_{th}^3)^{3/2} \exp(-v^2 / 2v_{th}^2)$ is the hot electron distribution, and $\omega_{DH} = (v_{\parallel}^2 + v_{\perp}^2 / 2) k_y / \omega_{ce} R_c$.

The last term in Eq. (III-1) has an imaginary part for real ω that can change sign if $\omega < \omega^*$, viz.,

$$I \equiv \text{Im} \int \frac{d^3 v F_e(k_{\parallel} v_{\parallel} - \omega^* - \omega_{DH})}{\omega - k_{\parallel} v_{\parallel} - \omega_{DH}} = -i\pi(\omega - \omega^*) \int d^3 v \delta(\omega - \omega_{DH} - k_{\parallel} v_{\parallel}) F_e \quad (III-2)$$

Even with k_{\parallel} so l is finite as ω_{DH} has a thermal width.

If we solve Eq. (III-1) under the assumption $\omega \gg \omega_{ci}$, we find that the unstable root has a real frequency,

$$\omega_0 = \text{Min} \left\{ \frac{\omega_{ci}}{\delta} q, \frac{\omega_{pi} q^{1/2}}{\left(1 + \frac{\omega_{pe}^2}{\omega_{ce}^2}\right)^{1/2}} \right\}$$

where

$$q = 1 + (1 - \alpha) \frac{k_{\parallel}^2 \tilde{\omega}_{pe}}{k_{\perp}^2 \omega_{pi}^2},$$

and the growth rate, γ , associated with these two forms are respectively given by

$$\frac{\gamma}{\omega_{co}} = -[1.1/2] \frac{\omega_{pi} \omega_{0l}^2}{k_{\perp}^2 v_{thl}^2} \quad (\text{III-3})$$

THEORY OF PLASMA PRODUCTION AND HEATING BY ENERGETIC ELECTRONS

R. C. Harding, C. " Hartman and E. B. Hooper, Jr.

The energy stored in the energetic (relativistic electron plasma produced by microwave electron-cyclotron resonance heating (ECRH) in the superconducting Levitron (SCL) can ionize injected gas and heat the resulting plasma.^{90, 91} Analytic and computational studies have been used to study the process.

Two thresholds must be surpassed to achieve strong heating by energetic electrons in the presence of ionization losses: (1) energy content in hot electrons, and (2) the energy transfer rate to dense plasma.

Consider a simple cylinder as in Fig. 55 in which a hot-electron plasma has been formed by ECRH with energy content $w_h = n_{eh} T_{eh}$. The energy confinement time for w_h is several seconds so that for the time scale of interest (0.1 sec or so), significant changes in w_h can be attributed exclusively to introduction of gas and resultant dense plasma.

When gas is introduced, w_h transfers by collisions to the gas and dense plasma at a rate given by

$$\frac{d}{dt} (n_{eh} T_{eh}) = -n_{eh} T_{eh} n_d \langle \sigma v \rangle_{hd} - \frac{n_{eh} T_{eh}}{\tau_h} - e V_i \left. \frac{dn_0}{dt} \right|_h \quad (\text{III-4})$$

where $n_d \langle \sigma v \rangle_{hd}$ is the thermalization rate of hot electrons with dense electrons, τ_h^{-1} is loss of hot electrons which experimentally is of order $n_d \langle \sigma v \rangle_{hd}$, and $e V_i (dn_0/dt)|_h$ is the energy loss to ionize neutrals ($V_i \approx 40$ -50 V/ion pair) by hot electrons. If the dense plasma reaches full density while its temperature is small, $T_{ed} < 5 \text{ V} < 50 \text{ V}$ (negligible ionization by dense plasma), and its energy confinement time is long (see later) compared with the buildup time to full density, the dominant term in Eq. (III-4) is ionization, and

$$\frac{d}{dt} (n_{eh} T_{eh}) \approx -e V_i \left. \frac{dn_0}{dt} \right|_h$$

or

$$\delta(n_{eh} T_{eh}) \approx V_i n_d \quad (\text{III-5})$$

Thus, to produce a dense plasma n_d , hot electron energy content $n_{eh} T_{eh} > V_i n_d$ is required. For $n_{eh} = 2 \times 10^{10}$, $T_{eh} = 250 \text{ kV}$, $V_i = 50$, roughly $n_d < 10^{14}$ can be ionized. This is the energy threshold.

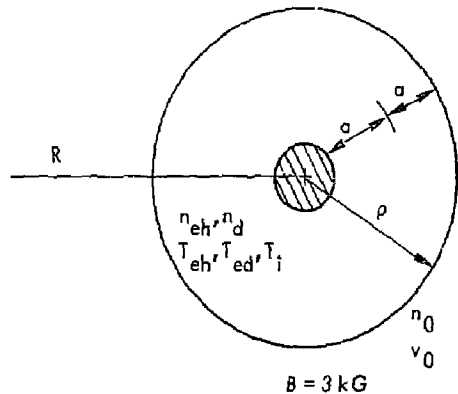


Fig. 55. Plasma configuration, $\rho \approx 15 \text{ cm}$, $a \approx 4 \text{ cm}$, $R = 40 \text{ cm}$.

To estimate the energy transfer threshold, consider the energy in dense electrons,

$$\frac{d}{dt} (en_d T_{ed}) = en_{eh} T_{eh} n_d \langle \sigma v \rangle_{nd} - e V_i \left. \frac{dn_0}{dt} \right|_d - \frac{en_d (T_e - T_i)}{\tau_{ei}} - \frac{en_d T_e}{\tau_{Ee}} \quad (III-6)$$

where $(dn_0/dt)|_d$ is ionization by the dense plasma and τ_{Ee} is the energy confinement time of the dense electrons. For heating $(d/dt)T_{ed} > 0$ and if dn_d/dt is small,

$$n_{eh} T_{eh} n_d \langle \sigma v \rangle_{nd} > V_i \left. \frac{dn_0}{dt} \right|_d + \frac{n_d (T_e - T_i)}{\tau_{ei}} + \frac{n_d T_e}{\tau_{Ee}} \quad (III-7)$$

where $V_i (dn_0/dt)|_d$ is ionization and excitation loss by dense electrons, $n_d (T_e - T_i)/\tau_{ei}$ is thermalization loss with the ions, and $n_d T_e/\tau_{Ee}$ is the energy loss rate across B. If burnout is not achieved, the first term of Eq. (III-7) is

$$V_i \left. \frac{dn_0}{dt} \right|_d \approx V_i n_d n_0 \langle \sigma v \rangle_{d0}$$

while for burnout,

$$V_i \left. \frac{dn_0}{dt} \right|_d \approx V_i \frac{n_0 v_0}{4} \times \frac{\text{surface}}{\text{volume}} \approx V_i \frac{n_0 v_0}{2a}$$

independent of n_d . In the second term of Eq. (III-7) the ion temperature is determined by collisional heating by dense electrons in competition with losses across B, by collisions with neutrals, or by charge-exchange, taking $T_i = 0$ as an overestimate of the heating power required. Finally, for the third term in Eq. (III-7) take $\tau_{Ee} = 100 \tau_{Bohm}$ or $\tau_{classical}/10$, whichever is least.

Taking $B = 3$ kG and assuming a singly ionized He plasma, Eq. (III-7) is approximately

$$1.8 \times 10^{19} \frac{n_{eh}}{T_{eh}} \geq \left[\begin{array}{l} 4 \times 10^{25} n_0 \langle \sigma v \rangle_{d0} \\ \text{(not burned out)} \\ 6.7 \times 10^{16} n_0 / n_d \\ \text{(burned out)} \end{array} \right] + 4.9 \times 10^{15} \frac{n_d}{T_{ed}^{1/2}} + \left[\begin{array}{l} 3.4 \times 10^{13} n_d T_{ed}^{1/2} \\ \text{(10 X classical)} \\ 2.6 \times 10^{14} \tau_{ed}^2 \\ \text{(100 X Bohm)} \end{array} \right] \quad (III-8)$$

where n 's are in 10^{12} cm^{-3} , T_{eh} is in keV, and T_{ed} is in eV. The quantity $\langle \sigma v \rangle_{d0}$ is a strong function of T_{ed} , i.e., $\langle \sigma v \rangle = 5.13 \times 10^{-20}$ (1 eV), 7.77×10^{-10} (10 eV), 3.95×10^{-9} (20 eV), 1.93×10^{-8} (100 eV). The separate terms of Eq. (III-8) R.H.S. are plotted versus T_{ed} in Fig. 56. Generally at high n_d and low T_{ed} ($\lesssim 5$ V), ion cooling or recombination dominates (neglected here); and at higher T_{ed} , either ionization losses or diffusion losses dominate, depending on n_0 .

The transition to burnout depends on T_{ed} and n_{ed} , and is given roughly by

$$\gamma/a \approx \frac{v_{i0}/a}{n_d \langle \sigma v \rangle_{d0}} \lesssim 1$$

Taking $v_{i0} = 5 \times 10^4$ cm/sec, $a = 4$ cm, $n_d = 10^{13}$, burnout occurs for $T_{ed} \gtrsim 10$ eV.

Next, fix T_{ed} at 10 eV, i.e., at the level of appreciable ionization rates, and use Eq. (III-8) to determine the heating threshold. This is shown in Fig. 57 for $T_{eh} = 100$ and 500 keV where if n_{ed}/n_0 exceeds the curves shown, heating proceeds. Above $n_d \approx 1.3 \times 10^{13}$, ion heating becomes dominant which only slows down the dense plasma heating rate.

Computational analysis was undertaken to provide a more precise description of the important processes involved in the plasma production and heating. Two types of calculations were made: (1) the number and energy of the energetic electrons were held fixed so that the equilibrium could be determined independent of the time evolution of the energy source, and (2) full-time dependent calculations were made. These will not be presented here.

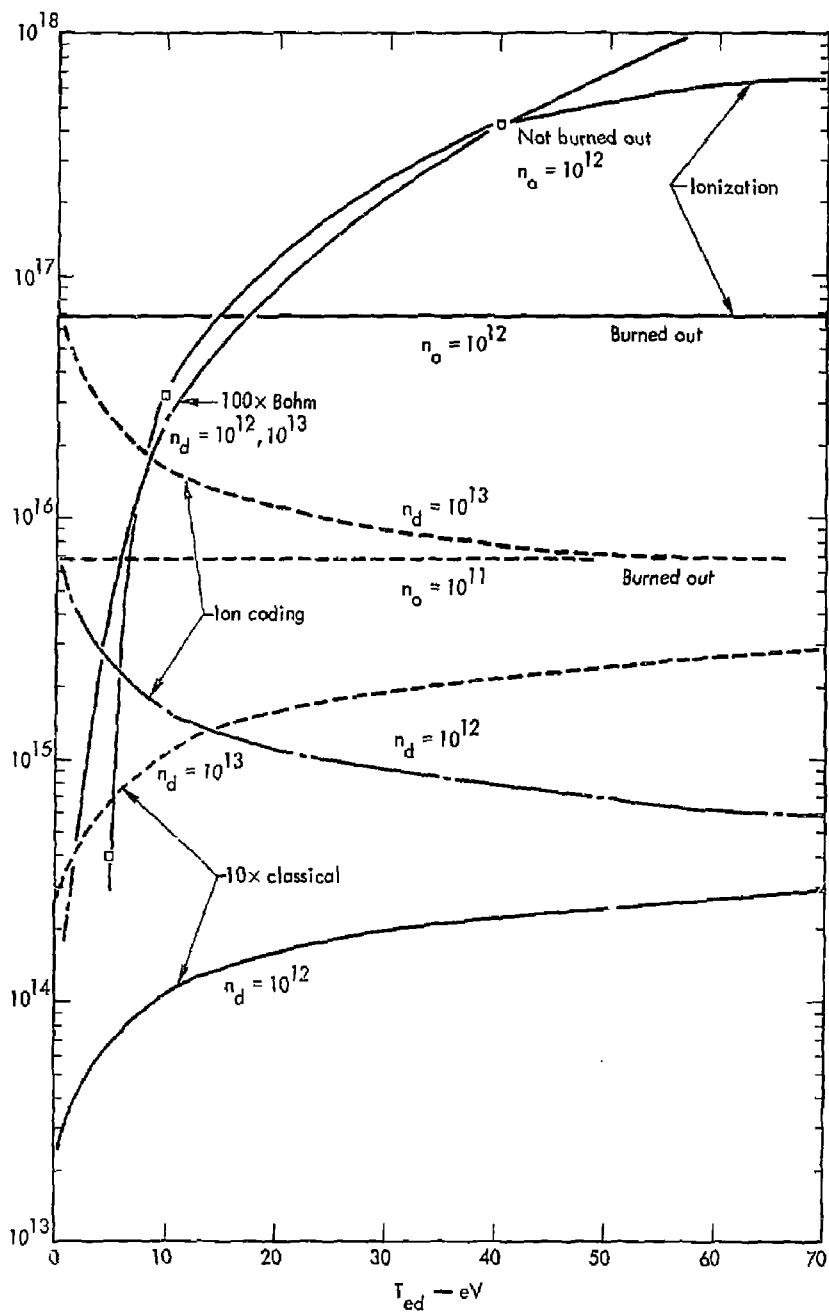


Fig. 56. The separate terms of Eq. (III-8) versus T_{ed} .

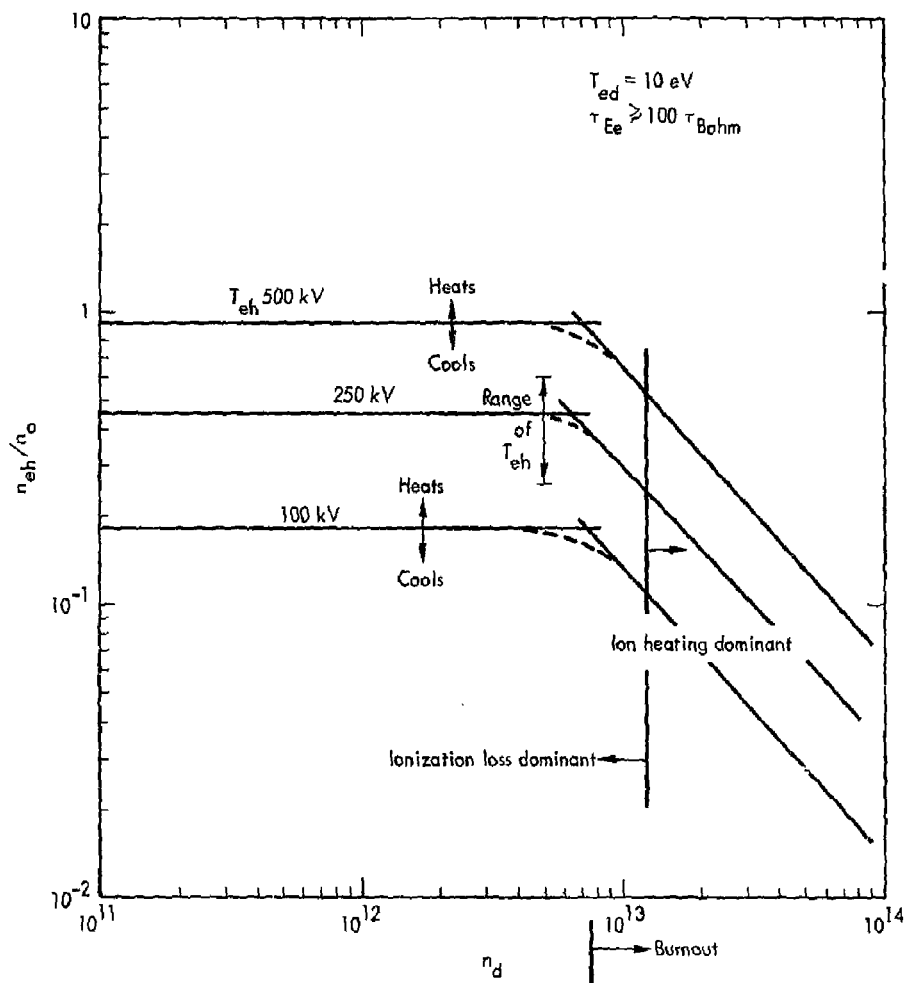


Fig. 57. Heating thresholds for fixed T_{ed} .

The computations were made on the CDC 6600 computer using the GEAR differential equation solver.⁹² Spatial dependences of the densities and temperatures were modeled so that total differential equations in time could be solved. As helium was used in most of the experiments, the code was written for it. Calculations in hydrogen were not made.

The density and temperature of five species were analyzed (see Table 6).

The neutral gas density, n_0 , was obtained from a model in which incident gas penetrated a mean-free-path, λ , determined by ionization and charge exchange.

The density was then averaged over a plasma thickness $L \approx 10$ cm to yield

$$n_0 = n_{02} (\lambda/L) (1 - e^{-\lambda/L}) \quad (III-9)$$

The rate of change of the density n_1 was obtained as the ionization of the gas minus ionization of He^+ and transport losses. The ionization source was reduced by a factor $f = 4(\lambda/L)^2 / (1 + 4(\lambda/L)^2)$, which modeled the fact that ionization near the plasma surface does not contribute significantly to the density.

Table 6. Analysis of five plasma species.

Species	Density	Temperature
He ⁰	n ₀ inside the plasma	fixed at 77° K
	n ₀₂ outside the plasma	fixed at 77° K
He ⁺	n ₁	T ₁
He ⁺⁺	n ₂	T ₂
Dense electrons	n _e	T _e
Energetic electrons	n _h	T _h

The rate of change of the density n_2 was obtained as the difference of ionization of He⁺ transport losses.

Recombination was assumed negligible in all cases. Transport was modeled as a combination of classical and Bohm, with arbitrary coefficients multiplying the two terms to permit exploring the plasma dependence on the transport character.

When hot electron energy decay was included, T_h was assumed constant and the density decay was given by

$$\frac{dn_h}{dt} = \frac{1}{T_h} \frac{d(n_h T_h)}{dt}$$

where $d(n_h T_h)/dt$ was given by the collisional losses which provided ionization. Relativistic cross sections⁹³ were used.

The electron density n_e was calculated from charge neutrality.

Temperature calculations were made in a similar manner. The ions were heated by electron collisions and cooled by transport and charge exchange. Collisions between the two species were included. Energy transport included classical, Bohm and neoclassical terms with arbitrary factors.

The rate of change of the electron temperature T_e included hot electron heating, cooling of the ions, and ionization losses. Transport was neglected.

Results for fixed n_h are presented in Figs. 58 and 59 for transport with and without Bohm-like transport. Two points should be emphasized:

1. The density is insensitive to the neutral density. This is because the electron temperature falls with neutral density so that the ionization rate falls and the transport increases. The balance is such that n_e is about constant for $n_0 \gtrsim 5 n_h$. The inclusion of a Bohm-like term has little effect on this result.

2. The temperatures depend critically on the transport, however. For classical scaling and low enough n_0 , heating dominates transport and no equilibrium occurs. This is a runaway effect, and occurs for $n_0 < n_h$. When Bohm-like scaling is included, the lifetime of plasma particles is limited and no true runaway occurs, although the temperatures continue to increase as n_0 is decreased.

The ion density is determined by the input of neutral gas balancing the losses. As the energetic electron density is increased, this feed becomes less effective because direct ionization of gas by the energetics becomes effective in burnout. For $n_h = 2.5 \times 10^{11} \text{ cm}^{-3}$, which was the goal of heating in the SCL, the equilibrium calculations indicated low ion densities. In this regime the time-dependent problem would have been needed for comparison with the SCL, and results would have depended critically on the initial plasma when the microwaves were terminated and gas was injected. As this regime was not reached in the experiment, it was not explored in detail.

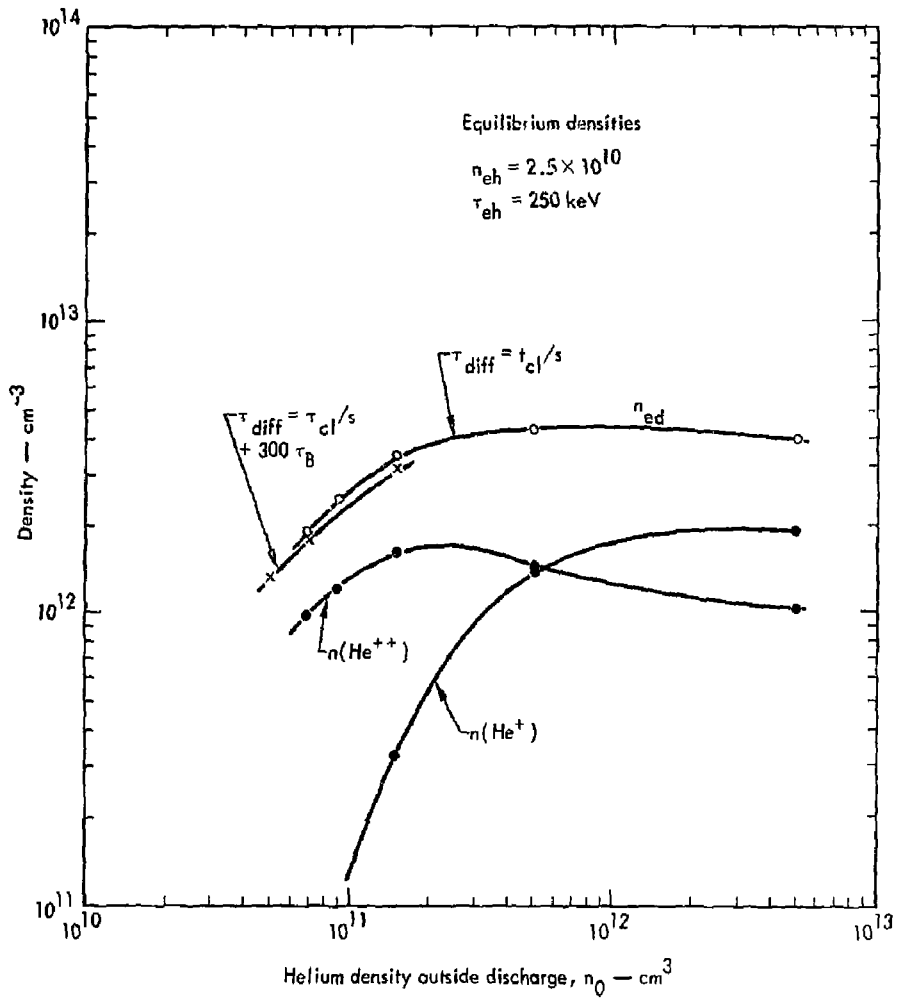


Fig. 58. Electron density n_e versus neutral He density n_0 for fixed n_h (with Bohm-like transport).

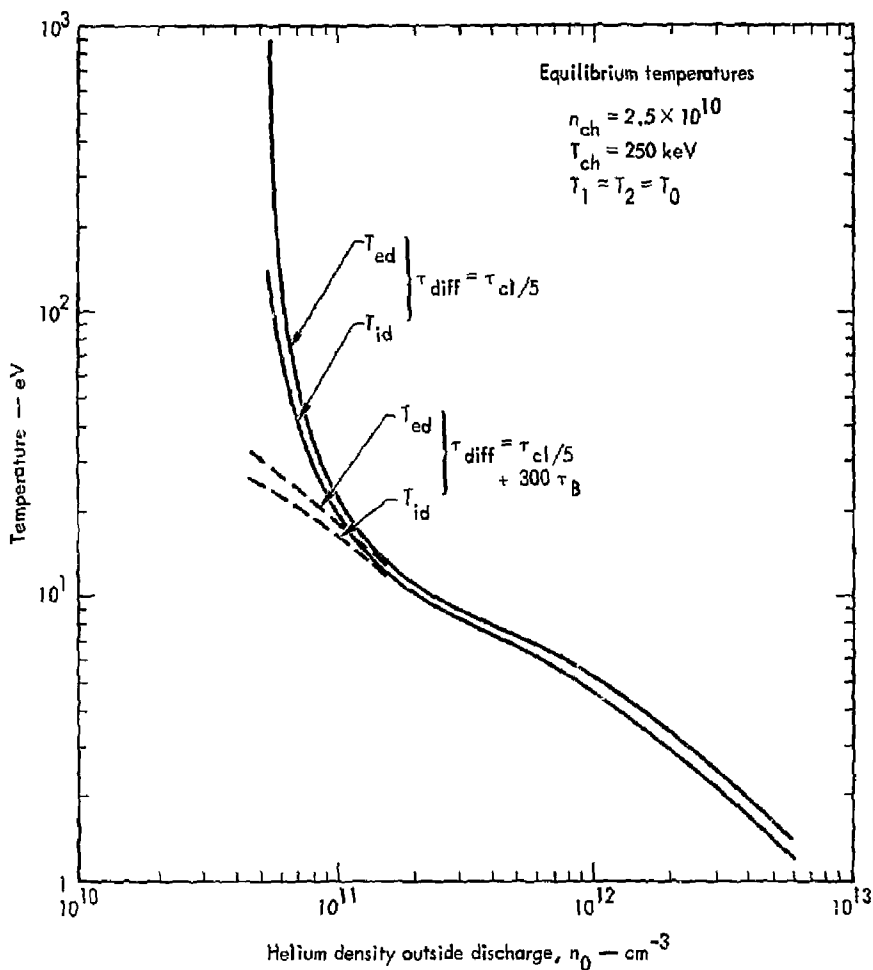


Fig. 59. Results for fixed n_k for transport without Bohm-like transport.

IV. Astron Program

INTRODUCTION

R. J. Briggs

The Astron program was terminated in February 1973. In this Annual Report, only a brief summary of the results obtained in the past year will be given since a final report which summarizes results from the past few years will be issued separately.

In the following section, highlights of the experimental results during the period July 1 to February 28, 1973 are given. Prominent among these is the achievement of E-layers with self-fields about half the strength required for field reversal by efficient trapping of a single pulse in a strong toroidal field. In the last section, a description of the design and operation of the beam delay line is presented. This unique device was not used extensively in experimental operations

because of the impending termination of the program, but it represents a substantial achievement in the transport and handling of intense relativistic beams, and for this reason it is described in some detail.

EXPERIMENTAL HIGHLIGHTS

R. J. Briggs, R. E. Hester, G. D. Porter, B. W. Stallard, J. Taska, C. W. Walker and P. B. Weiss

During the previous fiscal year, the Astron program evolved in a significant new direction, namely, buildup of the E-layer in a good vacuum. The primary motivation for this new approach was the prediction from simulation codes of a saturation in the current density of an electrically neutralized E-layer with multiple-pulse injection. This saturation, which arises from an axial heating of the existing layer by each new incoming pulse, should be offset by the axial compression that occurs when an unneutralized layer slowly neutralizes itself through ionization of the residual background gas. The option of E-layer buildup in vacuum was not open, however, until the Spring of 1971 when it was discovered that the precessional mode could be stabilized by a weak toroidal field. This discovery, the saturation phenomena described above, plus difficulties experienced in pulse injection through a plasma in the millitorr pressure experiments, culminated in the decision to proceed on a goal-oriented program aimed at short-term exploration of the vacuum stacking approach.

The primary goal of the Astron program during the past year, up to the point of termination in February 1973, was achievement of a reversed field E-layer by pulse stacking in vacuum. A journal article has been prepared that summarizes the results of these experiments,⁹⁴ and details will not be given here. The two aspects of E-layer formation in vacuum that were a major concern and were investigated in as much detail as possible during the time available were: (1) the choice of a resistor geometry that had sufficient axial focusing to hold the layer together during the trapping phase and sufficient energy loss to efficiently trap a single pulse, while still allowing enough radial room to prevent losses, and (2) the understanding, and elimination, of E-layer losses that occurred on millisecond time scales. Although considerable progress was made in these two areas, when the program was

terminated significant buildup of the E-layer in good vacuum had not been achieved. The short period of time available for these experimental studies did not allow a firm conclusion to be reached on the relative importance of the various phenomena that could be limiting the buildup and whether these limits were fundamental or not. However, it was clear that the vacuum stacking approach, which was initially appealing because of its relative simplicity, was not as simple a route to field reversal as was originally hoped.

During the last month of operation, an experimental test of trapping in a strong toroidal field ($B_\theta \approx B_z$) at relatively high plasma densities (high pressure) was carried out. The tank and resistor configuration at this time had been altered so that greatly increased radial room was available; this was known from single-particle orbit theory to be necessary for operation with a large B_θ field. The motivation for studying this regime was several-fold: (1) E-layer stability was experimentally known to be good when the ratio of beam density to plasma density was very small ($<10^{-2}$); (2) high gas pressures result in prompt electrical neutralization of the injected beam and excellent axial focusing which was suspected to be a problem with the vacuum trapping in the altered geometry; and (3) it was conjectured that a highly-conducting plasma in a strong B_θ field would result in a strong axial drag force on the incoming layer. The results achieved in the short period of time available were gratifying: Single-pulse trapping efficiencies of 50% were achieved, and short layers (~ 40 cm) with circulating currents up to 13 kA were formed that decayed stably. The peak diamagnetic strength achieved was about 75%, which corresponded to E-layer fields about half that needed for field reversal. The details of these measurements are given in a journal article to be published.⁹⁵

ASTRON BEAM DELAY LINE

N. C. Christofilos, R. E. Hester, C. A. Hurley, W. A. Sherwood, B. H. Smith, and R. L. Spoerlein

Introduction

The largest hardware development in the Astron Program during the past year was a beam transport system called a beam delay line. High-vacuum trapping experiments in Astron and supporting calculations indicated a need for increased injection current.

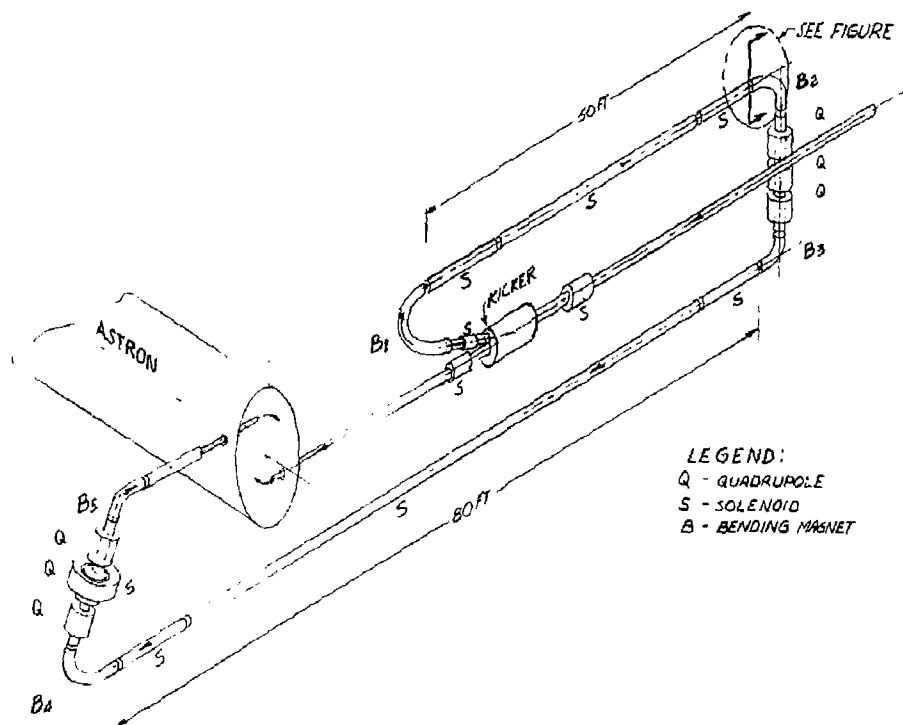


Fig. 60. Astron beam delay line.

Calculations demonstrated that increased injection current would increase the amount of charge trapped per pulse and would allow a trapping resistor design which gave greater radial room in Astron. Increased radial room appeared to be necessary for field reversal to occur. Experiments had shown that high-vacuum trapping was most effective with injected beam pulses of 150 nsec or less duration. The accelerator produces beam pulses of 300-nsec duration, therefore a decision was made to build a beam delay line into which the first 150 nsec of beam pulse could be diverted while the last half of the pulse fired straight ahead into the old transport system. The delay line was long enough to allow the two pulses to arrive at the Astron tank simultaneously. Figure 60 shows a diagram of the delay line.

The physics design of the beam transport was directed toward a system which would handle an energy spread of $\pm 1\%$ and would be convenient to operate. Where possible in the straight sections of the transport, long

solenoids were used to reduce the number of focusing elements required. The bending magnets are dispersive elements, therefore air-core quadrupoles are either superimposed over the bending magnets or located between bending magnets to refocus the beam. Art Paul of LBL ran the beam transport code to establish the physics design. Drs. Lloyd Smith and Al Warren of LBL were valuable consultants during the design phase.

Engineering and Construction

General Description

Useful space was limited to an aisle alongside and parallel to the accelerator. This constraint led to the odd shape of the delay line.

The beam is bent on a 7° angle into the delay line, with the following half kicked straight ahead. The first half travels 60 in. and then enters a 4-in.-i.d. pipe which is covered by a pulsed air-core, air-cooled, dipole magnet with a 24-in. bending radius and a bending

angle of 173° . Superimposed over this is a pulsed quadrupole magnet.

This is a novel bending magnet design. The magnet is powered by a pulsed 800-cps audio amplifier which can be synchronized with the accelerator pulse. The 4-in.-i.d. pipe in the bend is 40-mil-thick stainless steel. The wall thickness is thin enough to allow the a.c. fields from the bending magnet and quadrupole to penetrate the 4-in.-i.d. pipe and establish the required bending and focusing fields. A conducting shield surrounding the pulsed magnet protects the straight-through beam pipe from magnetic disturbance. This design was dictated by space problems and the need to isolate the two beam pipes magnetically.

The bend transports the beam upward and to the right on an angle 40° from horizontal so that when it emerges it is going straight in the opposite direction alongside the accelerator. The first straight section, approximately 50 ft. long, consists of a continuous solenoid surrounding an 8-in. vacuum pipe. It is constructed of 0.467-in. square hollow copper conductor wound on a 10-in.-diam aluminum tube which serves as a permanent support for the internal vacuum pipe. The 7-ft-long and 3-ft-long coils are wound in two layers of opposite helix pattern to eliminate net axial current flow. Each layer is a separate electric and hydraulic circuit element with coils powered in series and cooled in parallel. The end connections are made so the coils butt together to minimize dipoles. The end magnets of the straight section are powered individually as focus elements.

The second and third bends direct the beam forward again. Each coil bends the beam 90° on a 24-in. radius. Air-core, water-cooled, dipole and quadrupole coils surround an 8-in.-i.d. vacuum pipe. Between bends is a quadrupole triplet for x-y focusing.

Another straight continuous solenoid carries the beam into the Astron experimental area and into the last bends which are identical to the previous bends with the exception of an 8° rotation coil located over the center quadrupole to adjust for the helix bend prior to injection into Astron.

Steering coils are located at the entrance and exit to each bend. These are made of wire wound on a plane of 0.032-in.-thick G-10 epoxy laminate sheet. When wrapped around the continuous solenoid, the conductor wires are in a cosine distribution.

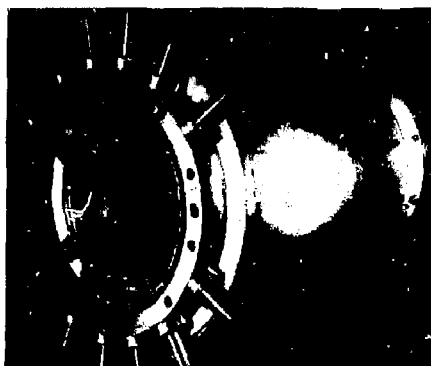


Fig. 61. Beam kicker.

Magnetic shielding is required around transport magnets which are close to the Astron main field coil. This is necessary to minimize disturbance of the beam by the Astron external field.

Bending Magnets

These magnets (Fig. 61) are constructed by placing 0.250-in.-square hollow conductors around the cross section of a torus in a modified cosine distribution similar to the magnet construction on the high-intensity storage ring.⁹⁶ Each conductor carries the same magnitude of current. The cosine distribution is determined by subdividing the area under the cosine θ curve into a number of equal area segments with a conductor then being placed at the center of each segment. The curvature effect of the torus requires the position of the conductors to be shifted from the cosine distribution to obtain a uniform field. Forty conductors are held in position by Bakelite rings which are glued to the toroidal vacuum tube. Four parallel water circuits are required for cooling.

The quadrupole magnets are constructed the same way with a cosine 2θ coil distribution. These are superimposed over the dipole magnets.

Vacuum System and Supports

Where the beam transport is straight, each section of vacuum pipe and magnet are a subassembly with the vacuum pipe supported within the magnet on rollers. Two wheeled dollies are clamped with bands to each end of the magnets. Tracks for the dollies

consist of a 6-in.-wide aluminum flange section on edge. Each section is installed at one station and rolled along the track to its final position.

Four 6-in. mercury diffusion pump units stationed along the line evacuate the 8-in. pipe to a pressure of 10^{-6} to 10^{-7} Torr. Each unit is connected to the vacuum pipe by a manifold having a pumping speed compatible with the system, yet leaving only a 2.5-in. gap between the transport magnets. Aluminum foil gaskets are used in the vacuum pipe to eliminate gasket damage due to radiation, thus minimizing maintenance.

Kicker Magnet Development for the Astron

150-nsec Delay Line

The kicker magnet used to divert the first half of the 300-nsec Astron beam pulse into the delay line is a novel design. The kicker magnet produces a magnetic field of about 50 G for a length of 34 in. and a width of 10 in. The risetime is less than 20 nsec. It normally operates at 42 G which produces a 7° deflection of the 6-MeV Astron beam which is the requirement of the delay line beam transport system.

A d.c. bias coil is installed around the kicker magnet so that the beam is delivered to the delay line until the kicker is excited and sends the beam down the straight-through beam line. This arrangement was chosen because the delay line is much more sensitive to minor time varying magnetic field fluctuations than is the straight-through beam line.

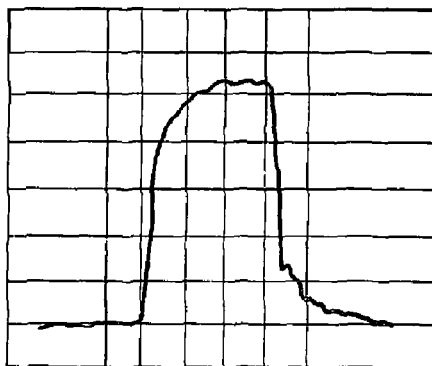
The kicker magnet is based upon a new principle of operation. It consists of 12 conductors arranged on a 10-in.-diam circle in such a way that an approximately $\cos\theta$ current density distribution occurs and a series of copper disks capacitively loads the conductors and reduces their characteristic impedance to 50 Ω . The $\cos\theta$ current distribution is the condition necessary to produce a uniform magnetic field; the 50- Ω characteristic impedance matches the magnet conductors to the input and output cables so that no reflections occur. Each conductor was fed from an RG 218 cable, thyatron switch and pulse line, and terminated with an RG 218 cable of sufficient length that any reflection would return at a time beyond the end of the pulse.

The 12 conductors of the kicker magnet were excited by 12 RG 218 cables. These were coupled to 12 cable-type pulse lines by six standard Astron switch

chassis. A photograph of the beam kicker is shown in Fig. 61.

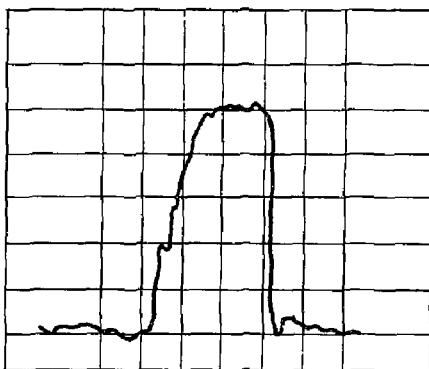
Operation of Delay Line

The initial operation of the delay line was done with low-current beams, 40 to 50 A. The low current was used while the beam diagnostics were checked out and a determination was made of the magnetic shielding required to isolate the beam line from the Astron field coils. In the final configuration, more than 90% of the beam injected into the delay line was transported to the Astron north inflector. The largest loss of beam current usually occurred in the first and last bends of the transport.



100 A/div \uparrow , 5 nsec/div \rightarrow

Fig. 62. Beam current monitor RBS29 output.



100 A/div \uparrow , 50 nsec/div \rightarrow

Fig. 63. Beam current monitor RBS19 output.

Figures 62 and 63 show the results of delay line operation. RBS 29 is the beam current monitor at the end of the straight-ahead beam line while RBS 19 is the beam monitor at the end of the delay line. The total injected current in this case is 1040 A. Normal injection currents for Astron range from 550 to 600 A.

It was originally anticipated that a 700-A beam could be injected into the delay line. However, the high level of rf instability in the accelerator when operating at the 700-A level produces too large an energy spread in the beam for it to be useful.

V. Neutral Beam Research and Development - Berkeley

(W.R. Baker, K.H. Berkner, W.S. Cooper, K.W. Ehlers, W.B. Kunkel, R.V. Pyle, and J.W. Stearns)

INTRODUCTION

The neutral-beam research and development effort at LBL has been concerned mainly with design, construction, and testing of ion sources of the general type described previously,^{2,3} but with improved performance. An important part of this program is the attempt to increase the physics understanding that is needed for the design of beams with more precisely controlled trajectories, e.g., converging beams.

ION SOURCES

The major construction activities are summarized in Table 7.

20 kV, 10 A (Equivalent) D⁰ Sources for the 2XII Experiment

These neutral beam sources are of the kind described in the previous annual report.²³ Two have been tested

and delivered to LLL and two to the Princeton PPL. Additional details are given in Ref. 97. The 10-A sources have been used as experimental devices for testing new ideas for these and other ion sources. The destruction of filaments due to occasional arcing essentially has been eliminated by sensing the beginning of a cathode spot and turning the arc off. The arc efficiency and radial density profile have been improved by changing the size and position of the annular anode. We expect to be able to decrease the divergence of the neutral beam and increase the gas efficiency by techniques mentioned below.

Low-Voltage, 10-sec BBII Source

This source has the following specifications: 1/2 A (equivalent) neutral hydrogen into BBII at 2 keV, 1 A at 3 keV, and 2 A at 5 keV, with a 10-sec pulse length. This source is designed to extract at 11 kV and decelerate the $p.25 \text{ A cm}^{-2}$ ion beam to the desired energy

Table 7. Major LBL neutral beam activities.

Expt.	Nominal max. voltage	Nominal pulse length	Gas	Target angular dimensions	Equiv. neutral current into plasma	Total extracted ion current	Total neutral equiv. current	Status
2XII	20 kV	30 ms	D ₂	$\pm 0.9^\circ \times \pm 1.8^\circ$	~10A	~16A	~18A	4 Built and tested
BBII	5 kV	10 sec	H ₂	$\pm 1.3^\circ \times \pm 1.3^\circ$	~ 2A	~ 5A	~ 6A	Partly built
2XII	20 kV	10 ms	D ₂	$\pm 0.9^\circ \times \pm 1.8^\circ$	~50A	~80A	~90A	Partly built

before neutralizing it. A slotted extractor will be used. The plasma source has been built and tested, extractor design tests are in progress, and power supplies and control circuits are nearly finished. As others have found before us, high-current, low-divergence, low-energy beams are difficult to obtain; our extractor tests to date have produced neutral beams that are low by about a factor of two at 5 kV. We hope to be able to operate this source without water-cooling the extractor electrodes; preliminary experiments with carbon electrodes are encouraging. An important part of the 10-sec plasma source development has been the demonstration that properly designed filaments can be operated with ac heater power without modulating the plasma density excessively.

50-A D⁰ Module

This module has the following specifications: 50-A (equivalent) neutral deuterium into 2XII at 20 keV with a pulse length of 10 msec, and a compact design to permit use of several adjacent modules for higher injected current. The design is similar to that of the 10-A D⁰ 2XII source, except that the beam is extracted from a 7 X 35 cm electrode array. Adjustments of the relative electrode positions will direct the beams from each of five 7 X 7 cm arrays toward the 2XII plasma. The construction of this neutral beam source and associated electronics is well along, and testing of the plasma source is about to start.

GENERAL DEVELOPMENT

New Ion Extractor Optimization Program

The program previously used for extractor design, although very useful, is not adequate for the present tasks. We have written a new program, WOLF, for calculating and optimizing ion extraction from realistic plasmas. The program treats symmetric or asymmetric two-dimensional extractors (slots), with no magnetic field. Ion flow with space charge is calculated by solving the equations of motion and Poisson's equation iteratively on a flexible triangular mesh attached to the boundaries. The emitting surface is assumed to be a flexible surface at the position of the plasma sheath. Ions are assumed to arrive at this surface with a distribution in directed velocities to simulate an ion wind; a finite ion temperature and the effects of electrons in the sheath will be included

later. The magnitude of the electric field E_0 on this surface must also be specified. The ion velocity distribution and E_0 must be assumed or derived from measurements of the plasma properties. The ion current density j_+ can be specified or treated as a variable. WOLF then varies the shape of the emitting surface (and j_+ , if desired) to obtain $E = E_0$ on this surface, in a least-squares sense; this is equivalent to specifying $j_+ = \text{constant}$ on the surface and determines the shape that the plasma sheath will assume in the vicinity of the extractor electrode. In addition, the program can vary the shape and potential of selected electrodes to minimize the beam divergence. This program is the first step toward a model containing enough physics of the plasma and of the extraction process to accurately predict the performance of a given extractor, and then to optimize the extractor design for a given task. WOLF was written by K. Halbach and S. B. Magyary in the Hilac group; it has successfully run test cases, and is now in the final stages of debugging.

Detailed measurements of plasma parameters in an operating ion source will be obtained to provide input data.

Diagnostics

Sputtering and discoloration of metallic plates struck at glancing incidence by the beam emerging from an extractor provides graphic, semi-quantitative evidence of beam trajectories from each of the 21 slots. The high optical quality of the individual beamlets is confirmed, and beamlet steering due to mechanical imperfections or misalignments is immediately apparent. Measurements have begun of gas collision cross sections of constituents of beam impurity. We hope that these will allow us to determine the levels of fast neutral impurity components in our beams.

Mechanical Tolerances and Beam Focusing

We have shown experimentally and computationally that a displacement of 0.001 in. in one of the extractor electrodes can change the angle at which the beam emerges by as much as 1°. This indicates the mechanical tolerances that must be held (in a variable temperature environment) as we progress to systems with less beam divergence, but also provides a way to focus the beam from an extended source. The 50-A source is designed to focus the beam in a plane perpendicular to the slots by adjusting the alignment of the slots of the

first two electrodes so as to make the individual beams from the five 7 X 7 cm slot arrays converge at 3.3 m from the source.

The beam divergence in the direction parallel to the long dimension of the slots is also affected, adversely or beneficially, by electrode shapes and imperfections. We are experimenting with curved electrodes to focus the beams in this direction.

As mentioned earlier, we have some evidence that it will be possible to use properly designed carbon or tungsten-coated carbon grids* in the 10-sec source without cooling, and still maintain the required tolerances.

Staging to Higher Beam Energy

We are attempting to raise the energy of a 10-A source to 40 kV by adding an additional electrode to give two 20-kV gaps plus a decel gap. This extractor has run satisfactorily with a total voltage of 20 kV, the limit of our present power supply.

Gas Efficiency

About 25% of the deuterium nuclei that go into the source as D_2 are accelerated. It is desirable to increase this efficiency as much as possible. One way to accomplish this is to add an impedance between the arc chamber and the neutralizer cell, thereby allowing the required pressure in the plasma source to be maintained with lower gas flow. We have raised the pumping impedance in a preliminary experiment by placing metal sheets several centimeters long (in the beam direction) between the beams emerging from the individual slots in the third electrode (in fact, this array of metal sheets can be the third electrode). The gas flow could be reduced about a factor of 2 in this case without appreciably reducing the neutral beam at the target. Use of this technique requires the precise control of beam trajectories mentioned earlier. Additional advantages of this technique will be beam collimation at the ion source, i.e., far from the hot

plasma region, and a decrease in the plasma density at the beginning of the neutralizer.

Electrical Equipment

A second high-level, neutral-beam-source test stand at LBL should be completed and fully operable by August. The filament and arc supplies were finished in February and have been in use for LLL BBII source research. The accel-decel and arc supplies are similar to those for the pulsed neutral-beam test stand now in use that was described in the FY 1972 CTR Annual Report. However, it will have the additional capability of pulse lengths up to 10 sec that is needed for the BBII source development.

The accel supply is designed to initially operate up to 20 kV and 10 A. It uses an Eimac 100-kW screen grid tube for a series regulator. The main power comes from an Alpha II Kenotron rectifier transformer reconnected from wye to delta secondary and equipped with a solid-state rectifier. Voltage control is by means of the induction voltage regulator (I.V.R.) of a Perkin rectifier unit and an electronic contactor. By the addition of three more Alpha II Kenotron-type transformers, it should be possible to increase the accel supply capability to 0-40 kV, 20 A.

The decel supply will provide up to 10 kV and 3 A continuously for a 10-A short pulse. It will be initially an adjustable fixed voltage system, but can easily be made fully programmable with the accel voltage regulator as a reference and then can be used for modulating the neutral beam energy if needed.

The arc supply is a 12-phase, 2000-A system similar to the one on the older test stand. It uses the I.V.R. of another of our Perkin rectifier units and an electronic contactor. The filament supply operates either a.c. or d.c. 0-15 V, 1500 A, and has I.V.R. control.

Pulsed power supplies for the 50-A, 20-kV, 10-msec neutral-beam source for the LLL 2XII facility have been designed and should be completed within the \$31,000 budget and ready for installation on one of the test stands by July 1. These supplies are in the form of compact modules with ratings as follows:

Accel supply: 0.25 kV at 85 A, 10 msec.

Decel supply: 0-5 kV at 15 A, 10 msec.

Arc supply: 0-100 V at 4000 A, 10 msec.

Fil supply: 0-15 V at 2200 A, continuous rating.

*G. W. Hamilton and J. E. Osher have used carbon grids coated with chemically-deposited tungsten in one of their MATS sources.⁹⁸

VI. High-Current Neutral Beam Development at LLL (J.W. Beal)

Jack W. Beal

The injection of very large currents of energetic, neutral beams is a method of producing and heating plasmas in certain controlled-fusion experiments at LLL. A critical requirement is therefore the development of high-current ion sources and compatible extraction and acceleration structures capable of producing such beams. To this end, a new program has been started at LLL to develop the next generation neutral beam source.

Our immediate effort will be directed toward the development of a usable deuterium beam of 200-A equivalent current at an energy of 20 keV. The beam pulse length for this operation will be from 2–10 msec.

Beam currents of this magnitude require a very large extractor area, even though extraction current densities of the order of 0.5 A/cm^2 are contemplated. Also, results of other research indicates that the extraction ion optics are very sensitive to the plasma density. Therefore, the ion source itself must be capable of producing the required density with sufficient uniformity over the entire extraction area. In addition, plasma density variations with time should be minimized. These requirements lead to a source design which avoids density fluctuations and noise.

We expect to draw heavily upon the recent experience of the LBL ion source development group. In particular, we will investigate the concept of a scaled-up version of the LBL electron-bombardment-type ion source with a multi-aperture extraction and acceleration system.

In an electron bombardment ion source, the arc discharge is produced between heated filaments (typically tungsten at $\sim 3000^\circ\text{K}$) and a surrounding anode. The electrons emitted from the filament follow trajectories which ionize the deuterium gas. The resulting plasma then fills the discharge chamber and diffuses through the extraction grid. To achieve the desired arc emission current, approximately 2000 cm^2 of filament surface are required. The arc discharge current required is approximately 20,000 A. Diagnostics will be available to observe the time dependence of the plasma as well as the ion emission density and uniformity over the emitting surface.

Simultaneously with the development of the discharge chamber, we will initiate a numerical and experimental program to optimize extractor design. We anticipate using a conventional accel-decel electrode system to extract and form the beam. Neutralization of the ion beam will be via a gas cell. Further diagnostics will be available to determine the properties of the extracted beam such as divergence, brightness, and neutralization efficiency.

VII. Plasma and Atomic Research – Berkeley

HIGH-FREQUENCY STARK EFFECT IN HYDROGEN AND HELIUM

William W. Hicks

Theory

Using methods previously discussed and applied to helium,⁹⁹ we have extended the theory of the high-frequency Stark effect to hydrogen. We have included the effect of a d.c. electric field, fine structure, and Doppler broadening on the line profiles. Computer codes have been generated which will calculate

the line profile for arbitrary frequency, rms-electric-field strength, d.c. electric field, and direction of observation. The computer codes for both hydrogen and helium have been integrated into a least-squares fitting program¹⁰⁰ which will produce a "best fit" solution for field frequency, rms electric field strength, and d.c. electric field, from a measured spectral line profile.

Experiment

In the experiment in which we apply a known high-frequency electric field to a weakly ionized hydrogen

plasma, we have measured the spectral line profiles H_{α} , H_{β} , H_{γ} and H_{δ} for the case $E_{rms} = 4$ kV/cm and frequency 1.17 cm^{-1} . The experiment has a d.c. electric field of strength 1 kV/cm perpendicular to the high-frequency electric field due to ambipolar diffusion to the walls of the small Geissler tube which houses the plasma. Using the least-squares fitting program discussed above to adjust the rms electric field strength and frequency for a best fit of the measured data yields results for the four spectral line profiles consistent to within 1% and which agree to within experimental error with an independent measurement of the field strength techniques.

MULTIPLE-BEAM SPECTROSCOPY

P. S. Rostler and B. D. Billard

A multiple-beam spectroscopic system has been constructed, tested and used to observe ion waves in a laboratory plasma. As has been explained elsewhere,¹⁰¹ this system was designed to provide a spatially localized nonperturbing measurement of the amplitude of one Fourier component of the fluctuations in the density of light sources within a plasma. Construction of the apparatus was completed during the last year. The system was tested with light from a small gas laser and found to perform as expected.

To further verify the spectroscopic theory, the apparatus was then used to observe ion waves launched through a helium plasma. The plasma, with $n_e \approx 10^{14} \text{ cm}^{-3}$ and $T_e \approx 3 \text{ eV}$, was produced in the existing beam-plasma machine by injecting a 4-kV, 30-mA electron beam into a chamber filled with 300 μ of helium. A magnetic field of 7 kG was present and a negatively biased Langmuir probe was used as a transmitter to launch ion waves along the field. As a control, the propagation of 1- μ sec pulses was studied by using a second probe as a receiver. Several plasma modes were seen, including one with a velocity near the expected ion sound speed $\sim 1 \text{ cm}/\mu\text{sec}$. The multiple-beam spectrometer, adjusted to observe a plasma wavelength of 0.39 mm, using light from the He-I 4471- \AA line, was then used to study sinusoidal oscillations (12 to 44 MHz) launched in the same manner with a probe. A maximum of signal amplitude was seen at 29.5 MHz. This corresponds to a phase velocity of 1.15 cm/ μ sec, in agreement with

the probe results. The magnitudes $\delta N_i/N_i \approx 0.001$ of the two signals were also of the same order. In the signal spectra taken from the multiple-beam spectrometer, one could see cancellation of noise due to differencing of the two photomultiplier outputs,¹⁰¹ and some effect of rapid modulation of the total plasma luminosity was also evident. A more complete discussion of these findings is in preparation.¹⁰²

Theoretical analyses of several aspects of the problem have also been completed. These include a discussion of photon noise, a mathematical description of multiple-beam spectroscopic systems, and an extension of the theory from two-beam correlations to higher order correlation functions.

We have begun to design and construct a different type of optical system which may be made achromatic. The present system is limited by coherence requirements to plasmas which emit sharp spectral lines to get the necessary intensity of light within a bandwidth of a few angstroms. The theory indicates that if the source observed emit light at different wavelengths, that light still contains the information on the source distribution if a system can be made to detect it. Possible advantages of such a system would be greater available light intensity and the relaxation of the restriction to line emission.

In the new design, the birefringent element of the present system is replaced by a triangular interferometer using polarization by reflection. We have made tests on a simple prototype interferometer without polarization. The tests used white light instead of the gas laser, and it was found that the interferometer could be adjusted to have a bandwidth of about 2000 \AA , from 5000 \AA to the red end of the spectrum at about 7000 \AA . In this range, the fringe spacing was constant (independent of wavelength) at about 2%. A corresponding resolution of the Fourier component of the plasma light source density fluctuations should be possible because the wavelength that such a system would observe corresponds to the fringe spacing.

A constricted discharge is being built which will provide another plasma to which spectroscopic techniques of this group may be applied. A turbulent plasma of about 1- to 100-eV electron temperature with densities of the order of 10^{11} cm^{-3} is anticipated.

We plan to continue this work through the next year.

BEAM-PLASMA INTERACTION

R. A. Hess

We have used the combined Zeeman and high-frequency Stark effects to make spatially and temporally resolved measurements of the electric field present in the beam-plasma described in the last Annual Report. The electron beam was chopped with a frequency of 500 kHz, 1.5 μ sec on and 0.5 μ sec off with a risetime of 10 nsec and a fall time of 100 nsec. The light was spectrally resolved with a Fabry-Perot interferometer and a grating monochromator in series and then detected with a photomultiplier. The signal from the photomultiplier was amplified, fed into a time-to-amplitude converter, then into a pulse-height analyzer. By accumulating this way for several minutes, we were able to measure the time-dependence of a given spectral component with a time resolution of 25 nsec (one channel of the pulse-height analyzer). Spatial resolution was accomplished by aiming the entire optical system at various regions of the plasma and by using Abel inversion when necessary to unfold the radial dependence of the light intensity.

The spectroscopic measurements can be summarized as follows: The helium plasma had a maximum density of $N_e \approx 5 \times 10^{13} \text{ cm}^{-3}$, an electron temperature of $T_e \approx 5 \text{ eV}$, and an ion temperature of $T_i \leq 0.15 \text{ eV}$. The electric field reached a maximum value of about 2 kV/cm near the edge of the beam, was less in the center of the beam, and was very small outside the beam. It increased roughly linearly along the beam and reached a peak 2 to 4 cm from where the beam entered the chamber. Two different directions for the electric field were observed for nearly the same beam and plasma parameters. In one case, the electric field was polarized randomly in direction and in the other case it was polarized perpendicular to the magnetic field and was random in azimuthal angle. The electric field grew so rapidly after the beam was turned on that the linear growth could not be observed; the instability grew from noise level to near saturation in less than 25 nsec, and then increased slowly after that. We can put an upper limit of about 3 nsec on the e-folding time. The frequency of the electric field was 74 GHz

(either the electron plasma frequency or the upper hybrid frequency, within the errors of the measurement), and had a relative bandwidth of $\leq 14\%$.

The instability after saturation appears to be a surface wave, possibly of the type discussed by Self;¹⁰³ it is not the simple electrostatic instability. Because of the finite geometry of the system and lack of knowledge of the wavelength of the instability, careful comparison of the measurements with theoretical predictions is not possible.

BERKELEY LASER PLASMA EXPERIMENT

T. R. Jarboe and A. F. Lietzke

Introduction

The fundamental purpose of the Berkeley Laser Plasma Experiment is to reliably produce an isolated plasma by laser irradiation of an isolated solid pellet. The facilities will be used for graduate student studies of these plasmas and their interaction with applied magnetic fields.

We have succeeded in consistently producing plasma from a 50- μ m-diam deuterium pellet with a Q-switched ruby laser beam ($<1 \text{ J}$) focused to a minimum diameter of 100 μ m. Effort this year has centered upon improving machine reliability, improving plasma symmetry, and application of simple diagnostics to assess various plasma parameters of interest.

Apparatus

The laser, pellet maker, detecting system, vacuum system, and magnetic field have been described in previous Annual Reports^{23, 41, 104} and remain essentially unchanged except for several important modifications: (1) The pellet beam (0–20/sec, random) is guided in its nearly vertical fall.¹⁰⁵ A final 10-cm free fall is allowed before it reaches the laser focal volume. The pellet beam FWHM is 3 mm, measured at the laser focal position. (2) The horizontal Q-switched laser beam ($<1 \text{ mrad}$ FWHM) is focused by a 10-cm lens. (3) The detection system has been changed for increased reliability. It consists of a lens focusing 90° scattered light from a focused vertical-pellet-illumination beam onto a photomultiplier tube positioned behind a three-slit mask. A logic system analyzes the shape, height, and timing of

three pulses corresponding to a falling pellet and automatically fires the laser when appropriate.

A subnanosecond risetime laser pulse has been achieved by integral mounting of a low-impedance, laser-triggered stripline to a Pockels cell situated between the laser oscillator cavity and the amplifiers.

Diagnostics

Up to six ion-collection biased probes have been used simultaneously for measurements of time of flight, charge symmetry, and current flux density. Total charge collection can be accomplished along the field direction when $B \neq 0$. Also, a magnetic loop has been used to observe the plasma interact with the B field.

Results

With a small focus ($\leq 100 \mu\text{m}$ diam), a significant fraction (80-90%) of the incident laser power flux density is absorbed and/or scattered for 10-15 nsec during the low-intensity portion of a normal Q-switch pulse (50 nsec FWHM, 0.5 J). Although an energetic plasma streams out from the focus ($KE \sim \text{few } 100 \text{ eV}$), changes in the pellet position of the order of one pellet radius make repeatedly asymmetric probe signals: "Back" toward the laser always gets a fast, large ion collection signal relative to all other probes. "Up," "down," "North" and "South" total charge collection is also asymmetric under the small focus condition. (The laser beam propagates from West to East.) Defocusing to 300- μm -diam achieves greater symmetry at the expense of plasma energetics. The probe signal is not consistent with predictions of simple theory. This may be due to the recombination following the rapid electron cooling in the expansion. Investigation of this is continuing.

For uniform $B \neq 0$, ion collection to probes perpendicular to B is markedly reduced and characterized by unpredictable bursts at times much later than the free expansion time. Asymmetry is also unpredictable. Increasing field from 1 to 5 kG causes (1) reduction in perpendicular probe collection and (2) increased axial charge collection. Bouncing of the plasma against the confining field can be seen. More refined studies are continuing.

Further Investigations

Investigations in the immediate future include more careful correlation of bounce frequency of the plasma to total charge so that one can rely on a large magnetic probe to determine plasma quantity. A plasma camera is expected to give details on azimuthal symmetry and radial size. Line recombination is expected to furnish information on the extent that the B-field reduces recombination; β determination will also be made. Lastly, the interaction of the streaming plasma with various magnetic obstacles at various distances will be investigated.

THEORETICAL STUDIES-GENERAL

Parallel Cascade for Beat Heating

B. I. Cohen and A. N. Kaufman

The amount of plasma heating due to resonant excitation of plasma oscillations by the heating of two parallel lasers, with subsequent cascade, was studied both analytically and numerically. The intensities required for reasonable efficiency far exceed the theoretical threshold for backscattering instability, in the case of steady-state. The possible usefulness of pulsing will be investigated next.

Space-Time Analysis of Nonlinear Interaction of Opposed Electromagnetic Waves

B. I. Cohen

Two intense electromagnetic waves interact strongly where their difference frequency approximately equals the local plasma frequency, resulting in an irreversible transfer of energy from the higher frequency wave to both the lower frequency wave and a Langmuir wave. In the case of a uniform plasma, the interaction of two opposed step-function pulses leads to convective growth which is most pronounced at the leading edge of the lower frequency wave. For a linear density profile, pulse-shape modification is found to occur only over a small spatial domain around the location of resonance.

VIII. CTR Technology

REACTOR STUDIES

R. W. Werner, G. A. Carlson, J. D. Lee,
M. A. Peterson, J. Hovingh, R. W. Moir

200-MWe Reactor System Design Study

A detailed design study of a low-power, 200-MWe, mirror machine reactor with direct conversion has been completed.¹⁰⁶ This first report of a series was principally concerned with the development of a consistent set of physics and engineering parameters, and presents detailed results of calculations for system elements and shows their interaction. Areas investigated include:

1. System power levels and energy balance
2. Characteristics of the plasma
3. Containment magnet
4. Sizing the expander
5. Scattering and charged particle leakage
6. Magnetic design of the direct converter
7. Blanket neutronics
8. Blanket thermal-hydraulic design
9. Tritium recovery
10. Neutron streaming and shielding
11. Expander-collector structural design
12. Sizing the collectors
13. Collector cooling and heat transfer
14. The effect of collector pressure on performance and cost
15. Effects of helium and hydrogen on collector elements

Reactor Component Studies

Liquid Metal Loop Experiment

Construction of the liquid lithium loop was completed in late February 1973. We conducted experiments between March and May to measure the pressure drop of lithium flowing in conducting wall pipe through transverse magnetic field. Flow rates ranged from 1 to 5 gpm and magnetic field strengths from 0 to 10 kG. The pressure drop increased linearly with flow rate and with the square of the magnetic field, thus confirming the form of the theoretical relationship for conducting fluid flow in conducting

wall pipe in a transverse magnetic field. The measured pressure drop was always somewhat less than predicted, probably because of contact resistance between the liquid and wall. (Contact resistance was not included in the theoretical analysis reported.¹⁰⁷) A comprehensive report on experimental/theoretical MHD flow of liquid lithium as been written.¹⁰⁸

Small-Angle Scattering and Selective Leakage

We have completed a study of the physics of Coulomb collisions and mirror machine confinement as it affects the achievable efficiency of the selective leakage of charged particles. The purpose of selected leakage in mirror machines (charged-particle leakage at only one mirror or leakage at a restricted area of one mirror) is to reduce the size and cost of direct conversion equipment. Selective leakage at a restricted area of one mirror can be accomplished by providing a region in one mirror which has a local minimum in field strength. If the local minimum region intersects all plasma drift surfaces, the precession of particles about the mirror machine axis ensures that all particles will periodically sample the local minimum. The dominance of small-angle scattering will cause preferential leakage at the location of the local minimum. The achievable efficiency of selective leakage is limited by single large-angle scatters into the strong mirror region loss cone and by cumulative small-angle scatters into the strong mirror region loss cone between consecutive samplings of the local minimum. Efficiency in a typical example case is 90%. A comprehensive report has been published.¹⁰⁹

Blanket Designs for Mirror Machines

We studied multi-tubular, lithium-cooled blanket configurations to develop at least one conceptual design satisfying the constraints imposed collectively by neutronics, MHD compatibility, materials problems, field geometrical configuration, and thermal-heat transfer. Recently completed studies of MHD effects on fluid flow¹¹⁰, and continuing neutronic studies which consider finite blanket voids and nonspherical blanket geometry were utilized to make evaluation of blanket performance easier. From this study, two complementary blanket

design concepts emerged. In the first, a relatively straightforward design approach was taken accepting substantial (tolerable) MHD pressure drops in return for design simplicity. In the second blanket design, the relative simplicity of the first design was sacrificed to minimize MHD pressure drops. The two blanket configurations developed demonstrated not only the feasibility of multitubular, lithium-cooled blankets, but also exposed some of the design trade-offs that were encountered.

Electrical Losses in Collectors

The cooling of direct-converter collector elements operating at very high potentials (200-200 kV) presents the difficult problem of transferring thermal energy out of a high-voltage system while preserving the necessary system electrical isolation. Convective cooling of collector elements has often been dismissed in favor of radiative cooling because of the possibility of excessive electrical leakage through the coolant. To determine if coolant electrical leakage was a serious problem, an analysis of a gas-cooled collector element of a direct converter was made. It was determined that for a given set of heat-transfer parameters, there was a maximum allowable coolant conductivity (10^{-4} V/m for a typical direct-converter element). The conductivity of high-pressure (~ 40 atm) helium coolant with typical trace impurities was calculated assuming only equilibrium thermal ionization. The value obtained was low enough to indicate that collector coolant electrical leakage would not be a serious problem.¹¹¹

Vacuum Pumping the Collector Region

The efficiency of a direct conversion system is in part dependent on the ion beam losses caused by charge-exchange and ionization with gases in the collector region. These ion beam losses decrease with a decrease in the collector region pressure, but the power required to operate a vacuum system increases with a decrease in the collector region pressure. Estimates of the pumping power requirements as a function of the ion beam parameters and the collector geometry were made. For a given beam power and collector pressure, there was an optimum collector size which minimized the collector and vacuum system capital costs.¹¹² Also, an estimate of the collector pressure required for maximum

reactor system efficiency was made for a given collector geometry and beam power.¹¹³

Recovery of Residual Ion Energy in Collectors

We investigated the recovery of the kinetic energy of the ions impacting the collectors of a direct converter. The energy of these ions would be transferred from the collectors by thermal radiation to a receptor cooled by a working fluid at a thermodynamically significant temperature. Collector temperatures, thermionic emission losses from the collector grid wires, and heat shield requirements were investigated as a function of the ion beam parameters and the direct converter dimensions. The removal of the kinetic energy of the ions from the collectors of a direct converter by thermal radiation is an acceptable alternative to convective-cooling of the collector elements.

Injector System Study

The efficiency of a mirror reactor system is strongly dependent on the injection system efficiency. An "in principle" injector model was analyzed using neutral beam injection into a plasma, and the injection system efficiency was investigated based on cited predictions of injector component performances for various ion types over a representative range of injection beam energies from 10 keV to 1 MeV. Based on the model chosen, deuterium or tritium atoms between 100 and 1000 keV can be injected into the reactor with an efficiency of 80 to 90% using negative ions. Without direct conversions of the unneutralized portion, injector ion beam efficiency will drop to 65 to 85%. For energies around 100 keV, D^+ ions can be used to obtain a system efficiency of about 75%, which is higher than can be obtained with D_2^+ or D_3^+ ions. The same model predicts the injection of 3He atoms to be 80% efficient below 200 keV using $^3He^+$ ions, and less than 70% efficient between 200 and 700 keV using $^3He^-$ ions.¹¹⁴

Fusion - Fission Hybrid Reactors

We investigated the power balance break-even, $n\tau$ for a closed (toroidal) fusion-fission reactor system as a function of the energy produced in the reactor blanket. For an increase in the energy produced in the blanket from 18.9 to 400 MeV per fusion at an

ion temperature of 20 keV, $n\tau$ decreases by a factor of 14.9 to 2×10^{12} particle-sec/cm³.¹¹⁵ We also investigated the power balance break-even point, $n\tau$, for an open (mirror) hybrid fusion-fission reactor system as a function of the energy produced in the reactor blanket. For an open system without direct conversion, an increase of the energy produced in the blanket from 18.9 to 400 MeV per fusion at an ion temperature of 300 keV the $n\tau$ decreases by a factor of 18.2 to 1.3×10^{13} particle-sec/cm³.¹¹⁶ On the basis of $n\tau$ criteria, a fission blanket appears to be of a greater benefit to an open hybrid system than to a closed system.

Materials

P. Mohr, C. Logan

Radiation Damage In 304 Stainless Steel Using 5-MeV Ni⁺⁺ ions

Stainless steel (Type 304) micro-tensile specimens bombarded with 5-MeV Ni⁺⁺ ions, to simulate neutron irradiation under stress and at elevated temperature, were examined by transmission electron microscopy (TEM) for evidence of the role of applied stress in determining the nature of induced damage. Apparently, random arrays of voids were induced by bombardment (~ 50 -180 DPA) in essentially all specimens examined. Void size and densities induced in unstressed control specimens were typically 100 Å and 1.5 - $2.0 \cdot 10^{16}$ /cm³ respectively. Specimens bombarded under stress (~ 5 ksi at 6000C) showed a much lower void density ($\sim 10^{15}$ /cm³), but in addition heavy sawtooth networks of dislocation lines, apparently pinned at the voids (pitch ~ 1000 Å), oriented approximately normal to the direction of applied stress (micrographs available).

Unfortunately, a high fraction of both record and control specimens was damaged or destroyed in thinning for TEM. Consequently, it has not been possible to correlate the observed effects of applied stress with the temperature and fluence variables exercised in the experiment. This (heavy ion simulation) program has been suspended (as a Mechanical Engineering Dept. research activity) in favor of the light ion (proton) simulation program proposed by Logan.¹¹⁷ The latter program has the advantage of utilizing accelerator facilities available at LLL and

yields specimens which are more tolerant to preparation for metallography.

Proton Simulation of 14-MeV Neutron Effects

A previously reported analysis had indicated that 16-MeV protons should create primary recoils with an energy distribution similar to that induced by 14-MeV neutrons. Low-fluence irradiations of pure copper have been performed utilizing 14-MeV neutrons [from the Insulated Core Transformer (ICT)], 16-MeV protons (from the cyclotroff), and a moderated fission neutron spectrum [from the Livermore Pool-Type Reactor (LPTR)]. Samples were examined with a transmission electron microscope. The character of the clusters produced by the protons is strikingly similar to that produced by the 14-MeV neutrons. There are distinctive features in both samples which are not found in the sample irradiated with fission neutrons. These are apparently associated with high-energy recoils. The higher energy irradiations also produced higher cluster density at all observable diameters, with the difference increasing to over an order of magnitude above 75 Å.

CTR TRITIUM TECHNOLOGY

R. Hickman

Examination of Tritium Problems

We examined several aspects of the overall tritium problem in fusion power reactors from slightly different points of view than previous authors. Most of these studies have been summarized in two reports.^{118, 119}

A detailed listing of the subjects treated in these reports seems inappropriate, but they are generally concerned with permeation of tritium in and through solids and liquids, isotopic separation, inventory estimates, and recovery schemes. The major conclusion drawn was that tritium-handling will be a difficult problem in a power plant. A long-term research and development program will be required to find materials and techniques for handling and containment which will satisfy the demanding requirements of radiation safety that are likely to be imposed.

In the latter of these two reports, we suggested that the solubility of tritium in certain molten

lithium alloys would be substantially lower than for pure lithium. Neutronic calculations indicated acceptable breeding ratios for several of these materials. Therefore, we have started an experimental program to determine some of the important physical and chemical properties of these alloys. The first system to be studied is lithium-lead. We have built equipment to prepare it and to measure its liquid density as a function of temperature (up to 1000°C) and composition. More precise knowledge of its density is needed to verify assumptions made for the neutronic calculations. Although these measurements seem fairly simple, they are complicated by the chemical reactivity and volatility of the alloys at high temperature. Hydrogen solubility is an obvious follow-on experiment, followed by corrosion behavior with potential blanket structural materials.

Another problem area we briefly studied was the possible chemical interactions of graphite in the blanket with tritium. Graphite would function as a neutron moderator and reflector. Assuming the graphite is metal-clad and that tritium could permeate through the cladding, it was possible to show that the graphite could act as a sink for tritium in an amount on the order of a kilogram. This conclusion was reached after we considered the possible reactions between tritium and reactor-grade graphite. We predict that no significant amount of hydrocarbons will form between tritium and pure graphite. Some tritium will, however, be adsorbed on both external and internal surfaces (depending on porosity), even at low tritium partial pressures and operating temperatures. More important is the role played by impurities. Reactor-grade graphite contains carbides of metals which, upon exposure to moist air, form hydroxides and then carbonates. Upon heating, the carbonates decompose with evolution of carbon dioxide. Some carbon dioxide is also released upon desorption of chemisorbed oxygen. If the carbon dioxide is present at pressures above 10^{-3} Torr and the tritium is present above 10^{-6} Torr, all the tritium can react. This prediction is based on a comparison of the relative free energy of the various chemical species which could be present and the appropriate chemical equilibrium constants under these conditions. Very thorough outgassing of the graphite

after it is clad should take care of most of this hold-up problem.

Tritium technology is being used to supply helium-doped niobium specimens for neutron radiation studies. This involves reacting niobium with tritium at high temperature, allowing the tritium to radioactively decay, and then stripping the tritium from the niobium leaving the helium in place. This procedure has come to be known as the "tritium trick." It is used in lieu of doping the niobium with something having a high n, α cross section and exposing in a reactor or implanting with energetic nuclei. The tritium trick is believed to be less disruptive to the material under study and to be experimentally less costly. Most of our effort was expended developing a technique for decontaminating the specimens after doping. Conventional vacuum outgassing at elevated temperature was unsuccessful. Recently developed is chemical gettering in which the specimens and an equal amount of titanium are submerged under molten lithium and equilibrated. After this treatment, specimens have typically had residual tritium activities of only a few microcuries. The success of this process appears to result from surface cleaning and elimination of chemical recombination of the tritium atoms to form molecules at the niobium surface.

Insulator/Lithium Compatibility Problem

It is desirable to minimize the MHD pumping loss in a fusion power reactor by electrically insulating the flowing lithium from the pipe. We have therefore started an experimental program to determine the compatibility between various ceramics, lithium, and the refractory metals. A suitable insulator must be stable in contact with flowing lithium and various refractory metals for over a year at temperatures of nearly 1200K. Additional criteria such as fabricability and susceptibility to radiation damage are not yet being considered.

The compatibility between four different ceramic materials, lithium, and four refractory metals is being studied in a series of capsule compatibility experiments. The ceramic materials chosen were the nitrides of aluminum and boron, and the oxides of calcium and yttrium. The choice of ceramics was

made primarily on the basis of greatest free-energy difference between the ceramic and the corresponding lithium compound. The refractory metals chosen were tungsten, molybdenum, columbium, and tantalum. The purpose of the experiments is not confined to studying the amount of attack of the ceramic, but also to try and determine what reactions occur so that the mechanism of attack can be understood.

The first series of tests was conducted on boron nitride at 12700K for 600 hr. They may be summarized by stating that the boron nitride was completely dissolved and the refractory metals converted to their respective borides. Tests are now underway on aluminum nitride, calcium oxide, yttrium oxide, and yttrium oxide doped with calcium and thorium oxide.

Hydrogen Diffusivity in Lithium

An experimental program has been started to determine the diffusivity of hydrogen in liquid lithium. Such information would be useful in calculating the rate of hydrogen removal when one of the steps is diffusion of hydrogen through stagnant lithium. An apparatus has been built and given preliminary tests. The apparatus is a modified Sievert's type in which the rate of absorption of hydrogen is measured by means of a sensitive mass flowmeter. The lithium is contained in a long thin molybdenum tube so that the boundary conditions for the unsteady-state diffusion process are well-defined. For comparison purposes, the diffusivity of hydrogen in sodium and of deuterium in lithium may also be determined.

MAGNET TECHNOLOGY

Magnets for Open-Ended Fusion Reactors*

We have studied many aspects affecting magnet design for open-ended fusion reactors.¹²⁰

Open-ended fusion reactors will require large, high-intensity magnetic fields with unique shapes, placing stringent demands on magnet materials and design. We have examined in detail a magnet which is based on the Yin-Yang coil configuration. Our study emphasizes the technological and physics requirements which must be satisfied in a mirror reactor. Analysis of the field strength and body forces within the conductor allowed the design of a realistic but complex support structure. Aspects

of neutral beams, finite length, stability, adiabaticity, density and power distribution are discussed. One example shows a magnet of 170 kG at the mirrors costing 164 million dollars (\$164M) and producing a 0.9 GW of nuclear power (not net electric) at 600 keV mean energy for a D-T plasma. At 210 keV for 0.9 GH the mirror magnetic field drops to 85 kG and the cost is \$45M. A simple mirror (non Minimum B) magnet with 170-kG mirror field producing 1 GW of nuclear power at 600 keV was estimated to cost \$17M.

Superconducting Magnet Development

C. D. Henning, R. L. Nelson, C. O. Ward

Development of aluminum-clad N_3Sn has continued for producing mirror fields greater than 100 kG. Earlier tests had confirmed the necessity for conservative cryogenic stability of such conductors in large magnet applications.¹²¹ As a result, the superconductors have been tested with extensive cooling channels between the magnet turns, and temperature differences have been minimized through the aluminum bonds and structural materials.

A typical test magnet is shown in Figure 64. For convenience, an open organic inter-turn spacer is used, although the eventual conductor would have the outer structural member of the conductor mechanically embossed to provide cooling between turns. Samples of embossed nickel have been produced and a contract to Battelle Memorial Institute has been written to produce long lengths of the material. The method is simple and inexpensive, and provides the necessary cold-working of the high-purity nickel for strength. Insulation between turns would be provided with a thin varnish coat or an oxide coating such as nickel black.

The test magnets are mounted as in Fig. 65 for installation into the 14-in. bore test facility constructed last year (Fig. 66). Since the axis of the magnets are perpendicular, radial fields above 60 kG can be produced on the N_3Sn tape. This is by far the most severe method of testing, producing large flux jumps when the diamagnetic currents exceed the critical current. Results of a typical test are given in Fig. 67. On the upper line, the external field is fixed while the transport current is raised. Quenching occurs when

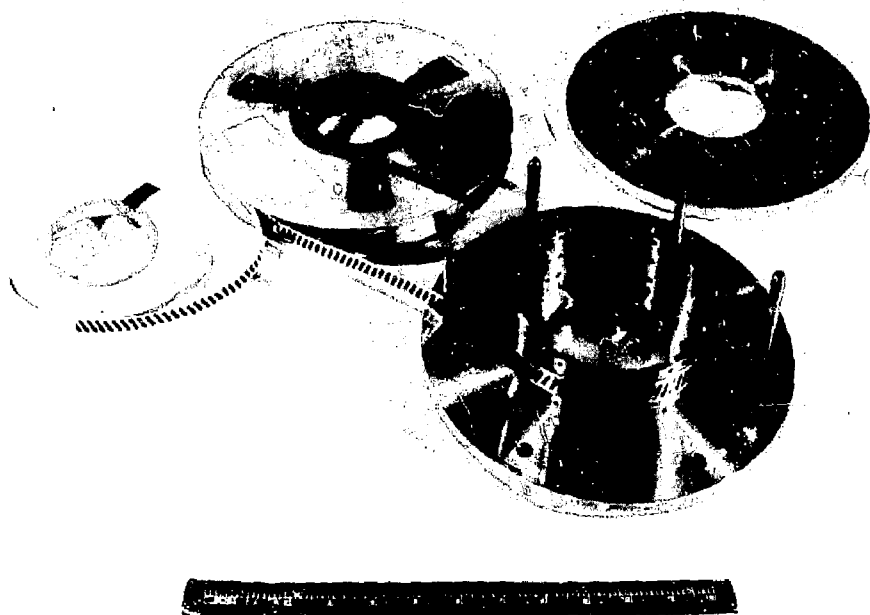


Fig. 64. Typical test magnet.

radial field exceeds 20 kG. The more severe method of presetting the magnet and sweeping the external field is shown by the lower line. (Before each test, the magnet was quenched in a zero external field to eliminate trapped flux and return the coil to the virgin state as near as possible). The data points shown correspond to currents and fields at which the magnet recovered from a massive flux jump. At higher currents, the magnet quenched when the total radial field exceeded 20 kG. Note that the lower line is quite level, indicating that the aluminum resistance is little affected by the increasing field. This particular conductor was capable of carrying 2000 A at 120 kG. However, the aluminum resistivity ratio was poor, only 2000, and the outer structural member was stainless steel of low thermal conductivity. As a result, the cryogenically stable current was only 400 A as compared to an expected 900 A. Further tests with nickel-clad conductors were better, but still there were differences between predicted and

measured results. Accordingly, liquid helium was circulated through the windings to prevent vapor locking during a flux jump. The stable current doubled, increasing the current density to the program goal of $10,000 \text{ A/cm}^2$. However, the magnet was too small to produce the 120 kG desired.

Other factors have been found which degrade the aluminum resistivity and the magnet performance. First, magneto-galvanic effects are observed with various orientations of the aluminum strip in a magnetic field as shown in Fig. 68. The lowest resistivity ratio, corresponding to the highest resistivity, occurs when the field is perpendicular to the face of the strip. Unfortunately, this is also the position of greatest instability in the superconductor. Earlier analysis by Sondheimer¹²² and Brandli and Olson¹²³ did not predict such an effect, but it has been observed independently by Feitz¹²⁴. However, even when including this magneto galvanic effect, the design resistivity ratio of 500 at 120 kG can still



Fig. 65. Test magnet mounting.

be achieved with aluminum having a bulk resistivity ratio above 5000. A second factor that degrades the aluminum resistivity is the peaking of the magneto resistance around 20°K . Here, the magneto resistance is four times higher than at 4.2°K . Since stable normal areas have been observed in our test magnets, we surmise that the conductor temperature is above the 18°K critical temperature for niobium tin. As such, the aluminum resistivity at 4.2°K upon which design calculations are made is degraded by a factor of 4. Coupling this with the previous galvanic magneto resistance observation could account for the lower stable currents observed in our test magnets. To be certain, the magneto galvanic tests will be repeated at 20°K , and magnet temperatures will be monitored.

An encouraging result was the insensitivity of the aluminum resistance to strain. In Fig. 69, the aluminum was bonded to various substrates that induced strains through differential thermal contraction. Note

that the strain effect is very small and generally consistent with earlier predictions. Accumulation of strain due to successive thermal cycles was found to be negligible, as well, and it was found that manufacturing strains could be annealed below 200°C , a temperature which is compatible with magnet insulation materials. We conclude that strain effects in aluminum will be of secondary importance.

Extensive work was done on the mechanical properties of high-purity nickel. The 4.2°K results (Fig. 70) show that adequate strength can be obtained through cold-working. Since yield strengths above 100 ksi are necessary, large cold reductions must be used. However, this occurs naturally when cooling channels are embossed into this nickel structural member. The Young's modulus is 32.5×10^6 psi, and the thermal conductivity is at least one hundred times better than that of stainless steel, as estimated by the Lorentz ratio and the

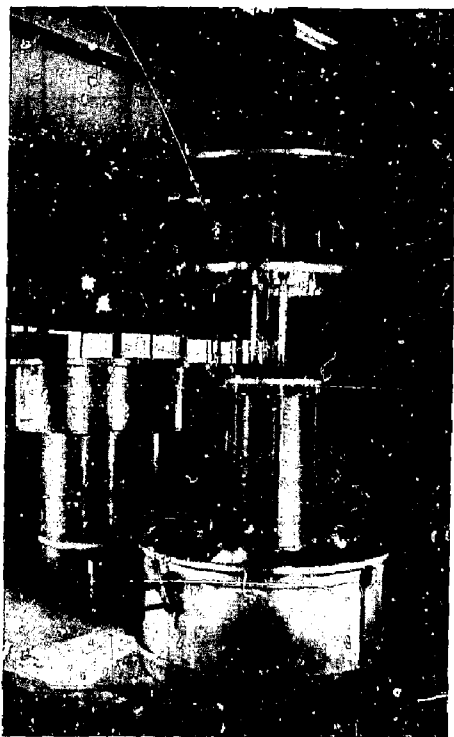


Fig. 66. 14-in. test bore facility.

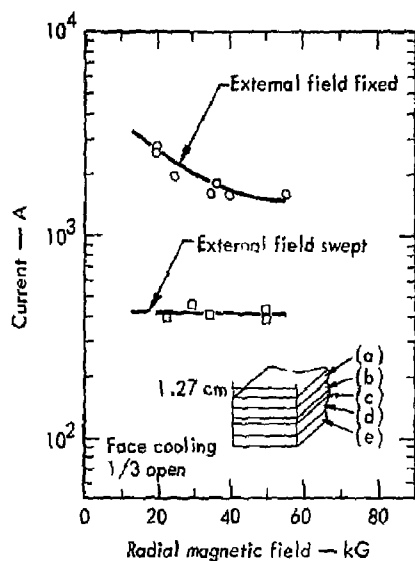


Fig. 67. Stability of aluminum, stainless steel clad Nb_3Sn . (a) Stainless steel 0.010; (b) aluminum 0.013, 2000 RRR; (c) Nb_3Sn 0.008; (d) aluminum 0.005, 2000 RRR; and (e) stainless steel 0.004.

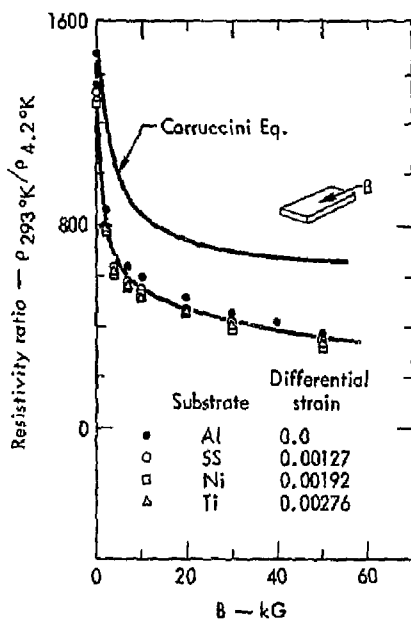


Fig. 69. Effects of strain on magnetoresistance.

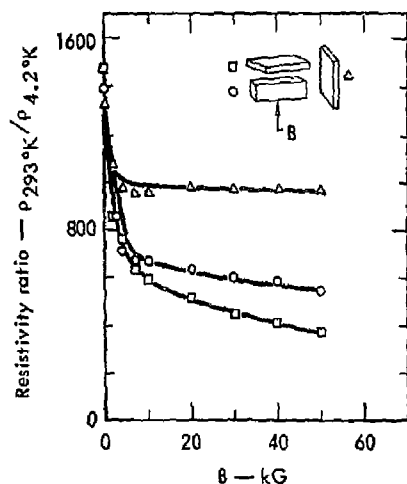


Fig. 68. Effects of orientation on magnetoresistance.

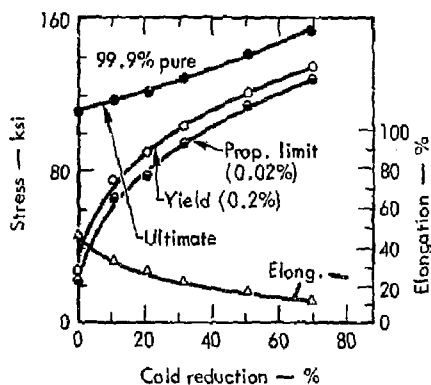


Fig. 70. Tensile properties of cold-rolled nickel-270 at 4.2° K.

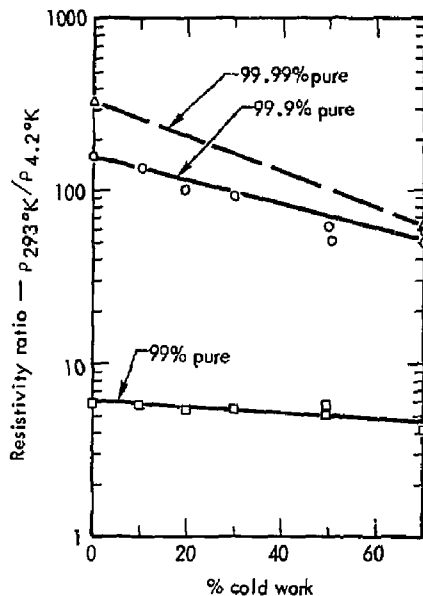


Fig. 71. Resistivity ratio of cold-worked nickel.
 $\rho_{293^{\circ}\text{K}} = 6.9 (\mu\Omega \text{ cm})$; $k = LT/\rho =$
 $14.5 \times \text{RR (mW/cm } ^{\circ}\text{K)}$.

resistivity data in Fig. 71. Either 99 or 99.9% pure nickel can be used; both are inexpensive, commercial-grade materials.

In summary, the mechanical properties of N_3Sn aluminum-nickel composite superconductors are well understood. Adequate means for aluminum bonding have been found, and better methods are under investigation. All aspects of aluminum resistivity are characterized except for magneto galvanic effects; these will require further work. Despite that,

cryogenic stability of N_3Sn superconductors has achieved the desired current density of $10,000 \text{ A/cm}^2$ at low fields with some circulation of helium to prevent vapor-locking in the magnet windings. To eliminate the need for circulation, aluminum resistivity ratios above 5000 will be necessary, and proper account must be taken of the aluminum magneto resistance near 20°K . Otherwise, it will be necessary to multifilament the niobium tin superconductor to avoid the high-temperature excursions from flux jumps.

IX. Talks and Publications

TALKS

First Topical Conference on RF Plasma Heating, Texas Tech. University, Lubbock, Texas, July 6-8, 1972

O. A. Anderson, D. H. Birdsall, C. W. Hartman, E. B. Hooper, Jr., R. H. Munger, Microwave Heating of Hot Electron Plasma in the Superconducting Levitron, UCRL-73881 Abstract, April 27, 1972.

1972 Cryogenic Engineering Conference, Boulder, Colorado, August 7-9, 1972

T. J. Duffy and C. E. Taylor, Refrigeration for the Livermore Superconducting Levitron, UCRL-73880 Preprint, April 27, 1972.

Fifth European Conference on Controlled Fusion and Plasma Physics, Grenoble, France, August 21-25, 1972

F. H. Coengsen, W. F. Cummins, A. W. Molyik, W. E. Nexsen and T. C. Simonen, Confinement Studies in 2XII, UCRL-74087 Preprint, August 18, 1972.

D. E. Baldwin, Collective Scattering as a Basis for 2X Decay, UCRL-73933 Abstract, May 17, 1972.

1st International Conference on Spectral Lines, Knoxville, Tenn., 28 Aug.-1 Sept. 1972

W. W. Hicks, Measurement of Hydrogen Spectral Line Profiles in Strong High-Frequency Electric Fields (LBL-983 Abstract).

International School on Fusion Reactor Technology, Erice (Trapani, Sicily) Italy, September 4-15, 1972

M. A. Hoffman, Magnetic Field Effects on the Heat Transfer of Potential Fusion Reactor Coolants, UCRL-73993 Preprint, June 23, 1972.

Second International Ion Source Conference, Vienna, Austria, September 11-16, 1972

J. E. Osher, Intense Ion and Neutral Beams with Low Energy, UCRL-74083 Preprint, August 15, 1972.

J. E. Osher, F. J. Gordon and G. W. Hamilton, Production of Intense Negative Ion Beams, UCRL-74082 Preprint, August 18, 1972.

K. W. Ehlers and W. B. Kunkel, Large-Area Uniform Quiescent Plasma Source for High-Current Ion Beam Production (LBL-915), in Proceedings of . . . , p. 259.

W. S. Cooper, K. H. Berkner, and R. V. Pyle, Production of Intense Ion and Neutral Beams with a Multiple-Slot, Large-Area Extractor (LBL-916), in Proceedings of . . . , p. 264.

Fourth International Conference on Magnet Technology, Brookhaven, N. Y., September 19-22, 1972

C. D. Henning, R. L. Nelson, H. L. Leichter, C. O. Mead, Experiments with Aluminum Bonded Nb₃Sn, UCRL-73860 Preprint, August 17, 1972.

Symposium on Plasma Heating and Injection, Varenna-Como, Italy, Sept. 21–Oct. 4, 1972

W. B. Kunkel, Progress in the Development of High-Intensity Neutral Beams (LBL-1018), in Proc. of . . .

Seventh Intersociety Energy Conversion Engineering Conference, San Diego, California, September 26–29, 1972

J. D. Lee, Neutronics of Sub-Critical Fast Fission Blankets for D-T Fusion Reactors (UCRL-73952 Preprint, 1972).

Mechanical Engineering Seminar, Tucson, Arizona, September 28, 1972

J. Hovingh, Controlled Fusion Power – A Solution to the Energy Crises, (UCRL-74223 Preprint, 1972).

1972 Annual Meeting of the Division of Plasma Physics of the American Physical Society, Monterey, California, November 13–16, 1972 [Published in Bull. Am. Phys. Soc. 17 (1972)]

M. E. Rensink, "Thin E-layer Equilibria," p. 1049.

L. D. Pearlstein and H. L. Berk, "Theoretical Aspects of Astron Build-up by Multiple Pulses," p. 1050.

E. P. Lee and L. D. Pearlstein, "Hollow Equilibrium and Stability of a Relativistic Electron Beam Propagating in a Preionized Channel," p. 1006.

R. M. Searing, "Excitation of Transverse Shear Waves in a Q-Machine," p. 975.

D. S. Prono, R. J. Briggs, and R. W. Bauer, "Measurement of Conductivity of the Plasma Channel Produced by a Current Modulated Relativistic Electron Beam," p. 982.

E. J. Lauer, J. M. Leary, R. W. Bauer, and R. J. Briggs, "Formation of Self-Focused Beam," p. 982.

F. H. Coensgen, W. F. Cummins, A. W. Molvik, W. E. Nexsen, and T. C. Simonen, "Plasma Confinement in 2XII," p. 1025.

J. H. Foote, "The Baseball II Digital-Computer Facility for Immediate and Automatic Experimental-Data Processing," p. 1047.

R. F. Post, "Influence of Ambipolar Potential on Convective Loss-Cone Instabilities in Mirror Machines," p. 1025.

L. S. Hall, "Quasi-One-Dimensional Fokker-Planck Equation for Loss Cone Diffusion," p. 979.

J. A. Byers, J. P. Holdren, J. Killeen, A. B. Langdon, A. A. Mirin, and M. E. Rensink, "Simulation of Pulse Trapping and Stacking in Astron Under Vacuum Conditions," p. 1050.

H. L. Berk and L. D. Pearlstein, "Instabilities Arising from B_θ and Plasma Background in Astron," p. 1049.

A. H. Futch and E. Thompson, "Decay of a Collisional Plasma Produced by Neutral Injection," p. 1004.

J. E. Osher, "Metastable Atom and U.V. Excitation as Corrections for Secondary Emission Type Fast Atom Detectors," p. 985.

R. K. Goodman, "Mass Analysis of the Low-Energy Ions in Baseball II," p. 1004.

W. L. Barr, B. C. Howard, R. W. Moir and R. R. Smith, "Numerical Studies of a Direct Energy Converter," p. 988.

R. W. Moir and W. L. Barr, "A Possible Direct Converter for Toroidal and Low Temperature Mirror Reactors," p. 988.

R. R. Smith, W. L. Barr and R. W. Moir, "Laboratory-Scaled Direct Energy Converter for Mirror Reactors," p. 988.

W. F. Cummins, T. N. Haratani, and G. C. Tyler, "2XII Data Systems," p. 1047.

C. C. Damm, J. H. Foote, A. H. Futch, R. K. Goodman, F. J. Gordon, G. W. Hamilton, A. L. Hunt, R. G. Mallon, J. E. Osher, and E. Thompson, "Plasma Characteristics in the Baseball II Mirror Experiment," p. 1004.

B. W. Stallard, N. C. Christofilos, G. D. Porter and P. B. Weiss, "Precessional Oscillations of the E-layer in High Vacuum," p. 997.

- G. D. Porter, "Calculations of the Axial Adiabatic Invariant for the Astron Experiment," p. 998.
- L. S. Hall and G. R. Haste, "Pressure Profiles of a Plasma in Hydromagnetic Equilibrium," p. 1063.
- W. E. Nexsen, Jr., W. F. Cummins, F. H. Coengsen, A. W. Molvik, T. C. Simonen, "Reduction of Neutral Analyzer Data," p. 985.
- T. K. Fowler and N. C. Christofilos, "Axial Compression of the Astron E-layer During Neutralization," p. 997.
- P. B. Weiss, N. C. Christofilos, G. D. Porter and B. W. Stallard, "Some Anomalous E-layer Losses in the Low Plasma Density Regime," p. 997.
- N. C. Christofilos, B. W. Stallard, G. D. Porter and P. B. Weiss, "Adiabatic Compression of the E-layer During its Neutralization Phase," p. 998.
- R. E. Hester, N. C. Christofilos, B. W. Stallard, G. D. Porter and P. B. Weiss, "Measurements of the High Vacuum Trapping Efficiency in Astron," p. 998.
- T. C. Simonen, F. H. Coengsen, W. F. Cummins, V. A. Finalyson, A. W. Molvik, G. H. Neilson, Jr., and W. E. Nexsen, Jr., "Radial and Longitudinal Electron Density Measurements in 2XII," p. 1025.
- C. W. Walker, N. C. Christofilos, B. W. Stallard, G. D. Porter and P. B. Weiss, "E-layer Stacking in High Vacuum," p. 998.
- J. Taska, N. C. Christofilos, B. W. Stallard, G. D. Porter and P. B. Weiss, "Late Adiabatic Compression of the E-layer," p. 998.
- E. B. Hooper, Jr., O. A. Anderson, D. H. Birdsall, C. W. Hartman, and R. H. Munger, "Dense Plasma Formation and Heating by Energetic Electrons in the Superconducting Levitron," p. 997.
- C. W. Hartman, O. A. Anderson, D. H. Birdsall, E. B. Hooper, Jr., J. Killeen, and R. H. Munger, "Hot Electron Plasma Equilibrium in the Superconducting Levitron," p. 997.
- O. A. Anderson, D. H. Birdsall, C. W. Hartman, E. B. Hooper, Jr., and R. H. Munger, "Hot Electron Plasma in Minimum $\partial B/\partial s$ Configuration," p. 997.
- R. P. Freis and C. W. Hartman, "Numerical Calculations of Magnetic Surfaces and Particle Orbits in a Toroidal Stellarator with Strong Helical Fields," p. 1039.
- J. Killeen, A. A. Mirin, P. M. Keeping and R. C. Grimm, "Numerical Studies of Radial Transport in Tokamaks," p. 1020.

APS Annual Meeting of the Division of Plasma Physics, Monterey, Calif., Nov. 13-16, 1972

- J. W. Stearns, K. H. Berkner, T. J. Morgan, and R. V. Pyle, Injection and Trapping of Neutral Deuterium Beams Containing $^3\text{H}_2$ Molecules (LBL-1066 Abstract), *Bull. Am. Phys. Soc.* 17, 973 (1972).
- R. A. Hess, Spectroscopic Study of Electric Fields in a Beam-Plasma Interaction (LBL-1076 Abstract), *Bull. Am. Phys. Soc.* 17, 1041 (1972).
- P. S. Rostler, W. S. Cooper, and W. B. Kunkel, Multiple-Beam Spectroscopy (LBL-1077 Abstract), *Bull. Am. Phys. Soc.* 17, 986 (1972).
- K. H. Berkner, W. R. Baker, W. S. Cooper, K. W. Ehlers, E. B. Hewitt, W. B. Kunkel, R. V. Pyle, and J. W. Stearns, Performance of an Intense Neutral Beam Source (LBL-1082 Abstract), *Bull. Am. Phys. Soc.* 17, 973 (1972).
- K. W. Ehlers, W. R. Baker, K. H. Berkner, W. S. Cooper, W. B. Kunkel, A. F. Lietzke, and R. V. Pyle (LBL-1083 Abstract), *Bull. Am. Phys. Soc.* 17, 973 (1972).
- F. Thompson and K. H. Berkner, Observation of Collisional Trapping in Baseball II (LBL-1084 Abstract), *Bull. Am. Phys. Soc.* 17, 973 (1972).
- A. Kaufman, D. Nicholson, M. Mostrom, and B. Cohen, Nonlinear Interaction of Opposed Electromagnetic Waves (campus), *Bull. Am. Phys. Soc.* 17, 1060 (1972).
- B. Cohen and A. Kaufman, Steady State Cascade of Transverse Modes in Plasma Beam Heating (campus), *Bull. Am. Phys. Soc.* 17, 1059 (1972).

- M. Mostrom, A. Kaufman, and D. Nicholson, Nonlinear Attenuation of an Intense Electromagnetic Beam by Induced Scattering in a Plasma Density Gradient (campus), Bull. Am. Phys. Soc. 17, 1065 (1972).
- G. M. Wheeler and R. V. Pyle, Low-Frequency Waves, Stabilization, and Particle Transport in an HCD Plasma (Stanford), Bull. Am. Phys. Soc. 17, 1012 (1972).

Texas Symposium on Technology of Controlled Thermonuclear Fusion Experiments and Engineering Aspects of Fusion Reactors, Austin, Texas, November 20--22, 1972

- G. W. Hamilton, A Design Study of a 14,000 Ampere Injection System for a Fusion Reactor, (UCRL-74034 Abstract and Summary (1972)). (UCRL-74096 Preprint, (1972)).
- B. H. Smith, L. L. Reginato and W. L. Dexter, An Engineering Study of the Electrical Design of a 1000 Megawatt Direct Converter for Mirror Reactors (UCRL-74047 Preprint (1972)).
- R. W. Moir and C. E. Taylor, Magnets for Open-Ended Fusion Reactors, (UCRL-74048 Abstract and Summary (1972)). (UCRL-74326 Preprint (1972)).
- R. W. Werner, G. A. Carlson, J. D. Lee, J. Hovingh and M. A. Peterson, Progress Report No. 1 on the Design of a 200 MWe Mirror Fusion Reactor, (UCRL-74054 Preprint, (1972)).
- R. G. Hickman, Some Problems Associated with Tritium in Fusion Reactors (UCRL-74057 Rev. 1 Preprint, 1972).

APS Fourth Annual Meeting of the Division of Electron and Atomic Physics, Menlo Park, Calif., 29 Nov.--1 Dec. 1972

- W. S. Cooper, Spectroscopic Measurements of High-Frequency Electric Fields in Plasmas by the Combined Zeeman and Stark Effects (LBL-1030 Abstract), Bull. Am. Phys. Soc. 17, 1144 (1972). Invited Paper.
- K. H. Berkner, R. V. Pyle and J. W. Stearns, Destruction Cross Sections of 266, 600, and 1200 keV H₂O in Li Vapor, and H₂ and N₂ Gases (LBL-1088 Abstract), Bull. Am. Phys. Soc. 17, 1131 (1972).

Symposium on the Anomalous Absorption of Intense High-Frequency Waves, Los Alamos, N. M., Mar. 1-2, 1973

- A. Kaufman, C. Max, B. Cohen, M. Mostrom, and D. Nicholson, Laser-Plasma Interactions in a Density Gradient (campus).

1973 Particle Accelerator Conference, San Francisco, California, March 5-7, 1973

- V. K. Neil and R. K. Cooper, RF System Random Frequency Error and its Effect on a Bunched Beam (UCRL-74297 Abstract, 1972).
- J. W. Beal, R. K. Cooper, W. A. Lamb, V. K. Neil, D. S. Prono, L. Smith and D. F. Wright, A Device for Bunching Relativistic Electrons (UCRL-74356 Preprint, 1973).

CTR Theory Meeting, Austin, Texas, March 12-13, 1973

- J. A. Byers, J. P. Holdren, A. B. Langdon, J. Killeen, A. A. Mirin, M. E. Rensink and C. G. Tull, Review of Results from Astron Computational Models, (UCRL-74589 Abstract, February 26, 1973).
- E. P. Lee, Evolution of a Relativistic Beam in a Torus, (UCRL-74591 Abstract, February 22, 1973).
- J. Dibiase and J. Killeen, Time Dependent Resistive Instability Calculations, (UCRL-74592 Abstract, February 26, 1973).
- W. A. Newcomb, The Drift Shock, (UCRL-74593 Abstract, February 23, 1973).

- H. L. Berk and D. E. Baldwin, Wave Reflection in Mirror Machines, (UCRL-74593 Abstract, February 27, 1973).
 J. R. Miskes and A. H. Futch, Some Observations on Mirror Losses, (UCRL-74597 Abstract, February 27, 1973).
 D. E. Baldwin and H. L. Berk, Sensitivity of the Drift-Cone Mode to Orbit Diffusion, (UCRL-74598 Abstract, February 26, 1973).
 B. McNamara and D. Fuss, Toroidally Linked Minimum-B Mirror Fields Having $-V$, (UCRL-74599 Abstract, February 26, 1973).
 H. L. Berk and C. W. Hartman, Stability of a Hot Electron Plasma, (UCRL-74600 Abstract, February 27, 1973).

IEEE Meeting, New York, N. Y., March 26-29, 1973

- R. F. Post, Nuclear Fusion by Magnetic Confinement, (UCRL-74445 Preprint, 1973).

12 Symposium on Electron, Ion, and Laser Beam Technology, Cambridge, Mass., May 21-23, 1973

- K. W. Ehlers, W. R. Baker, K. H. Berkner, W. S. Cooper, W. B. Kunkel, R. V. Pyle, and J. W. Stearns, Design and Operation of an Intense Neutral Beam Source (LBL-1589).

International Conference on Photonuclear Reactions and Applications, Pacific Grove, California, March 26-30, 1973

- P. B. Weiss, Energy Calibration of the Astron Accelerator, (UCRL-74491 Summary, 1973).

Third International Symposium on Toroidal Plasma Confinement, Garching, Germany, March 26-30, 1973

- C. W. Hartman, O. A. Anderson, D. H. Birdsall, E. B. Hooper, Jr., and R. H. Munger, Plasma Confinement and Heating in the Livermore Superconducting Levitron, (UCRL-74621 Preprint, 1973).

PUBLICATIONS

The Physics of Fluids

- K. G. Moses, R. W. Bauer and S. D. Winter, "Behavior of Relativistic Beams Undergoing Hose Motion in a Plasma Channel," 16 436 (March 1973).
 N. C. Christofilos and T. K. Fowler, "Axial Compression of the Astron E-Layer During Neutralization," 16 713 (1973).
 E. P. Lee and L. D. Pearlstein, "Hollow Equilibrium and Stability of a Relativistic Electron Beam Propagating in a Preionized Channel 16, 904 (1973).
 Marvin E. Rensink, "E-Layer Compression By a Toroidal Magnetic Field 15, 2391 (1972).
 Marvin E. Rensink, "Thin E-Layer Equilibria" 16, 443 (1973).
 H. L. Berk, and L. D. Pearlstein "Theoretical Aspects of Astron Build-up by Multiple Pulses" 15, 2396 (1972).
 T. K. Fowler, "Stability of the Tearing Mode in Astron", 15, 2075 (1972).
 Liu Chen, A. B. Langdon, M. A. Lieberman, "Shielding of Moving Test Particles in Warm, $1 \leq \beta$ Plasmas", 9 311 (1973).

The Journal of Computational Physics

- D. V. Anderson and J. Killeen, "Computation of Stable Equilibria in Minimum B Mirror Devices" 10, 133 (1972).
 A. B. Langdon, "Remarks on "Energy Conserving" Plasma Simulation Algorithms" 12, 247 (1973).

M. Brettschneider, J. Killeen and A. A. Mirin, "Numerical Simulation of Relativistic Electrons Confined in an Axisymmetric Mirror Field," 11, 360 (1973).

Nuclear Fusion

R. P. Freis, "Efficiency of a Direct-Conversion Collector for a Fusion Reactor" 13, 247 (1973).

J. R. Hiskes, "Atomic and Cluster Injection Into D-T Mirror Fusion Power Systems" 12, 423, (1973).

R. W. Moir and W. L. Barr, "Venetian Blind" (Direct Energy Converter for Fusion Reactors) 13, 35 (1973).

K. H. Berkner, T. J. Morgan, R. V. Pyle, and J. W. Stearns, Yields and Trapping of Neutral Deuterium Beams Containing $3H_2$ Molecules (LBL-1026), 13, 27 (1973).

The Review of Scientific Instruments

T. J. Fessenden, "The Aptren On-Line Beam Energy Analyzer" 43, 1090 (1972).

T. J. Fessenden, B. W. Stallard and G. C. Berg, "Beam Current and Position Monitor for the Astron Accelerator" 43, 1789 (Dec. 1972).

Annals of Physics

W. A. Newcomb, "The Perfect Gyroscopic Fluid" 72, 29 (1972).

Physical Review Letters

R. E. Aamodt and J. A. Byers "Particle Motion in Magnetic Mirrors with High Frequency Electric Field Fluctuations" 29, 1305 (1972).

W. C. Condit and D. Pellinen "Impedance and Spot Size Measurements on an Intense Relativistic Electron Beam Device" 29, 263 (1972).

Bruce I. Cohen, Allan N. Kaufman, and Kenneth M. Watson, Beat-Heating of Plasma (LBL-?, campus?), Phys. Rev. Letters 29, 581 (1972).

A. N. Kaufman and B. I. Cohen, Nonlinear Interaction of Electromagnetic Waves in a Plasma Density Gradient (LBL-2010), 30, 1306 (1973).

Physical Review A

K. H. Berkner, Isaac Bornstein, Robert V. Pyle, and J. Warren Stearns, Charge Fractions and Excited-Atom Populations of 8- to 100-keV Deuterium Beams Emerging from Solid Films of C, Mg, Nb, and Au (LBL-746), Phys. Rev. A 6, 278 (1972).

IEEE Transactions on Magnetics

R. J. Cooper, V. K. Neil, W. R. Woodruff, Optimum Permanent Magnet Dimensions for Repulsion Applications, (UCRL-74137 Preprint, Oct. 30, 1972) IEEE Trans. Magnetics IX, 125 (1973).

Physics Today

R. F. Post, "Fusion Power - Problems, Progress and Prospects" 26, 30 (1973).

Particle Accelerators

V. K. Neil and R. K. Cooper, "The Effect of Random RF Voltage Fluctuations on a Bunched Beam" Vol. 4, pp. 75-79, 1972.

The Journal of Applied Physics

N. C. Christofilos, A. B. Langdon, G. D. Porter and M. E. Rensink "Resistor Focusing of the Injected Electrons in the Astron" 44, 660 (1973).

Ph.D. THESIS

R. A. Hess, Study of Beam-Plasma Instability by Spectroscopic Methods (LBL-1531, Dec. 1972).

W. M. Tang, Finite Beta and Finite Geometry Effects on Microinstabilities in Mirror Confined Plasmas, (UCRL-51265, Aug. 18, 1972).

References

1. D. V. Anderson and J. Killeen, J. Comp. Phys. **10**, 133 (1973).
2. J. B. Taylor, Phys. Fluids **6**, 1529 (1973).
3. J. P. Holdren, Nucl. Fusion **12**, 267 (1972).
4. L. S. Hall, Phys. Fluids **15**, 882 (1972).
5. A. H. Futch, Jr., J. P. Holdren, J. Killeen and A. A. Mirin, Plasma Phys. **14**, 211 (1972).
6. J. Killeen and K. D. Marx, Methods Comp. Phys. **9**, 421 (1970).
7. L. S. Hall, Phys. Fluids **15**, 710 (1972).
8. C. W. Horton, Jr., Propagation and Reflection of the Loss-Cone Mode in an Inhomogeneous Plasma, Ph.D. Thesis, Univ. Calif., San Diego (1967).
9. D. E. Baldwin and J. D. Callen, Phys. Rev. Letters **28**, 1686 (1972).
10. H. L. Berk, Unfinished Theoretical Problems in Mirror Research, Lawrence Livermore Laboratory, Rept. UCID-16293 (1973).
11. C. B. Moler and G. W. Stewart, An Algorithm for the Generalized Matrix Eigen Problem, $Ax = \lambda Bx$, Computer Science Dept., School of Humanities and Sciences, Stanford University, Rept. STAN-CS-232-71 (1971).
12. J. B. Taylor and B. McNamara, Phys. Fluids **14**, 1492 (1971).
13. R. E. Aamodt and D. E. Baldwin, Electron Scattering by Enhanced Fluctuation in Quiescent 2XII Decay, Lawrence Livermore Laboratory, Rept. UCID-16202 (1973).
14. H. L. Berk, L. D. Pearlstein and J. G. Cordey, Phys. Fluids **15**, 891 (1972).
15. L. D. Pearlstein and D. Bhadra, Phys. Fluids **12**, 213 (1969).
16. O. Buneman, J. Comp. Phys. **1**, 517 (1967).
17. R. L. Morse and C. W. Nielson, Phys. Fluids **14**, 830 (1971).
18. J. P. Boris, in Proc. Fourth Conf. Numerical Simulation of Plasmas, J. P. Boria and R. A. Shanny, Eds., (Office of Naval Research, Arlington, Va., 1971), p. 3.
19. O. Buneman, Stanford University Inst. of Plasma Research, Rept. Suipr-467, p. 5 (footnote).
20. O. Buneman, in Relativistic Plasma, O. Buneman and W. Pardo, Eds. (Benjamin, New York, 1968), p. 205.
21. A. B. Langdon, Phys. Fluids **15**, 1149 (1972).
22. A. B. Langdon, B. F. Lasinski and W. L. Kruer, Plasma Heating at One-Quarter Critical Density, Lawrence Livermore Laboratory, Rept. UCRL-75018 (1973).
23. Controlled Thermonuclear Research Annual Report, July 1971 through June 1972, Lawrence Livermore Laboratory, Rept. UCRL-50002-72 (1972).
24. I. B. Bernstein, Transport in Axisymmetric Plasmas, Lawrence Livermore Laboratory, Rept. UCRL-74505 (1973). Submitted to Phys. Fluids.
25. H. P. Furth, J. Killeen and M. N. Rosenbluth, Phys. Fluids **6**, 459 (1963).
26. B. Coppi, J. M. Greene and J. L. Johnson, Nucl. Fusion **6**, 101 (1966).
27. R. D. Gibson and K. J. Whitman, Plasma Phys. **10**, 1101 (1968).
28. D. C. Robinson, Plasma Phys. **13**, 439 (1971).
29. H. P. Furth, P. H. Rutherford and H. Selberg, Princeton Plasma Physics Laboratory, Rept. MATT-897 (1972).
30. V. D. Shafranov, Zh. Tech. Fiz. **40**, 241 (1970).
31. L. S. Solovov and V. D. Shafranov, in Reviews of Plasma Physics, Vol. 5, M. A. Leontovich, Ed. (Plenum Press, New York, 1970).
32. D. Fuss and B. McNamara, "Magnetic Fields Having -V" and Min-B," Sherwood Theory Meeting, University of Texas, Austin, Texas, April 1973.
33. B. McNamara and A. B. Langdon, Efficient Use of Disc for Large Programs, Lawrence Livermore Laboratory, Rept. UCRL-74707 (1973).

34. J. R. Hiskes, The Form of the Cascade Solution, Lawrence Livermore Laboratory, Rept. UCID-16121 (1972).
35. J. R. Hiskes, Recommended Excitation and Ionization Cross Sections for Cascade, Lawrence Livermore Laboratory, Rept. UCID-16307 (1973).
36. W. A. Newcomb, The Drift Shock, Phys. Fluids Letters (to be published) (Preprint UCRL-74593).
37. R. K. Goodman and A. L. Hunt, Rev. Sci. Instr. 42, 1359 (1971).
38. D. O. Hayward and B. M. W. Trapnell, Chemisorption (Butterworths, London, 1964), p. 281.
39. P. A. Redhead, J. P. Hobson and E. V. Kornelsen, The Physical Basis of Ultra-High Vacuum (Chapman and Hall, London, 1968), p. 81.
40. W. Band, An Introduction to Quantum Statistics (D. Van Nostrand, New York, 1955), Chap. 5.
41. Controlled Thermonuclear Research Annual Report, July 1970 through June 1971, Lawrence Livermore Laboratory, Rept. UCRL-50002-71 (1971).
42. A. L. Gardner, A Null Method of Measuring Microwave Phase Shifts, Lawrence Livermore Laboratory, Rept. UCRL-7978 (1964).
43. J. E. Osher, Metastable Atom and UV Excitation as Corrections for Secondary Emission-Type Fast Atom Detectors, Lawrence Livermore Laboratory, Rept. UCID-16283 (1973). Also Bull. Am. Phys. Soc. 17, 985 (1972).
44. G. W. Hamilton and R. W. Moir, Conditions for Landau Damping and Wave Reflections in Open-Ended Magnetic Well Plasmas, Lawrence Livermore Laboratory, Rept. UCRL-50900 (1970).
45. C. C. Damm et al. Phys. Rev. Letters 24, 495 (1970).
46. J. H. Foote, Calculated Ion-Density Spatial Distribution in Alice Baseball I, Lawrence Livermore Laboratory, Rept. UCID-15647 (1970).
47. T. K. Fowler and M. Rankin, Plasma Phys. (J. Nucl. Energy, Part C) 4, 311 (1962).
48. K. D. Marx, Phys. Fluids 13, 1355 (1970).
49. D. V. Sivukov, in Reviews of Plasma Physics, Vol. 4, M. A. Leontovich, Ed. (Consultants Bureau, New York, 1966), p. 93.
50. L. Spitzer, Physics of Fully Ionized Gases, 2nd Ed., (Interscience, New York, 1962), p. 134.
51. K. H. Berkner, W. B. Cooper and R. V. Pyle, "Multiple Aperture Extractor Design for Producing Intense Ion and Neutral Beams," in Proc. Symp. Ion Sources and Formation of Ion Beams, Brookhaven National Laboratory, Rept. BNL-50310 (1971), p. 165.
52. W. S. Cooper, private communication (August 1972).
53. J. R. Coupland and A. C. Riviere, "The Beam Divergence from a Single-Aperture, Three-Electrode Accel-Decel Extraction System," in Proc. 2nd Intern. Conf. Ion Sources, Vienna, Austria, 1972, p. 168.
54. J. E. Osher, F. G. Gordon and G. W. Hamilton, "Production of Intense Negative Ion Beams," in Proc. 2nd Intern. Conf. Ion Sources, Vienna, Austria, 1972, p. 876.
55. J. E. Osher, "Intense Ion and Neutral Beams with Low Energy," Ibid., p. 234.
56. J. E. Osher and G. W. Hamilton, "An Intense 1-kV Ion Source for Controlled Fusion Research," in Proc. Symp. Ion Sources and Formation of Ion Beams, Brookhaven National Laboratory, Rept. BNL-50310 (1971), p. 171.
57. G. W. Hamilton and J. E. Osher, "A Design Study of a 14,000-Ampere Injection System for a Fusion Reactor," to be published in Proc. Texas Symp. Controlled Thermonuclear Experiments, Technol. Fusion Reactors, Austin, Texas, Nov. 20-22, 1972.
58. K. W. Ehlers and W. B. Kunkel, in Proc. 2nd Intern. Conf. Ion Sources, Vienna, 1972, p. 259; W. S. Cooper, K. H. Berkner and R. V. Pyle, Ibid., p. 264.
59. F. H. Coensgen et al., 2XII Program Plan, Lawrence Livermore Laboratory, Proposal 102, Feb. 1973.
60. F. H. Coensgen et al., in Proc. 5th European Conf. Controlled Fusion and Plasma Physics, August 1972, Vol. II, p. 71. (Also UCRL-74087).

61. D. E. Baldwin and J. D. Callen, Phys. Rev. Letters **28**, 1683 (1972).
62. J. Killeen and J. D. Marx, Methods in Computational Physics, Vol. 9 (Academic Press, New York, 1970), pp. 422-489.
63. C. B. Wharton et al., "New Results in Turbulent Heating," in Proc. 4th Intern. Conf. Plasma Phys. Controlled Thermonuclear Fusion Res., Madison, Wisc., June 1971 (IAEA, Vienna, 1971), Vol. II, p. 25.
64. V. D. Shapiro, Soviet Phys. JETP **17**, 416 (1963); and Ya B. Fainberg, V. D. Shapiro and V. I. Shevchenko, Soviet Phys. JETP **30**, 528 (1970).
65. M. Seidl and P. Sunka, Nucl. Fusion **7**, 237 (1967).
66. L. Spitzer, Jr., Physics of Fully Ionized Plasmas (John Wiley and Sons, New York, 1962).
67. R. J. Burke, Experimental Determination of the Deceleration of Fast Ions in a Dense Plasma: The Coefficient of Dynamical Friction, Lawrence Livermore Laboratory, Rept. UCRL-51175 (1972).
68. C. F. Barnett et al, Atomic and Molecular Collision Cross Sections of Interest in Controlled Thermonuclear Research, Oak Ridge National Laboratory, Rept. ORNL-3113 (1964).
69. F. H. Coengsen, W. F. Cummins, W. E. Nexsen, Jr. and T. C. Simonen, Initial Operation of 2XII, Lawrence Livermore Laboratory, Rept. UCRL-51208 (1972).
70. T. C. Simonen et al., Microwave Measurement of 2XII Radial and Longitudinal Electron Density Profiles, Lawrence Livermore Laboratory, Rept. UCRL-51348 (1973).
71. W. E. Nexsen, Jr. et al., Bull. Am. Phys. Soc. **17**, 985 (1972).
72. W. E. Nexsen, Jr. and F. H. Coengsen, Bull. Am. Phys. Soc. **16**, 1246 (1971).
73. J. P. Holdren, Nucl. Fusion **12**, 267 (1972).
74. D. E. Baldwin et al., in Proc. 4th Conf. Plasma Phys. Controlled Thermonuclear Fusion Research, Madison, Wisc., June 1971 (IAA, Vienna, 1971), Vol. II, p. 135.
75. G. C. Tyler, "Automatic Data Processing System for 2XII," in Proc. 4th Symp. Energy Problems of Fusion Research, Naval Research Laboratory, April 20-23, 1971.
76. W. F. Cummins, Rev. Sci. Instr. **41**, 2 (1970).
77. C. J. Anderson, Lawrence Livermore Laboratory, Internal Document ENR-72-18 (Aug. 11, 1972); ENE-73-5 (Feb. 9, 1973); ENE-73-6 (March 6, 1973); ENE-73-8 (March 23, 1973). Readers outside the Laboratory who desire further information on LLL internal documents should address their inquiries to the Technical Information Department, Lawrence Livermore Laboratory, Livermore, CA 94550.
78. C. J. Anderson, Lawrence Livermore Laboratory, Internal Document ENE-73-16 (June 28, 1973).
79. R. W. Moir and J. D. Lee, Criteria for Design of an Adiabatic Expander for a Direct Energy Converter, Lawrence Livermore Laboratory, Rept. UCRL-51351 (1973).
80. R. W. Moir, W. L. Barr, R. P. Freis and R. F. Post, in Proc. Conf. Plasma Phys. Controlled Thermonuclear Fusion Research, Madison, Wisc., June 1961 (IAEA, Vienna, 1971), Vol. III, pp. 315-328.
81. F. B. Marcus and C. J. H. Watson, Sixth European Conf. Controlled Fusion and Plasma Phys., Moscow, USSR, 1973.
82. R. W. Moir, W. L. Barr and T. N. Haratani, Optimization of Collector Efficiencies for Direct Energy Converters for Fusion Reactors, Lawrence Livermore Laboratory, Rept. UCRL-51321 (1973).
83. R. R. Smith and S. Rompel, A Two-Zone Potential Relaxation Scheme for Handling Grid Wires, Lawrence Livermore Laboratory, Rept. UCRL-51383 (1973).
84. R. W. Moir and W. L. Barr, Nucl. Fusion **13**, 35 (1973).
85. W. L. Barr et al., A Preliminary Engineering Evaluation of a "Venetian Blind" Direct Energy Converter for Reactors, Lawrence Livermore Laboratory, Rept. UCRL-74636 (1973). (Submitted to IEEE Trans. Plasma Sci.)
86. R. R. Smith, Plasma Expander for Venetian Blind Direct Converters, Lawrence Livermore Laboratory, Rept. UCRL-51373 (1973).

87. O. A. Anderson, D. H. Birdsall, C. W. Hartman, E. B. Hooper, Jr. and R. A. Meinger, Phys. Rev. Letters **31**, 10 (1973).
88. O. A. Anderson, D. H. Birdsall, C. W. Hartman and E. B. Hooper, Jr., Phys. Rev. Letters **32**, 274 (1974).
89. C. W. Hartman, Phys. Rev. Letters **26**, 826 (1971).
90. O. A. Anderson and C. W. Hartman, Plasma Heating in the Superconducting Levitron by Energetic Electrons, Lawrence Livermore Laboratory, Rept. UCRL-50824 (1970).
91. O. A. Anderson et al., in Plasma Phys. Controlled Nucl. Fusion Res., **1**, 103 (1973).
92. A. C. Hindmarsh, GEAR: Ordinary Differential Equation Solver, Lawrence Livermore Laboratory, Rept. UCID-30001, Rev. 1 (1972).
93. L. Pages, E. Bertel, H. Joffe and L. Sklavenitis, Atomic Data, **4**, 1 (1972).
94. R. E. Hester et al., High-Vacuum Trapping Experiments on the Astron, Lawrence Livermore Laboratory, Rept. UCRL-74990 (1973). (Submitted to Phys. Fluids.)
95. R. J. Briggs et al., Efficient Trapping of High-Level E-Layers in a Strong Toroidal Field, Lawrence Livermore Laboratory, Rept. UCRL-74673. (Accepted by Phys. Fluids for Nov. 1973 issue.)
96. J. W. Beal, Quadrupole Fields in a Toroidal Geometry for the High-Intensity Storage Ring, Lawrence Livermore Laboratory, Rept. UCID-15735 (1970).
97. K. W. Ehlers et al., Nuclonics **10** 8; 10 40 (1952).
98. G. W. Hamilton and J. E. Osher, private communication.
99. W. W. Hicks, R. A. Hess and W. S. Cooper, Phys. Rev. A **5**, 490 (1972).
100. K. Halbach, A Program for Inversion or System Analysis, Lawrence Berkeley Laboratory, Rept. UCRL-17436 (1967).
101. P. S. Rostler, W. S. Cooper and W. B. Kunkel, Bull. Am. Phys. Soc. **17**, 986 (1972); also see UCRL-50002-72 (1972).
102. P. S. Rostler, Multiple-Beam Spectroscopy, Lawrence Berkeley Laboratory, Rept. LBL-2014, in preparation.
103. S. A. Self, J. Appl. Phys. **40**, 5217 (1969).
104. Controlled Thermonuclear Research Annual Report, July 1969 through June 1970, Lawrence Livermore Laboratory, Rept. UCRL-50002-70 (1970).
105. T. R. Jarboe and W. R. Baker, Lawrence Berkeley Laboratory, Rept. LBL-2069 (submitted to Rev. Sci. Instr.).
106. R. Werner et al., Progress Report (No. 1 & 2) on Design Considerations for a Low-Power Experimental Mirror Fusion Reactor, Lawrence Livermore Laboratory, Rept. UCRL-74054. Presented at the Texas Symp. Controlled Thermonuclear Experiments and Technol. of Fusion Reactors, Austin, Texas, Nov. 20-22, 1972.
107. M. A. Hoffman and G. A. Carlson, Calculation Techniques for Estimating the Pressure Losses for Conducting Fluid Flows in Magnetic Fields, Lawrence Livermore Laboratory, Rept. UCRL-51010 (1971).
108. G. A. Carlsen, "Magnetohydrodynamic Pressure Drop of Lithium Flowing in Conducting Wall Pipe in a Transverse Magnetic Field - Theory and Experiment". To be presented at the ANS First Topical Meeting, San Diego, April 16-18, 1974, Preprint UCRL-75307.
109. G. A. Carlsen, Selective Leakage of Charged Particles in Mirror Machines, Lawrence Livermore Laboratory, Rept. UCRL-51434 (1973).
110. M. A. Hoffman, "Magnetic Field Effects on the Heat Transfer of Potential Fusion Reactor Coolants." Presented at the Intern. School of Fusion Reactor Technol., Erice (Trapani, Sicily) Italy, UCRL-73993 (1973).
111. M. A. Peterson, Lawrence Livermore Laboratory, Internal Document TRM-39 (April 12, 1973).
112. Jack Hovingh, Lawrence Livermore Laboratory, Internal Document TRM-30 (August 21, 1972).

113. R. W. Werner et al., "Progress Report No. 1 on the Design of a 200-MWe Mirror Fusion Reactor." Presented at the Texas Symp. Technol. Controlled Thermonuclear Fusion Experiments, Engrg. Aspects Fusion Reactors, Austin, Texas, Nov. 20-22, 1972. Lawrence Livermore Laboratory, UCRL-74054 (Abstract).
114. J. Hovingh and R. W. Moir, Efficiency of Injection of High-Energy Beams into Thermonuclear Reactors, Lawrence Livermore Laboratory, Rept. UCRL-51419 (1973).
115. J. Hovingh, Lawrence Livermore Laboratory, Internal Document TRM-43 (May 16, 1973).
116. J. Hovingh, Lawrence Livermore Laboratory, Internal Document TRM-45 (May 18, 1973).
117. C. M. Logan, Proton Simulation of Displacement Effects Induced in Metals by 14-MeV Neutrons, Lawrence Livermore Laboratory, Rept. UCRL-51224 Rev. 1 (1972).
118. R. G. Hickman, "Some Problems Associated with Tritium in Fusion Reactors," presented at the Texas Symp. Technol. Controlled Thermonuclear Fusion Experiments Engrg. Aspects Fusion Reactors, Austin, Texas, Nov. 20-22, 1972, Lawrence Livermore Laboratory Rept. UCRL-74057, Rev. 2 (1972).
119. R. G. Hickman, "Tritium in Fusion Power Reactor Blankets." Lawrence Livermore Laboratory, Rept. UCRL-74633 (1973). Submitted to Nucl. Technol.
120. R. W. Moir and C. E. Taylor, "Magnets for Open-Ended Fusion Reactors," presented at the Texas Symp. Technol. Controlled Thermonuclear Fusion Experiments Engrg. Aspects Fusion Reactors, Austin, Texas, Nov. 20-22, 1972.
121. C. D. Henning, et al., "Experiments with Aluminum Bonded Nb₃Sn," in Proc. Fourth Intern. Conf. Magnet Technol. (1972), pp. 521-528.
122. E. H. Sondheimer, Phys. Rev. 80, 401 (1950).
123. G. Grandli and J. L. Olsen, Mater. Sci. Eng. 4, 2 (1969).
124. W. Feitz, Intermagnetics General, private communication.